Growth and Doping of Carbon Nanotubes and Graphene

SALEH MARZOQ B. ALLUQMANI

Growth and Doping of Carbon Nanotubes and Graphene

By

Saleh Marzoq Alluqmani

A thesis submitted in partial fulfilment of the requirements
for the degree of Doctor of Philosophy

Department of Physics
University of Durham

December, 2014

Abstract

Single walled carbon nanotubes (SWCNTs) have been doped with nitrogen (N) by two ion-mediated approaches: directly through irradiation with N^+ ions and by a novel indirect technique, creating defects through Ar^+ ion irradiation which then react with nitrogen upon annealing in a N_2 atmosphere. X-ray photoelectron spectroscopy (XPS) was then employed to determine the chemical environment of the nitrogen within the resulting SWCNT material. Depending upon the exact preparation conditions, nitrogen in graphitic (substitutional) pyridinic and pyrrolic configurations could be identified. Nitrogen doping through the novel method was found to introduce the largest concentration of chemisorbed nitrogen within the SWCNT films, dominated by thermodynamically unstable pyrrolic species at low process temperatures (500ºC). The maximum concentration of nitrogen in graphitic sites was achieved by direct ion bombardment, although both XPS and Raman spectroscopy indicated that this approach to doping led to the greatest damage. The ability to vary both bsolute and relative composition of chemisorbed nitrogen species is expected to be valuable for a range of fundamental studies, particularly of the catalytic behaviour of these materials.

The growth of graphene on copper under atmospheric pressure using a soft solid source (nonadecane) is reported. It is found that the growth rate is best described by a model which involves the continuous supply of reactive species during the entire growth period. This observation is explained in terms of the formation of decomposition produces which reside on an otherwise clean surface after nonadecane desorption and provide a series of 'mini carbon sources' for graphene growth. XPS analysis indicates that, as expected, increased growth temperature leads to greater graphitisation at the surface (and hence graphene 'quality') which is not accompanied by any substantial change in island size and coverage. It is found that although graphene islands can be produced it is not possible to form continuous films, demonstrating the limitations of this technique.

Although limited in some ways, the use of soft solid precursors for graphene growth allows the ready introduction of potential dopant materials. XPS, Raman and SEM data provide strong evidence that a PDMS precursor can be employed in atmospheric pressure solid-phase CVD to produce graphene heavily doped with silicon, which has not been previously achieved. Since silicon-doped graphene is predicted to possess a band gap related to the Si concentration, this may provide a route to produce a graphene-based material of use in digital electronics.

Table of Contents

List of Abbreviations

AES	Auger Electron Spectroscopy
AFM	Atomic Force Microscopy
APCVD	Atmospheric Pressure Chemical Vapour Deposition
BE	Binding Energy
BWF	Breit-Wigner-Fano
2D	Tow-dimensional
CNT	Carbon Nanotubes
CVD	Chemical Vapour Deposition
FETs	Field Effect Transistors
BSE	Backscattered electrons
CL	Cathodoluminescence
CN	Carbon Nanotube
CNT	Carbon nanotube
DB	Dangling Bond
DFT	Density Functional Theory
DWCNT	Double-walled carbon nanotube
EBIC	Electron-beam induced conductivity
EELS	Electron energy loss spectroscopy
ESCA	Electron Spectroscopy for Chemical Analysis
FEL	Fast entry load-lock
FET	Field Effect Transistor
FIB	Focused Ion Beam
FWHM	Full-width half-maximum
GHL	Gas Handling line
GNRs	Graphene Nanoribbons
GPIB	General Purpose Interface Bus
HiPCO	High pressure carbon monoxide disproportionation
HOPG	Highly Oriented Pyrolytic Graphite
HRTEM	High resolution transmission electron microscopy
iLA	in-plane Longitudinal Acoustic phonon
iLO	in-plane Longitudinal Optic phonon
iTA	in-plane Transverse Acoustic phonon
iTO	in-plane Transverse Optic phonon
oTA	out of plane Transverse Acoustic phonon
oLA	out of plane Longitudinal Optic Phonon
IMFP	Inelastic Mean Free Path
JMAK	Johnson-Mehl-Avrami-Kolmogorov
LEED	Low Energy Electron Diffraction
MWCNT	Multiple-Walled Carbon Nanotube
OM	Optical Microscopy
PAN	Polyacrylonitrile
PDMS	polydimethylsiloxane
PMMA	Polymethylmethacrylate
POM	Polarised Optical Microscopy
ppm	*parts per million*
QMS	Quadrupole Mass Spectrometer
ORR	Oxygen Reduction Reaction
RS	Raman Spectroscopy

RBM	Radial Breathing Mode
RFA	Retarding Field Analyser
SE	Secondary Electrons
SEM	Scanning Electron Microscopy
sccm	standard cubic centimetres per minute
SPM	Scanning Probe Microscope
STM	Scanning Tunneling Microscopy
SWCNT	Single-walled Carbon Nanotube
SWNTs	Single-Walled Carbon Nanotubes
SWT	Stone-Wales-Thrower
TEM	Transmission Electron Microscopy
UHV	Ultra-High Vacuum
UPS	Ultra-violet Photoemission Spectroscopy
VUV	Vacuum Ultra-Violet
XPS	X-ray Photoemission Spectroscopy

Declaration

No part of this thesis has been submitted elsewhere for any other degree or qualification. The content of this thesis is the author's own work, unless otherwise stated in the text. The sample preparation, measurement and data analysis was carried out by the author, with the exception of the Raman measurements reported in this thesis (Chapters 4 and 6), which were performed by Prof. Andrew Beeby of the Department of Chemistry, Durham University. The SEM measurements presented in Chapters 4 and 5 were made in conjunction with Mr Leon Bowen of the G.J. Russell Electron Microscopy Facility. The XPS measurements reported in Chapter 4 were made with the help of Dr. Lidija Šiller and Dr Ross Little of the School of Chemical Engineering and Advanced Materials, University of Newcastle and those in Chapters 5 and 6 with the help of Dr. Šiller.

Acknowledgements

I am very grateful to my supervisor, Dr. Michael R. C. Hunt, for his invaluable contribution during my PhD course. This period of my PhD would not have been possible without his patience, academic and personal support. Dr. Hunt's supervision on my work cannot be thankfully expressed by own words.

I must thank University of Durham and Department of Physics and Center of Materials Physics (CMP) for their help, support, training and making my PhD study possible.

I would like to extend my gratitude to Dr. Lidija Siller and Dr. Ross Little, in Newcastle University, for giving me the opportunity to carry out XPS and RS experiments and helping me to acquire my data presented in this thesis.

Thanks must go Mr. Duncan McCallum, David Pattinson and Mr. John Dobson for their technical assistance and discussions on laboratory issues.

I also gratefully thank Mr Leon Brown for his kind assistance and helpful discussion on SEM measurements.

I am indebted to thank deeply the Ministry of Higher Education, Umm Al Qura University in Saudi Arabia, and Saudi Arabian Culture Bureau in London, who generously sponsor and support my PhD degree.

I am especially grateful to my parents for their patience, family and my friends for their emotional support through the time of PhD.

Finally, thanks go for everyone who gives me technically or personally support in any way to my work or my PhD life in the UK or in Saudi Arabia.

Saleh Marzoq Alluqmani, Durham UK, 2014

Chapter 1

Introduction

This chapter provides a short introduction to single walled carbon nanotubes and graphene materials. It includes a description of their structure and most significant properties. Growth, doping and potential applications are discussed, placing the work of this thesis into context.

1.1 Carbon nanotubes (CNTs)

Scientific interest in carbon nano-structures started seriously after Kroto *et al.*[1] discovered a closed cluster of sp^2-hybridised carbon containing precisely 60 carbon atoms arranged in a truncated icohosahedron – the same as that of a modern soccer ball. This material, which became known as buckminsterfullerene or C_{60}, initiated an enormous explosion in nano-carbon research and several other all-carbon closed shell molecules (fullerenes), such as C_{70}, were also discovered. In their experiments Kroto *et al.* used a laser vaporisation method to produce a plume of graphitic soot containing C_{60}, which initially limited the quantity of material which could be produced and hence the ability of the scientific community to investigate its properties. However, this discovery led others to focus on the production of macroscopic quantities of fullerenes, and Krätschmer and Huffman[2] achieved this using an arc discharge between graphite electrodes under a He atmosphere. In 1990, Iijima studied the surfaces of electrodes which had been used in the production of fullerene-containing soots by the Krätschmer-Huffman technique using high resolution transmission electron microscopy (HRTEM)[3]. His observations led him to the (re-)discovery of cylinders of graphitic carbon which were termed 'carbon nanotubes' (CNTs). CNTs were first discovered around 1952 by Radushkevich *et al.* and perhaps were observed earlier[4,5]. However, little comment was made at the time and it was only after Iijima's observation that significant attention was directed towards these novel nanostructures. Research on CNTs is now very active due to the outstanding physical properties displayed by these structures such as ultra-high strength, thermal conductivity and their electrical behaviour.

CNTs have a promising future in many different areas of research and applications. The electrical properties of CNTs (such as ballistic transport over micron lengthscales) may, in future, enable them to play a very significant role in molecular scale electronics because silicon and other materials are known to approach their limits at this scale[6]. The ability of CNTs to behave as semiconductors or metals depending on their geometry has led to the demonstration of transistors with CNTs as active elements which might eventually find themselves in integrated circuits and lead to a revolution in the computer industry[6]. With a diameter of around 1-3 nm, a single-wall carbon nanotube (SWCNT) is the smallest conducting wire to date and does not suffer from the problems of electromigration found in thin copper wires[7]. It is not only the electrical behaviour of CNTs which can be exploited in

applications. Due to the structure of CNTs, they have significant flexibility without fracture which, along with their high aspect ratio, offers excellent behaviour for scanning probe microscope tips[8]. Furthermore, it is possible to see CNTs as a nanosize container system to be used in drug delivery for cancer treatment or in novel nanomaterials[9].

CNTs can be classified into two categories: the first, known as multi-walled carbon nanotubes (MWCNTs), Fig 1.1(a), consist of two or more concentric graphitic cylinders with a spacing between the layers of about 0.34 nm (similar to that between the layers of graphite) and an outer diameter typically in the range of 10 – 20 nm (quite often two-layered MWCNTs are referred to as double-wall carbon nanotubes, or DWCNTs). MWCNTs were the first form of CNTs observed by Iijma[3]. The second type of nanotube is the single walled carbon nanotube (SWCNT) which was first observed in 1993 by Iijima *et al.*[10]. SWCNTs consist of a single cylindrical layer of graphite and have a diameter ranging from 0.4 to approximately 2 nm. Fig 1.1(b) shows an image of a SWCNT which was taken by scanning tunnelling microscopy (STM). As a result of their small diameter and good uniformity, they can be regarded as an ideal carbon fibre. When SWCNTs are grown they often combine to form bundle structures called ropes consisting of several tens of nanotubes as shown in Fig 1.1(c).

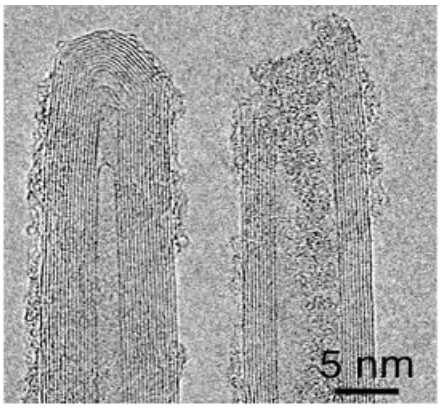

(a)

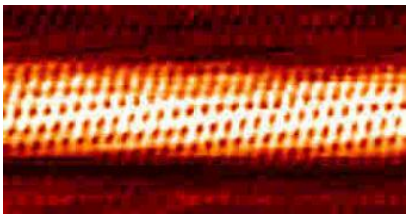

(b)

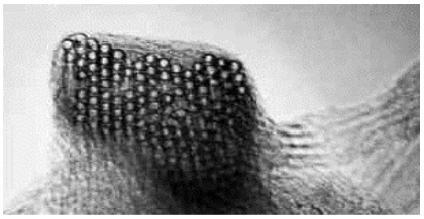

(c)

Fig. 1.1: Carbon nanotube categories: (a) TEM image of two MWCNTs[3], (b) Scanning tunnelling microscope (STM) image of a SWCNT[11], (c) TEM image of a bundle of SWCNTs[12].

SWCNTs are formed, at least in a thought experiment, by rolling a single graphene sheet into a seamless tube and capping each end by half a carbon fullerene. The geometry of the nanotube is specified by the direction of rolling and circumference of the tube. After rolling to form a CNT, a 'roll-up vector' (also known as a chiral vector or Hamada vector), **r,** can be defined, expressed as a linear combination of basis vectors **a** and **b** of the two-dimensional hexagonal graphene mesh:

$$\mathbf{r} = n\mathbf{a} + m\mathbf{b}$$

where *n* and *m* are considered as primitive indices, as illustrated in Fig. 1.2.

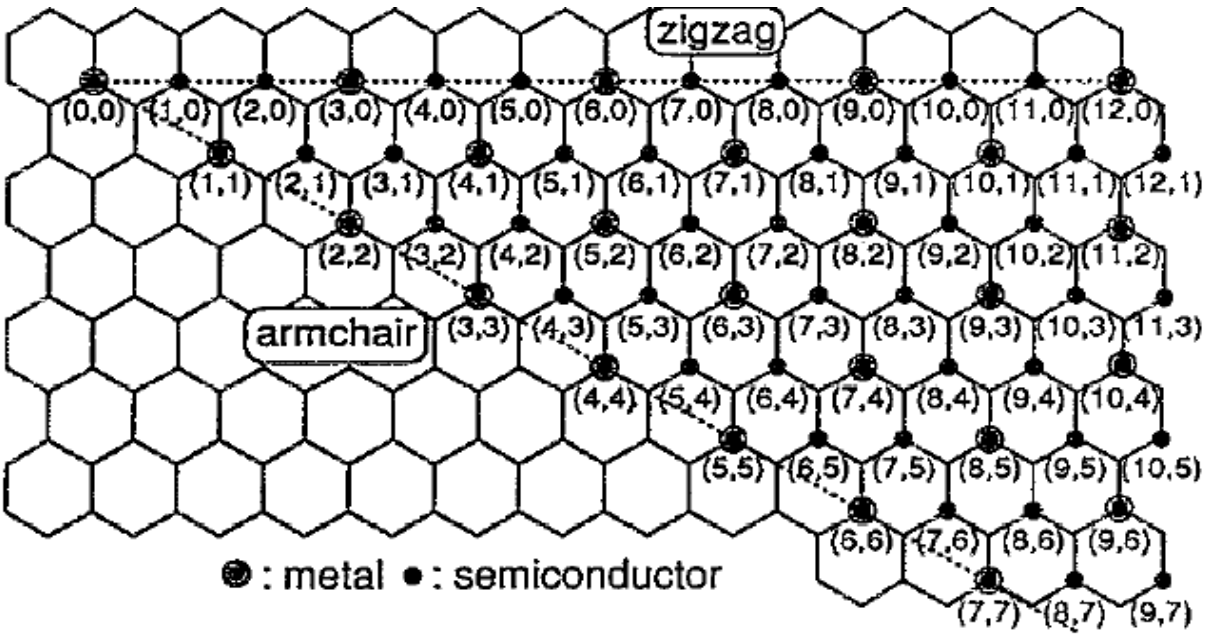

Fig. 1.2: Schematic of a graphene sheet with unitary vectors **a** and **b**. A nanotube is equivalent to rolling a graphene sheet from the origin to a point (*n*,*m*) in the lattice. Figure taken from Ref [13].

Carbon nanotubes can thus be classified into families which display differing electronic behaviour depending on the value *n* and *m*. The (*n*,0) type of nanotubes are in general called

zigzag due to the orientation of the carbon bonds along the circumference of the nanotube. Zigzag SWCNTs are achiral with a wrapping (or chiral) angle, θ, of 0º. The (*n*,*n*) types are referred to as *armchair nanotubes* and are also achiral with a wrapping angle of θ = 30º. Finally nanotubes with indicies (*n*,*m*) are chiral and have wrapping angles between 0º and 30º.

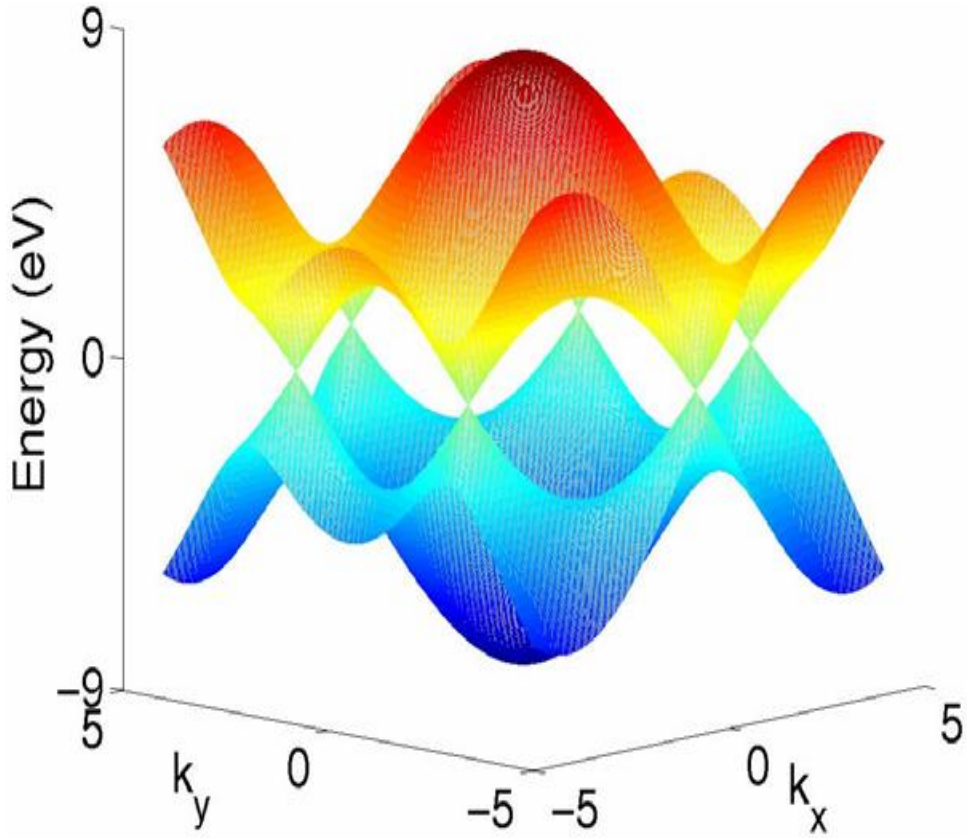

Fig. **1.3:** The band structure of a graphene sheet[14].

The wrapping of the nanotube, as expressed by its indices, plays a key role in defining its electrical properties. SWCNTs can be either metallic or semiconducting depending on their index[14,15]. In a graphene sheet, which may be regarded as a zero band gap semiconductor, the conduction and valence bands touch at 'Fermi points' which are located at the corners of the first Brillouin zone as illustrated in Fig. 1.3. This unusual band structure has significant effects on the electronic behaviour as the overlap between the electronic states in adjacent sheets in a graphene crystal gives rise to a finite concentration of valence band holes and conduction band electrons leading to a semi-metallic property. When a nanotube is formed, boundary conditions are imposed by the periodicity of the nanotube around the

circumference and each graphene band splits into a number of one-dimensional sub-bands which may be represented by an index *'j'*. In this case, it is obvious from Fig. 1.4 that the nanotubes allowed electronic energy states are occurred at the cuts through the graphene band structure. The splitting of the graphene band is caused by the specification that the circumferential component of the electron wave vector '**k**' must satisfy the condition $\mathbf{k}.\mathbf{r} = 2\pi j$ where '**r**' is the chiral vector and *'j'* is an integer. When these cuts pass through a 'K'-point (Fermi point) the tube is metallic, whereas if no sub-band cuts the Fermi point the tube is semiconducting (Fig. 1.4). Simple calculations show that a CNT is metallic if $n - m = 3i$ where i is an integer[16], and is semiconducting otherwise with a band gap inversely proportional to nanotube diameter, demonstrating the influence of quantisation and dimensionality on the electrical transport properties of the nanotube.

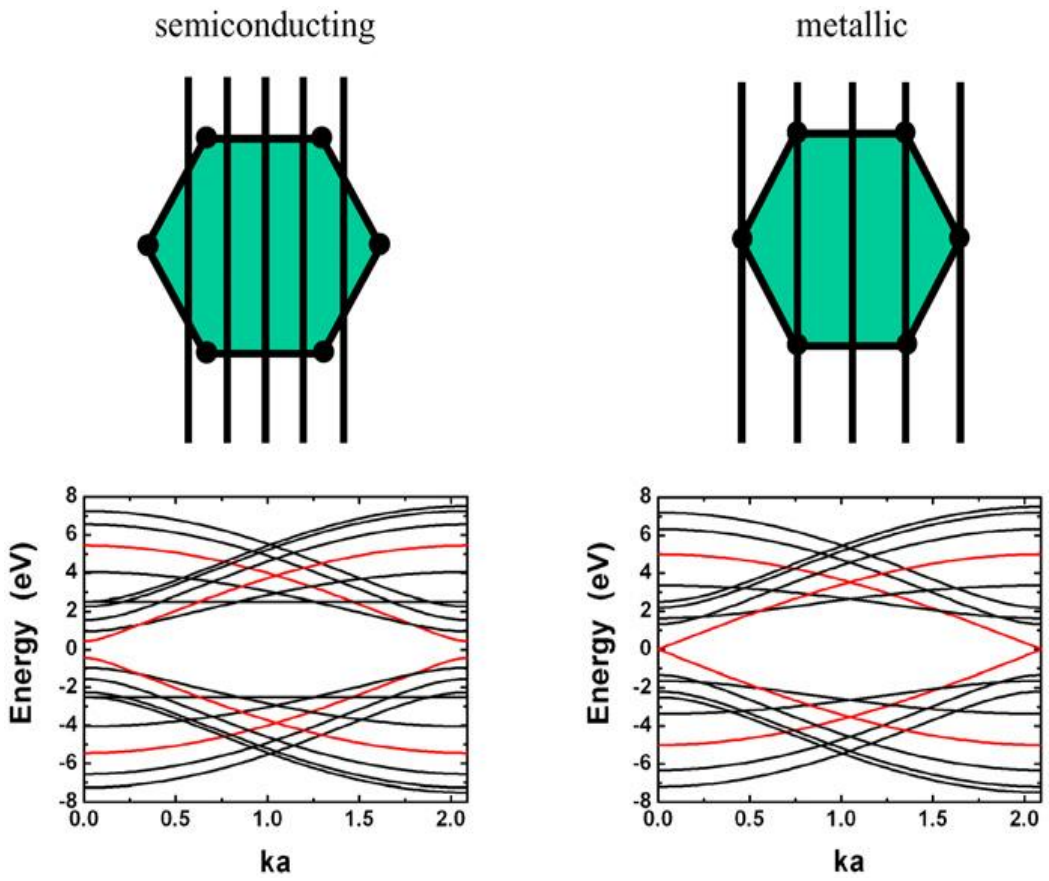

Fig. 1.4: Illustration of one-dimensional sub-bands associated with allowed values of wavevector in the direction of quantisation leading to semiconducting and metallic CNTs, and examples of bandstructures for semiconducting and metallic zigzag CNTs[14].

Chemically, CNTs are often considered to be inert to interaction with ambient atmosphere due to their structural similarity to graphite. However, as a result of their curvature they may, in practice, be more reactive than graphite or graphene sheets – in particular the high curvature at nanotube end caps and in smaller diameter CNTs can lead to significantly greater sensitivity to the surrounding environment[17,18]. Furthermore, any real nanotube will contain defects, which can arise during growth or as the result of handling and purification. There are a number of different point vacancy types in SWCNTs, such as vacancies, interstitials and bond rotations[19,20,21,22,23,24,25,26,27], which will be discussed below. These defects can drastically modify the electronic properties and chemical reactivity of CNTs. For example, point defects like vacancies break the SWCNT symmetry and introduce acceptor and donor states into the band structure, but do not change the overall SWCNT topology[28]. As a result they can impact every passing charge carrier and can therefore change the nanotube conductance, *G*, as a function of applied bias. Furthermore, defect sites can significantly contribute to the response of CNTs to gas adsorption in which the localisation of charge can create active sites for initiating a reaction[28]. Reactive defects in CNTs help to promote charge transfer, chemisorption and covalent bonding between CNTs and species in their environment, thus enhancing their response as chemical sensors. However, we note that the sensitivity of CNTs to gas adsorption is still a controversial issue due to a lack of experimental consensus[29,30].

In electronic devices, CNTs are used as field emission sources[31,32] for flat panel displays[33], lamps[34], gas discharge tubes providing surge protection[35], and in x-ray[36] and microwave generation[37]. Samsung has showed several generations of prototypes, including a 9-inch (23-cm) red-blue-green colour display that can reproduce moving images[33]. CNTs also are the strongest and most stiff materials existing in nature. SWCNTs in particular have a Young's modulus approximately 1 TPa and tensile strength of nearly 50 GPa, which are greater than Young's modulus (200 GPa) and tensile strength (400 MPa) of stainless steel[38,39,40]. These excellent mechanical properties have led NASA to develop materials based on CNTs for space applications[41]. Moreover, CNTs are readily available components for sensors and probes. Possible chemical sensor applications of nanotubes are interesting because nanotube electronic transport and thermopower are very sensitive to substances that affect the amount of injected charge[29]. In terms of probes, nanotube tips can open up the AFM imaging world. They contribute effectively towards improved resolution and decreasing tip surface forces in many fields of research such as biology, biotechnology,

metrology and nanoelectronics[8]. Last but not least, CNTs have been shown to have potential applications in fuel storage and for fuel cells that could power electric vehicles or laptop computers[40].

1.2 Defects in CNTs

As mentioned briefly in the previous section, defects can significantly influence the physical properties of CNTs such as their chemical reactivity, electrical and mechanical behaviour. Indeed, CNTs can be considered as ideal materials for studying, investigating and manipulating the possible influences of defects, in particular because SWCNTs exhibit one-dimensional behaviour and hence a defect can have a major impact on electrical and mechanical response. For example, CNTs with point defects show not just a non-linear increase in electrical resistance but complex voltage-dependent transport behaviour. Point defects have also been demonstrated to increase the chemical reactivity of nanotubes improving their characteristics as sensing elements, improving the solubility of the nanotubes allowing further chemical elaboration and changing their mechanical behaviour. However, much research remains to be done to determine and understand the detailed influence of defects on these properties. Moreover, as we discuss below, there are a variety of defect types which differ in stability and number within a typical CNT, and the link between changes in physical properties and the type of defects present is being increasingly well understood[19,42,43,44,45].

The ability of defects to dramatically alter nanotube behaviour even at low densities opens up the possibility of changing the properties of nanotubes in a controlled way if we can fully understand the impact of defects and how to introduce them in a selective and spatially controlled manner. A particularly promising route to achieve this goal is to modify CNTs a process termed *functionalisation*, which is a focus of this thesis. Depending on the types of defect introduced changes may result in either short range or long range effects in CNTs, which are possible to observe by differing experimental approaches[42,43,44].

As a result of the one-dimensional nature of CNTs defects like line and screw dislocations cannot be found in these materials but it is possible for them to appear in graphene (a two-dimensional material)[45]. The behaviour of point defects is more complicated in CNTs than in graphene (or graphite) due to the circumferential, curvature-induced strain in the former. As a result defect stabilities depend precisely on their position inside the lattice, as well as on tube diameter and helicity[45]. In the following sections, the key point defects in CNTs - vacancies, interstitials and bond rotations and ring defects will be discussed.

1.2.1 Vacancies

One of the most typical defects predicted to exist in CNTs is the vacancy, Fig 1.5. Mono-vacancies can originate from a missing atom in the hexagonal structure of the nanotube wall. The energy cost associated with monovacancy formation without subsequent structural relaxation has been calculated to be 7.8 eV due to the substantial energy required to break strong intraplanar C-C bonds in the nanotube[20]. The simplest way to introduce such vacancies into the nanotube lattice is by 'knock-on' (atom displacement out of the tube wall). This process can be achieved by particle irradiation, using beams of electrons, protons or ions (discussed in the next section). Vacancy defects result in three dangling bonds (Fig. 1.5(a)) which will rehybridise or react with surrounding molecules. When reconstruction occurs two of the dangling bonds bridge to form pentagon ring leading to a structure called a 5-1db defect which leaves only a single dangling bond (db)[21,22] (shown in Fig. 1.5(b) terminated by a hydrogen atom). The 'bare' (non hydrogenated) structure costs around 5.6 eV – the reduction in formation energy of the reconstructed defect with respect to the unreconstructed defect arising from the difference between the energy gain resulting from satisfaction of two dangling bonds and the energy cost of the resultant distortion of the carbon nanotube lattice[46]. Vacancies in CNT structures (unlike graphite)[40] interact with adsorbed gases and provide spontaneous reaction pathways to saturate dangling bonds[19]. The interaction of vacancy defects with nitrogen, either in the ambient or during the defect formation process (using nitrogen ions as projectiles to create the vacancies) will be investigated in Chapter 4 as a route for the doping of single-wall carbon nanotubes.

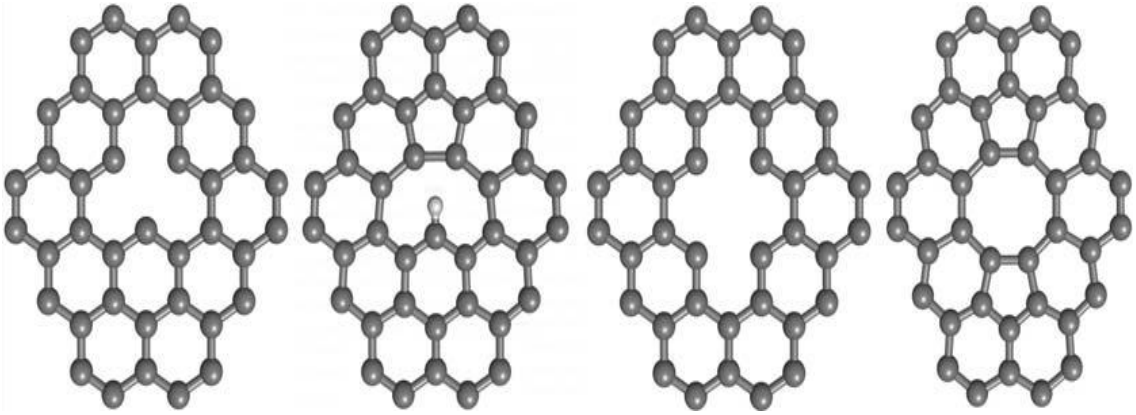

Fig. 1.5: Small vacancy defects in graphitic carbon. Mono-vacancy (a) before and (b) after reconstruction and H-termination of the remaining dangling bond. Di-vacancy (c) before and (d) after reconstruction[19].

1.2.2 Interstitials

The interstitial is a second important type of defect. This kind of defect consists of the presence of an additional atom in the structure which is not located on a lattice site. In carbon nanotubes these defects locate on the inner or outer surface and are also referred to as adatoms. The primary source of interstitial defects is the displacement of lattice atoms by knock-on damage under particle irradiation. The interstitials are created when displaced atoms diffuse away from the vacancy site from which they originate rather than recombining with a vacancy. In a graphite crystal they will usually remain confined, and will be accommodated by production of a covalent link across two neighbouring graphene sheets. This type of interstitial will migrate within and between graphene layers until it binds to a vacancy site to produce a stable vacancy-interstitial complex called a Frenkel defect[19]. In CNTs, theoretical studies have suggested that an interstitial is highly mobile[23,24] and that, as a result, these defects are likely to be short-lived[25].

1.2.3 Bond rotations

Bond rotations are favourable and are the dominant defects to be found in CNTs. The most simplest bond rotation defect is the Stone-Wales-Thrower (SWT) defect[26,27]. In the formation process for this defect, one bond rotation can change four hexagons of a pristine CNT structure to new forms of rings – two pentagons and two heptagons (sometimes labelled 5-7-7-5), and involves an energy cost of about 3.5 eV. Fig 1.6(b) shows SWT defects in the hexagonal network of a CNT wall. Although the SWT defect has the ability to influence the physical properties of CNTs, it is very difficult to observe by experimental techniques. For example, the difficulties of clean sample preparation, (during the synthesis and deposition process) prevent sufficiently high atomic resolution in electron microscopy[19]. SWCNTs have a tiny diameter (a few nm) and when deposited from solution they congregate with co-deposited carbonaceous adsorbates and solubilised contaminants. Moreover, CNT imaging remains complicated by curvature and electronic delocalisation. The consequences of these problems are that defects like SWT defects are exceptionally difficult to identify. It has been shown that SWCNTs have a complex energy landscape for SWT defects which includes formation barriers of no less than 9 eV and dissolution barriers of 5.5 eV[47]. This former seems to prevent the formation of any SWT defect at all, but this barrier drops very quickly in the presence of interstitials. When formed, SWT defects are long lived in CNTs after the initial synthesis, being trapped in the lattice by the high dissolution barrier[47].

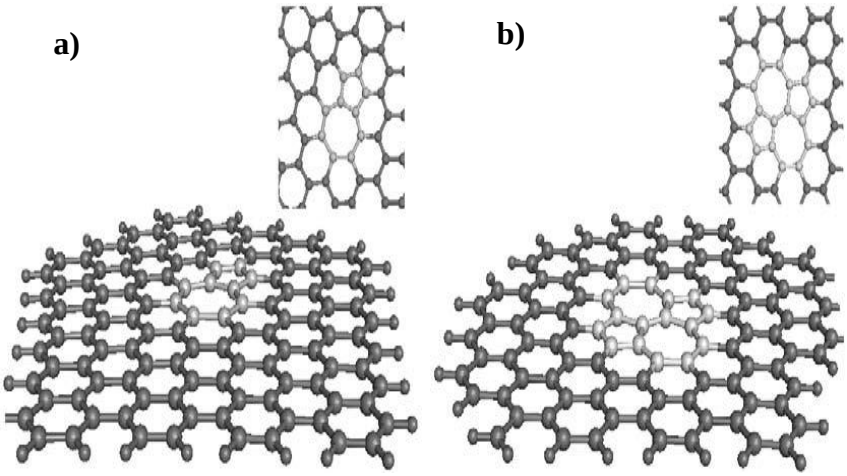

Fig. 1.6 (a) A single 5-7 defect and (b) a 5-7-7-5 Stone-Wales configuration. Sighting along the zigzag edges in a side view visualization clarifies the nucleation of a dislocation by the 5-7 defect, and the absence of long-range disorder in the Stone-Wales case[19].

Another form of bond rotation can be formed by converting two hexagons to one pentagon and one heptagon. The new ring is called a 5-7 defect, as shown in Fig.1.6(a). These rings of pentagons and heptagons play a key factor for extended structures of CNTs in which both diameter and chirality can change whilst maintaining a continuous graphitic structure without dangling bonds[19].

1.3 Functionalisation approaches

CNTs have the possibility to be functionalised in a wide variety of different ways due to their unique structure and morphology[48,49,50]. Functionalisation techniques can introduce dopants or surface functional groups that tailor the structural and electronic properties of nanotubes for specific applications, for instance the doping of semiconducting CNTs could be crucial for their use in semiconductor technology. New materials such as nitrogen doped SWCNTs and Au decorated SWCNTs have the possibility to be used in solar cells and sensor technologies[51,52,53]. Fig 1.7 illustrates schematically the possible ways in which CNTs may be modified[49].

Direct substitution of foreign atoms, such as nitrogen or boron, hold out the promise of modifying the electronic behaviour and chemical reactivity of CNTs without significantly perturbing their structure. In this case, an N (or B) atom directly substitutes for a carbon atom in the hexagonal network of the nanotube wall and, depending on the position of the substituent, the electronic behaviour changes. These structural arrangements are known as wall functionalisation, (Fig 1.7(a)[49]). Such functionalisation can be achieved by careful control of growth conditions or through a variety of post-growth treatments. CNTs are extremely sensitive to substitutional N incorporation, which means that there is a high possibility to tailor their properties such as altering their chemical reactivity whilst maintaining a low defect content[50,53,55,55,56], as is explored further in Chapter 4 of this thesis.

Intercalation within CNT bundles, as illustrated in Fig 1.7 (b) and (c), is an alternative approach to modification[49,50]. SWCNTs bundles can be used in this way as templates to create nanocrystalline semiconducting systems in van der Waals inter-tubular gaps, for

example. It has been shown that nanoparticles of CdSe, CdS and ZnSe can been incorporated into the bundle gaps. This leads to a dilation of the SWCNT lattice[57]. However, doping nanotubes by this method still requires further experimental and theoretical investigation[50,57]. Endohedral doping, illustrated in Fig 7(d) and (e)[49], is a further approach for functionalisation which does not require a covalent bond to be formed with the carbon atoms within the nanotube wall. The large space within the nanotube itself means that guest molecules, including fullerenes[48,58], can fill the inner cavity of SWCNTs[49,50]. Fullerene encapsulates form chains in which the molecules are coupled by van der Waals interactions and these arrays are known as 'peapods'. Endohedral doping can be achieved by thermally annealing the SWCNTs in the presence of the dopant and observed in real time by the use of high-resolution transmission electron microscope[58].

Sidewall functionalisation through the chemical attachment of monatomic species to the nanotube outer wall, such as fluorination, shown in Fig 1.7(f)[49], is an effective means of controlling nanotube electronic behaviour[49] but suffers from the relative inertness of the nanotube walls. Indeed, fluorination by aggressive approaches such as heating in F_2 gas is often used as the starting point for further chemical elaboration and fluorinated SWCNTs with stoichiometries up to C_2F can be produced and used as the starting point for, for example, organic functionalisation of the sidewall[59,60,61] Such functionalisation (shown in Fig. 1.7(g))[49] can also be achieved by carboxylic group substituted benzene diazonium salts[62,63,64,65]. Chen *et al.,* have reported functionalisation of oxidised carbon nanotubes by long chain alkylamines via acylation with the result that the solubility of the modified nanotubes is improved in organic solvents[66]. Non-covalent approaches can also be used to bind species to the nanotube sidewalls through π-stacking as presented in Fig. 1.7(h)[49]. This approach depends on the interaction of π orbitals via van der Waals forces between the tube surface and the wrapped material and has been achieved using surfactants such as sodium dodecyl sulphate[62,67] and benzlkonium chloride[68], proteins and DNA[69]. It has been shown that the non-covalent sidewall functionalisation increases the solubility and processability of CNTs in aqueous media, which is highly important for any biological application.

In this thesis the focus is on direct substitution into the sidewalls of single walled carbon nanotubes by post-growth techniques. There are several issues with post-growth doping of SWCNTs that are still unaddressed: these include dopant concentration, distribution and

localisation under annealing conditions. In particular, the majority of experimental studies have focussed intensively on doped MWCNTs[70,71,72,73,74,75,76].

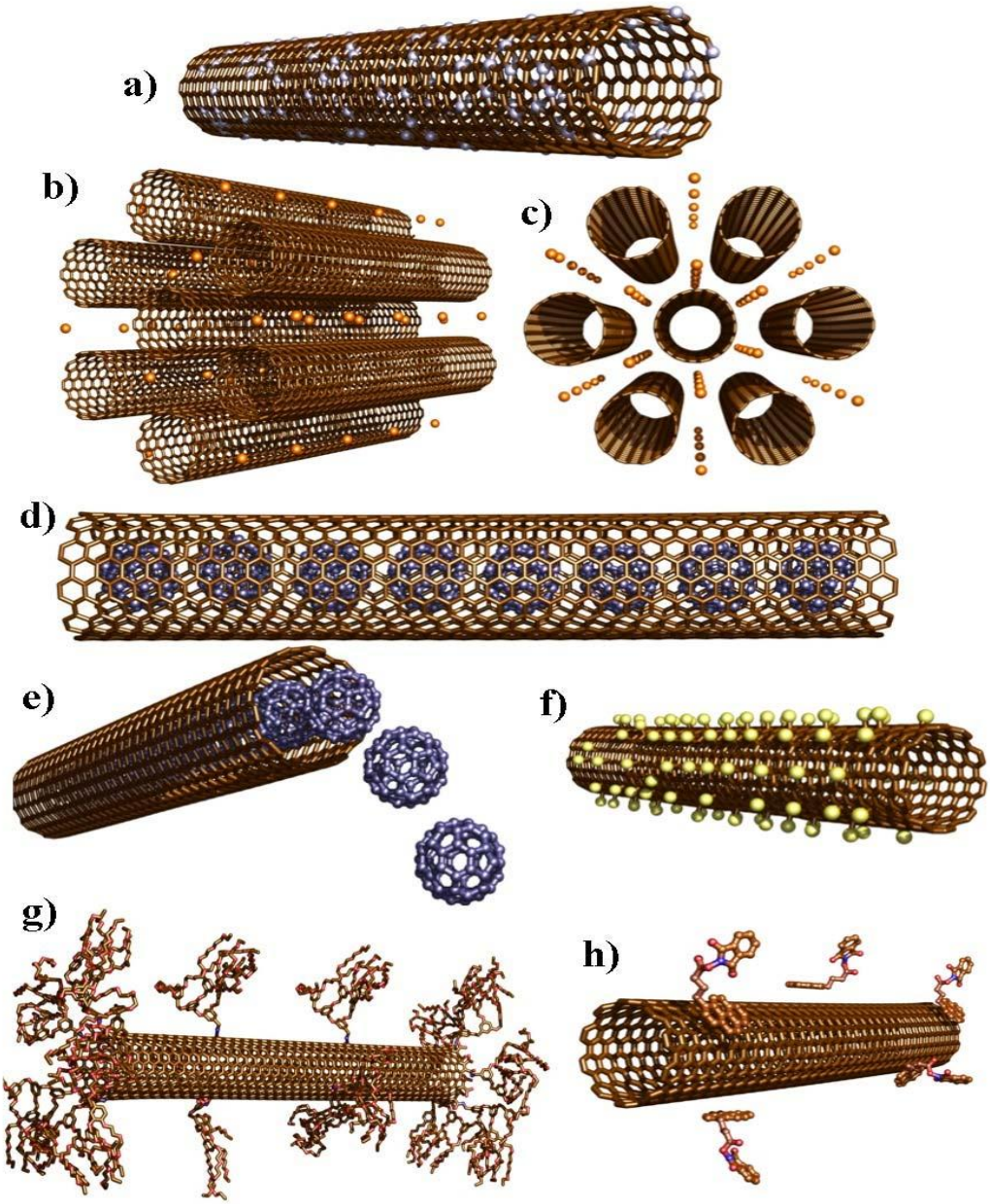

Fig. 1.7: Different approaches to chemical modification of carbon nanotubes. (a) substitutionally doped single-walled nanotubes (b,c) nanotube bundles intercalated with atoms or ions, (d,e) peapods: SWNTs filled with fullerenes (other endohedral fillings are possible), (f) fluorinated tubes, (g) covalently functionalised tubes and (h) functionalised nanotubes *via* π-stacking of the functionality and the tubes. Figure taken from Ref.[49].

1.4 Ion Irradiation

Ion irradiation is one of the most effective modification methods for introducing dopant atoms and creating defects in CNTs. Indeed, experiments show very interesting results demonstrating how defects change the electrical and chemical behaviour of CNTs upon irradiation and that they display a response distinctly different from that of graphite and diamond[77]. The most significant advantages of ion irradiation are: (i) the controlled production of defects and functional groups within carbon nanotubes, and (ii) the large degree of freedom in selection of irradiation parameters (such as energy, flux) and species (reactive versus non-reactive ions) which has the potential to introduce selectivity in the defect production/functionalisation process.

The ability to selectively modify the behaviour of carbon nanotubes through the introduction of defects may enable the production of nanotubes with properties suitable for specific applications (smart materials). A basic understanding of the nature of the defects produced by ion irradiation of carbon nanotubes and the reactivity or functionalisation of the resulting defects is a necessity if this goal is to be achieved. Although defects in graphite have been studied since 1950s, due to the importance of this material as a moderator in nuclear fission reactors[78], there is still no comprehensive understanding of annealing and agglomeration. Therefore, an understanding of irradiated CNTs can also help us to better understand the nature of defects in graphite.

Substantial progress in the study of the properties of defects and irradiation effects has been achieved by high resolution transmission electron microscopy (HRTEM) and computer-based atomistic simulations[70]. In addition, X-ray photoelectron spectroscopy (XPS) has been used in ion irradiation experiments to monitor changes in valence and core peaks, which are very sensitive to the type of carbon-carbon bonding and the presence of non-carbon species[71,72,73,74]. During ion irradiation experiments, substantial amounts of damage can be created within nanotubes depending upon irradiation conditions. Under ion irradiation two types of defects are primarily found: point defects (vacancy-interstitial) and defects of higher dimensions (C adatoms)[75]. It was found, though molecular dynamics simulations, that single vacancies (monovacancies) are the most prolific defects in CNTs irradiated by inert gas ions, and C adatoms on both external and internal sides of CNTs walls were also common[76,79].

The damage of SWCNTs by Ar^+ ions irradiation has been characterized theoretically at low energies (but nevertheless greater than the defect creation threshold energy, E_d). In this case, the number of defects increases with the incident energy up to 600 eV and then remains practically constant[77]. In contrast, at higher energy defect production in isolated SWCNTs drops because the nuclear collision cross section for defect production decreases[77]. However, the energy of carbon recoils is sufficiently high such that they will damage SWCNTs (this phenomenon can happen at incident energies higher than 1 keV[77]). In graphite, single vacancies reconstruct due to Jahn-Teller distortion. However, in CNTs the reconstruction is much stronger due to the curvature and inherent nano-size of the system which leads to a much greater flexibility within the lattice. Moreover, it is easier for CNTs to contract locally to heal the hole and thus saturate energetically unfavourable dangling bonds. Di-vacancies also reconstruct with a formation energy of 8.7 eV in graphite and 7.7 eV in CNTs. Further theoretical effort has focussed on how the dangling bonds associated with one or more vacancies might serve for interconnection of CNTs providing chemical sensitivity, or for incorporating dopants. Adatom adsorption onto sites above C-C bonds results in different adsorption energies and also local rearrangements. Bond rotation defects such as the SWT defect (Section 1.2.3) can also appear after irradiation. These defects could be responsible for the release of excessive strain within defective CNTs[80,81,82].

Furthermore, a number of more complex defects can be formed in MWCNTs and bundle structures (ropes). Fig.1.8, for example, schematically illustrates vacancies (V) and adatoms (A) in a carbon nanotube sidewall (Fig. 1.8(a)), and how defect-mediated covalent bonds between adjacent SWCNTs can occur (Wigner defects) (Fig. 1.8(b)) and finally, how high irradiation lead to interwall links and amorphisation in MWCNTs. (Fig. 1.8(c))[77].

Two important parameters in terms of irradiation in CNTs are: (i) ion mass (light or heavy ions) and (ii) irradiation dose (low or high). In MWCNTs, heavy ion irradiation can be used in a creative way and high dose irradiation amorphizes CNTs[48]. In terms of SWCNTs, low dose irradiation is used for studying the atomic structure and properties of CNTs, for example an irradiation dose of 10^{11} ions/cm^2 by 30 keV Ar^+ was reported[83]. Low-dose irradiation of SWCNTs with 120 eV Ar^+ ions can illustrate the effect of defects on SWCNTs (mono vacancies and di-vacancies can observed), and also lead to a dramatic drop in the conductance of CNTs[63].

It has been suggested that irradiation of SWCNTs with nitrogen ions is an effective method to dope the nanotubes with minimal structural disruption. Theoretical studies have demonstrated that the amount of substitutional N inserted into nanotubes by ion irradiation could reach up to 40% of the sp^2 bonded material[84]. Doping SWCNTs by using N^+ ions with incident energies of 3 keV[55] and 300 eV[56] has been investigated with XPS (discussed in greater detail in Chapter 4). These studies showed that N atoms can be incorporated in a range of different bonding configurations depending on the ion energy, dose and post-implantation annealing.

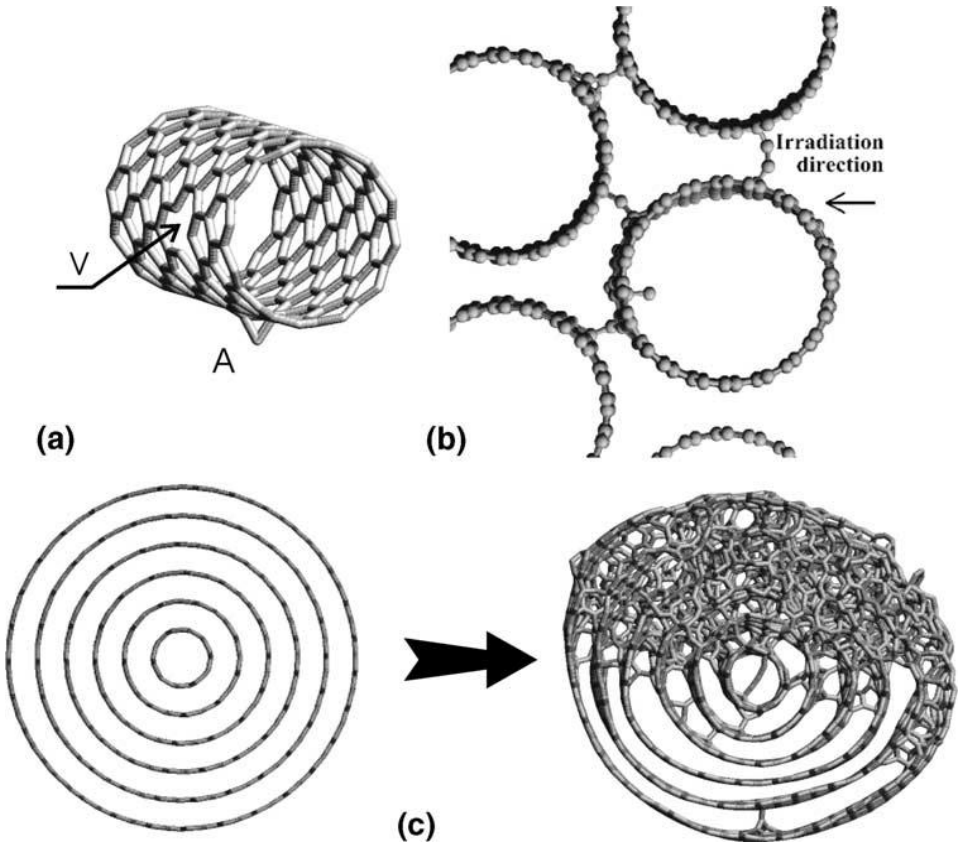

Fig. 1.8: (a) Vacancies (V) and adatoms (A) at the sidewall of a SWCNT. (b) Covalent bonds between SWCNTs in a nanotube bundle. (c) The atomic network of a MWCNT before and after high irradiation dose. Figure taken from Ref.[77].

1.5 Graphene

Graphene is a single two dimensional layer of graphite. It has been found experimentally that this structure can be thermodynamically physiochemical stable and that the in-plane sp^2 bonding of the carbon atoms gives rise to exceptional physic-chemical properties[85,86,87,88]. Isolated graphene was first produced in the form of flakes with lateral dimensions of around several microns by mechanical exfoliation of graphite using Scotch tape by Geim, Novoselov and co-workers in 2004[85] and led to the award of the 2010 Nobel Prize for Physics. The electronic properties of graphene were first explored using tight-binding calculations by Wallace in 1947[89] who found the material to be a zero band gap semiconductor. At that time, and indeed until the isolation of graphene, the existence of purely two-dimensional materials was a topic of debate because it was thought that such a structure is unstable thermodynamically[90]. Although the isolation of graphene by Geim and Novoselov[85] provoked intense scientific interest the formation of single graphitic layers (i.e, graphene) on transition metals by chemical vapour deposition (CVD) and segregation of carbon atoms on catalytic substrates has been known since the 1960s[91,92,93]. The key driving interest in graphene nowadays arises from its potential uses in electronics and semiconductor technology as a potential replacement for silicon, which has long been predicted to be close to its fundamental materials limits for device fabrication. However, much research is required before graphene is capable of meeting these requirements[85,90,94].

Graphene has the highest charge carrier mobility of any known material. As a result there has been a huge interest in graphene-derived electronic circuits, such as suspended graphene field effect transistors (FETs), which have displayed mobilities of up to 2×10^5 cm^2/Vs and full ballistic electron transport through a 1.2 µm long channel[85,94]. Graphene is also one of the strongest materials known with a strength of 42 N/m^2 and Young modulus of 10 TPa[95]. These properties are coupled with outstanding thermal conductivity, measured to be in the range of 4.84-5.30 kW/mK[96] and a single layer enables the transmission of 97% of visible light[97], suggesting applications as a transparent conducting material.

The graphene structure is a two-dimensional hexagonal mesh of carbon atoms each of which is in an sp^2 hybridisation state, leading to three sp^2 lobes oriented at 120° to one another in a plane, and a π orbital oriented in the perpendicular direction. The three sp^2

orbitals form three in-plane σ bonds with their nearest neighbours in the hexagonal carbon network. It is these bonds which are primarily responsible for the outstanding mechanical properties of this material and make graphene the strongest currently known material in nature. The perpendicular π orbitals overlap with one another to form a delocalised electron cloud which is responsible for the conductivity of this material[95,98]. The graphene lattice consists of a two atom basis labelled as A and B in Fig. 1.9 (Ref. [99]).

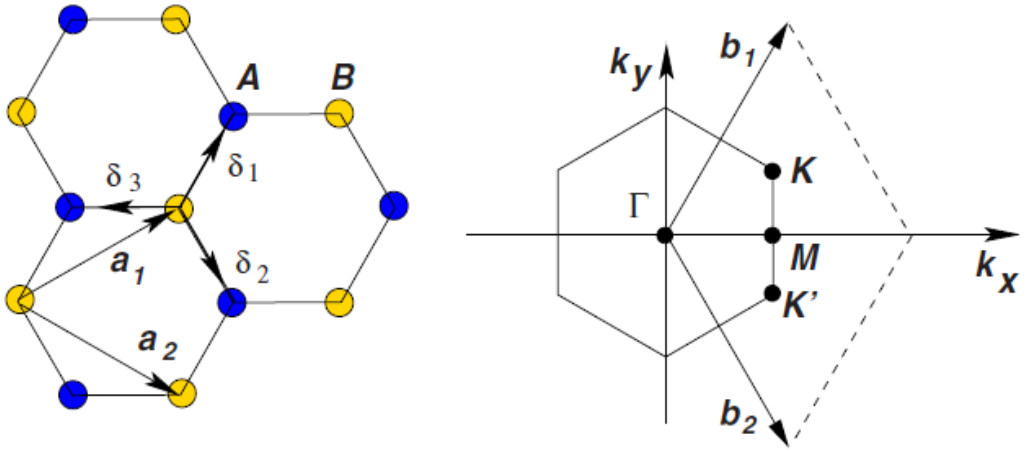

Fig 1.9: Real space (left) and reciprocal space (right) lattice of graphene[99].

The π-orbital derived conduction (π*) and valence (π) bands touch each other at six points located at the corners of the graphene Brillouin Zone, labelled *K* and *K'* (the two inequivalent points are three-fold symmetric) known as the Dirac points (Fig. 1.10). At these points the band energy dispersion is nearly linear leading to a zero effective mass. Therefore, rather than being described by the Schrödinger equation, the electrons behave as massless fermions which are governed by the Dirac equation[100] leading to a range of exotic phenomena. The zero band gap which arises at the Dirac points does, however, pose a disadvantage for the use of graphene in digital electronics since the on-off ratio of any FET produced from this material will be small[85,94,99,100].

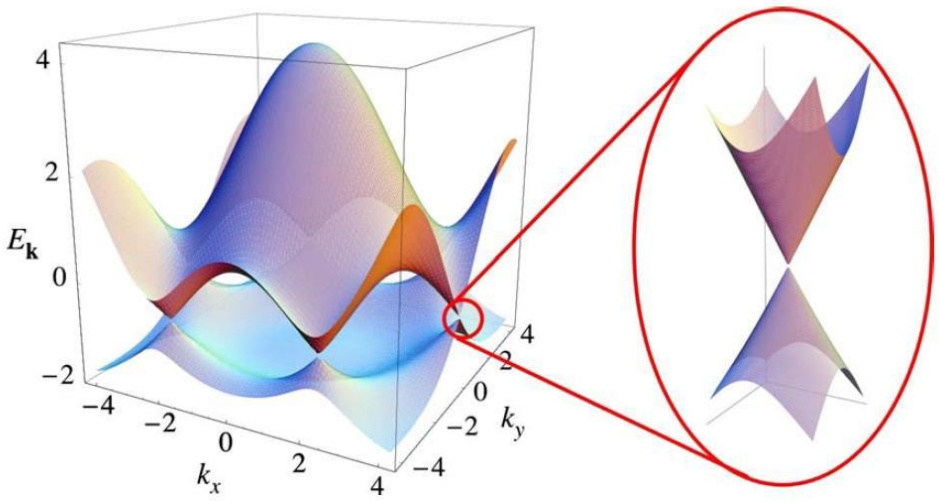

Fig 1.19: Graphene conduction (π^*) and valence (π) band structure[99].

Since the discovery of graphene a number of different methods of producing this material have been developed. As mentioned above, graphene was first obtained from bulk highly ordered pyrolytic graphite (HOPG) by mechanical exfoliation using Scotch tape (micromechanical cleavage)[85,90,101]. To form monolayer graphene an energy input of the order of 2 eV/nm^2 is required to overcome the weak interlayer van der Waals forces in HOPG and a force of about 300 nN/μm^2 is applied[102]. The resulting graphene flakes can then be deposited onto a range of surfaces simply by contact. Oxidised silicon with an oxide thickness of 90 nm or 280 nm is a particularly popular substrate – the oxide layer is inert and insulating enabling the intrinsic electrical properties of the graphene film to be accessed and optical interference effects which occur at these oxide thicknesses result in sufficient contrast that a monolayer of graphene is visible by optical microscopy[103]. Mechanical exfoliation can produce graphene with properties which are close to those predicted theoretically, such as a carrier mobility of the order 10^6 cm^2/Vs[104,105]. A drawback of this approach to graphene production is that there are often impurities and contamination associated with the adhesive tape. Such contamination can lead to degradation of mobility[106,107], but can be solved by heat treatment under an Ar/H_2 atmosphere at 200°C or *in situ* Joule heating[108]. A more serious issue associated with mechanical exfoliation is that the area of graphene flakes obtained by this approach is limited and the method is slow, requiring an experienced scientist to locate the graphene among the associated exfoliation debris. The lack of scalability and difficulty

means that this approach is unsuitable for mass production. However, graphene created by this method is of the highest quality and can be used as both as a reference for material produced by other means and as a test bed for fundamental physical studies.

An alternate approach for the production of graphene, which results in high quality films is the sublimation of silicon from SiC. Loss of silicon from the (0001) or (000-1) surface at elevated (typically >1400°C) temperature under vacuum leads to a carbon-rich surface and, ultimately, surface graphitisation[109,110.111.112]. The wide band gap of SiC enables the intrinsic electronic properties of the resulting graphene film to be exploited. However, SiC wafers are extremely expensive and this, coupled with the high temperatures involved in the process, limit the scalability of this approach.

A lower cost approach to graphene growth, albeit one which currently produces films of lower quality than the two methods discussed above is chemical vapour deposition (CVD), which due to its simplicity, relatively low cost, and scalability has rapidly become the focus of most graphene growth research. In this approach a catalytic metal surface (typically a transition metal) is exposed to carbon containing precursors at elevated temperatures, usually at low pressure. The decomposition of the precursors at the catalyst surface can, under the correct conditions, produce monolayer or few layer graphene[113,114,115]. An understanding and control of the growth mechanism and, through that, control of the number of graphene layers is crucial to the CVD technique along with the vital role played by the solubility of carbon in the catalyst[116]. Recent reports have demonstrated that Cu substrates are extremely promising for producing large areas of graphene with uniform coverage[117,118]. The negligible solubility of carbon in copper even at elevated temperatures results in a self-limiting surface mediated process[119,88]. However, the poor electrical properties, resulting from scattering due to the presence of grain boundaries, still limit the utility of this approach. There is therefore an intense focus on producing single crystal graphene with a 'perfect' (i.e., close to theoretical) electronic behaviour[120,121,122,123,124,125]. Another significant issue which arises from the CVD growth of graphene on metal surfaces is that it is necessary to transfer the as-grown films onto a suitable substrate for electrical measurement, a process which may also lead to degradation[126,127].

Recently, solid precursors have begun to be explored as an alternative to the gas-phase delivery of precursors in conventional CVD, due to the potential for simplification of

the growth method and the possibility for spatial selectivity in graphene growth. For example, precursor materials as diverse as Polymethylmethacrylate (PMMA)[128], amorphous carbon[129] and Polyacrylonitrile (PAN) have been used with copper catalysts, while PMMA[130,131] and C_{60} have been used to produce graphene on Ni[132]. An advantage of the solid phase growth approach is that doped graphene can be achieved *in situ* by solid precursors containing foreign atoms which are desirable for opening a graphene band gap[133]. However, this approach has the same problem of polycrystallinity (and hence grain boundaries) as the closely related conventional CVD approach. Given the novelty of solid precursor based growth techniques, significant further development should still be possible and growth from solid precursors is the focus of Chapters 5 and 6 of this thesis. In particular, it is recognised that for a wide range of applications in digital electronics, pseudo spin-tronics, terahertz technology and infrared nano photonics and for efficient energy conversion and storage[134,135,136] a band gap is required, and Chapter 6 explores doping with a suitable heteroatom (Si) which is predicted[137] to open a band-gap in graphene without changing its topography.

1.6 Organisation of this thesis

This thesis is organised as follows: Chapter 2 describes the theoretical basis of the experimental techniques used in this work; Chapter 3 presents details of sample preparation and of the experimental apparatus used to obtain the results which form the basis of this thesis. Chapter 4 reports the results of ion irradiation mediated approaches for the nitrogen doping of single wall carbon nanotube films measured using X-ray photoelectron spectroscopy and Raman spectroscopy. Chapter 5 details the solid-phase CVD synthesis of graphene from a soft solid hydrocarbon precursor, nonadecane, focussing on the kinetics of growth and on the influence of growth temperature on the resulting films. Chapter 6 presents evidence for the formation of silicon-doped graphene from solid-phase CVD growth using a silicon-containing precursor, polydimethylsiloxane; Finally, Chapter 7 presents a summary of the main conclusions of the experimental work reported in this thesis and briefly outlines potentially productive avenues for future research building upon the results presented here.

1.7 Summary

This Chapter provided a brief introduction to carbon nanotubes and graphene, outlining the structure and electronic properties of these materials. The production of carbon nanotubes and graphene was described and methods for tailoring their physical properties through doping discussed.

1.8 References

1. H.W. Kroto, J. R. Heath, S.C. O'Brien, S.C. Curl, and R.E. Smalley, Nature **318**, 162 (1985).
2. W. Krätschmer, L.D. Lamb, K. Fostiropoulos, and D.R. Huffman, Nature **347**, 354 (1990).
3. S. Iijima, Nature **354**, 56 (1991).
4. V.L. Radushkevich, V.M. Lukyanovich, Zhurn Fisic Chim **26**, 88 (1952).
5. M, Monthioux, V.L. Kuznetsov, Carbon **44**, 1621 (2006).
6. G. Philip and Ph. Avouris, Scientific American 62 (2000).
7. S.J. Tans, H. Michel, et at, Nature **386**, 474 (1997).
8. N.R. Neil and J.V. Macpherson, Nature nanotechnology **4**, 483 (2009).
9. P.M. Ajayan, Chem. Rev. **99**, 1787 (1999).
10. S. Iijima, T. Ichihashi,Nature **363**, 603 (1993).
11. J.W.G. Wildoer, L.C. Venema, A.G. Rinzler, R.E. Smalley, C. Dekker, Nature **391**, 59 (1998).
12. A. Thess, R. Lee, P. Nikolaev, H. Dai, P. Petit, J. Robert, C. Xu, Y.H. Lee, S.G. Kim, A.G. Rinzler, D. T. Colbert, G.E. Scuseria, D. Tomanek, J.E. Fischer, R. E. Smalley, Science **26**, 483 (1996).
13. R. Saito, M. Fujita, G. Dresselhaus, and M.S. Dresselhaus, Appl. Phys. Lett. **60,** 2204 (1992).
14. M.P. Anantram and F.Leonard, Rep. Prog. Phys. **69**, 507 (2006).
15. M.S. Dresselhaus, G. Dresselhaus, and R. Saito, Phys. Rev. B **45**, 6234 (1992).
16. N. Hamada, S. I. Sawada, and A. Oshiyama, Phys. Rev. Lett. **68,** 1579 (1992).
17. P.M. Ajayan, T.W. Ebbesen, T. Ichihashi, S. Iijima, K. Tanigaki, and H. Hiura, Nature **362**, 522 (1993).

[18] S.C. Tsang, P. J. F. Harris, and M. L. H. Green, Nature **362**, 520 (1993).

[19] P.J.F. Harris, 'Carbon Nanotubes and Related Structures: New Materials for the Twenty-First Century', Cambridge University Press, 1999.

[20] E. Kaxiras, and K.C. Pandey, Phys. Rev. Lett. **61**, 2693 (1988).

[21] P.M. Ajayan, V. Ravikumar and J.C. Charlier, Phys. Rev. Lett. **81**,1437 (1998).

[22] A.J. Lu, and B.C. Pan, Phys. Rev. Lett. **92**, 105504 (2004).

[23] C.H. Xu, C.L. Fu, and D.F. Pedraza, Phys. Rev. B **48**, 13273 (1993).

[24] K. Nordlund, J. Keinonen, and T. Mattila, Phys. Rev. Lett. **77**, 699 (1996).

[25] R.H. Telling and M.I. Heggie, Philosophical Magazine **87**, 4797(2007).

[26] G.J. Dienes, Journal of Applied Physics **23**, 1194 (1952).

[27] A.J. Stone and D.J.Wales, Chemical Physics Letters **128**, 501(1986).

[28] J. Liu, A.G. Rinzler, H. Dai, J.H. Hafner, R.K. Bradley, P.J. Boul, A. Lu, T. Iverson, K. Shelimov, C.B. Huffman, F. Rodriguez-Macias, Y.-S. Shon, T.R. Lee, D.T. Colbert, and R.E. Smalley, Science **280**, 1253 (1998).

[29] P.G. Collins, K. Bradley, M. Ishigami, and A. Zettl, Science **287**, 1801 (2000).

[30] J. Kong, N. R. Franklin, C.W. Zhou, M.G. Chapline, S. Peng, K.J. Cho, and H.J. Dai, Science **287,** 622 (2000).

[31] W.A. de Heer, A. Châtelain, D. Ugarte, Science **270**, 1179 (1995).

[32] A.G. Rinzler *et al*., Science **269**, 1550 (1995).

[33] N.S. Lee *et al*., Diamond Relat. Materials **10**, 265 (2001).

[34] Y. Saito, S. Uemura, Carbon **38**, 169 (2000).

[35] R. Rosen *et al*., Appl. Phys. Lett. **76**, 1668 (2000).

[36] H. Sugie *et al*., Appl. Phys. Lett. **78**, 2578 (2001).

[37] O. Zhou, personal communication.

[38] B.I. Yakobson, C.J. Brabec, and J. Bernholc, Phys. Rev. Lett. **76**, 2511 (1996).

[39] M.F. Yu, O. Lourie, M.J. Dyer, K. Moloni, T.F. Kelly, and R.S. Ruoff, Science **287**, 637 (2000).

[40] F.J. Ribeiro, D. J. Roundy, and M. L. Cohen, Phys. Rev. B **65**, 153401 (2002).

[41] Dong Qian, J Wagner, and Wing Kam Liu, Appl. Mec. Rev. **55**, 495 (2002).

[42] A. Hirsch, Angewandte Chemie-International Edition **41**, 1853 (2002).

[43] S. Banerjee, T. Hemraj-Benny and S.S.Wong, Adv. Mater. 17 17 (2005)

[44] X. Lu and Z.F. Chen, Chemical Reviews **105**, 3643 (2005).

[45] J. M. Carlsson, Physica Status Solidi B **243**, 3452 (2006).

[46] S. Berber, and A. Oshiyama, Physica B-Condensed Matter **376**, 272 (2006).

47. C.P. Ewels, M.I. Heggie and P.R. Briddon, Chemical Physics Letters **351**, 178 (2002).

48. A. Hirsch, Angew Chem. Int. Ed. **41**, 1853 (2002).

49. M. Glerup, V. Krstic, C. Ewels, and M. Holzinger, 'Doping of Carbon Nanotubes', 'Nanomatereials and Nanodevices', ed. W. Chen, American Scientific, Los Angeles (2007).

50. P. Ayala, R. Arenal, M. Rümmeli, A. Rubio, T. Pichler, Carbon **48**, 575 (2010).

51. K. Gong, F. Du, Z. Xia, M. Durstock and L. Dai, Science **323**, 760 (2009).

52. Z. Zanolli, R. Leghrib, A. Felten, J-J. Pireaux, E. Llobet and J-C. Charlier, ACS Nano 5, 4592 (2011).

53. D. Jana, C.-L. Sun, L.-C. Chen and K.-H. Chen, Prog. Mater. Sci. **58**, 565 (2013).

54. J.Y. Yi and J. Bernholc, Phys. Rev. B **47**, 1708 (1993).

55. F. Xu, M. Minniti, C. Giallombardo, A. Cupolillo, P. Barone, A. Oliva, et al. Surf. Sci. **601**, 2819 (2007).

56. F. Xu, M. Minniti, P. Barone, A. Sindona, A. Bonanno, A. Oliva. Carbon **46**, 1489 (2008).

57. M. Nath, P. Teredesai, D.V.S. Muthu, A.K. Sood and C.N.R. Rao, Curr. Sci. **85,** 956 (2003).

58. M.D.C. Gimenez,-Lopez, A. Chuvilin, U. Kaiser and A.N. Khlobystov, Chem. Commun. **47**, 2116 (2011).

59. E.T. Mickelson, C.B. Huffman, A.G. Rinzler, R.E. Smalley, R.H. Hauge, and J.L. Margrave, Chem. Phys. Lett. **296,** 188 (1998).

60. P.J. Boul, J. Liu, E.T. Mickelson, C.B. Huffman, LM. Ericson, I.W. Chiang, K.A. Smith, D.T. Colbert, Chem. Phys. Lett. **310**, 367 (1999).

61. R.K. Saini, I.W. Chiang, H. Peng, R. E. Smalley, W.E. Billups, R.H. Hauge, and J.L. Margrave, J. Am. Chem. Soc. **125**, 3617 (2003).

62. J. Liu, A.G. Rinzler, H.J. Dai, J.H. Hafner, R.K. Bradley, P.J. Boul, A. Lu, T. Iverson, K. Shelimov, C.B. Huffman, F. Rodriguez-Macias, Y.S. Shon, T.R. Lee, D.T. Colbert, R.E. Smalley, Science **280**, 1253 (1998).

63. K.F. Fu, W.J. Huang, Y. Lin, L.A. Riddle, D.L. Carroll, Y.P. Sun, Nano Letters **1**, 439 (2001).

64. J.L. Bahr, J.P. Yang, D.V. Kosynkin, M.J. Bronikowski, R.E. Smalley, J.M. Tour, J. Am.Chem. Soc. **123**, 6536 (2001).

65. J.L. Bahr, J.M. Tour, Chem. Mat. **13**, 3823 (2001).

66. J. Chen, M.A. Hamon, H. Hu, Y. S. Chen, A.M. Rao, P.C. Eklund, R.C. Haddon, Science **282**, 95 (1998).

[67] G.S. Duesberg, M. Burghard, J. Muster, G. Philipp, S. Roth, Chem. Commun., 435 (1998).

[68] S. Bandow, A.M. Rao, K.A. Williams, A. Thess, R.E. Smalley, P.C. Eklund, J. Phys. Chem. B **101**, 8839 (1997).

[69] B.R. Azamian, J.J. Davis, K.S. Coleman, C.B. Bagshaw, M.L.H. Green, J. Am. Chem. Soc. **124**, 12664 (2002).

[70] D. Tomanek, J. Phys. Condens. Matter **17**, R413 (2005).

[71] D.Q. Yang, J. Rochette, and E. Sacher, Langmuir **21**, 8539 (2005).

[72] B. Ni, R. Andrews, D. Jacques, D. Qian, M. B.J. Wijesundara, Y. Choi, L. Hanley, and S.B. Sinnott, J. Phys. Chem. B **105**, 12719 (2001).

[73] Y. Zhu, T. Yi, B. Zheng, and L. Cao, Appl. Surf. Sci. **137**, 83 (1999).

[74] C. Morant, J. Andrey, P. Prieto, D. Mendiola, J. M. Sanz, and E. Elizalde, Phys. Stat. Sol. **203**, 1069 (2006).

[75] A. Hashimoto, K. Suenaga, A. Gloter, K. Urita, and S. Iijima, Nature (London) 430, 870 (2004).

[76] A.V. Krasheninnikov, K. Nordlund, M. Sirviö, E. Salonen, and J. Keinonen, Phys. Rev. B **63**, 245405 (2001).

[77] A.V. Krasheninnikov, K. Nordlund, Nucl. Instr. and Meth. in Phys. Res. B **216,** 355 (2004).

[78] P.A. Thrower and R.M. Mayer, Phys. Stat. Sol. (a) **47**, 11 (1978).

[79] A.V. Krasheninnikov, K. Nordlund, and J. Keinonen, Phys. Rev. B **65**, 165423 (2002).

[80] B.I. Yakobson, Appl. Phys. Lett. **72**, 918 (1998).

[81] M.B. Nardelli, B.I. Yakobson, and J. Bernholc, Phys. Rev. B **57**, 4277 (1998).

[82] G.G. Samsonidze, and B.I. Yakobson, Phys. Rev. Lett. **88**, 065501 (2002).

[83] P. Vincent, A. Brioude, C. Journet, S. Rabaste, S.T. Purcell, J.L. Brusq, and J.C. Plenet, J. Non-Cryst. Solids **311**, 130 (2002).

[84] J. Kotakoski, A.V. Krasheninikov, Yuchen Ma, A.S. Foster, K. Nordlund, and R.M. Nieminen, Phys. Rev. B **71**, 205408 (2005).

[85] K.S. Novoselov, A.K. Geim, S.V. Morozov, D. Jiang, Y. Zhang, S.V. Dubonos, I.V. Grigorieva, A.A. Firsov, Science **306**, 666 (2004).

[86] Y. Zhang, Y.W. Tan, H.L. Stormer, P. Kim, Nature **438**, 201 (2005).

[87] K.S. Novoselov, E. McCann, S.V. Morozov, V.I. Fal'ko, M.I. Katsnelson, U. Zeitler, D. Jiang, F. Schedin, A.K. Geim, Nat. Phys. **2**, 177 (2006).

[88] A.K. Geim, Science **324**, 1530 (2009).

89. P.R. Wallace, Phys. Rev. **71,** 622 (1947).

90. A.K. Geim and K.S. Novoselov, Nat. Mater. **6**, 183 (2007).

91. A.E. Karu, J. Appl. Phys. **37**, 2179 (1966).

92. C. Oshima and A. Nagashima J. Phys.: Conden. Matter **9**, 1 (1997).

93. M. Eizenberg and J.M. Blakely, Surf. Sci. **82**, 228 (1979).

94. K.I. Bolotin, K.J. Sikes, Z. Jiang, M. Klima, G. Fudenberg, J. Hone, P. Kim, H.L. Stormer, Solid State Commun. **146**, 351 (2008).

95. C. Lee, X. Wei, J.W. Kysar, and J. Hone, Science **321**, 385 (2008).

96. Q. Liang, X. Yao, W. Wang, Y. Liu, and C.P. Wong, ACS Nano **5**, 2392 (2011).

97. R.R. Nair, P. Blake, A.N. Grigorenko, K.S. Novoselov, T.J. Booth, T. Stauber, N.M.R. Peres, A.K. Geim, Science **320**, 1308 (2008).

98. A. Jorio, M.S. Dresselhaus, R. Saito, and G. Dresselhaus, 'Raman Spectroscopy in Graphene Related Systems', (John Wiley & Sons, 2011).

99. H. Castro Neto, F. Guinea, N.M.R. Peres, K.S. Novoselov, and A.K. Geim, Rev. Mod. Phys. **81**,109162 (2009).

100. K.S. Novoselov *et al*., Nature **438**, 197 (2005).

101. K.S. Novoselov, D. Jiang, F. Schedin, T.J. Booth, V.V. Khotkevich, S.V. Morozov, A.K. Geim, Proc. Natl. Acad. Sci. **102**, 10451 (2005).

102. Y. Zhang, J.P. Small, W.V. Pontius, P. Kim, Appl. Phys. Lett. **86**, 073104 (2005).

103. P. Blake, E. W. Hill, A.H. Castro Neto, K.S. Novoselov, D. Jiang, R. Yang, T.J. Booth, A.K. Geim, Appl. Phys. Lett. **91**, 063124 (2007).

104. P. Neugebauer, M. Orlita, C. Faugeras, A.-L. Barra, M. Potemski, Phys. Rev. Lett. **103**, 2 (2009).

105. C.R. Dean, A.F. Young, I. Meric, C. Lee, L. Wang, S. Sorgenfrei, Nat. Nanotech. **5**, 722 (2010).

106. J.-H. Chen, C. Jang, S. Xiao, M. Ishigami, M.S. Fuhrer, Nat. Nanotech. **3**, 206 (2008).

107. K.I. Bolotin, K.J. Sikes, Z. Jiang, M. Klima, G. Fudenberg, J. Hone, P. Kim, H.L. Stormer, Solid State Commun. **146**, 351 (2008).

108. M. Ishigami, J.H. Chen, W.G. Cullen, M.S. Fuhrer, E.D. Williams, Nano Lett. **7**, 1643 (2007).

109. I. Forbeaux, J. Themlin, J. Debever, Surf. Sci. **442**, 9 (1999).

110. P. Sutter, Nat. Mater. **8**, 171 (2009).

111. J. Hass, R. Feng, T. Li, X. Li, Z. Zong, W.A. de Heer, P.N. First, E.H. Conrad, C.A. Jeffrey, C. Berger, Appl.Phys. Lett. **89**, 143106 (2006).

[112.] K.V. Emtsev, A. Bostwick, K. Horn, J. Jobst, G. L. Kellogg, L. Ley, J.L. McChesney, T. Ohta, S.A. Reshanov, J. Röhrl, E. Rotenberg, A.K. Schmid, D. Waldmann, H. B.Weber, T. Seyller, Nat. Mater. **8**, 203 (2009).

[113.] S. Park, R.S. Ruoff, Nat. Nanotech. **4**, 217 (2009).

[114.] K.S. Kim, Y. Zhao, H. Jang, S.Y. Lee, J.M. Kim, K. S. Kim, J.-H. Ahn, P. Kim, J.-Y. Choi, B.H. Hong, Nature **457**, 706 (2009).

[115.] A. Reina, X. Jia, J. Ho, D. Nezich, H. Son, Nano lett. **9**, 30 (2008).

[116.] C. Mattevi, H. Kim, M. Chhowalla, J. Mat. Chem. **21**, 3324 (2011).

[117.] X. Li, W. Cai, J. An, S. Kim, J. Nah, D. Yang, R. Piner, A. Velamakanni, I. Jung, E. Tutuc, S.K. Banerjee, L. Colombo, R.S. Ruoff, Science **324**, 1312 (2009).

[118.] X. Li, C. W. Magnuson, A. Venugopal, R.M. Tromp, J.B. Hannon, E.M. Vogel, L. Colombo, R.S. Ruoff, J. Am. Chem. Soc. **133**, 2816 (2011).

[119.] X. Li, W. Cai, L. Colombo, R.S. Ruoff, Nano lett. **9**, 4268 (2009).

[120.] K. Kim, Z. Lee, W. Regan, C. Kisielowski, M. F. Crommie, A. Zettl, ACS Nano. **5**, 2142 (2011).

[121.] P.Y. Huang, C.S. Ruiz-Vargas, A.M. van der Zande, W.S. Whitney, M.P. Levendorf, J.W. Kevek, S. Garg, J.S. Alden, C.J. Hustedt, Y. Zhu, J. Park, P.L. McEuen, D.A. Muller, Nature **469**, 389 (2011).

[122.] L. Tapasztó, P. Nemes-Incze, G. Dobrik, K. Jae Yoo, C. Hwang, L.P. Biró, Appl.Phys. Lett. **100**, 053114 (2012).

[123.] D. Geng, B. Wu, Y. Guo, L. Huang, Y. Xue, J. Chen, G. Yu, L. Jiang, W. Hu, Y. Liu, Proc. Natl. Acad. Sci. **2012**, 1 (2012).

[124.] W. Wu, L.A Jauregui, Z. Su, Z. Liu, J. Bao, Y.P. Chen, Q. Yu, Adv. Mater. **23**, 4898 (2011).

[125.] Q. Yu, L.A. Jauregui, W. Wu, R. Colby, J. Tian, Z. Su, H. Cao, Z. Liu, D. Pandey, D. Wei, T. F. Chung, P. Peng, N.P. Guisinger, E.A. Stach, J. Bao, S.-S. Pei, Y.P. Chen, Nat. Mater. **10**, 443 (2011).

[126.] T. Yoon, W.C. Shin, T.Y. Kim, J.H. Mun, T.-S. Kim, B.J. Cho, Nano lett. **12**, 1448 (2012).

[127.] Z. Sun, D.K. James, J.M. Tour, J. Phys. Chem. Lett. **2**, 2425 (2011).

[128.] Z. Sun, Z. Yan, J. Yao, E. Beitler, Y. Zhu, J.M. Tour, Nature **468**, 549 (2010).

[129.] H. Ji, Y. Hao, Y. Ren, M. Charlton, W. H. Lee, Q. Wu, H. Li, Y. Zhu, Y. Wu, R. Piner, R.S. Ruoff, ACS Nano **5**, 7656(2011).

[130.] S.-J. Byun, H. Lim, G.-Y. Shin, T.-H. Han, S. H. Oh, J.-H. Ahn, H.C. Choi, T.-W. Lee, J. Phys. Chem. Lett. **2**, 493 (2011).

[131.] Z. Yan, Z. Peng, Z. Sun, J. Yao, Y. Zhu, Z. Liu, P.M. Ajayan, ACS Nano **5**, 8187 (2011).

[132.] L.M.A. Perdigao, S.N. Sabki, J.M. Garfitt, P. Capiod, P.H. Beton, J. Phys.Chem. **115**, 7472 (2011).

[133.] H.J. Shin, W.M. Choi, S.-M. Yoon, G.H. Han, Y.S. Woo, E. S. Kim, S.J. Chae, X.-S. Li, A. Benayad, D.D. Loc, F. Gunes, Y.H. Lee, J.-Y Choi,. Adv. Mater. **23**, 4392 (2011).

[134.] P. San-Jose, E. Prada, E. McCann, H. Schomerus, Phys. Rev. Lett. **102**, 247204 (2009).

[135.] M. Tonouchi, Nature Photon. **1**, 97 (2009).

[136.] F. Wang, Y. Zhang, H. Tian, C. Girit, A. Zettl, M. Crommie, Y. R. Shen, Science **320**, 206 (2008).

[137.] M.S.S. Azadeh, A. Kokabi, M. Hosseini and M. Fardmanesh, Micro and Nano Lett. **6**, 582 (2011).

Chapter 2

Experimental Techniques

This chapter provides a brief introduction to the techniques used to obtain the data presented in this thesis. The basic principles and the theoretical background of these techniques are discussed. Particular emphasis is placed on the information which can be obtained from carbon nanomaterials such as nanotubes and graphene.

2.1 Introduction

There are a number of powerful experimental techniques which are suitable for investigating the physical and chemical properties of carbon nanomaterials such as carbon nanotubes (CNTs) and graphene. Among the most common tools currently used are X-ray photoelectron spectroscopy (XPS)[1,2,3,4,5,6,7,8], scanning electron microscopy (SEM)[9,10,11,12], Auger electron microscopy (AES)[13,14], optical microscopy (OM)[15,16,17,18,19] and Raman Spectroscopy (RS)[20,21,22,23]. Each technique provides complementary information, but none is able to provide a complete picture of the nanomaterial studied, highlighting the importance of a multi-technique approach to CNT and graphene characterisation even though this is not often adopted in studies published in the literature.

The need for multiple experimental tools is highlighted if we briefly consider the information about the material under examination that each technique furnishes. XPS provides valuable insight into the chemical structure and elemental composition of a sample surface[3,4], whereas SEM is a powerful tool which can provide a picture of the morphology of a surface (and, at least in the simple imaging modes described below, qualitative information on sample composition – other imaging modes, not employed here, are required for more quantitative data)[9,11]. The presence and two-dimensional morphology of islands of graphene can also be determined by both unpolarised and polarised optical microscopy. Polarised optical microscopy (POM) uses the birefringence of some materials in order to create contrast enabling their visualisation[16,18]. Although the symmetry of graphene should preclude birefringence, there are circumstances in which optical anisotropy appears to be induced[15], so enabling POM to function as a simple detection technique. In unpolarised OM graphene may be observed if the substrate is subject to some post-growth treatment, such as oxidation[18,19], in order to create contrast. Raman spectroscopy probes the vibrational structure of solids, so indirectly indicating composition, perfection, layer thickness, etc. as described below. Due to its ease of use and the well-understood phonon spectra of carbon nanomaterials[21,22]. Raman spectroscopy is often the technique of choice for nanotube and graphene characterisation in the literature but provides only a qualitative measure of the defects present.

2.2 X-ray Photoelectron Spectroscopy (XPS)

2.2.1 Introduction

The photoelectric effect – the emission of electrons brought about by absorption of light – was first observed by Hertz in 1887 and explained by Einstein 1905[24]. When a photon (of energy, *hν*) is incident upon an atom and has sufficient energy (larger than the binding energy, *BE*, of an electron), it can transfer its energy to one or more electrons and the electron(s) will be ejected from the atom with a certain kinetic energy (*KE*). In the simplest approximation (Koopman's Theorem), the binding energy is simply the difference between the incident photon energy and the kinetic energy of the electron according to Eq. 2.1[24]:

$$KE = h\nu - BE \qquad (2.1)$$

The binding energy of the photoelectron is able to provide key information such as the identity of the atom from which it originated and, if the atom is part of a molecule or a solid material, the nature of the bonding of that atom with its neighbours and the fundamental electronic excitations of that material. Therefore, spectroscopic analysis of photoelectron energy is an extremely valuable tool and forms the basis of the technique of photoelectron spectroscopy which was originally developed by Kai Siegbahn and led to being his awarded the 1981 Nobel Prize for Chemistry. Photoelectron spectroscopy using sufficiently a high energy photons to liberate core electrons is known as X-ray photoelectron spectroscopy (XPS) or Electron Spectroscopy for Chemical Analysis (ESCA) and has become common tool for chemical analysis[24]. Fig 2.1 schematically illustrates a typical XPS experimental system and the various energies associated with the photoemission process.

Since core electrons are only weakly perturbed by their chemical environment they are especially valuable in atomic/chemical identification, providing a spectroscopic 'fingerprint' of the elements present within a material. When combined with photoionisation cross-sections and the experimental parameters under which spectra are acquired, the relative intensity of photoelectron lines from different elements can provide quantitative and detailed information on elemental composition[24,25,26]. Moreover, the small perturbation of core-level binding energies brought about by changes to the local atomic environment through bonding

to neighbours enables the determination the chemical state(s) of each element (as discussed in section 2.3.2).

Valence band features can also aid in understanding local bonding and electronic structure. Although XPS can be used to produce valence band spectra the relatively poor resolution of XPS and the low cross-section for photoemission of valence electrons by x-rays means that lower photon energies are favoured for valence band spectroscopy, typically in the visible ultra-violet (VUV). Photoelectron spectra taken with VUV radiation is typically known as ultraviolet photoemission spectroscopy (UPS). It should be noted that the rather arbitrary division between XPS and UPS is based on the photon energies available from laboratory based sources and that at a synchrotron, which is a continuously tunable photon source, photon energy selection is usually made on the basis of cross-section and depth considerations and can often fall between the two extremes of typical laboratory sources[24].

It is important to note that XPS is very surface sensitive because the inelastic mean free path of the photoemitted electrons is small. It is identical to the escape depth *l* which typically varies from 2 to 20 nm depending on the material, core-level and excitation energy.

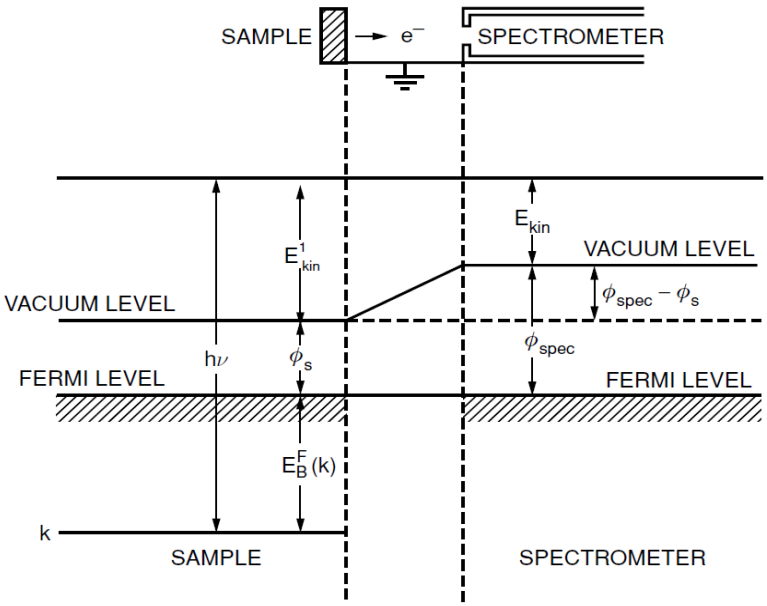

Fig 2.1: Schematic representation of the photoemission process[24].

When a core electron is emitted in the photoelectric process, the inner shell of the atom (*A*) is ionised. So energy conservation requires

$$E(A) + h\nu = E(A^*) + E_{KE} + \phi$$

$$E_{KE} = h\nu - [E(A^*) - E(A)] - \phi = h\nu - E_B - \phi \qquad (2.2)$$

where ϕ is the spectrometer workfunction, $E(A)$ is the energy of the neutral atom and $E(A^*)$ the energy of the core-ionised atom, E_{KE} is the kinetic energy of photoelectron, $h\nu$ is the incident energy of the photon, and E_B is the binding energy of electron.

In order to obtain a spectrum, it is usual to use an electrostatic energy analyser to select the electrons by kinetic energy. The most common analyser used in XPS incorporates two concentric hemispherical plates across which an appropriate bias is maintained. Electrons are deflected by the radial electric field and a narrow energy band is chosen by apertures places at the entrance and exit of the hemispheres. The *pass energy* is the kinetic energy of the electrons that will pass through the spherical analyser without deflection. Electrons with higher or lower energy will not be transmitted. The intensity of the detected photoelectrons may then be plotted against *KE* to show the photoelectron spectrum. There are many considerations which must be taken in account in order to obtain useful data[24]. For example, the spectrometer must be calibrated to a suitable reference, such as the Fermi level of a conductive sample in direct contact with the spectrometer, Fig. 2.1. Such a reference is only valid if the sample is also sufficiently conductive (although it does not have to be metallic). Calibration to a reference then allows the conversion of photoelectron kinetic energy to binding energy in a reliable manner. In order to quantify the composition of a sample reliably the transmission function of the spectrometer – the efficiency with which it detects electrons of different kinetic energies – must also be known. For the XPS measurements presented in this report the spectrometer was calibrated with a silver test sample, which is a common standard.

2.2.2 Factors influencing X-ray Photoelectron Spectra

Koopman's theorem states that the binding energy of a photoelectron is simply the negative of its atomic orbital energy according to Eq. 2.3[24]:

$$E_{BE} = E_f\,(N\text{-}1) - E_i\,(N) \qquad (2.3)$$

where the subscripts *i* and *f* correspond to initial and final states, *N* and *(N-1)* are the number of electrons in the system. However, Koopman's theorem is an idealisation and what are known as initial state and final state effects change the measured electron binding energies from those which are predicted.

The initial state of the system is the ground state of the electronic system within an atom, molecule or solid. 'Initial state effects' are the changes in core-level orbital energy associated with the formation of a molecule or solid compound. Although these changes are small compared with those which occur for valence electrons, they result in the shift of core photoelectron lines by up to a few electron-volts. Such binding energy changes can be easily detected and provides the basis of the chemical state identification possible with the technique[24,25]. Table 2.1 shows typical initial state shifts in carbon containing compounds which can be used to identify the bonding in CNTs.

Compound type	C1*s* BE range (eV)
C (Carbon)	284.25 - 286.5
C-N (nitrogen)	285.25 – 288.5
C-O (oxygen)	286 – 291.5

Table 2.1: Binding energies of the C1*s* line for carbon in different chemical environments.

'Final state effects' originate from states which are related to the system configuration after the photoemission process. Final state effects have different causes such as relaxation, excitation and spin-orbit coupling[24]. The relaxation effect is the most obvious final state effect and occurs when the energies of valence levels and shallow core-levels respond to the reduction in screening of the nuclear charge after ejection of a core electron. Relaxation, which occurs simultaneously with photoemission of the core electron leads to a lower energy final state than would occur if the electrons remaining on the atom were frozen and, as a result of conservation of energy, the emitted photoelectron has a high kinetic energy (or apparently lower binding energy). It is also possible that the atom may be left in an excited state after ejection of a core electron, leading to second final state effects which are satellite features in the photoelectron spectrum associated these excitations.

The excitation of electronic transitions within the atom (molecule or solid) leads to what are known as 'shake-up' features. These features produce photoelectrons that have lost energy through excitation of valence electrons from an occupied energy level to an unoccupied higher level. Shake up peaks (sometimes called loss peaks because intensity is lost from the fundamental photoemission peak) are most likely from aromatic structure formation, unsaturated chemical bonds or transition metal ions. If the primary photoelectron transfers sufficient energy to the valence electron to ionise it from the atom, the photoemission loss peak is known a 'shake-off' peak. The shake-off satellite peaks of the photoemission signal can include many possible energies which are lower than the photoemission peak. However, this feature disappears within the background intensity. The third final state effect is spin orbit coupling. It occurs for final states for all core levels except the symmetric *s*-level. This is a result of interaction of the spin angular momentum (*s*) of electron with its orbital angular momentum (*l*). In fact, doublet or multiple peaks in the photoelectron spectrum arise from doublet and multiple splitting of the orbital momentum. The energy separation between the two peaks is known the spin-orbit splitting, Δ_{so}.

2.2.3 Analysis of X-ray Photoelectron Spectra

In a photoelectron spectrum quantification is required to determine the properties of the material under investigation, for example the energy width of given line is determined by the life-time of the associated core hole in an ideal atomic system and can have further

contributions from disorder, low energy excitations in a solid and the resolution of the spectrometer. Line widths are usually described by the full width at half maximum (FWHM) of a given peak, since this quantity is readily accessible from the spectra. Another important factor is relative peak intensity. The intensities of various photoelectron lines are important for quantification since they depend on the relative quantity of the materials present. However, effects of cross-section for photoemission and analyser transmission need to be taken into account in such calculations. If one assume that the elemental concentration into the sample is uniform over given depth, then the atomic percentage of each atomic species wirhen a solid can be found as,

$$\%n_i = \frac{N_i}{\sum N_i} \times 100 \qquad (2.4)$$

when N_i is corresponding to the species atoms *i*, which is given by the following:

$$I_{ij} = C.T(E_k).L_{ij}(\gamma).\sigma_{ij}.N_i.\lambda(E_k)cos\theta_E \qquad (2.5)$$

where I_{ij} is the area of peak *j* from element *i; C* is an instrumental constant; $T(E_k)$ is the transmission function of the analyser (which determines the efficiency of detection of a photoelectron of energy E_k); $L_{ij}(\gamma)$ is the angular asymmetry factor for the orbital *j* of element *i*, which is under consideration; σ_{ij} is the photoionisation cross section of peak *j* from element *i*; N_i is the concentration of element *i* at a distance *z* below the surface of the sample; $\lambda(E_k)$ is the inelastic mean free path length at energy E_k, and θ_E is the emission angle of the photoelectrons measured with respect to the surface normal[24].

2.3 Raman Spectroscopy (RS)

2.3.1 Introduction

Raman scattering of light was first experimentally detected by the Indian scientist C.V. Raman in 1928[27]. In the same time, this observation has been also discovered by L. Mandelstam[28]. As a result of Raman's observations, he was awarded the Nobel Prize in

Physics in 1930. Raman Spectroscopy has become a widespread tool in materials research after the introduction of the laser light in the mid-1960s[25,29]. Raman spectroscopy has developed into a powerful diagnostic technique which can provide information on the chemical structure, elemental composition, vibrational and electronic states of a sample. Practical Raman spectroscopy is a fast and non-destructive procedure and no specialised sample preparation is usually required. As a result, measurements may be obtained under ambient conditions and for a wide variety of sample states (e.g., powder, solid, liquid, supported by a substrate etc.)[29,30]. As a non-invasive technique Raman spectroscopy can also be applied to samples held in specialised environments such as high pressure, high/low temperature, vacuum, although such conditions will not be applied to the measurements presented in this thesis.

2.2.2 The basics of Raman Spectroscopy

Raman scattering of light is an inelastic process which occurs between a monochromatic photon of laser light at low energy (typically in the visible region of the spectrum) and an atom or solid resulting in the creation or annihilation of one or more vibrational quanta. In this process, the electric field of the photon interacts with the electrons in the atom or solid exciting them to a virtual or (in the case of *resonant* Raman scattering) real electronic state[29]. The electric field of the excited electron perturbs the ionic core of the atom in the molecule or solid and may create a phonon in the crystal lattice or vibration in a molecule, and as a result inelastic scattering occurs. The scattered light mainly contains photons of the same energy as the incident light, i.e., elastically scattered photons. The process of elastic scattering is called Rayleigh scattering and dominates Raman spectra unless specific steps are taken to remove the elastic line – most Raman instruments use a notch filter to remove Rayleigh scattered light from the signal before analysis. On the other hand, a small minority of photons (typically about 1 in 10^7) are inelastically scattered, losing or gaining quanta of vibrational energy; in this case the scattering is known as the Raman Effect. If the energy of photon is transferred from the photon to the atom/lattice, the scattered light will be of lower energy leading to what are known as Stokes lines and if the energy is transferred from lattice to the photon, scattered light will be higher in energy (anti-Stokes lines)[30,31], Fig. 2.2.

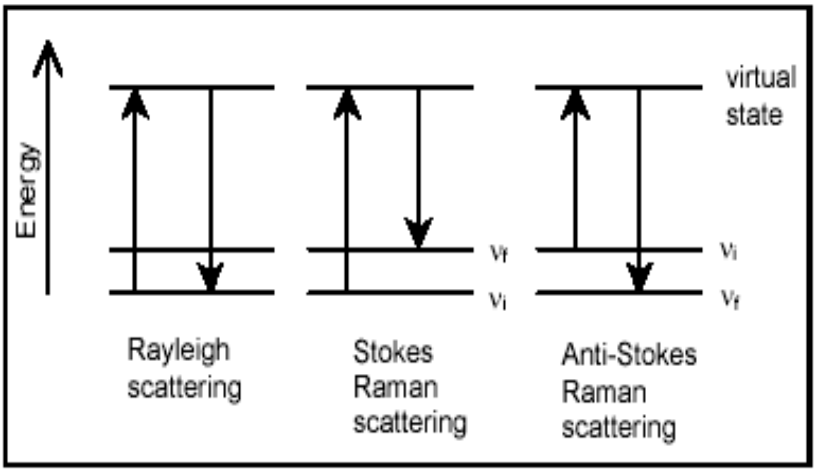

Fig. 2.2: The quantum illustration for different cases of scattering[31].

In each of Raman scattering processes, when non-resonant, the incident photon excites an electron into an unstable higher energy *'virtual'* state and then the electron decays back to a lower level, emitting a scattered photon. The virtual electronic state is not a well-defined energy level of the system, rather it is an excited state which does not correspond to a stationary state of the electronic system but which is sufficiently short lived that its existence satisfies the Heisenberg uncertainty principle. The energy level diagrams for the Rayleigh, Stokes and anti-Stokes scattering schemes are presented in Fig. 2.2. Raman scattering can only be seen at vibrational modes which have dynamic electric quadruple moments.

In a Raman spectrum, the energy shift (or Raman shift) is determined by the difference between the wavelength or energy of the incident photon and the scattered (anti-)Stokes light due to phonon (annihilation) creation. The magnitude of this shift is usually measured in units of wavenumber (cm^{-1}). Knowing the phonon dispersion relations of a solid, it is possible to predict the allowed Raman scattering processes and consequently the Raman spectra. It is also observed that the intensity of Stokes lines is higher than the anti-Stokes, the ratio between the two dependent on phonon thermal population. Indeed, the ratio between the Stokes and anti-Stokes lines of a given mode can be used to determine the local temperature of the sample.

2.2.2 Characteristics of graphene and nanotube Raman Spectra

The characteristic Raman spectra of graphitic systems, including nanostructured solids such as fullerenes, graphene and carbon nanotubes[21,22]. provides rich information about the

structure and perfection of these materials. Indeed, Raman spectroscopy has probably become the most widespread technique for investigation of these materials systems. As a result there are several extensive reviews dedicated to this subject (e.g., Ref 23) and we shall limit our discussion to a brief overview necessary to understand the results presented in this thesis.

The phonon dispersion of graphene is key to understanding Raman spectra from the complete range of graphitic nanostructures. Since the unit cell of graphene has two carbon atoms in inequivalent locations, their vibration can be either in-phase or out-of-phase resulting in acoustic or optical phonon modes respectively. For each mode, vibration of the two atoms can be in the carbon-carbon bond direction in-plane, resulting in what are known as in-plane longitudinal acoustic phonons (iLA) and in-plane longitudinal optic phonons (iLO). In-plane vibrations perpendicular to the carbon-carbon direction leads to in-plane transverse acoustic phonons (iTA) and in-plane transverse optic phonons (iTO). Vibrations which are perpendicular to the plane containing the carbon atoms produce out of plane transverse optic phonons (oTA) and out of plane longitudinal optic phonons (oLA). As a result of the combination of these cases, there will be six branches in the phonon dispersion relation for for graphene, as illustrated in Fig. 2.3(a). The spectrum of monolayer graphene obtained from these phonon dispersions can be given in Fig. 2.3(b).

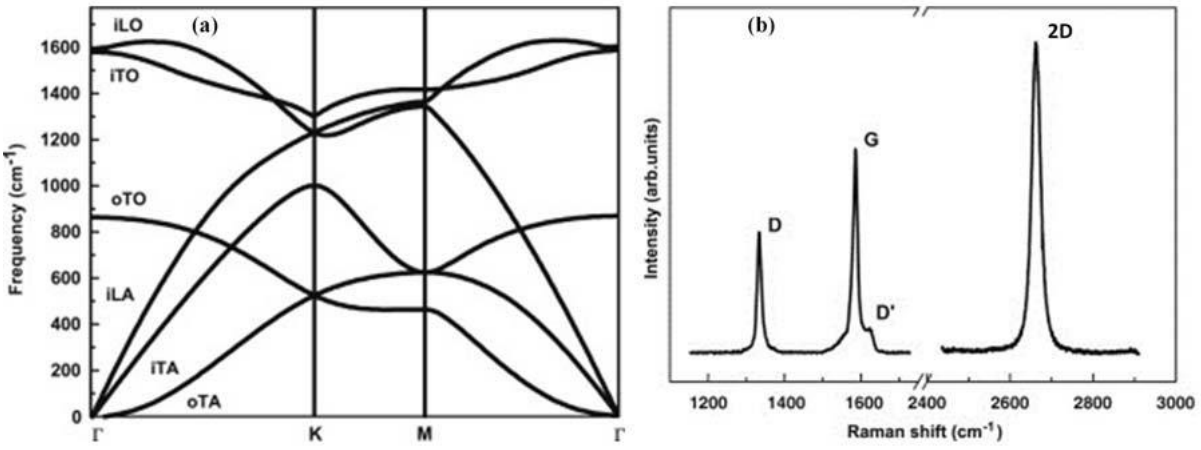

Fig. 2.3: Phonon dispersion (a) and Raman spectrum of graphene (b)[22].

The most visible bands in the Raman spectrum of graphene are the G-band and the 2D-band which can be seen at approximately 1580 cm^{-1} and 2700 cm^{-1} respectively (Fig. 2.3(b)). The G band is assigned to two doubly degenerate phonon modes iTO and iLO (Fig. 2.4(a)) at the Brillouin zone centre (Γ) due to first order Raman scattering processes involving only

absorption and emission of phonons as displayed in Fig. 2.4(d). It is also seen from Fig. 2.4(a) that the D-band, which occurs around 1350 cm^{-1}, is due to a double resonance (DR) Raman scattering process involving one (iTO) phonon and one crystal defect near the *K* point. The occurrence of a DR event starts with an electron around the valley point *K* which absorbs an incident photon and gets elastically scattered by a defect in the crystal to another electronic state centred on the valley point *K*'. The electron is inelastically scattered back to the original valley by an electron-phonon interaction finally emitting photon by combining with the original hole. There are two events included in the DR process, one elastic scattering event caused by a defect of the crystal and, one inelastic event caused by electron-phonon interactions. The process leading to the 2D-band is similar to the DR process for the D band except that both scattering events are inelastic, caused by interaction of electron with two phonons of equal and opposite wavevector as illustrated in Fig. 2.4(b). The 2D-band is so-called because it can occur at around twice wavenumber of D-band. Due to the different scattering mechanisms, the 2D-band can be present in graphene spectrum even if the D-band is negligible. One further band which can be also seen in the graphene Raman spectrum is termed the D'-band. It also originates from a DR process, but in this case, an electron is scattered into a neighbouring state on the same circle around the *K* or *K*' valley point. It is worth mentioning that the DR process which gives rise to the D'-band needs one defect and one iLO phonon for activation as can be seen in Fig. 2.4(c).

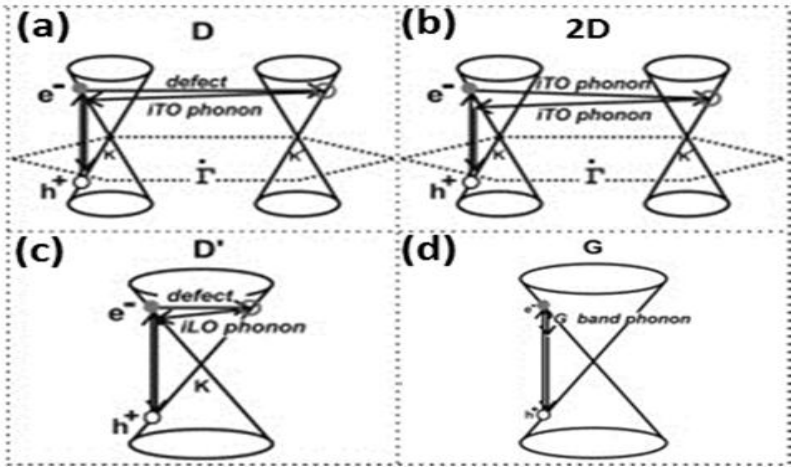

Fig. 2.4: Double Resonance Process for: (a) *D* peak, (b) *2D* peak and (c) *D'* peak. (d) single resonance process involved in G peak. Figure taken from Ref [22].

The most characteristic features of the Raman spectra of carbon nanotubes are: (a) the G-band, located around 1500 to 1600 cm^{-1} – the origin of which has been described above; (b) the D-band, centred at around 1300 cm^{-1}, which indicates the presence of defects in the crystal structure of the nanotube; and (c) a 2D band, which is located at around 2600 cm^{-1}. There is a group of bands which can appear between 400 cm^{-1} and 1200 cm^{-1} which are known as the intermediate frequency phonon modes (IFM) and a combination of acoustic and optical modes (iTOLA). For SWCNTs, the exceptional modes are the radial breathing modes (RBMs), which are located in the region of 200 to 400 cm^{-1}, and the M-mode centred at 1750 cm^{-1}. In addition, in SWCNTs the G-band is seen to be split into G^- and G^+ modes (Fig. 2.5).

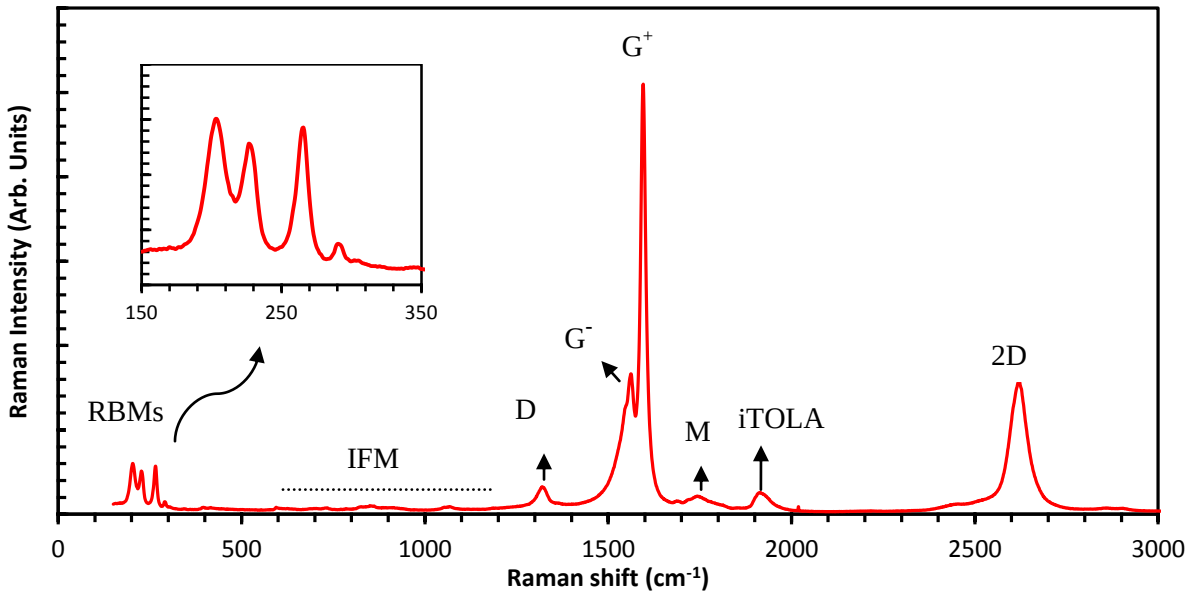

Fig. 2.5: Raman spectrum from a SWCNT sample. The main features of interest are labelled and described in the text. The detail of the radial breathing modes is illustrated in the inset.

The RBM feature in the Raman spectra of SWCNTs is associated with radial motion of the SWCNT walls[21]. The RBM frequencies have a strong diameter dependence and as a result can be used as a significant signal to investigate the diameter distribution of a SWCNT sample[21], although care needs to be taken as the signal will be dominated by those nanotubes which are in resonance with the incident laser light[21]. As mentioned above, the G-band is split into two distinct peaks (G^- and G^+). These separate peaks are associated with atomic displacement in the circumferential direction and along the nanotube axis respectively[21]. The

G^--band is dependent on the nanotube diameter (a down shift in the G^--band frequency from that of 2D graphite (1591 cm^{-1}) corresponds to reduced CNT diameter [21]), but the G^+-band is diameter independent. Shifts in the G^+-band may be induced by charge transfer due to the presence of dopants such as nitrogen, boron or silicon through band softening[23,32,33].

2.5 Optical Microscopy (OM)

2.5.1 Introduction

Light microscopy is a readily accessible and inexpensive tool for the microstructural analysis of a wide range of solid materials. Although the use of light microscopy in materials characterisation is now more than one hundred years old it can, nonetheless, still provide valuable insights into materials as diverse as thin films, metals, ceramics and polymers[34].

2.5.2 Imaging modes

When light is reflected from the surface of an object both the amplitude and the phase of the light may undergo change, leading to the possibility of a number of different modes of imaging. The two imaging modes used in this thesis, *bright-field* and *polarized light* microscopy rely on amplitude and phase variation respectively.

Bright-field imaging is the most common mode used in microscopy. In this approach the sample is uniformly illuminated by a controlled light source. For the opaque solid samples examined in this thesis *epi-illumination* is employed in which the light is incident upon the sample through the objective lens. The differences in the strength of reflection of light from different areas of the sample (which may be dependent on wavelength as, for example, in a heat tinted sample showing interference colours – see below) leads to contrast which provides information on the sample microstructure.

In polarized optical microscopy (POM) the optical anisotropy of materials is investigated. Optical anisotropy originates from light travelling with different velocities in different crystallographic directions within a sample and usually associated with materials with a non-cubic crystal structure. The technique involves the illumination of a sample with polarized light, generated by passing the light through a polarizing filter, which transmits only light waves in which the electric field oscillates in a given plane parallel to the direction

of propagation. The polarized light passes through the objective whereupon it is analysed by a second polarizer (analyser). If the filter and analyser are oriented such that their axes are at 90° to one another, known as *crossed polars*, then reflection from (or transmission through) an isotropic sample would lead to extinction and no image can be observed. However, when polarized light impinges upon an optically anisotropic medium the light splits into two waves which travel with differing velocities along the optical axes of the sample. This difference in velocity can introduce a phase difference between the two components resulting in light which may be circularly polarized, elliptically polarized or polarized at 90° to the original light, dependent on the exact value of the phase difference. As a result when interrogated by the analyser the resulting light may have finite intensity so producing contrast which may be associated with the physical properties of the sample.

Although isotropic materials do not change the polarization state of the transmitted or reflected light and are thus unable to generate contrast in POM, anisotropy may be introduced through a number of mechanisms such as elastic deformation[15] or coupling of a film with a supporting substrate[17]. It has been postulated that the identification of planar graphene islands grown on copper substrates by POM, despite the two dimensional optical isotropy of the pristine material is the result of one or other of these phenomena. Fig. 2.7 shows the interference colour contrast of a graphene film produced on a copper substrate.

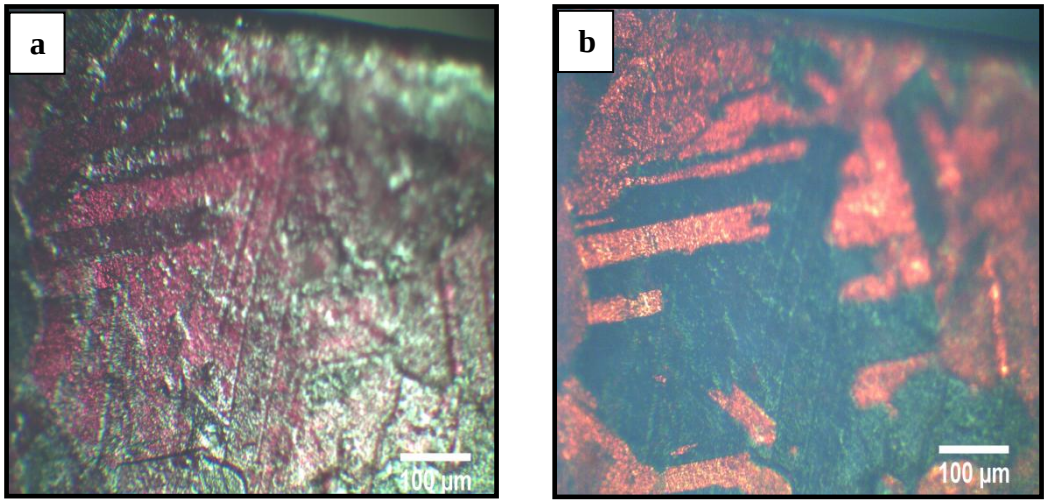

Fig. 2.7: POM image of graphene grown on Cu substrate. Optical Images (a) and (b) have been taken without and with the use of polarised light respectively. The birefringence property of graphene can be used to distinguish graphene areas grown on copper substrate.

2.5.3 Resolution, Brightness and Contrast

It is important to note that magnification simply relates the size of the image to that of the original object. The observation of detail depends upon the resolution – the minimum distance between two points at which they still can be distinguished. The resolution in an optical microscope is limited by the phenomenon of diffraction and can be understood by considering the behavior of light passing through a narrow circular aperture. When light from a point source passes through such an aperture the resulting diffraction pattern has the form of a central spot surrounded by a series of concentric diffraction rings of decreasing intensity. The central region is known as the *Airy disk*[35] and two identical luminous point objects may be distinguished from one another when the centres of their Airy disks are separated by a distance, *d*, such that the centre of one disk falls in the first minimum of the second (the *Rayleigh criterion*). Using this model, it can be shown[36] that the resolution, *R*, of a microscope is given by:

$$R = \frac{0.61\lambda}{n \sin \theta} \qquad (2.7)$$

where θ is the half angle of the cone of light captured by the objective and n is the refractive index of the medium in which the sample and objective are embedded. The quantity $n \sin \theta$ is often known as the numerical aperture (*NA*) of the objective lens. It is therefore clear that resolution is improved either when using light of a shorter wavelength of when the refractive index of the medium between sample and lens is increased (e.g., by using oil rather than air). Using realistic values for wavelength and *NA* it is estimated that the best resolution of an optical microscope is approximately 200 nm. The resolution of the unaided eye is approximately 75 μm. Therefore, given a microscope resolution of 0.2 μm microscope magnifications significantly above 75/0.2 = 375 will not improve the sharpness of the magnified image and will also reduce the field of view. Hence, such high magnifications are often termed 'empty magnification'[37].

In order for the microstructure of an object to become apparent it is necessary not just to have sufficient resolution and magnification, it is also a requirement that the object have sufficient brightness and contrast. The variation of brightness in a microscope in reflected light can be related to *NA* and *M* by:

$$Brightness \propto \frac{(NA)^4}{M^2} \qquad (2.8)$$

It is clear from this equation that the brightness of an image decreases rapidly for increasing magnification, imposing the requirement of a bright light source for sample illumination. However, a uniformly bright object provides no information on microstructure and sufficient variation in light intensity – contrast – between different regions is required. Contrast in an optical microscope can be defined as:

$$Contrast = \frac{I_1 - I_2}{I_2} \qquad (2.9)$$

where I_1 is the intensity originating from the brighter region and I_2 from the darker. For differences in light intensity to be visible the contrast has to be larger than a critical value known as the *contrast threshold*. This quantity varies with the brightness of the image. In a bright image the threshold may be only ~0.03 whilst for a dim image it may exceed 2.

There are a number of methods which can be used to generate colour contrast in the bright field imaging of microstructures, amongst which is the process known as 'heat tinting'[34]. In this method the sample is gently annealed in ambient atmosphere and is thus oxidized. The rate of oxidation is strongly dependent on the phase and composition of the material and as a result different regions show different levels of oxidation. When the oxide layers are sufficiently thick interference colours can be generated which creates desired contrast. In graphene growth on metal surfaces heat tinting has been shown to often be an effective visualization tool[17] due to the protection against oxidation offered by any graphene present. However, care must be taken to ensure that the heating regime chosen is sufficient to create the desired contrast but not severe enough to substantially damage the graphene itself[18].

2.6 Auger Electron Spectroscopy (AES)

2.6.1 Introduction

The development of Auger electron spectroscopy (AES) begun with the discovery of the Auger effect by Pierre Auger in 1932[24] when he observed that several pairs of tracks could be seen in a cloud chamber containing inert gas ionised by x-rays. Later Robison and his colleagues utilised magnetic fields to analyse the energy of electrons in Auger's experiment[38]. It was seen that the energy of some electrons in the chamber were independent of the energy of the incident x-ray photons, unlike photoelectrons. The fixed energy electrons, which are characteristic of the elements from which they are emitted, later became known as *Auger electrons.* The elemental specificity of the electron energies associated with the Auger effect was first employed for the study of the surface composition of a material by Lander in 1953[39]. Since Lander's pioneering work, this technique has become an important analytical tool in surface science research.

2.6.1 The physics of the Auger process

The Auger process occurs when core electrons absorb energy and are released from an atom. The core hole is filled by an electron from a higher lying level which loses energy via a radiationless process to a third electron which is then emitted from the atom, leaving it doubly ionised. This is illustrated in Fig 2.8: an electron on the *K* shell of an atom is ionised by either x-ray photons or electrons (typically in the energy range of 1 keV to 10 keV). As a result of this process, the ionised electron is removed and a second electron in a higher shell of the atom (in this case L_1) relaxes and occupies the core hole. The energy loss associated with this process is transferred to the third electron, which is usually located in the shell higher than the shell of the second electron ($L_{2,3}$. in Fig. 2.8), resulting in emission with a characteristic energy. These are the Auger electrons.

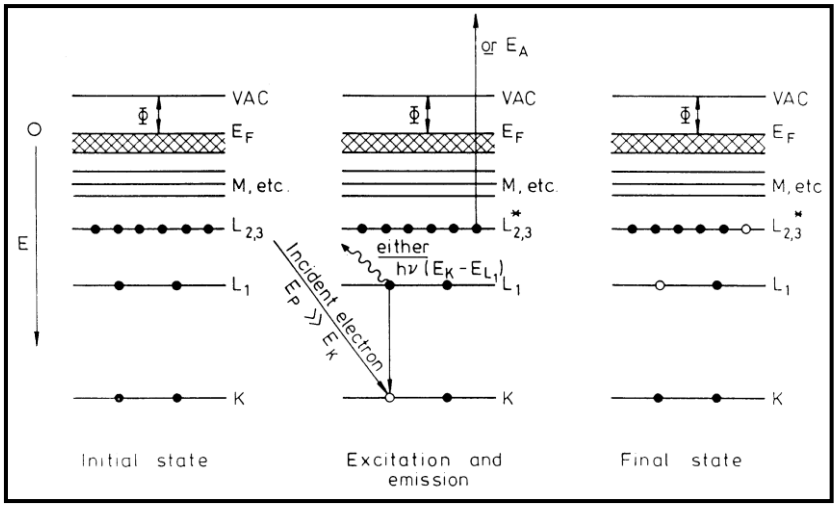

Fig. 2.8: Schematic diagram showing the a $KL_1L_{2,3}$ Auger transition[40].

Auger electron emission can be detected from free atoms, molecules or solid materials. The emitted electrons are labelled by the levels involved in the Auger process: for example an Auger electron emitted due to a transition involving the ionisation of a core hole in the *K* (n = 1) shell, followed by relaxation from the L_1 (n = 2, l = 0) shell and emission from the $L_{2,3}$ shell (n = 2, l = 1) is known as a $KL_1L_{2,3}$ or simply a *KLL* Auger electron. If the Auger process involves the valence band of a solid material, the valence shell is often given the label *V* and the Auger transition is then referred to as *KVV*, *LVV* or *MVV*. For lights elements, Auger peaks are easily identifiable, where as with heavier elements interference of multiple peaks is common due to their large number of transitions.

The kinetic energy of an Auger electron is given by:

$$E_{ABC}(Z) = E_A(Z) - E_B(Z) - E_C(Z) - \varphi_s \qquad (2.10)$$

where, *ABC* is the label of the Auger transition, *Z* is the atomic number of the atom involved and φ_s is the work function of the solid material. According to Eq. 2.10, it is therefore possible to calculate and identify the Auger electron energies from experiment.

2.6.2 Auger Electron Emission Spectra

In order to record the Auger electron spectra presented in this thesis, an electron beam was used to ionise the core levels of surface atoms in the samples under study. Fig. 2.9 and Fig 2.10 illustrate the energy distributions of Auger electrons, obtained using an incident electron beam energy of 1.5 keV from a sample of graphene grown on copper foil. One may notice that there are many low energy electrons present in the direct spectrum most of which are the result of inelastic scattering or secondary electron emission (the inelastically scattered electrons may originate from the incident beam, core and valence or Auger electrons which have lost energy to the sample). It is clear from Fig. 2.9 that it is difficult to detect the Auger component in the direct spectrum as it is a relatively weak signal on a strong background. As a result, when using electron excitation the differentiated spectrum is usually presented. Differentiation improves the visibility of the weak Auger signal because these signals are relatively rapid variations in intensity with respect to electron energy superimposed on a slowly varying background of inelastic and secondary electrons. Hence, when differentiating the spectrum, regions with a larger intensity versus energy gradient become more apparent. There are two ways used to differentiate an Auger spectrum: numerical differentiation and electronic differentiation. In the case of numerical differentiation, the direct spectrum is first obtained and there converted to differentiated spectrum by a standard numerical process. Electronically differentiated spectra are collected by using lock-in amplifier, as described in Chapter 3.

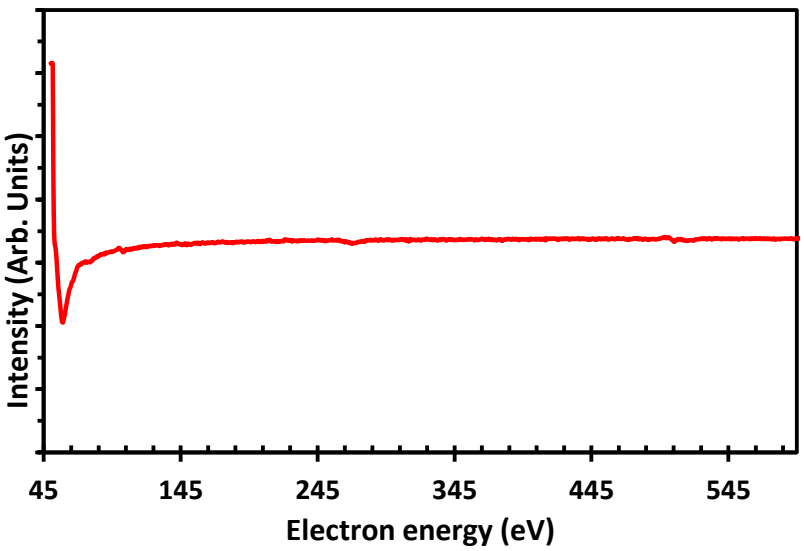

Fig. 2.9: Direct Auger electron spectrum of graphene on a copper substrate.

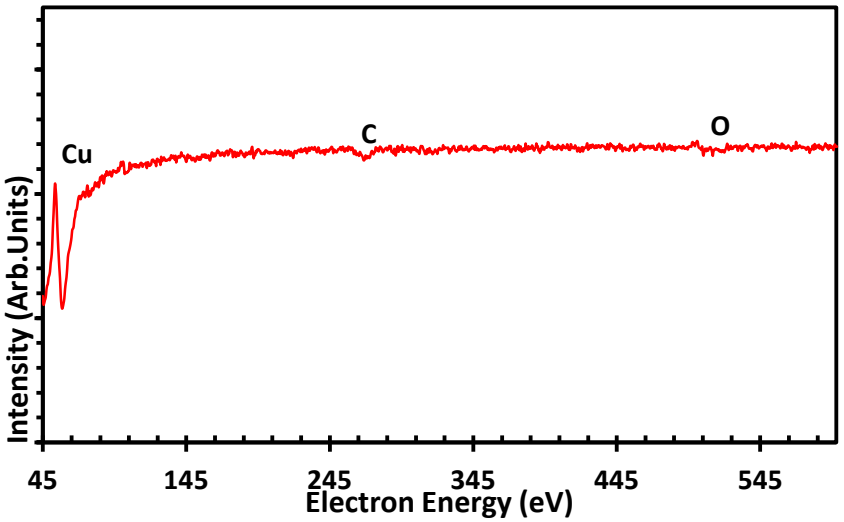

Fig. 2.10: Differentiated version of the Auger spectrum shown in Fig. 2.9.

Auger intensities are usually quantified by the peak-to-peak height in a differentiated spectrum. The magnitude of an Auger signal depends on several factors:

$$I_A = I_0 \, \sigma_A \, \gamma_A \, (1 + r) \, \lambda_A \, (E_A) \cos (\Theta) \, FDR \, \rho_A \qquad (2.11)$$

where, I_A is the density of an Auger transitions of an element, I_0 is the current of primary electron beam, σ_A is the ionisation cross section, γ_A is the Auger transition of probability, $(1+r)$ is the backscattering factor, λ_A is the inelastic mean free path of the Auger electron and Θ is the emission angle of the Auger electron to surface normal. F is the solid angle of acceptance of analyser; D is the intensity response of the detector, R is the surface roughness factor and ρ_A is the density of element.

Auger spectra of graphitic materials only display a *KLL* transition, often termed *KVV*, as explained above. The *KLL* transition of carbon gives rise to an Auger peak located around 270 eV. A typical C *KVV* peak from a graphitic material is presented in Fig. 2.11. AES can be used to investigate the chemical composition of graphitic materials due to its very high sensitivity. The dependence of the C *KVV* lineshape on the valence band structure of solid materials means that additional information can be deduced from a detailed investigation of Auger carbon peak shape. In particular, by comparing measurements of the peak width, *W*, with that of carbon containing reference samples, the nature of the hybridisation state of the

carbon may be understood[41]. Changes in lineshape may be induced by, for example, the presence of chemically bound species such as substitutional N or Si[42,43,44].

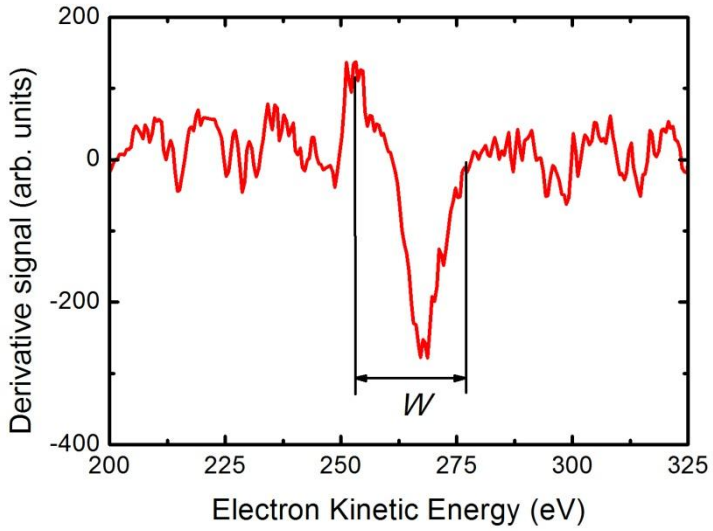

Fig. 2.11: Differential C *KVV* Auger electron spectrum of graphene on copper substrate

2.7 Scanning Electron Microscopy

2.7.1 Introduction

The scanning electron microscope (SEM) is the most commonly used form of electron microscope, being employed in fields as diverse as forensic investigation and semiconductor quality control[37]. Image formation in the SEM is based on the principle of detecting a signal generated by a fine electron beam probe (with energy typically in the range of 2 – 30 keV) which is scanned across the surface of a sample in a digitized raster pattern, building up an image point-by-point. As a result, the diameter of the incident electron beam (and the interaction of that beam with the sample, as discussed below) determines the maximum possible resolution in the SEM. There are a number of signals which arise as the result of the interaction of the electron beam with the solid which can potentially be used to provide spatially-resolved information. Among these are the secondary electrons (SE), backscattered electrons (BSE), specimen current, electron-beam induced conductivity (EBIC), Auger electrons, X-rays and cathodoluminescence (CL) (Fig 2.12)[37]. Only the first two signals are

used to generate the images presented in this thesis, and we will therefore limit our discussion to SE and BSE imaging.

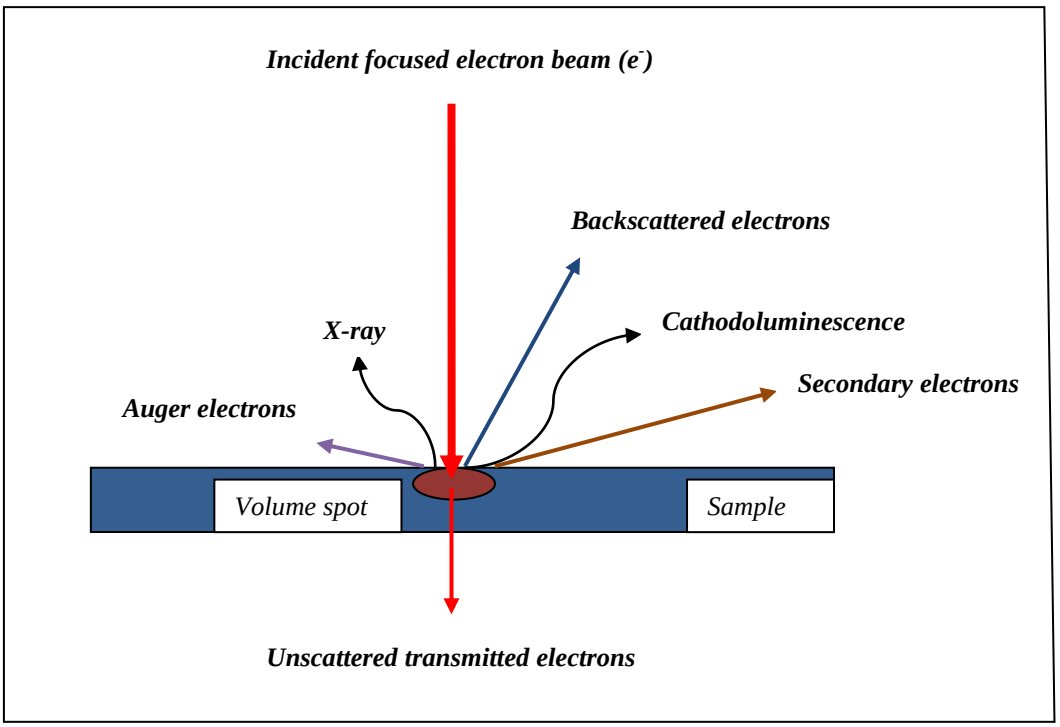

Fig. 2.12: Schematic representation of the interaction of focused electron beam with the surface of a sample. Various signals are generated from this interaction, as shown.

2.7.2 Basic Principles of electron-solid interaction

In order to understand the SE and BSE modes of imaging in the SEM it is necessary to consider the behavior of the electrons in the probe beam as they are incident upon the sample. Electrons interact strongly with matter (leading to the surface sensitivity discussed in XPS in section 2.2.1 of this chapter), and we expect the incident electrons to be strongly scattered by the sample. Most scattering events are small angle, but it is possible for incident electrons to be quasi-elastically backscattered (scattered through an angle greater than 90°) through single or multiple collisions and re-emerge from the surface of the sample, creating the BSE signal.

Inelastic scattering causes the incident electrons to lose energy as they travel into the sample and the volume of the sample which contains most of the scattered electrons is known as the *interaction volume* (Fig. 2.13). As shown in Fig. 2.13, this volume is pear-shaped as scattering causes the beam to spread laterally with depth. The extent of this region below the surface – the *penetration depth* – is a function of both the material (it is smaller with higher average atomic number, *Z*) and the energy of the incident beam (increasing as a power of the beam energy). The inelastic scattering processes which occur within this volume include those which lead to the emission of secondary electrons.

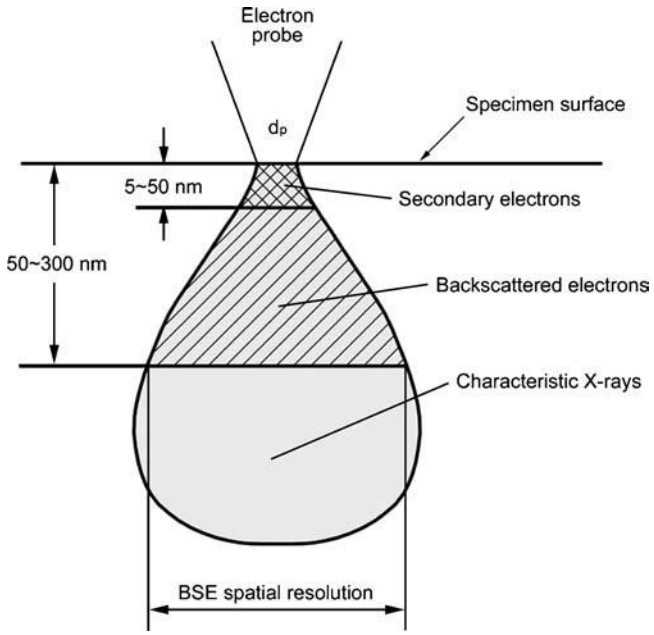

Fig. 2.13: Schematic diagram of electrons and sample surface interaction[34].

SEs have typical energies which are <100 eV and, as a result, they scatter strongly and the distance they travel within the sample is small (of the order of 1-2 nm). Only those created close to the surface (within the *escape depth*) may escape. The number of SEs which escape from the sample surface ranges typically from 0.1 to 10 per incident electron and is a strong function of the incident probe angle with angles furthest from the normal producing the greatest SE yield. The variation of electron yield, δ, with the angle of the beam to the normal, θ varies as:

$$\delta(\theta) = \delta(0)/\cos\theta \qquad (2.12)$$

As a result the SE yield (as detected by an Everhart-Thornley detector[34,37]) provides topographic information on the sample with raised or recessed features appearing to have a bright outline.

As stated above, the BSE signal arises from the quasi-elastic scattering of incident electrons such that they can re-emerge from the sample. The cross-section for such large angle scattering varies as Z^2, and is therefore more pronounced for heavier elements. The *backscatter coefficient*, η, measures the ratio of backscattered electrons escaping from the sample to the number of incident electrons. As can be seen in Fig. 2.14, this quantity increases monotonically with Z although sub-linearly. In consequence, contrast in BSE images can arise from variations in chemical composition. As a result of the higher energies of the BSEs in comparison with the SEs, the former originate from deeper within the solid and sample a larger portion of the interaction volume, leading to a lower resolution[37].

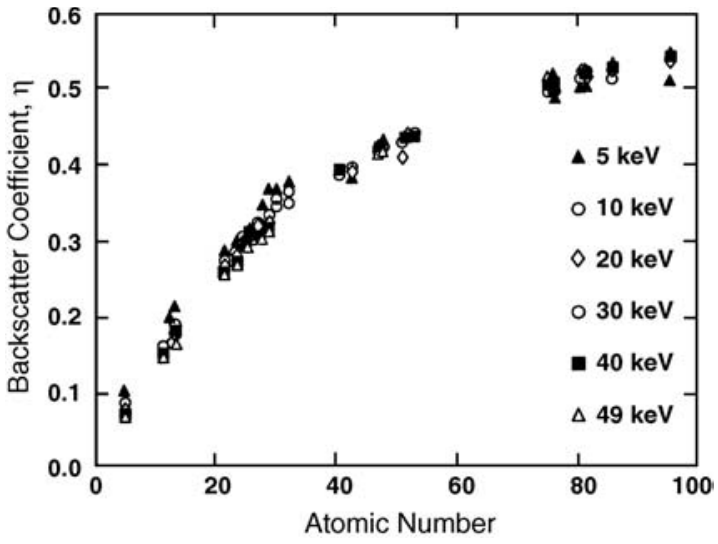

Fig. 2.14: Backscatter coefficient as a function of atomic number of specimen atoms[34].

It is possible to mix both SE and BSE signals to create a total 'mixed' signal providing elements of topographic and elemental contrast. This approach has been successfully applied by Yang *et al.*[12] in order to investigate the growth of single and few-layer graphene on copper foils: it was found that a mixture of 15% BSE signal to 85% SE signal enabled the resolution of multiple graphene layers, so providing insight into the growth process.

Fig 2.15 provides an example of SEM imaging of graphene synthesised on a copper substrate (as detailed in chapter 5), the contrast in the images is provided by SE.

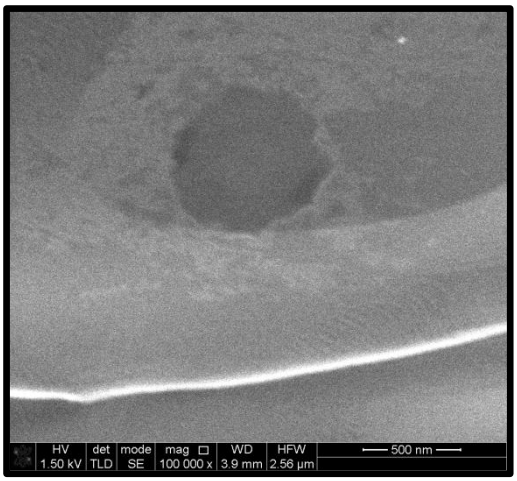

Fig. 2.15: SEM image of a graphene domain.

2.8 Summary

The basic theory underpinning the operation of the major experimental tools applied in this thesis (XPS, OM, RS, AES and SEM) have been described in detail. Particular emphasis has been placed on those aspects of the techniques which have yielded the data presented in the later chapters of this work.

2.9 References

[1.] K.H. An, J.G. Heo, K.G. Jeon, D.J. Bae, C.Jo, C.W. Yang, C.-Y. Park, and Y.H. Lee, Appl. Phys. Lett. **80**, 4235 (2002).
[2.] W. Zhao, C. Song, B. Zheng, J. Liu, and T. Viswanathan, J. Phys. Chem. B **106**, 293 (2002).
[3.] C. Morant, J. Andrey, P. Prieto, D. Mendiola, J.M. Sanz and E. Elizalde, Phys. Stat. Sol. **203**, 1069 (2005).
[4.] A.K. Chakraborty, J. Jacobs, C. Anderson, C.J. Roberts and M.R.C. Hunt, J. Appl, Phys. **100**, 084321 (2006).
[5.] F. Xu, M. Minniti, C. Giallombardo, A. Cupolillo, P. Barone, A. Oliva, et al. Surf. Sci. **601**, 2819 (2007).
[6.] A.K. Chakraborty, R.A.J. Woolley, Y.V. Butenko, V.R. Dhanak, L. Siller and M.R.C. Hunt, Carbon **45**, 2744 (2007).

[7.] F.**X**u, M. Minniti, P. Barone, A. Sindona, A. Bonanno and A. Oliva. Carbon **46**, 1489 (2008).
[8.] H. Liu, Y. Zhang, R. Li, X. Sun, S. Desilets, H. Abou-Rachid, M. Jaidann and L.-S. Lussier, Carbon **48**, 1498 (2010).
[9.] X. Li, W. Cai**,** J. An**,** S. Kim, J. Nah, D. Yang, R. Piner. A. Velamakanni, I. Jung, E. Tutuc, S. K. Banerjee, L. Colombo and R. S. Ruoff, Science **324**, 1312 (2009).
[10.] J. Kim, F. Kim and J. X. Huang, Matter. Today **13**, 28 (2010).
[11.] A.W. Robertson and J.H. Warner, Nano Lett. **11**, 1182 (2011).
[12.] F. Yang, Y Liu, W. Wu, W. Chen, L. Gao and J. Sun, Nanotechnology **23**, 475705 (2012).
[13.] M. Xu, D. Fujita, J. Gao and N. Hanagata, ACS Nano **4**, 2937 (2010).
[14.] R.M. Houchin,Ph. D. Thesis, University of Durham, UK (2011).
[15.] T. Jiang D. Emerson, T. Twarowski, D. Finkenstadt and J. Therrien, Phys. Rev. B **82**, 235430 (2010).
[16.] D.W. Kim, Y.H. Kim, H.S. Jeong and Hee-Tae Jung, Nuture Nanotech **7**, 29 (2012).
[17.] K. Kertesz, A.A. Koos, A.T. Murdock, Z. Vertesy, P. Nemes-Incze *et al*., Appl. Phys. Lett. **100**, 213103 (2012).
[18.] C. Jia, J. Jiang, L. Gan and X. Guo, Sci. Rep. **2:707**, 1 (2012).
[19.] S. Chen, L. Brown, M. Levendorf, W. Cai, S. Ju, J. Edgeworth, et al., ACS Nano **5**, 1321 (2011).
[20.] A.C. Ferrari and J. Robertson, Phys. Rev. B **61**, 14095 (2000).
[21.] M.S. Dresselhaus, G. Dresselhaus, R. Saito, and A. Jorio, Phys. Rep. Sec. Phys. Lett. **409**, 47 (2005).
[22.] L.M. Malard, M.A. Pimenta, G. Dresselhaus, and M. S. Dresselhaus, Phys. Rep. **473**, 51 (2009).
[23.] R. Saito, M. Hofmann, G. Dresselhaus, A. Jorio and M.S. Dresselhaus, Ad.v Phys. **60**, 413 (2011).
[24.] J.C. Vickerman and I.S. Gilmore, 'Surface Analysis- The Principal Techniques', (John Wiley and Sons, Singapore 2008).
[25.] G. Friedbacher and H. Bubert, 'Surface and Thin Film Analysis: A Compendium of Principles, Instrumentation, and Applications', (Wiley-VCH, Weinheim 2011).
[26.] J.F. Watts and J. Wolstenholme, 'An Introduction to Surface Analysis by XPS and AES', (John Wiley and Sons, Chichester 2003).
[27.] C.V. Raman and K.S. Krishnan, Nature **121**, 501 (1928).
[28.] G. Landsberg and L.A. Mandelstam, Naturewissenschaften **16**, 557 (1928).
[29.] J.R. Ferraro, K. Nakamoto and C.W. Brown, 'Introductory Raman Spectroscopy', (Academic Press, USA 2003).
[30.] S.E. Smith and G. Dent, 'Modern Raman Spectroscopy- A Practical Approach', (John Wiley and Sons, Chichester 2005).
[31.] J.M. Hollas, 'Modern Spectroscopy', (John Wiley and Sons, Chichester 2004).
[32.] S. Suzuki and H. Hibino, Carbon **49**, 2264 (2011).
[33.] J. Campos-Delgado, I.O. Maciel, D. A. Cullen, D.J. Smith, A. Jorio, M.A. Pimenta, H. Terrones and M. Terrones, ACS Nano **4**, 1696 (2010).
[34.] Y. Leng, 'Materials Characterization: Introduction to Microscopic and Spectroscopic Methods', John Wiley and Sons, Singapore (2008).
[35.] E. Hecht, 'Optics', Addison-Wesley, Reading (1989).
[36.] G.F. Lothian, 'Optics and its uses', (van Nostrand Reinhold, New York 1975).
[37.] R.F. Egerton, 'Physical Principals of Electron Microscopy: An Introduction to TEM, SEM and AEM', (Springer, New York 2005).
[38.] C.L. Briant, R.P. Messmer, 'Auger Electron Spectroscopy', (Academic Press, Boston 1988).

[39] H. Robinson, Proc. Roy. Soc. A **104**, 455 (1923).
[40] D. Briggs, M. P. Seah, 'Practical Surface Analysis'. (John Wiley and Sons, Chichester 1994).
[41] J.C. Lascovich, R. Giorgi, and S. Scaglione, Appl. Surf. Sci.**47**, 17 (1991).
[42] B. Cuo, Q. Liu, E Chen, H. Zhu, L. Fang. and J. R. Gong, Nano Lett. **10**, 4975 (2010).
[43] M.C.S. Escano, T. Q. Nguyen and H. Kasai, Chem. Phys. Lett. **515**, 85 (2011).
[44] M.S.S. Azadeh, A. Kokabi, M. Hosseini and M. Fardmanesh, Micro and Nano Lett. **6**, 582 (2011).

Chapter 3

Experimental Instrumentation

In this chapter, equipment and methods employed to acquire data in this thesis are briefly described. The experimental procedures associated with the various measurements undertaken are also outlined.

3.1 Ultra High Vacuum (UHV) ion gun system

The ion bombardment modification of single-wall carbon nanotubes (SWNTs) presented in Chapter 4 of this thesis was carried out in a home-built ultra-high vacuum (UHV) system housed in the Department of Physics, Durham University, UK. The UHV system (Fig. 3.1) consisted of a main chamber, with a base pressure of ~1 x 10^{-8} mbar (without baking) and a fast-entry lock (FEL) system (base pressure ~1 x 10^{-7} mbar) which enables rapid sample introduction without breaking vacuum. A cold-cathode ion gun (VG AGS2), a quadrupole mass spectrometer (Leybold Inficon) and sample manipulator were mounted on the main chamber (Fig. 3.2). The main chamber was pumped by a 150 l s^{-1} turbomolecular pump (Leybold) backed by an Edwards two-stage rotary pump (E2M8), whilst the FEL was pumped with a 70 l s^{-1} Varian turbomolecular pumped backed by an Edwards E2M5 rotary pump. The main chamber pressure was measured with an ion gauge (VG VIG17) and that in the FEL by a Penning gauge, with backing pressures measured with Pirani gauges.

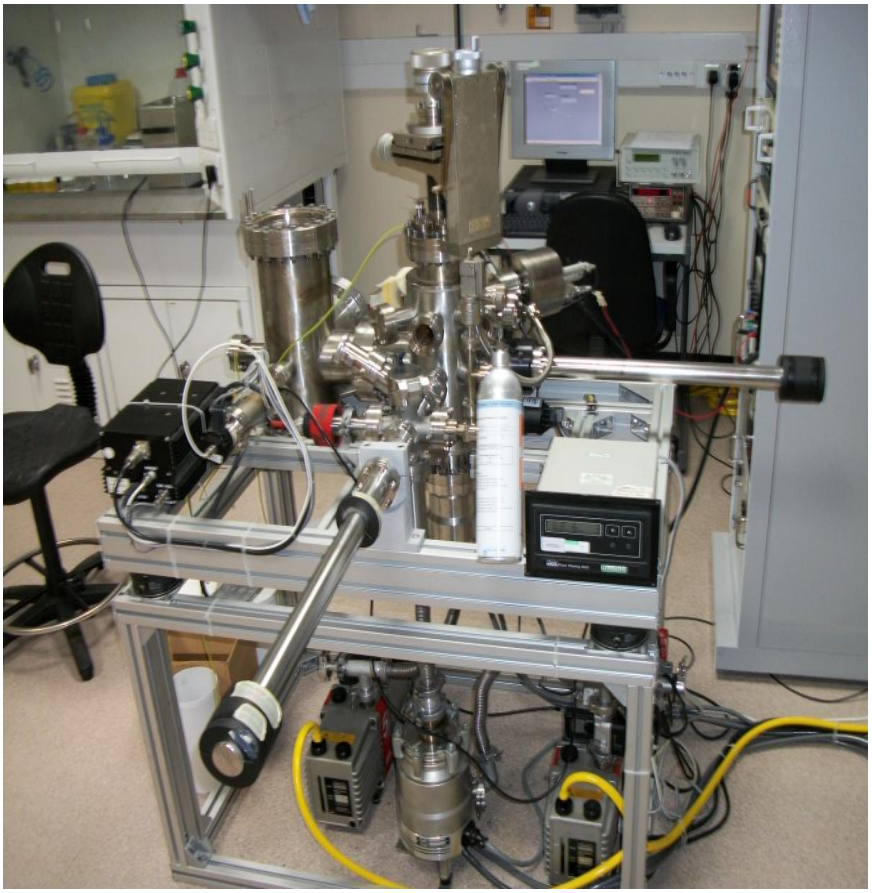

Fig. 3.1: Ultra High Vacuum (UHV) ion gun system at Durham.

The SWNTs used in Chapter 4, produced by the HiPCO method, were sourced from Carbon Nanotechnologies Incorporated, U.S.A. Gross contamination was removed from the carbon nanotubes by stirring in concentrated hydrochloric acid for 8 hours at room temperature, filtered and washed with deionized water. A suspension of the resultant material was then produced by placing a small quantity in semiconductor grade residue-free isopropyl alcohol. A film of carbon nanotubes was then produced by drop-wise deposition of the suspension onto a tantalum foil support. The nanotube film was allowed to dry after each drop of suspension was added and the process continued until an optically thick film, free from any pinholes, had been produced. The key advantage of this approach to film deposition is that it is gentle in comparison with many other purification and dispersion approaches used in the literature[1,2,3,4] and does not introduce any unwanted contamination – for example, it is almost impossible to remove sodium contamination from SWNTs suspended in sodium dodecyl sulphate, a common surfactant employed for this task. SWNT films produced by our approach have been thoroughly characterised by Houchin[5] and found to be highly pure.

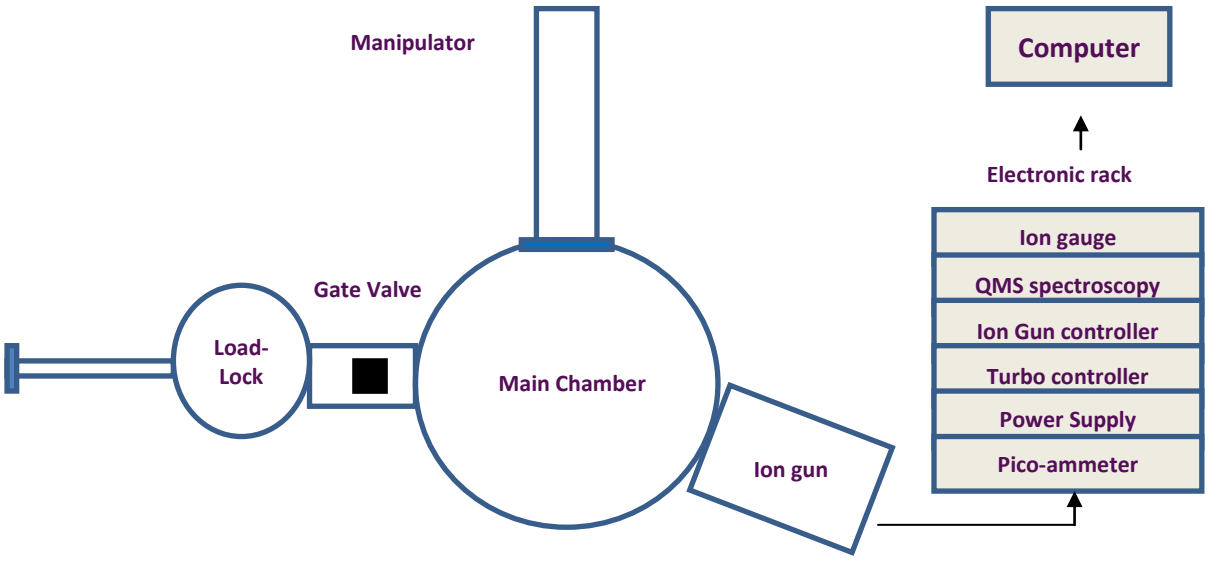

Fig. 3.2: Outline of Ultra High Vacuum (UHV) ion gun system

Once prepared, SWNT films were introduced into the ion gun UHV system through the fast entry lock and irradiated with Ar^+ or N^+ ions with an energy of 2.5 keV. A gas handling line (GHL) was used to bleed 99.995% purity gas into the ion gun through a precision leak valve. The GHL was evacuated with a turbomolcular pump to a pressure of ~5 x 10^{-5} mbar then back-filled to between ~1 and 12 bar and the process repeated three times to purge impurities and ensure an overpressure of the gas. Once the gas had been admitted into the ion gun the pressure in the main chamber rose to ~1 x 10^{-5} mbar during ion gun operation (such high operating pressures meant that baking the chamber was unnecessary). The quadrupole mass spectrometer was used to monitor gas quality and ensure that the Ar/N gas dominated any residual species (such as organic solvents, water, oxygen etc.) which might otherwise be present in the chamber.

Ion irradiation was typically undertaken with an ion energy of 2.5 keV (selected to ensure stable ion gun operation over the beam current ranges of interest). A focus voltage of 2.0 keV was applied to the ion gun lens to ensure that the beam was spread evenly over the sample surface. The optimum focus voltage to appropriately de-focus the beam had been determined in a series of experiments in which beam current was monitored as the sample was moved in the plane perpendicular to the axis of the ion gun with the manipulator. By considering the variation of sample current with position and the size of the sample it was possible to estimate the beam footprint and uniformity. The sample current measurements suggested the beam profile was flat, except at the very edges, resembling a smoothed 'top-hat' function. The sample current was measured by a picoammeter (Keithley 485) and was a complicated function of beam energy, ion type and gas pressure. No bias correction was usually applied to the sample to correct for secondary electron emission, but previous work[5] had suggested that there was a minimal contribution to the sample current form these sources under the conditions used in this work. The picoammter was connected to a computer via a GPIB interface and LabVIEW software was used to accurately determine the bombardment time and ion dose. In a typical experiment the sample was held facing way from the ion gun and the gun switched on and allowed to stablise (a process which took between 10 minutes and half an hour, depending on conditions). Once the beam current was deemed to be sufficiently stable, the sample was rotated to face the ion gun and the sample current and exposure time recorded at 1 second intervals by the LabVIEW code.

The cold cathode ion gun utilised in this thesis is a standard tool most usually employed in cleaning and smoothing sample surfaces in UHV. Fig. 3.3 shows the structure of the ion gun. The cold cathode gun relies on ionization of the gas used for bombardment in a discharge, which occurs within a relatively high pressure (typically a few mbar) cell, known as the *ionisation cell*, within the gun[6]. Gas is admitted to the ionisation cell, which consists of an outer wall which acts as the cathode and an toroidal inner electrode which acts as the anode. A bias is applied between the cathode and anode which ignites a discharge in the chamber. The discharge is formed when atoms are ionised by collision with electrons which are accelerated by the potential between the electrodes. These electrons can originate from a variety of 'adventitious' sources such as cosmic rays, thermal excitation at the extreme tail of the temperature distribution etc. Once a collision occurs further electrons are liberated leading to a cascade. As a result of this process, a plasma can be produced. An external electromagnet is used to extend the electron's path length (by causing the electrons to describe helical orbits) so increasing the number of collisions. The magnetic field also assists in constraining the produced plasma inside the ionisation chamber. Ions are extracted from the plasma, and are focussed before being accelerated towards the sample which is kept at ground potential to prevent charge build up. The beam energy is given by the acceleration voltage applied to the cathode.

The key advantage of a cold cathode ion gun as opposed to those employing a filament for ionisation is that it can be used with a variety of both inert and active gases including N_2, O_2, and H_2. Moreover, this particular model of ion gun is designed specification for large area sample irradiation and even when focussed the beam diameter is typically 5 mm (Ref. [6]). Hence, the gun is ideal for the thin film irradiation experiments reported in Chapter 4 of this thesis.

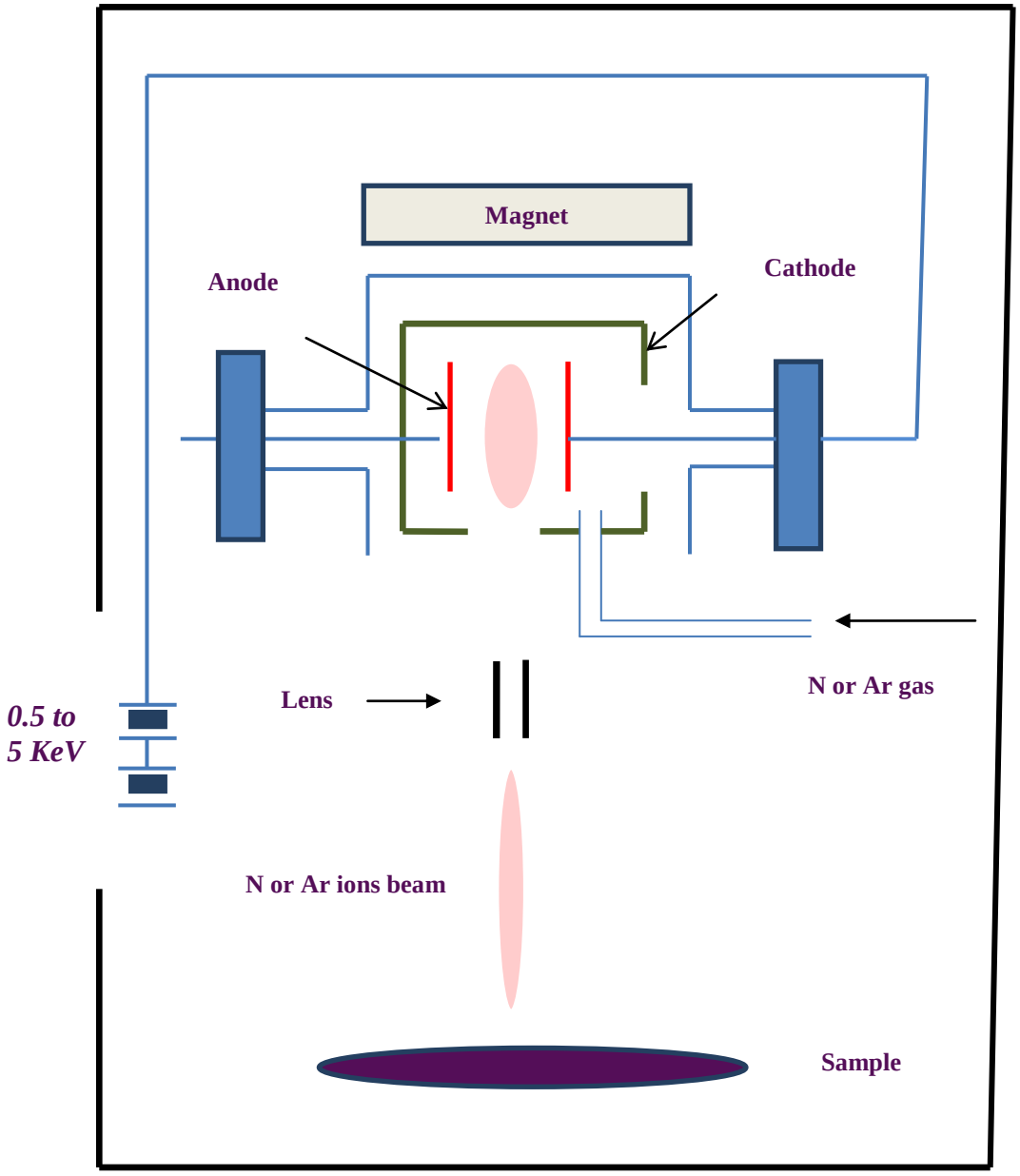

Fig. 3.3: Schematic of cold cathode ion gun.

3.2 X-ray photoelectron spectrometer

The x-ray photoemission spectroscopy (XPS) measurements reported in this thesis were performed off-site using a Kratos Axis Ultra instrument based in the school of Chemical Engineering and Advanced Materials, Newcastle University with data analysis performed in Durham. A schematic of a typical XPS system is presented in Fig. 3.4. The Kratos Axis Ultra

is equipped with a dual anode Al/Mg x-ray source with a 500 mm Rowland circle monochromator with quartz crystals for Al Kα radiation (1486.6 eV photon energy), a 165 mm mean diameter hemispherical electron analyser with multichannel detection and a four-axis computer-controlled manipulator. The UHV system housing the instrument consists of a FEL, preparation chamber, and measurement chamber with a typical system pressures in the low 10^{-9} mbar range[7].

The monochromator in the Axis Ultra spectrometer contains quartz crystals mounted on the circumference of a 500 mm circle and is configured to diffract x-rays of a chosen wavelength (Al $K\alpha_1$, $h\nu$ = 1486.6 eV) onto the sample. This process reduces the natural width of the Al $K\alpha_1$ line (about 0.9 eV) to <0.26 eV in the monochromated beam and removes both satellite radiation and the background due to Bremmstrahlung, improving signal to noise and resolution, and enabling a higher precision interpretation of the spectra. The resulting x-ray beam has a footprint of about 1 mm diameter upon the sample surface and the region analysed can be further narrowed, if required, by appropriate choice of conditions for the 'spot size aperture' of the electron analyser[7].

The Axis Ultra spectrometer may be used for either imaging or spectroscopy and is operated exclusively in the latter mode for the work presented in this thesis. For spectroscopy the analyser behaves as a conventional hemispherical analyser, and we shall briefly discuss this mode of operation alone. Electrons emitted from the sample are focussed by the objective lens system onto the spot size aperture, which selects the sample analysis region and size. The 'slot aperture' with 'hybrid magnification' settings (see below) was used to obtain the spectra presented here. This combination of aperture and lens settings is appropriate for high sensitivity spectroscopy and samples a surface area of 700 x 300 μm^2. An electrostatic lens is then used to retard (or accelerate) the photoelectrons to the pass energy of the analyser (between 5 eV and 160 eV in the Axis Ultra). The pass energy is the kinetic energy at which electrons can pass from the centre of the entrance slit, through the 165 mm mean radius hemispherical analyser to the central exit slit. Electrons with higher or lower kinetic energy cannot pass through the analyser and are not detected. The Axis Ultra is equipped with an exit plate which has eight exit slots enabling parallel collection of electrons at well defined energies on the eight channel electron multipliers (one per slit) in the detection system.

In practice the finite size of the entrance and exit slits results in a finite spectrometer resolution, which degrades with increasing pass energy (although this is offset by increased collection efficiency). The resolution of a typical hemispherical electron analyser is given by:

$$\frac{\Delta E}{E_p} = \frac{s_1+s_2}{2r} + \alpha \qquad (3.1)$$

where E_p is the analyser pass energy, ΔE is the energy resolution, s_1 and s_2 are the entrance and exit slit diameters (typically the entrance/exit slits are circular in a hemispherical analyser), r the mean analyser diameter and α is the angular divergence of the electrons with respect to the normal of the entrance slit[8]. Clearly, the two main routes by which one can improve analyser resolution is by either increasing the mean radius of the analyser (which is why the Axis Ultra spectrometer uses a rather large 165 mm mean radius analyser) and by decreasing the pass energy. The latter comes at the cost of reduced signal and is typically used when looking at narrow spectral regions, such as individual lines where the loss of signal can be offset by increased acquisition time.

The analyser in the Axis Ultra instrument differs from a conventional hemispherical analyser in that the lens system incorporates a magnetic immersion lens. The lens piece sits below the sample and produces a magnetic field which extends above the sample and so focuses the photoelectrons onto the spot size aperture. In 'hybrid magnification' mode the magnetic immersion lens is used in conjunction with a conventional electrostatic lens to provide maximum signal. Once the electrons pass through the spot size aperture an electrostatic lens changes the electron kinetic energy to the pass energy of the analyser and focuses the image of the spot size aperture onto the entrance slit. By sweeping the acceleration/retardation voltage a photoelectron spectrum can be generated. A typical survey spectrum from a single-walled carbon nanotube sample, of the type discussed in chapter 4, is shown in Fig. 3.5.

The spectra presented in this thesis were obtained with Al Kα radiation in normal emission geometry (0° take-off angle) with a total instrumental resolution of ~0.48 eV, calibrated by an Ag test sample. All spectra were analysed and fitted using a χ^2 analysis approach (non-linear least squares with points weighted by errors derived from the Poisson distribution) with the Unifit 2007 software package produced by Leipzig University,

Germany[9,10,11]. Relative sensitivity factors for each element were derived from the CasaXPS library specific to the Kratos Axis Ultra spectrometer.

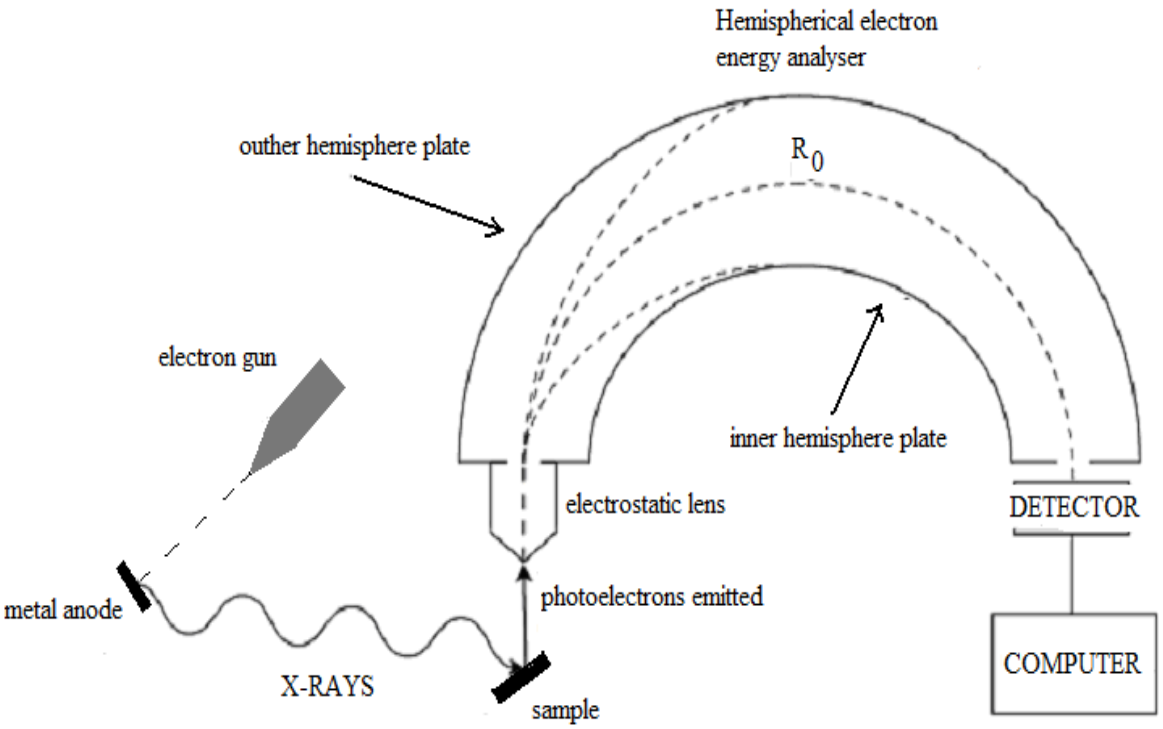

Fig. 3.5: Schematic view of a typical XPS system with hemispherical analyser[12].

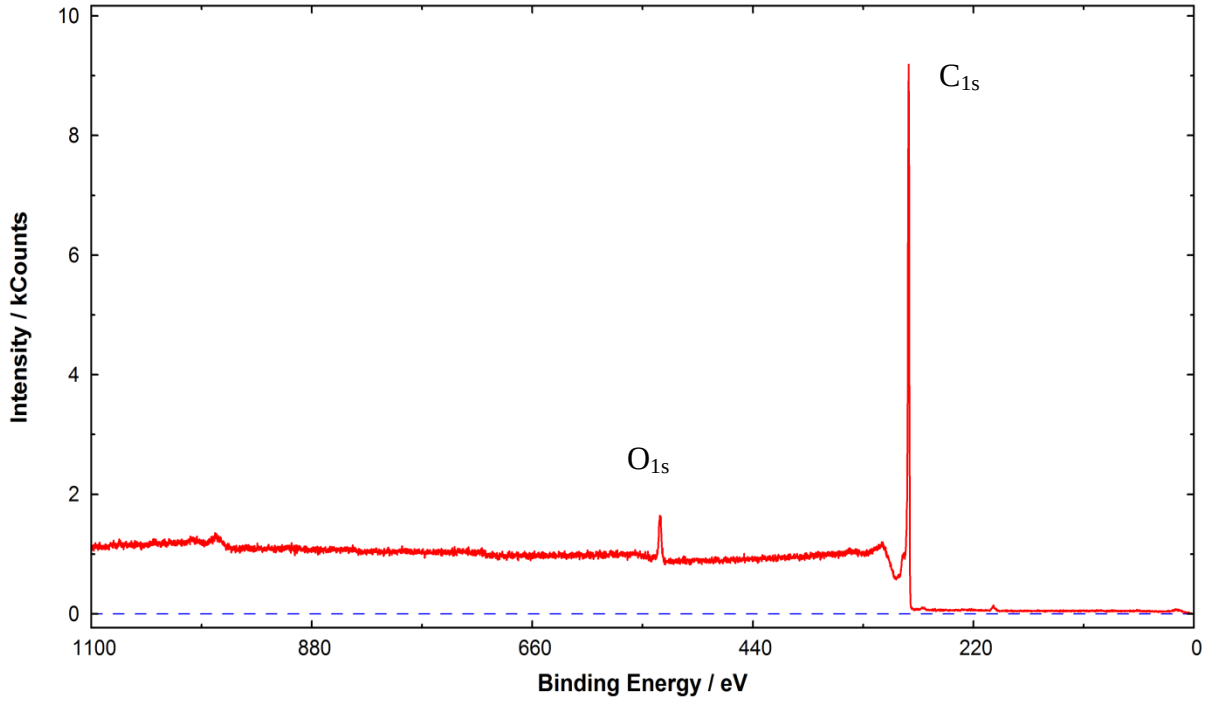

Fig. 3.5: XPS Survey of a SWCNT.

3.3 Raman Spectroscopy (RS)

3.3.1 Horiba Jobin-Yvon LabRAM spectrometer at Durham

The Raman spectroscopy experiments presented in this thesis were performed in the Department of Chemistry, Durham University using a *Horiba Jobin Yvon Ltd*. LabRAM HR Raman system, Fig. 3.6. The spectrometer is equipped with three excitation lasers: an air cooled Nd:YAG laser (532 nm), an air-cooled HeNe laser (633 nm) and a diode laser (785 nm). Lasers used in Raman experiments must also give good wavelength stability and low background emission. The selected beam is focussed on the sample with a confocal microscope (Olympus BX41) enabling the selection of a small (representative) field of view from the sample. The scattered light is then analysed by an 800 mm spectrograph with an ultimate resolution of 1-2 cm^{-1}, with a notch filter assembly removing the Rayleigh scattered light.

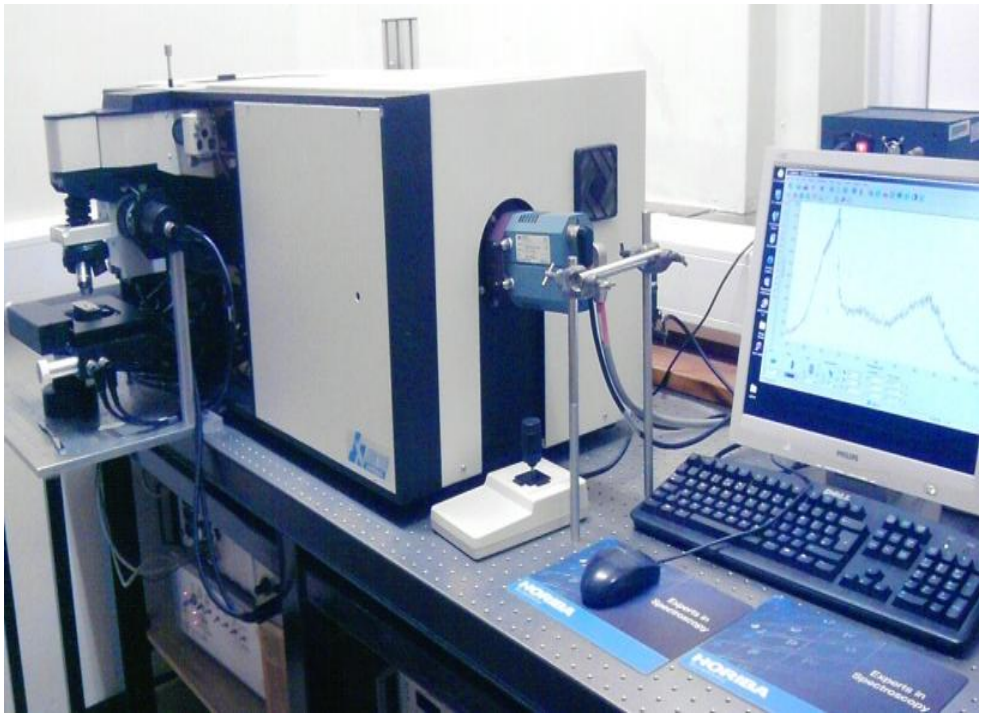

Fig. 3.6: *Horiba Jobin Yvon LabRAM* Raman spectrometer located in Durham.

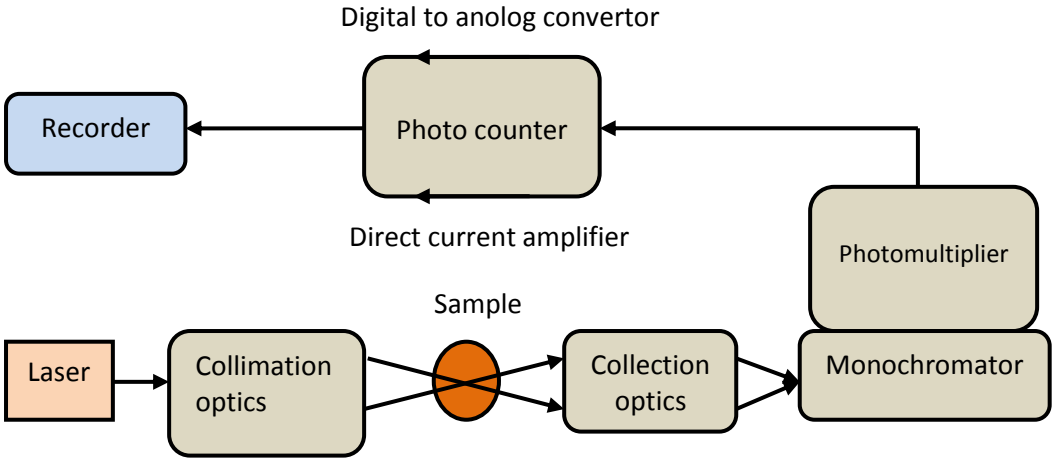

Fig. 3.7: Layout of Raman Spectrometer used for the Raman measurements adapted from[13].

The layout of a typical Raman spectrometer is shown schematically in Fig. 3.7. The laser excitation source is used to provide a coherent and monochromatic beam of high intensity which then excites the targeted surface area. To further enhance the Raman signals, the laser should be concentrated on the sample surface by focussing optics, because a clean Raman spectrum is proportionally related to the intensity of exiting incident beam. The need for

intense laser light is due to the low cross-section for Raman scattering: typically only one photon in 10^7 is inelastically scattered (unless the light is resonant with electronic transitions in the sample or a surface enhanced Raman scattering substrate is employed). As a result the signal is quite weak. The scattered photons are then collected by collection optics and focussed on the notch filter, filtering out the Rayleigh scattered signals. The Raman scattered photons are passed to a 1024 pixel charge coupled device (CCD) detector which records the intensity of Raman signal as a function of wavenumber (cm^{-1}) which is then plotted as the Raman spectrum. Noise in the CCD detector is reduced through Peltier cooling.

The LabRAM spectrometer was used to measure the Raman spectra of pristine and irradiated SWCNTs presented in Chapter 4 and the doped graphene films in Chapter 6. SWNT films were prepared as outlined in Section 3.1 and either measured as-is or subjected to ion irradiation before measurements. The samples were then transferred under air to the Raman spectrometer. All measurements were obtained at room temperature and without further preparation.

3.4. Home-made CVD system for graphene growth

The chemical vapour deposition (CVD) growth of graphene reported in this thesis was undertaken in the Department of Physics at Durham University. Growth was carried out at atmospheric pressure without the use of pumping system in order to explore low-cost routes to graphene production. The CVD apparatus consisted of a horizontal cylindrical tube furnace (Carbolite), a gas flow meter (Platon GTF1 AHD) and gas bubbler which regulated the flow of various gases into the furnace tube and gas lines. A photograph of the tube furnace and gas flow connections is shown in Fig. 3.8 and the system is illustrated schematically in Fig 3.9.

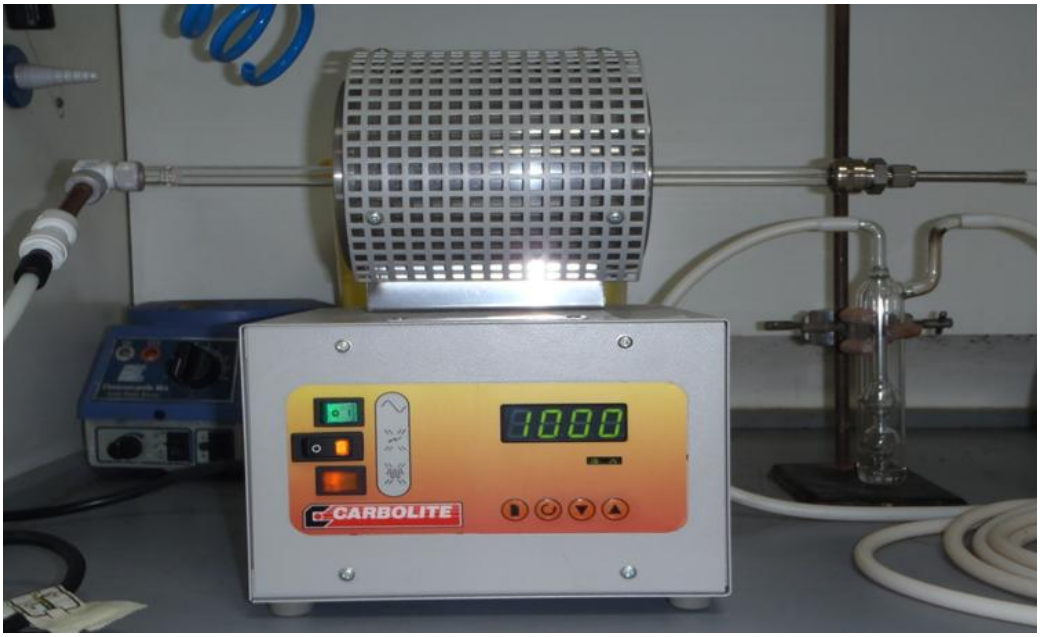

Fig. 3.8: The furnace from the CVD graphene growth system at Durham.

The Carbolite furnace has a heating coil surrounding the inner wall of a cylindrical shell. The furnace temperature can be controlled from room temperature to 1000°C (measured with a K-type thermocouple) with a variable ramp rate and can be also pre-programmed in order to let the system to be retained at a desired temperature for known period of time and then cooled either naturally or at a pre-defined 'ramp down' rate. The thermocouple can measure the temperature at the central region of the furnace and so the sample should be accurately placed at the central region of the furnace. The CVD reactor includes a 70 cm long quartz tube with 25 mm diameter, half of the length of which is placed inside the cylindrical ceramic work tube of the furnace, such that the midpoint of the tube coincides with the midpoint of the furnace. This quartz tube is connected to a gas flowmeter and the other side is exhausted to a fume hood to ensure that flammable gases are appropriately controlled.

Graphene growth was performed on copper substrates which could be fixed, with PDMS or Nonadecane precursor as appropriate, inside a curved ceramic boat and pushed from the exhaust arm of the quartz tube to a pre-marked position of the centre of the furnace by a copper rod (see Fig. 3.10). Thus, it is certain that the given temperature by the furnace meter is precisely the temperature of the inserted substrate. A gas handling line was attached to the gas flow meter to meet the quartz tube which provides a mixed nitrogen and argon for

substrate conditioning (see below), or argon alone gas for graphene growth. The flow meter can control gas flow in the range from 0 to 320 standard cubic centimetres per minute (sccm).

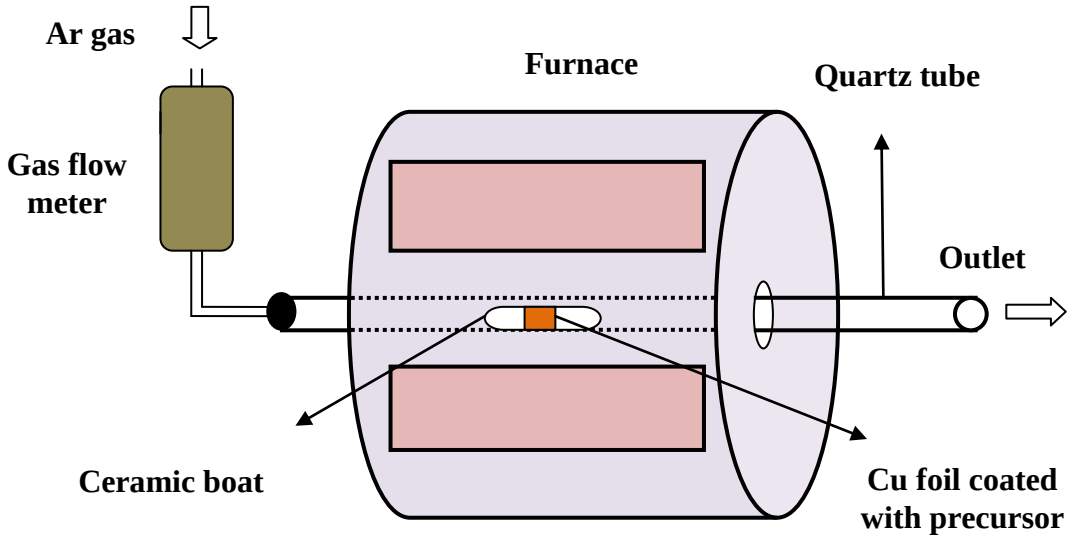

Fig. 3.9: Schematic diagram of the CVD set up used for the growth of graphene.

Pure copper foil (99.9%) was obtained from *Advent Research Materials Ltd* and cut into samples 5 x 7 mm^2 in area for graphene growth. Before introduction into the CVD reactor samples were pre-treated by two steps summarised in Tables 3.1 and 3.2. The samples were first subjected to was solvent cleaning and etching, carried out in an ultrasonic bath, in order to improve morphology and remove surface impurities which would result in the deposition of amorphous carbon at high temperatures in the CVD furnace. Samples are treated by (*i*) Acetone for 10 minutes to remove any organic impurities, (*ii*) Acetic acid (5%) for 10 minutes to remove the native oxide layer, (*iii*) isopropyl alcohol (IPA) for 10 minutes to remove the acetone and acid residues and finally (*v*) the copper substrate is placed in se-ionised water for 10 minutes to remove residual solvents. The rationale for this cleaning procedure is the need to remove organic contamination and oxides which would have an uncontrolled influence on graphene growth and the improvements in surface morphology resulting from acetic acid etching reported in the literature[14,15,16]. After cleaning, samples were allowed to dry in ambient atmosphere and then were pressed between two clean glass slides to ensure that they were completely flat.

Acetone	Acetic	IPA	De-ionised water
10 min	10 min	10 min	10 min

Table 3.1: Details of the initial copper substrate cleaning step used in CVD graphene growth.

The second procedure was the thermal annealing summarized in Table 3.2 which is used for two purposes; (*i*) to remove copper oxide resulting from re-oxidation during storage in air after the initial cleaning stage and (*ii*) to increase the grain size of polycrystalline copper substrate. Large grain size is preferred for graphene growth due to the reduction of the disruption to film growth associated with substrate grain boundaries. Thermal annealing was performed in the CVD furnace. The quartz tube was fed by a mixture of nitrogen (95%) and hydrogen (5%) to keep the surrounding ambient inert and to avoid oxidation of copper. The annealing was performed for 10 hours at 1000°C and then copper substrate was taken from the quartz tube once it had cooled to room temperature.

Procedure	Step	Temperature	Gases Used	|Time
1	Ramping up	1000°C	Mixed N_2/Ar	50 min
2	Annealing	1000°C	Mixed N_2/Ar	600 min
3	Ramping down	22°C	Mixed N_2/Ar	150 min

Table 3.2: Parameters used in the second stage of substrate preparation.

Fig. 3.10 shows the optical micrographs demonstraing the effect of substrate pre-treatment on surface morphology. It is known that smooth and clean copper foils are an important factor to allow reproducible synthesis of graphene layers with large size and high quality[16,17,18]. It is found that impurities and particles on copper surface before graphene synthesis cause serious problems such as discontinuities and grain boundaries in the graphene and increase the occurrence of multilayer flakes ,where some particles work as multilayer graphene nucleation seeds[16,17,18]. Analytical scanning electron microscopy using x-ray analysis have revealed that the white particles are mainly Si, Ca, Pt, Ru, and Ce[16]. Chemical

and thermal annealing processes are helpful in reducing the concentration of impurity particles on the copper surface and increase surface smoothness as can been seen from Fig. 3.10.

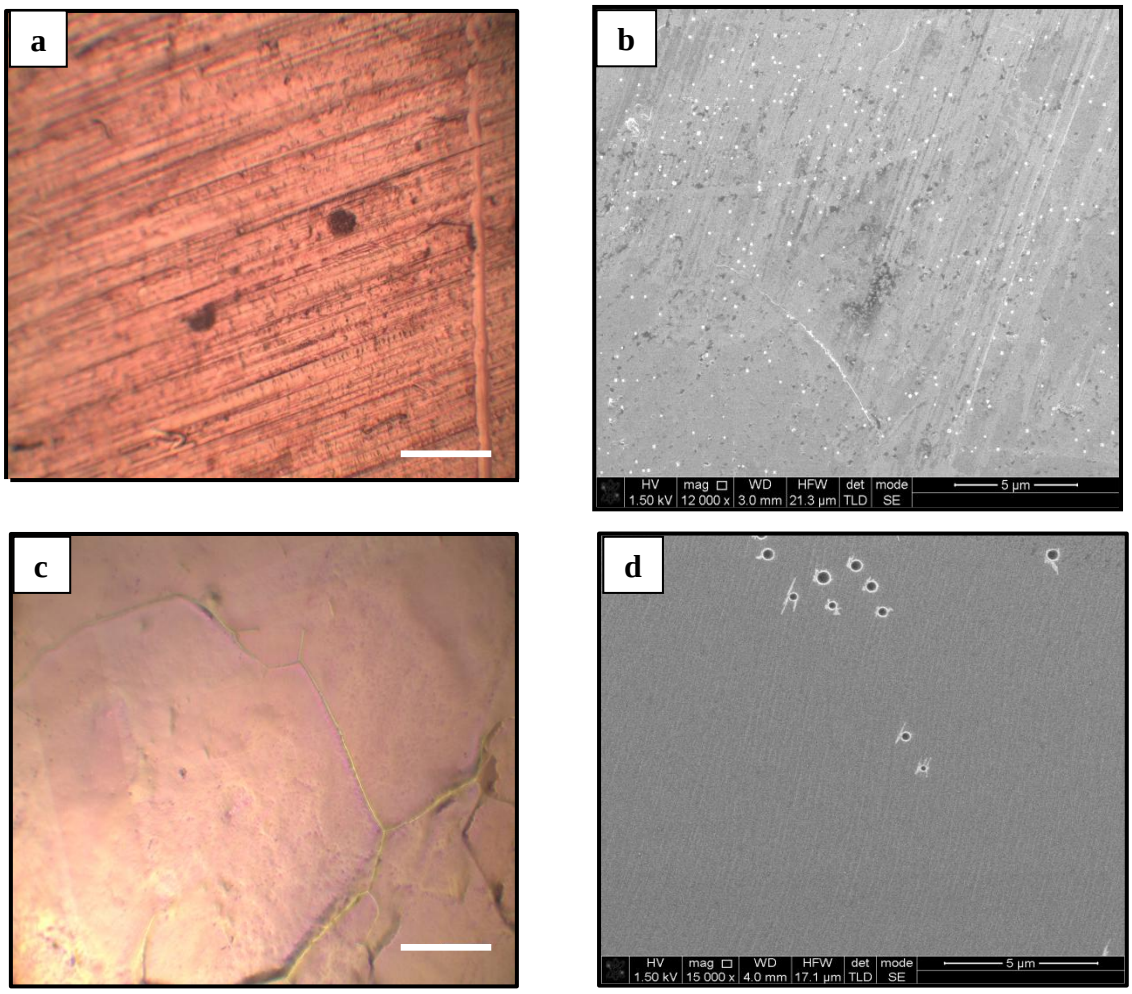

Fig. 3.10: The effect of pre-treatment processes on copper surface morphology; (a) and (b) show optical and SEM images of surface before pre-treatment respectively and, (c) and (d) after pre-treatment. Optical image size of the scale bar is 100 µm.

The main method for graphene growth employed in the current work is the use of solid hydrocarbon materials as carbon feedstock to produce graphene. Although gas-phase graphen growth is the most commonly used technique reported in the literature[19], the use of gas-phase precursors to graphene growth introduces the need for complex gas handling using combustible gases, is potentially costly and offers no potential for simple control over the region of the sample in which graphene growth is promoted. The relative advantages and disadvantages of the two growth approaches are discussed in Chapter 5. The solid phase growth process we use is similar to that found in the work done by Sun *et al.*[20], who

employed a variety of waste materials in their method. The two precursor sources used in the work reported here were nonadecane ($C_{19}H_{40}$) – a model hydrocarbon source – and a mixture containing between 70-90% polydimethylsiloxane (PDMS) and 10% silicon dioxide. The latter material was used in an attempt to incorporate silicon dopants into the graphene lattice, as detailed in Chapter 6. The growth process was carried out at atmospheric pressure and in this case the ceramic boat and pre-treated copper substrate were situated in the furnace, while a variable quantity of precursor material was placed on the top of the substrate in direct contact. A constant flow of argon (320 sccm) was maintained throughout time the sample resided in the reactor, which keeps an inert atmosphere and works as a carrier gas. In order to find the optimum growth conditions parameters such as growth time, growth temperature and the amount of hydrocarbon source were varied; the growth temperatures used were between 850°C and 1000°C; the growth time spent at the required temperature was varied between 5 minutes to 600 minutes with heating at a ramp rate of 20 °C/min and the amount of precursor ranged from 5 mg to 30 mg for nonadecane and was fixed around 5 mg for PDMS. The position of the substrate at the centre of the furnace was accurate to ±3 mm and the length of each substrate was 7 mm. On the basis of furnace calibration, temperature variability across the substrate and between different growth trials was in the order of approximately 2°C – it is found that the temperature dropped off by 2°C/cm for the first 1.5 cm either side of the mid-point. After the growth process, selected samples were oxidised by heating in air on a hot plate (200 °C for 15 min) – the 'heat tinting' method described in Section 2.5.3 or by dipping in H_2O_2 order to enhance the visualisation of graphene on copper foils, both processes having been reported as effective in generating contrast between graphene and uncovered regions of a copper substrate[15,21].

3.5. Polarized Optical Microscopy (POM)

The optical micrographs reported in this thesis were obtained with a GX L3030 polarised optical microscope at the Department of Physics, University of Durham. The microscope has objectives to produce the image and to magnify it to be presented in a convenient manner, a light source to illuminate the sample, a light condenser to concentrate the light in narrower area on the sample surface, a stage to hold the sample, a stand to hold all the optical microscope components and allow fine and coarse focusing, a polarizer below the sample, a polarising analyser above the sample, a slot for insertion of various compensators, a number

of lenses for observing the back focal plane of the objective, and a camera connected to a computer for data capture. Fig. 3.11 (a) illustrates the imaging process whilst Fig. 3.11(b) presents a photograph of the microscope used. Details of the operation of polarising microscopes are given in Chapter 2.

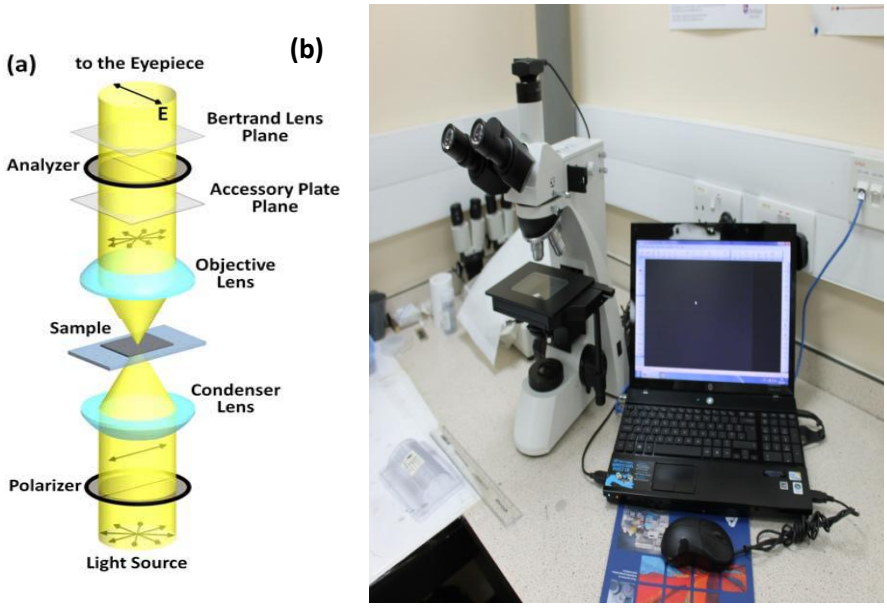

Fig 3.11: (a) A schematic showing the imaging process in a polarising optical microscope[22], and (b) the GX L3030 polarised optical microscope used at Durham.

Since graphene has an optical transparency of 97%, its identification and observation can be challenging. Post-growth oxidation of the substrate, as described in Section 3.4 above offers a means to create contrast[15,21] but relies on there being a partial coverage of graphene and the processing steps may damage the graphene overlayer. Several groups have reported the presence of optical anisotropy in graphene sub-monolayer islands[15,22,23], although the exact origin of this phenomenon is still not fully understood.

3.6. Auger Electron Spectroscopy (AES)

Auger electron spectra were obtained in the Department of Physics, Durham University using a four-grid low energy electron diffraction (LEED) system (Omicron SPECTALEED) acting as retarding field analyser (RFA), which was housed in an ultra-high vacuum system also containing a scanned probe microscope (Omicron VT-SPM) – the latter not used in the studies presented in this thesis. The UHV system consists of a fast entry load lock (FEL), from which samples may be transferred into the chamber housing the LEED system. The base pressure in this chamber was 5×10^{-11} mbar, however, the graphene samples produced and analysed in this thesis generally showed significant outgassing under the electron beam due to desorption of physisorbed contamination (most likely originating from exposure to atmosphere as the samples were taken from the growth furnace and stored in air before being introduced into the UHV system). As a result chamber pressures were typically between 1×10^{-8} mbar and 5×10^{-8} mbar during measurement. Analysis with a mass spectrometer mounted on the UHV system showed that the desorbing species were dominated by water (peaks at mass 18, 17 and 16 corresponding to H_2O and its cracking products OH and O). The UHV systems can be seen in Fig. 3.12.

Fig 3.13 shows a block diagram illustrating the apparatus used for AES. In front of the screen are four concentric spherical sector mesh grids. The grid closest to the sample is grounded to enable the electrons emitted from the sample to travel through a region free of electric fields before reaching the analyser. This prevents any change in energy of the emitted electrons. The second and third grids are connected together and a sinusoidally modulated voltage applied to them. The grids are linked together in order to provide a region of uniform field which acts to energy analyse the electrons. The final grid is grounded to reduce capacitive coupling with the screen, which acts as a current collector.

Energy analysis in a RFA works as follows[25]. If a retarding potential V_0 is applied to the middle grids electrons are collected in an energy range given by:

$$\int_{eV_o}^{E_0} N(E)dE \qquad (3.2)$$

where $N(E)$ is the number of electrons emitted from the sample as a function of energy, E and $E0$ is the incident beam energy (the maximum electron energy which can originate from the sample, resulting from elastic scattering). Clearly the integral of the electron energy spectrum is not particularly useful and the spectrum and its derivatives can be recovered by applying a sinusoidal modulating voltage, ΔV to the grids, such that:

$$\Delta V = \sin \omega t \qquad (3.3)$$

with ω the angular frequency of oscillation. By using a Taylor series expansion it can be shown that the current arriving at the screen is composed of a series of harmonic frequencies $\omega, 2\omega, 3\omega...$[25]. To first order the first harmonic has an amplitude proportional to $N(E)$ and the second harmonic (2ω) is proportional to $dN(E)/dE$. Since, as described in Chapter 2, it is desirable to collect the derivative signal in electron excited AES, a lock-in amplifier is used to select the 2ω signal and hence record $dN(E)/dE$.

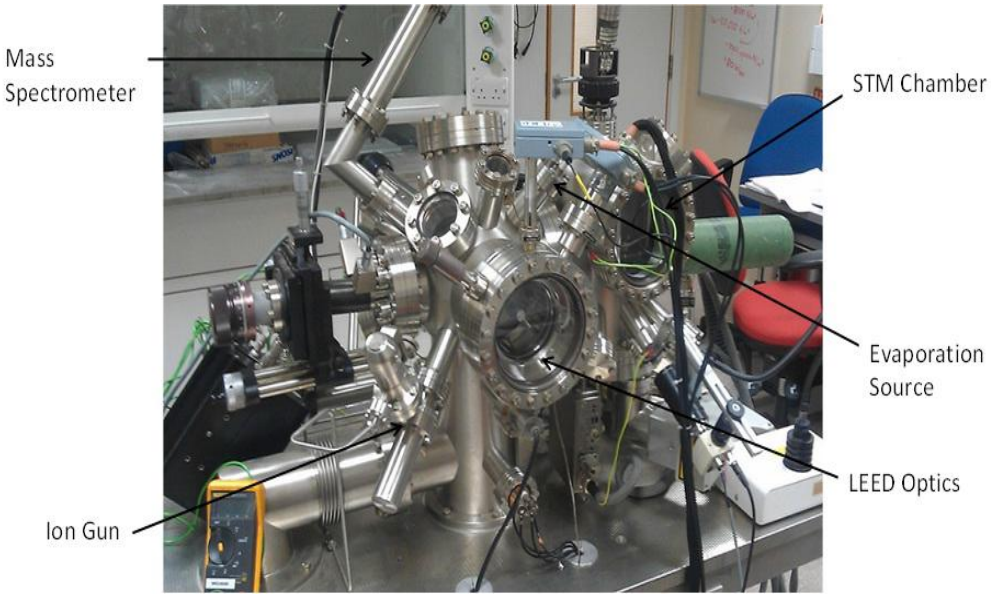

Fig. 3.12: UHV-VTSPM system at Durham

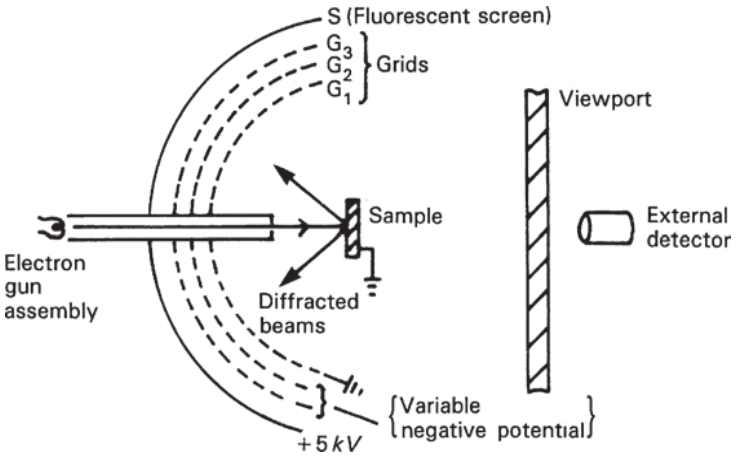

Fig. 3.13: Schematic layout of a RFA based Auger electron spectrometer[26].

3.7. *FEI-Helios Nanolab 600i dual beam FIB/SEM System* at Durham

In this thesis, a *FEI-Helios Nanolab 600i dual beam FIB/SEM system* is extensively used to investigate the morphology, shape and distribution of graphene grown on copper substrates. This instrument, based in the Faculty of Science Electron Microscopy Facility at Durham University, has a focused ion beam *(FIB)* column and an electron beam column for scanning electron microscopy *(SEM)*. It is in the latter mode that the instrument was used in order to generate the data presented in this thesis. A photograph and a schematic diagram of the apparatus are presented in Fig. 3.14 and 3.15, respectively.

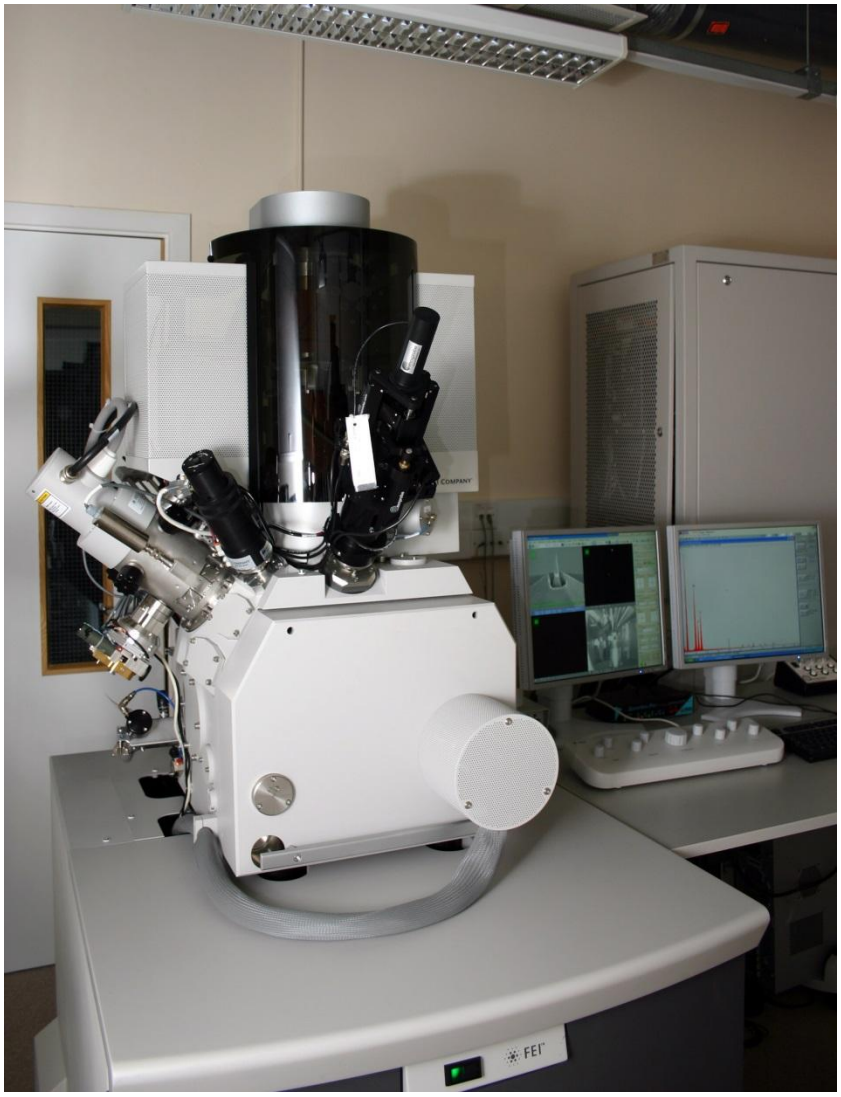

Fig. 3.14: A photograph of the *FEI-Helios Nanolab 600i dual beam FIB/SEM system* used in Durham.

This instrument consists of four parts; *(i)* the ion and electron columns which are located at the top of the apparatus, *(ii)* an evacuated chamber under the columns, *(iii)* gas delivery tools and *(iv)* a computer system with specialised software which allows one to control all the procedures that are needed for imaging process.

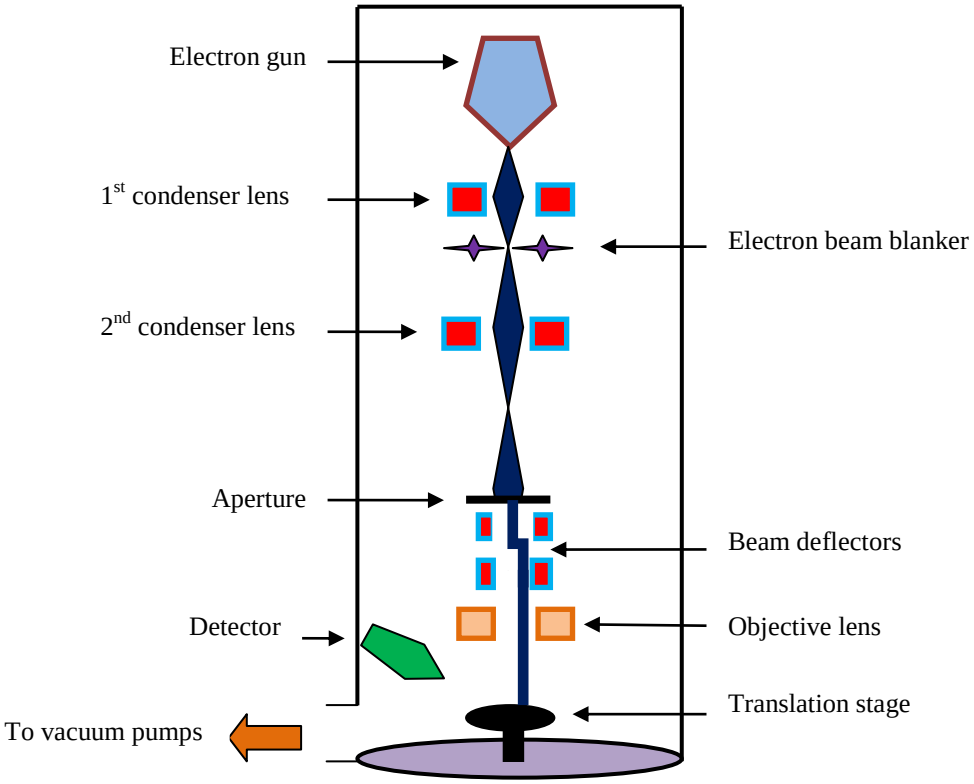

Fig. 3.15: Schematic diagram of the SEM components adapted from[27].

The incident beam used in imaging the sample (as described in Chapter 2) is produced from electrons emitted from an electron gun located at the top of the column. The importance of the electron gun arises from its role in determining the imaging performance of the system: First, it is the virtual source size which defines the spot volume at surface sample and sets the resolution of the system. Second, it is the brightness which is associated with the current density in the incident electron beam. The Helios Nanolab SEM column is based on a Schottky field emission source. This source consists of a conductive needle with a low work function that can be heated up to emit excited electrons, forming an intense beam. These electrons can be directed to the target by applying an electric field and accelerated in a vertical path under a high voltage. A number of electrostatic or magnetic lenses are utilised to focus the incident electron beam to a precise point onto the sample surface. The Helios Nanolab has an ultimate resolution of 0.9 nm at a beam energy of 15 keV, an incident beam energy which can be varied between 350 eV and 30 keV and maximum beam current of 22 nA[28]. A beam energy of 1.5 keV was typically employed to obtain the images of graphene/copper samples presented in Chapters 5 and 6 of this thesis.

Fig. 3.16: Photograph of the secondary electron detector.

Figure 3.16 is a photograph obtained of the sample chamber of the *FEI-Helios Nanolab* and labels the key components such as the secondary electron detector. Secondary electrons, generated by the focussed beam impinging on the sample surface, are picked up by a positively biased grid and accelerated to the scintillator. Upon striking the scintillator the electrons create a flash of light which is amplified by the photomultiplier and converted to a current proportional to the number of detected electrons from the sample surface. The resulting intensity as a function of beam position is used to generate a digital image which can be seen on the display screen. The detector is protected from unwanted electrons (e.g., those scattered within the chamber and not originating directly from the sample) by surrounding it with a Faraday cage[27,29]. The details of secondary electron detection and image formation in the SEM are discussed in detail in Chapter 2.

3.8. Summary

This chapter provided a brief description of a number of different experimental instruments and sample preparation methods used to obtain the measurements presented in this thesis. These techniques have been employed in the analysis and investigation of SWCNTs and graphene, as discussed in detail in Chapters 4, 5 and 6.

3.9. References

1. D. Chattopadhyay, I. Galeska, and F. Papadimitrakopoulos, Carbon **40**, 985 (2002).
2. T-J. Park, S. Banerjee, T. Hemraj-Benny and S. S. Wong J. Mater. Chem. **16**, 141 (2006).
3. X.H. Chen, C. S. Chen, Q. Chen, F. Q. Chen, G. Zhang and Z.Z. Chen, Mater. Lett. **57,** 734 (2002).
4. Y. Kim and D.E. Luzzi, J. Phys. Chem. B **109**, 16636 (2005).
5. R.M. Houchin,Ph. D. Thesis, University of Durham, UK (2011).
6. 'AG2 Ion Source Manual', VG Microtech, Surrey, (1987).
7. 'Axis Ultra DLD Manual', Kratos Analytical, Manchester (2005).
8. H. Lüth, 'Solid Surfaces Interfaces and Thin Films'. (Springer, Berlin, 2010).
9. R. Hess, T. Chasse and R. Szargan, 'Unifit 2002 – universal analysis software for photoelectron spectra', Anal. and Bioanal. Chem. **375,** 856 (2003).
10. R. Hesse, T. Chasse, P. Streubel and R. Szargan, 'Error estimation in peak-shape analysis of XPS core-lvel spectra using UNIFIT 2003: how significant are the results of peak fits?', Sur. Interface Anal. **36**. 1373 (2004).
11. R. Hesse, P. Streubel and R. Szargan, 'Improved accuracy of quantitative XPS analysis using predetermined spectrometer transmission functions with UNIFIT2004', Surf. Interface Anal. **37**, 589 (2005).
12. B.P. Straughan and S. Walker, 'Spectroscopy', (Chapman and Hall, London 1976).
13. D.P. Strommen and K. Nakamoto, "Laboratory Raman Spectroscopy", (John Wiley & Sons Inc., New York, USA 1984).
14. S.M. York, S. Haq, K.V. Kilway, J.M. Phillips and F.M. Leibsle, Surf. Sci. **522**, 34 (2003).
15. C. Jia, J. Jiang, L. Gan and X. Guo, Sci. Rep. **2:707**, 1 (2012).
16. S.M. Kim, A. Hsu, Y-H Lee, M. Dresselhaus, T. Palacios, K.K. Kim and J. Kong, Nanotechnology **24**, 365602 (2013).
17. G.H. Han, F. Gunes, J.J. Bae, E.S. Kim, S.J. Chae, H-J. Shin, J-YChoi, D. Pribat and Y.H. Lee, Nano Lett. **11**, 4144 (2011).
18. H. Kim, C. Mattevi, M.R Calvo, J.C. Oberg, L. Artiglia, S. Agnoli, C.F. Hirjibehedin, M. Chhowalla, and E. Saiz, ACS nano **6**, 3614 (2012).
19. N. Reckinger, A. Felten, C.N. Santos, B. Hackens and J.F. Colmer, Carbon **63**, 84 (2013).
20. Z. Sun, Z. Yan, J. Yao, E. Beitler, Y. Zhu and J.M. Tour, Nature **468**, 549 (2010).
21. S. Chen, L. Brown, M. Levendorf, W. Cai, S. Ju, J. Edgeworth, et al., ACS Nano **5**, 1321 (2011).
22. T. Lee, B. Senyuk, R.P. Trivedi and I.I. Smalyukh,. "Optical Microscopy of Soft Matter Systems" arXiv:1108.3287 (2011).
23. D. W. Kim, Y. H. Kim, H. S. Jeong and Hee-Tae Jung, Nuture Nanotech **7**, 29 (2012).
24. K. Kertesz, A.A. Koos, A.T. Murdock, Z. Vertesy, P. Nemes-Incze et al., Appl. Phys. Lett. **100**, 213103 (2012).
25. D.P. Woodruff and T.A. Delchar, 'Modern Techniques of Surface Science', (CUP, Cambridge 1994).
26. J.C. Vickerman and I.S. Gilmore, 'Surface Analysis- The Principal Techniques', (John Wiley and Sons, Singapore 2008).

[27.] J.I. Golstein, D.E. Newbury, P. Echlin, D.C. Joy, A.D. Romig Jr., C.E. Lyman, C. Fiori and E. Lifshin,'Scanning electron microscopy and X-ray microanalysis', (Plenum Press, New York and London 1992).
[28.] Helios NanoLab 600i. Technical report FEI.
[29.] M.S. Sultan, Ph. D. Thesis, University of Durham, UK (2013).

Chapter 4

Nitrogen doping of SWCNTs mediated by ion irradiation

This chapter investigates the changes in chemical bonding and elemental composition of single walled carbon nanotubes (SWCNTs) induced through irradiation by medium energy (several keV) N^+ and Ar^+ ions at low flux. X-ray photoelectron spectroscopy (XPS) and Raman spectroscopy have been used to track changes as a function of flux and ion species. It is found that the nature of the nitrogen species incorporated in the carbon nanotubes varies sensitively with preparation conditions. XPS core-level binding shifts confirm that substitutional (graphitic) nitrogen acts as an n-type dopant and that the influence on carrier concentration of other bonding configurations is negligible. Whilst the evolution of X-ray photoelectron spectra can be easily correlated with nitrogen content and bonding type, the behaviour of Raman spectra is found to be more complex.

4.1 Introduction

As outlined in Chapter 1, carbon nanotubes (CNTs) are an exciting area of current research because they offer the potential for application in a wide variety of fields and their unique structure renders them of basic scientific interest. Although many of the intrinsic properties of carbon nanotubes, such as their strength[1,2,3] and thermal conductivity[4,5,6] are desirable, chemical and structural modification provide a route to tailor their behaviour for specific applications through changing electronic structure, chemical reactivity or by combining the two enabling sensing[7,8,9,10,11,12,13,14,15], for example. CNTs may be modified by many methods. For example, the modification of nanotube properties by controllably introducing defects and heteroatoms opens the door for a range promising technological applications and further modification, and is the focus of the research reported in this chapter. Fig 4.1 shows the various possible mechanisms through which doping of CNTs can be achieved[16]. The incorporation of foreign species may be endohedral with the dopants located within the inner bore of the nanotubes, involve intercalation of dopants into the interstices between nanotubes within a tightly packed bundle or through substitutional doping in which one or more dopant atoms is directly incorporated into the nanotube wall. Chemical functionalization – the attachment of functional groups to the surface of a nanotube[17] is also an approach frequently used to modify the behaviour of carbon nanotubes. However, such functionalisation generally produces structural and electronic impacts far more significant than is usually understood by the term 'doping' – such as the opening of a large band gap and redistribution of valence states upon covalent attachment of functional groups see Ref. [17] and references therein.

One interesting means for the modification of CNTs is through doping by nitrogen. Nitrogen-doping of SWNTs creates active sites which not only facilitate chemical functionalization[18] but can also form the basis of sensor devices[19]. For example, the influence of a number of gases and solvent vapours on the conductivity of N doped CNT samples were investigated by Villalpando-Paez *et al.*[15], the films showing high sensitivity and good response times. Surface activation (i.e., increased surface reactivity) also make N doped nanotubes candidate materials for the storage of gases and/or metals. Similarly, surface 'activation' of MWCNTs with nitrogen has been found to improve their biological compatibility[20]. Stable doping of nanotubes can also make them highly attractive for use in nanoelectronics, with ballistic conduction measured in N-doped metallic SWCNTs. The

active sites on nitrogen-doped CNTs have also been shown to catalyse the oxygen reduction reaction (ORR), which is an important process in the operation of fuel cell and has thus received significant attention[21,22,23]. The nitrogen doped nanotubes were found to be much more robust than conventional electrodes and resistant to poisoning. In addition to having a modified chemistry, N doped CNTs have enhanced electrical properties and can, for example, be used in field emission devices since the presence of N is able to influence the electron emission properties of the CNTs[24,25,26,27,28]. It is the promise offered by nitrogen doping which motivates the focus of the work reported in this chapter.

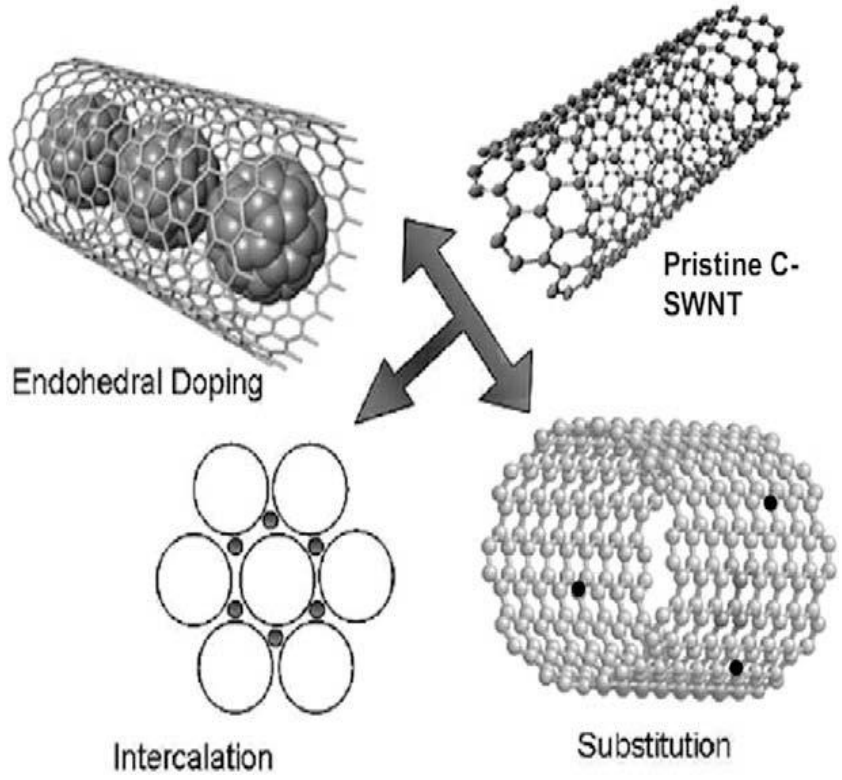

Fig. 4.1: Schematic illustration of the various routes by which foreign species may be doped into SWCNTs[16].

The study of N doping of CNTs started in 1993 in work by Yi *et al.*[29], which theoretically investigated subsitutional doping of CNTs by nitrogen and boron. This was followed by the experimental production of nitrogen doped CNTs by Droppa *et al.*[30] who used arc-discharge under a nitrogen-helium atmosphere and by Glerup *et al*., using nitrogen-rich precursors[31], in order to produce N-doped SWCNTs. The doping concentration of the CNTs, at less than 2%, was low compared with CNTs produced in later work. Although early work employed arc-

discharge synthesis, chemical vapour deposition has been more commonly used for the production of substitutionally doped nitrogen-containing nanotubes but has mainly been successful in producing MWCNTs[32,33,34] with a wide range of concentrations reported. It is of interest to note, as Ewels *et al.* point out[35], many conventional CVD processes use nitrogen or nitrogen-containing mixtures as their inert gas atmosphere which may lead to accidental nitrogen incorporation, particularly in the presence of defects. Indeed, it is shown in Section 4.3.1.1 that exposure of defective SWCNTs to the ambient not only leads to the presence of oxygen-containing species, as previously reported[36], but also to small quantities of chemisorbed nitrogen, highlighting the activity of defects even towards nominally inert gases.

An alternative to the incorporation of nitrogen (and other dopants) into CNTs during the growth process is post-growth treatment. Post-growth processing of nanotube material opens the potential for doping which may be more selective either in terms of nanotube type of physical location, although presents its own set of challenges. Post-growth chemical substitution of nitrogen into SWCNTs was attempted by Goldberg *et al.*[37] using B_2O_3 and nitrogen gas at elevated temperature. However, the nanotubes were highly damaged and contained less than 1% nitrogen. This method has also demonstrated the side effect of increasing the diameter of the CNTs from an average of 1.4 nm to 3.2 nm. The increase in CNT diameter may be caused by coagulation of nanotubes to eliminate dangling bonds formed by the doping process. D.C. magnetron sputtering of CNT films was more successful and nitrogen concentrations of 15-30% have been achieved[38] but accompanied by significant damage to the nanotube structure.

A novel approach to post-growth nitrogen incorporation into SWCNTs was first proposed by Krasheninnikov and co-workers[39,40] involving the low energy irradiation of nanotubes with N ions. Using molecular dynamics simulations it was shown that irradiation of SWCNTs with N ions led to the formation of substitutionally doped nitrogen in addition to vacancy defects, with substitutional nitrogen comprising a maximum of almost 50% of the non-pristine sites for an incident ion energy of 50 eV[39]. As pointed out by Kotakoski *et al.*[39], it could be expected that this percentage would be increased by annealing as a result of the migration of dopant atoms and their interaction with vacancies, suggesting a very promising route to control both the composition and electronic structure of SWCNTs.

Among the first attempts to dope SWCNTs in this way were those made by Yamamoto *et al.*[41] who used a mass selected beam of $^{14}N^{+}$ ions with energies of 25 and 30 eV. Electron energy loss spectroscopy (EELS) performed in a transmission electron microscope was used to detect nitrogen incorporated in the SWCNTs. Due to the relative lack of sensitivity of the technique a clear signal at the nitrogen *K* edge could only be detected for ion doses of 2.2×10^{15} ions/cm^2, which was found to be above the threshold for amorphisation. However, irradiation of a field effect transistor (FET) structure consisting of a single SWCNT was performed with a ion dose around three orders of magnitude smaller than the amorphisation threshold (corresponding to an estimated N concentration of 450 ppm) which led to a change from *p*-type to *n*-type behaviour, indicating that nitrogen doping of the SWCNT had been achieved. Xu *et al.* irradiated SWCNT films with N^{+} ions at beam energies of 3 keV[42] and 300 eV[43], followed by annealing at temperatures up to 1000˚C, XPS being employed to follow the changes in composition and bonding. N1*s* lines were clearly observed for doses as low as 1.7×10^{14} ions/cm^2 for irradiation with 300 eV ions. The nitrogen core line could be decomposed into components associated with pyridinic, sp^3 hybridised, substitutional and oxidised nitrogen, the precise ratio of which depended upon dose and annealing treatment, Fig. 4.2. The results of Xu *et al.*[42,43] will be discussed in more detail in Section 4.3.1.1, when they are compared with the results presented in this thesis.

The great advantage of ion irradiation doping is that focused ion beams may be used to enable spatially-resolved doping allowing the production of device structures. Moreover, CVD grown N doped nanotubes show inhomogeneities in concentration[44,45] which may be eliminated by the greater control over the doping process offered by direct ion irradiation. A further benefit of the use of ion irradiation is that it is usually performed under a controlled atmosphere (high to ultra-high vacuum) with a well-defined background gas composition. Hence, impurities such as hydrogen, which are extremely hard to detect experimentally and which could arise from gas-phase impurities or decomposition of hydrogen-containing feedstock species[35] can be dramatically reduced or eliminated.

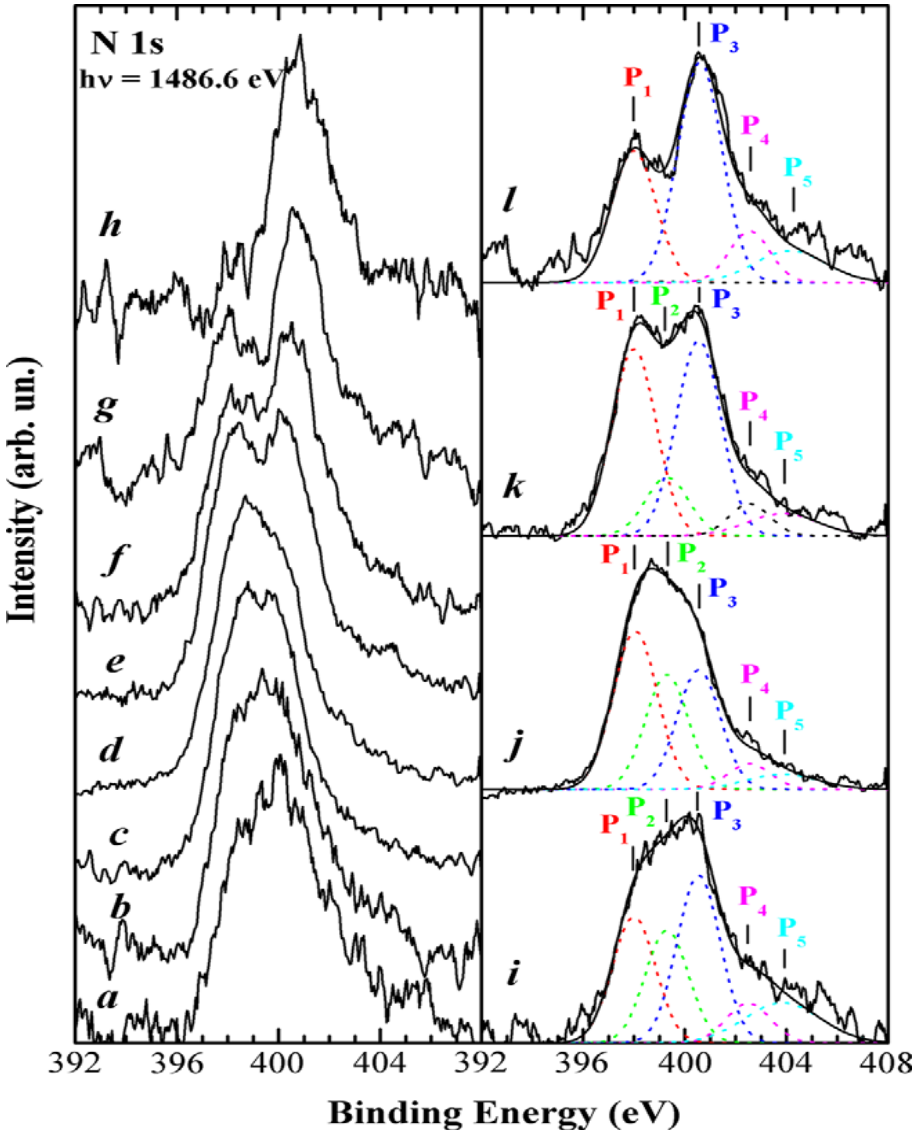

Fig. 4.2: The main components in N1*s* core level photoelectron spectra obtained by Xu *et al*[43]. Left panel: Normalized N 1*s* core level photoemission spectra for ion doses of (a) 1.7 x 10^{14} ions/cm^2; (b) 3.6 x 10^{14} ions/cm^2; (c) 9.6 x 10^{14} ions/cm^2; (d) 2 x 10^{15} ions/cm^2; and post-irradiation annealing at temperatures of (e) 400˚C; (f) 600˚C; (g) 800˚C; and (h) 1000˚C. Right panel: N 1*s* line shape curve fitting schemes for (i) 2.6 x 10^{14} ions/cm^2; (j) 2.2 x 10^{15} ions/cm^2; (k) 500˚C; and (l) 800˚C. Details are discussed in Section 4.3.1.1.

To date, most experimental studies of nitrogen doped CNTs have focused on MWCNTs, since these are generally easier to fabricate. However, most theoretical studies have focused on SWCNTs, and often relatively small diameter achiral (armchair or zigzag) nanotubes, due to the computational costs involved in investigating the larger unit cell sizes required to model MWCNTs or chiral SWCNTs. By directing experimental studies towards SWNCTs, the data presented in this chapter should be more readily comparable with theoretical work. Moreover, the finite penetration depth of the ions into nanotube material

coupled with the development of collision cascades would suggest that ion-irradiation doping of MWCNTs is likely to be inhomogeneously distributed over the nanotube walls with the likelihood that outer walls will be more heavily doped than inner walls. This follows on from transmission electron microscope observations[46] of Ar^+ ion irradiated nanotubes that indicate that outer walls are damaged much more rapidly. It is notable that in CVD growth of nitrogen-doped MWCNTs (discussed below) the opposite variation of doping with radial position is found to occur: CVD grown N doped MWCNTs show greater concentration of nitrogen in the inner walls[47,48,49]. Park *et al.* argued that this behaviour is due to the greater stability of substitional nitrogen in smaller diameter walls[49], although Ewels *et al.*[35] suggest that the catalyst may play a key role.

The morphology of nitrogen doped SWCNTs is similar to that of pristine material[30,31]. As a result, disorder is small and transport measurements on metallic N-doped SWCNTs have shown room-temperature ballistic conduction over several hundred nm at room temperature[50]. The situation is very different for MWCNTs, where CVD grown nitrogen containing tubes show disordered morphologies, such as the 'bamboo structure'. Although the focus of this work was on nitrogen doping of SWCNTs, development of ion implantation doping techniques also offers the possibility of nitrogen doping pre-grown multi-wall nanotubes hence maintaining the morphological characteristics of the undoped nanotubes.

There are several potential structural models for the bonding of nitrogen in carbon nanotubes. The three most likely configurations, based on analogy with a range of chemical are pyridinic (two-fold co-ordinated nitrogen), pyrrolic (substitutional in a five-fold ring) and graphitic (substituted into the hexagonal graphitic network). Nitrogen-vacancy structures of various kinds have also been proposed. Including substitutional nitrogen pairs[51,52] and nitrile (CN) groups. Some of the potential configurations of substitutional nitrogen in the graphitic lattice are shown in Fig 4.3, from Ref. [43] (although it is unclear how the maximally *trivalent* N atoms could adopt the configuration shown in Fig. 4.3(d)). Following the notation of Xu *et al.*[43] the substituent atom can be labelled as X-*n*<hyb>Y $Z^{-\alpha}$ X^{β} where X is the substiuent atom, *n* is the number of nearest neighbours (assumed to be of the same species and in the same hybridisation state), <hyb> is the hybridisation state of the substituent, $-\alpha$ is the number of atoms of species of Z removed from the lattice and β is the number of substituent atoms included in the lattice.

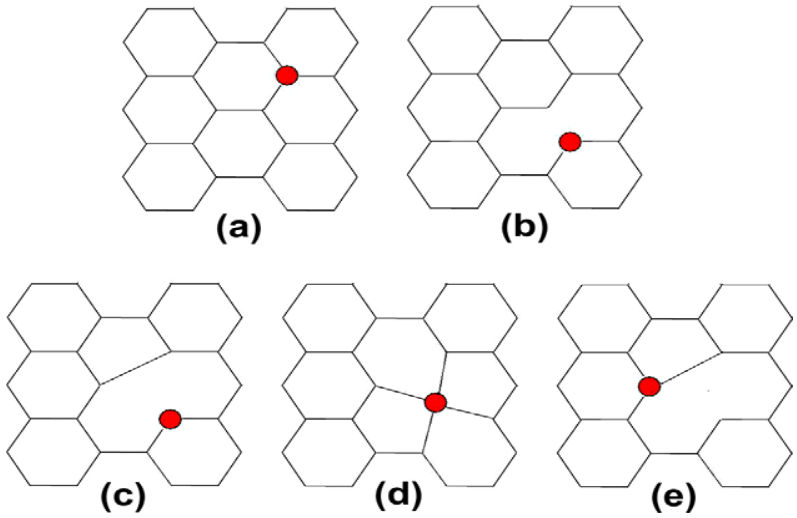

Fig. 4.3: Schematic representation of some possible N–C bonding configurations with a nitrogen dopant atom inserted in a graphitic network: (a) substitutional N–3sp^2C $C^{-1}N^1$; (b) pyridine-like N–2sp^2C $C^{-1}N^1$; (c) pyridine-like N–2sp^2C $C^{-2}N^1$; (d) N-4sp^3C $C^{-2}N^1$; and (e) pyrrole-like N–3sp^3C $C^{-2}N^1$ (from Ref. [43]).

It has been argued that, in addition to being directly incorporated into the CNT wall, interstitial nitrogen can sit on the nanotube surface bridging a broken C-C bond in the wall[39]. However, the surface migration barrier of such a species is found to be quite low – 1.1 eV[40] – and will thus be sufficiently mobile at room temperature to either coalesce with other defect structures on the nanotube wall or combine with another interstitial nitrogen and desorb as gaseous N_2.

There are significant differences between the pyridine (N–2sp^2C $C^{-1,2}N^1$), pyrrole (NN–3sp^3C $C^{-2}N^1$) and graphitic (N–3sp^2C $C^{-1}N^1$) bonding configurations in terms of electronic structure, in particular on nanotube doping. It has been argued[53] on the basis of a simple chemical bonding picture, that only graphitic nitrogen gives rise to a donor state. In the pyridine arrangement the sp^2 hybridised nitrogen atom forms two in-plane σ bonds and contributes a single electron to the delocalized π-bonding network. The remaining two valence electrons both occupy a single in-plane non-bonding orbital with p_x character. In the case of pyrrole-like bonding nitrogen is sp^3 hybridised with three valence electrons used to

form three σ bonds and the remaining two electrons donated to the π bond associated with the five-membered ring which, containing six-electrons, is considered to be graphite-like. In the case of substitutional incorporation of nitrogen into the graphitic nanotube wall the nitrogen is sp^2 hybridised, three valence electrons are used for in-plane σ bond formation and one electron donated to the π-derived 'valence' band. This leaves a single electron which must occupy the π*-derived 'conduction' band of the nanotube, so leading to *n*-type doping.

Nevidomskyy *et al.*[54] used density functional theory (DFT) to investigate the influence of substitutional nitrogen on the behavior of SWCNTs. In a semiconducting (8,0) nanotube the state associated with the nitrogen was localized over 3 nm, but was found to be delocalized in a (5,5) metallic nanotube. However, Lammert *et al*.[55], suggest that for realistic situations, semiconducting and metallic nanotubes behave similarly. Nevidomskyy *et al.*[54], Yi and Bernholc[29] and Lammert and co-workers[55] have all found that substitution leads to a donor state, as predicted by the simple chemical bond arguments discussed above.

There is some debate as to which type of bonding configuration is active for chemical reactions and catalysis in N doped CNTs. Mo *et al.*[23] argue, on the basis of a combined XPS and voltammetry study, that nitrogen in a pyridinic configuration is the most active catalyst site for the oxygen reduction reaction (ORR), which plays an important role in the operation of fuel cells. In contrast, Lee *et al.*[22] suggest, on the basis of XPS and DFT calculations, that a porphyrin-like moiety forms on N-doped MWCNTs grown with a Fe catalyst, and that this is the active site for the ORR. Luo and co-workers[56] achieved doping by a single nitrogen species (pyridinic) in graphene layers grown on copper and suggest on the basis of their voltammetry measurements that pyridinic nitrogen may not be an effective species for promoting the ORR. A key element in solving this controversy is the requirement for CNT samples containing differing concentrations of the various N bonding configurations, but which are otherwise identical (diameter distribution, defect density, impurity levels etc.). As we demonstrate in this chapter, various treatments based around ion irradiation-mediated incorporation of nitrogen into SWCNTs offer great promise in achieving these needs.

It is important to note that whichever the route that substitutional defects are incorporated into the CNT lattice, there is a possibility that defects may be formed, which also have an important effect on the geometric and electronic properties of a CNT (see Ref. [17] and references therein). The most typical (and simplest) type of defect is the single vacancy,

which results when a single, isolated carbon atom is removed from the hexagonal graphitic wall structure (for example, by an external process such as Ar^+ ion irradiation[57,58,59]). In this process, the single vacancy creates three dangling bonds (DBs), which can immediately recombine yielding the 5-1 DB defect. This defect involves the union of two dangling bonds forming a five-membered ring and leaving a single carbon atom with a reactive DB, as discussed in Chapter 1, Section 1.4. This type of defect plays a vital role in the reactivity of CNTs and could enable the introduction of foreign atoms and dopants such as nitrogen into CNTs structure, as predicted by Hou and co-workers for the case of graphene[60], In Section 4.3 of this Chapter it will be demonstrated that ion irradiation induced defects (which are primarily mono and poly vacancies[61]) are sufficiently reactive that they are even able to combine with N_2, a gas typically regarded as rather unreactive, so incorporating nitrogen atoms into the CNT lattice.

4.2 Experiment

As described in Chapter 3, SWCNTs produced by the HiPCO method were sourced commercially from Carbon Nanotechnologies Inc, USA and have been fully characterized in previous work[36]. The nanotubes were dispersed ultrasonically in high-purity residue free 2-propanol (Aldrich) to create a uniform suspension. After this process, suspension was deposited in step-wise way on copper-beryllium substrate (5×7 mm^2) to produce a visibly thick film. The copper-beryllium substrate was used to provide a conducting contact to the film – the film thickness is larger than both the penetration depth of the incident ions, the information depth associated with XPS (both around a few nm) and that associated with Raman spectroscopy (see below, Section 4.3.2.1). The resulting samples are mounted on a sample holder between two tantalum clips, which give good electrical contact to the SWCNTs film. After, samples were loaded into an ultra high vacuum (UHV) chamber for irradiation with Ar^+ or N^+ ions

Irradiation was performed in a custom-built ultra-high vacuum system with a base pressure of ~5×10^{-9} mbar in the Physics Department at Durham University. Ar^+ or N^+ was introduced into the main UHV chamber by a leak valve. The sample was irradiated by a defocussed beam from a filamentless ion source (described in detail in Chapter 3) to different doses with the beam incident normally upon the sample surface (i.e., beam aligned at an

angle, $\theta = 90^{\circ}$ to the surface) to maximise ion penetration into the sample, which is expected to vary as sin θ. The purity of the gas from which the ions were formed was monitored by a quadrupole mass spectrometer (QMS). The ion gun was operated at a beam energy of 2.5 keV, with a 2 keV focusing voltage and the sample current was 1.3 μA for Ar^+ irradiation and 0.4 μA for N_2^+, measured at room temperature without correction for secondary electron emission, unless otherwise stated. As a result of the lack of correction for secondary emission and the contribution to the current from ions falling on the sample holder outside the film the ion doses should be regarded as indicative and suitable for comparison between samples rather than absolute.

Nitrogen was introduced into the SWCNTs by two routes: the already established approach direct irradiation with N^+ ions[42,43] and by a novel indirect route using reactive defects created by Ar^+ ion irradiation. In the latter case sample were irradiated by Ar^+ ions to a dose of 12±1 μC, which is well below the threshold for amorphisation[62] in order to create defects, which are primarily expected to be vacancies[61]. The defective SWCNT films were then transferred, through air to the Carbolite furnace also used for graphene growth (described in Chapter 3, Section 3.4). These samples were then annealed under a nitrogen flow at atmospheric pressure for an hour at a given temperature. All samples were allowed to cool down to room temperature before being removed for Raman and XPS analysis.

XPS was performed *ex-situ* for analysing the core levels of SWCNTs. A Kratos Axis Ultra instrument based in the School of Chemical Engineering and Advanced Materials, Newcastle University was used for the measurements and is described in Chapter 3, Section 3.2. Core level spectra were obtained from a hemispherical analyser using photons of 1486.6 eV energy produced by a monochromated Al K_α X-ray source. Typical system pressure was in the low 10^{-9} mbar range and the total instrumental resolution about 0.48 eV. All XPS spectra presented in this work are referenced to the Fermi level of a silver test sample which was regularly introduced into the XPS system for calibration purposes. All spectra analysed and fitted by the Unifit software package from Leipzig University.

The Raman spectroscopy data presented in this thesis was measured using a *Horiba Jobin Yvon LabRam* spectrometer, based in the Department of Chemistry at Durham University, with a CCD detector using an excitation wavelength of 532 nm which is described in more

detail in Chapter 3, Section 3.3. Raman measurements were performed for undoped and doped SWCNTs on copper substrate at room temperature in air. The system resolution and photon energy were 0.1 cm^{-1} and 2.33 eV, respectively.

4.3 Results and Discussion

4.3.1 XPS of nitrogen doped SWCNTs

4.3.1.1 N1s spectra from nitrogen doped SWCNTs

Fig 4.4 shows the N1*s* core level spectrum a SWCNT film after an N^+ ion dose of 24±2 μC/cm^2 ((1.5±0.1) x 10^{14} ions/cm^2) at room temperature. A clear broad peak can be observed in the spectrum indicating the presence of nitrogen in the sample. The shape and breadth of the peak indicates the presence of more than one component, demonstrating the presence of nitrogen in more than one bonding configuration. In order to obtain more detailed information N1*s* spectra were a series of peak functions consisting of Gaussian-Lorentzian sums and a Shirley type background[63]. In our fitting approach we use the minimum number of physically reasonable peaks (e.g., of width greater than or equal to instrumental resolution), which produce residuals as free as possible of any significant systematic variation (see bottom panel of Fig. 4.4). All fit parameters (position, width, Gaussian: Lorentzian ratio etc.) are allowed to vary through the fitting process without constraint. In order to determine the global minimum of the fit error and to estimate the error on the fit parameters a number of fitting runs have been undertaken, with different starting conditions. The fit selected is that which has the minimum χ^2 value associated with it. Typical N1*s* spectra such as that shown in Fig. 4.4 were best fit with two fit components, located at binding energies of ~399.7 eV and ~400.5 eV. Samples which had been left in ambient atmosphere for an extended period of time produced spectra which were better fit with four components with binding energies of 398.6, 399.4, 400.3 and 402.2 eV, as shown in Fig.4.5. The result of fitting the N1*s* spectra from the nitrogen-doped SWCNT samples produced in this work are summarised in Table 4.1 (where all peak positions derived from the data have an approximate error of ±0.1 eV unless otherwise stated).

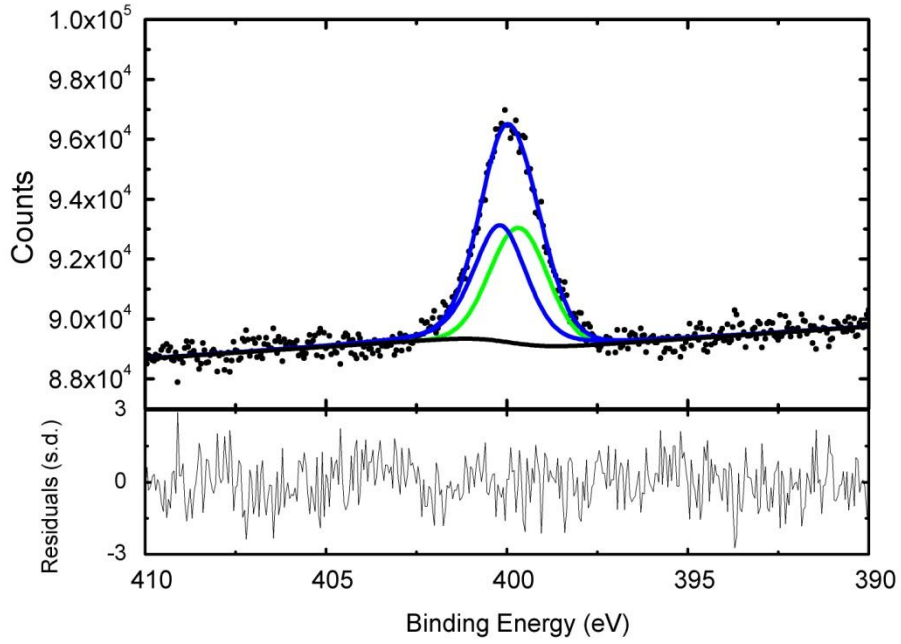

Fig. 4.4: Top panel: N1*s* core level spectrum of a SWCNT film irradiated with 2.5 keV N^+ ions to a dose of 24 μC/cm^2. The dots are the experimental data, the lines refer to fitted components, described in detail in the text. Bottom panel: fit residuals in units of standard deviation of the experimental data.

Identification of the species associated with the N1*s* components shown in Figs. 4.2, 4.4 and 4.5 can be made on the basis of two different schemes devised to explain photoemission data from CN_x compounds which have themselves been the focus of intense experimental investigation due to the prediction of superhard properties[43] . Xu *et al.* [43,42] have followed an identification scheme based on the binding energy calculations performed by Souto *et al.*[64] and by Johansson and Stäfström[65]: in Fig. 4.2 the component P_1 at a binding energy of ~398 eV is attributed to N atoms bound to three C atoms in a sp^3 tetrahedral geometry (pyrrolic nitrogen), a second component, labelled P_2, is located at ~399.3 eV and is interpreted as arising from N atoms bound to two sp^2 hybridised C atoms at the edge of 'disrupted' CNTs or at 'defect' locations (pyridinic nitrogen), the P_3 component has a binding energy of 400.5 eV and is attributed to N inserted substitutionally in a sp^2 hexagonal graphite network ('graphitic N'), P_4 and P_5 are centered at 402.3 and 403.4 eV respectively, and are attributed to N-O bonds in various oxides[66,67]. However, some of these assignments, particularly those peaks of P_1 and P_2 are controversial. For instance, Ripalda *et al*. suggested that the P_1 component is associated with N bound to two C atoms in a sp^2 pyridine-like

configuration, but that P_2 is due to (unspecified) ion bombardment induced defects[68] this assignment being supported by x-ray absorption measurements performed by Shimoyamam *et al.*[69] and earlier theoretical work by Casanovas *et al.*[70].

In order to determine the appropriate assignment of the various components in the N1*s* spectrum we appeal to the considerable body of work, both experimental and theoretical, which has already addressed this issue in carbon nanotubes and the related system of nitrogen-doped graphene. Rather than detail each individual study, a summary of the results from the literature regarding the interpretation of N1*s* core level data are presented in Tables 4.2 (nanotubes) and 4.3 (graphene). It can be seen from these tables that the majority of studies, particularly those which are more recent, follow a scheme in which components at binding energies around 398-399 eV (P_1 in Fig. 4.2) are associated with pyridinic nitrogen, that with a binding energy of ~399.5 eV (P_2) is due to pyrrolic nitrogen, that at ~401 eV (P_3) is due to graphitic nitrogen and that peaks at higher energies are variously ascribed to oxides and molecular nitrogen. Since we find a peak with binding energy of 405.5±0.1 eV after prolonged exposure of the samples to ambient atmosphere, we attribute this component (P_4) to nitrogen in the form of oxides bound to the nanotube surface. This scheme is used to label the peaks in Fig. 4.5 and in Table 4.1, forming the basis of the interpretation of the data and discussion below. It is worth noting that after annealing samples for an extended period in N2 gas we also find a component with binding energy between 405 and 407 eV, which rapidly disappears upon annealing. We attribute this high binding energy peak to molecular nitrogen, which will be both weakly bound and have a core hole poorly screened in comparison with nitrogen chemically incorporated into the SWCNTs. For consistency this peak is labelled P_5, but it should be noted that the origin of this feature is, due to the large difference in binding energy, likely to be different from the component of the same label in the work of Xu *et al.*[42,43] (Fig. 4.2)

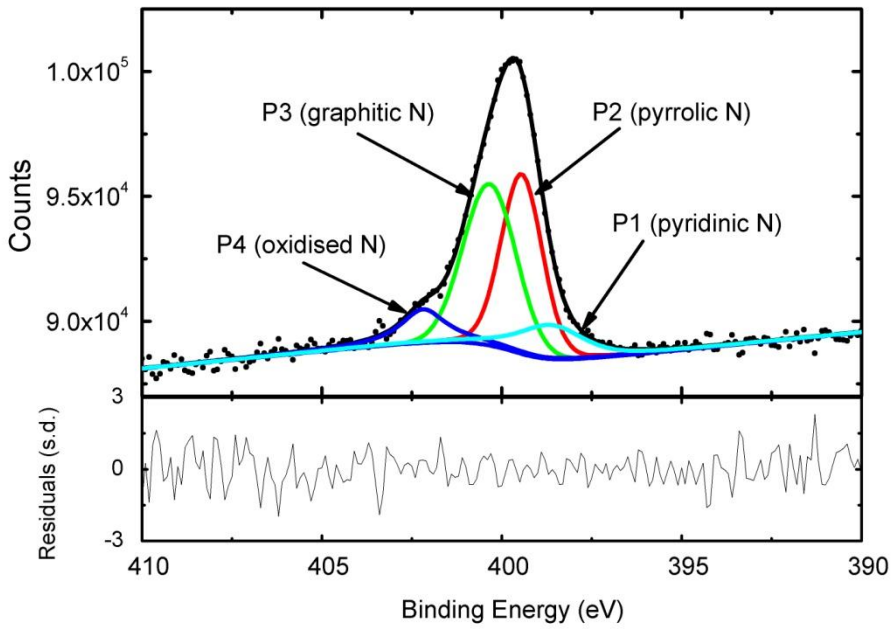

Fig. 4.5: Top panel: N1*s* core level spectrum of a SWCNT film irradiated with 2.5 keV N^+ ions to a dose of 20 μC/cm^2 and then exposed to ambient atmosphere for several weeks. The dots are the experimental data, the lines refer to fitted components, described in detail in the text. Bottom panel: fit residuals in units of standard deviation of the experimental data.

It has been reported[41] that SWCNT films irradiated with mass-selected $^{14}N^+$ ions of 25 and 30 eV show the presence of amorphous carbon at doses of 1.7 x 10^{15} ions/cm^2, becoming completely amorphous by a dose of 2.2 x 10^{16} ions/cm^2. These amorphisation doses are similar to those observed in studies of inert gas ion irradiation of CNTs: In their photoelectron spectroscopy study of SWCNT films irradiated with 3 keV Ar ions, Chakraborty *et al.*[17,57] found evidence of amorphisation (through the emergence of a sp^3 related component to C1*s* photoelectron spectra) at an ion dose of ~1.3 x 10^{15} ions/cm^2, whilst Brzhezinskaya and co-workers[71] determined the onset of amorphisation in MWCNT films due to irradiation with 1 keV Ar^+ ions at ~6.25 x 10^{14} ions/cm^2 by the appearance of a component in Auger electron spectra at an energy of 278 eV. Therefore in order to remain below the onset of significant irradiation induced amorphisation and to ensure that flux (0.4 μC/cm^2) and time were sufficient to enable accurate determination of ion dose, irradiation was undertaken for a limited range of ion doses up to a maximum of 100±5 μC/cm^2.

Peak	**Position and width (eV)**	**N0 (20μC/cm^2 N_2)**	**N1 (24μC/cm^2 N_2)**	**N2 (100μC/cm^2 N_2)**	**Ar0 (4μC/cm^2 Ar + air)**	**Ar1 (12μC/cm^2 + N_2 500ºC)**	**Ar2 (12μC/cm^2 + N_2 600ºC)**	**Ar3 (12μC/cm^2 + N_2 700ºC)**
P1	Position	398.6	-	-	-	399.4	399.2	399.1
(pyridinic)	FWHM	2.1	-	-	-	1.2	1.7	1.6
P2	Position	399.5	399.7	399.9	399.9	400.3	400.0	
(pyrrolic)	FWHM	1.3	1.9	1.3	1.8	1.1	1.5	
P3	Position	400.3	400.2	400.6	-	401.5	400.6	400.7
(graphitic)	FWHM	1.7	1.7	1.6	-	1.2	1.5	1.5
P4	Position	402.2	-	-	-	402.5	-	-
(oxides)	FWHM	1.5	-	-	-	1.1	-	-
P5	Position	-	-	-	405.2	406.1	407.0	-
(molecular N_2)	FWHM	-	-	-	4.2	1.4	1.3	-
N content		3	2	5.6	0.4	9.6	3.7	1.3
at.% Graphitic N at. %		0.6	0.8	3.9	0	1.8	0.8	0.6

Table 4.1: Parameters used in the fitting of the N1*s* line of nitrogen-doped SWCNT films.

Material	*P1*	*P2*	*P3*	*P4*	*Max N conc.*	*Ref.*
CVD MWCNT	399 eV (graphitic)		401 eV (C-NH2)		~1 at.%	[33]
CVD MWCNT	~399 eV (pyridinic, exact value depends on catalyst type)		~401.8 eV (graphitic, exact position depends on catalyst)		1.2 at.%	[72]
Theory SWCNT	399.04 (N3V) 400.12, (N2V) 400.62 (NV)		401.68 (graphitic)			[72]
CVD MWCNT	399.1 (pyridinic)		401.3 (graphitic, armchair)	402.7 (graphitic, chiral)	1.2 at.%	[73]
CVD MWCNT	399 (pyridinic)		401.5 (graphitic)	404.9 (molecular N_2)		[74]
Theory SWCNT	399.1 (pyridinic, graphite) 399.2 (pyridinic (7,7) SWCNT) 399.5 (pyridinic, (12,0) SWCNT) 398.9 (pyridinic, (10,4) SWCNT)		401.7 (graphitic, graphite) 401.9 (graphitic, (7,7) SWCNT)	403.2 (graphitic, (12,0) SWCNT) 403.3 (graphitic, (10,4) SWCNT)		[73]
CVD MWCNT	398.3 (pyridinic)	399.7 (pyrrolic)	400.8 (graphitic)	403.3 (oxidized N)	6.56%	[23]
CVD MWCNT	398.6 (pyridinic)	400.4 (pyrriolic)	401.4 (graphitic)		10 at.%	[75]
CVD SWCNT	398 (pyridinic)		401 (pyrrolic)		3.6%	[21]
CVD MWCNT	398.4 (pyridinic)	400.1 (pyrrolic)	401.2 (graphitic)	402.9 (oxidized) 404.8 (molecular)	2.59%	[76]
CVD MWCNT	398.6 (pyridinic)	400.5 (pyrrolic)	401.3 (graphitic)	402-405 (oxidized)	2.89 at.%	[77]
CVD MWCNT	398 (pyridinic)		400.8 (graphitic)	403.5 (oxidized N)	8.0at.%	[22]
CVD SWCNT	398.9 ('Non-aromatic NC2 and NC3 structures')		401.0 (graphitic)	403.0 (molecular N2)	13.7at.%	[30]

Table 4.2: Position of N1*s* components found for nitrogen doped nanotubes in the literature.

Material	*P1*	*P2*	*P3*	*P4*	*Max N conc.*	*Ref.*
CVD Graphene	~398.25 – 398.4 399.0 (pyridinic)	~400 (unknown)	400.85-401.4 (graphitic)	397.25 (adsorbed N)	-	[78]
Ion irradiation few layer graphene	398.45 (pyridinic)	399.5 (pyrrolic)	400.92 (graphitic centre)	402.82 (graphitic, valley)	20 at.%	[79]
Ion irrad 4 layer graphene/ SiC(0001)	398.4 (pyridinic)	-	400.6 (graphitic)	402.6 (molecular N_2)	-	[80]
CVD graphene	398 (pyridinic)	400.5 (graphitic)	401.5 (graphitic)	406 (molecular N_2)	3.8 at.%	[81]
CVD graphene	399.3-399.4 (pyridinic)	-	-	-	16%	[82]
CVD Graphene	398.3 (pyridinic)	400.5 (pyrrolic)	-	-	-	[83]
CVD Graphene	-	400.1 (pyrrolic)	-	-	-	[84]

Table 4.3: Position of N1*s* components found for nitrogen doped graphene in the literature.

Upon increasing the N^+ irradiation dose from 20 μC/cm^2 to 100 μC/cm^2 we find a increase in the nitrogen content from 2±1 to 5.6±0.5 at.%, as might be expected. However, the ratio of pyrrolic to graphitic carbon decreases from ~0.9 to ~0.4, indicating that as irradiation progresses there is an increased likelihood that nitrogen will be found in a 'graphitic' substitutional site. This behaviour is very different from that reported in the work of Xu *et al.* for both 3 keV[42] and 300 eV[43] (Fig 4.2) nitrogen irradiation, where increasing irradiation leads, in addition to an overall increase in nitrogen content, to a significant increase in the intensity of peak P_1 (associated with pyrrolic nitrogen by Xu *et al.* but on the balance of the literature, most likely associated with pyridinic nitrogen, as described above). Xu *et al.* explain their results in terms of 'increasing vacancy-vacancy interactions', but it is notable that the ion dose at which there is a noticeable change in the N1*s* lineshape (2 x 10^{15} ions/cm^2 at 300 eV[43]) is above the amorphisation thresholds discussed above. Indeed at lower doses, the N1*s* lineshapes observed by Xu *et al.*[42,43] appear very similar to those which are reported here.

On the basis of the N1*s* spectra it can be concluded that N^+ ion irradiation of SWCNT films leads primarily to the incorporation of nitrogen in substitional 'graphitic' and pyrrolic sites (schematically depicted in Figs. 4.3(a) and 4.3(e) respectively), with some oxidation (formation of N-O_x bonds) and rearrangement to pyridinic bonding after extended exposure to ambient atmosphere. That the N-O_x signal is still relatively small (~10% of the total N content) after more than a month in ambient atmosphere indicates the relatively low reactivity of the nitrogen incorporated into the SWCNT lattice. The 'graphitic' nitrogen is associated with the loss of a single carbon atom from the SWCNT lattice (Fig. 4.3(a)) and the pyrrolic nitrogen with the loss of two carbon atoms (Fig, 4.3(e)), which is compatible with the expectations of defect formation upon ion irradiation of SWCNT structures[61].

A question which arises from the results of nitrogen ion irradiation and discussion above, is the role that defect structures might play in the incorporation of nitrogen atoms into the walls of a SWCNT. To address this question, an alternate route for doping was investigated. As described in Section 4.2, SWCNT samples were irradiated with an approximately equal dose (12±4 $\mu C/cm^2$) of Ar+ ions at 2.5 keV, which is well below the amorphisation threshold. The irradiated samples were then exposed to a flow of N_2 gas at atmospeheric pressure at different temperatures and subsequently investigated by XPS. A single sample was also irradiation with Ar^+ ions to a dose of 4±1 $\mu C/cm^2$ and exposed to ambient atmosphere.

Ar^+ ions, which are inert, are able to create vacancy related defects in SWCNTs[59,61,85] but do not chemically modify the films. Based on the molecular dynamics simulations of Tolvanen *et al.*[61] we expect the primary defects to be monovacancies with a lesser concentration of divacancies and other more complex structures. As described in Chapter 1, reconstruction of a monovacancy defect results in a five membered ring eliminating a pair of dangling bonds leaving a single under co-ordinated carbon atom, while a divacancy can reconstruct to satisfy all dangling bonds forming two pentagons and an octagonal ring[86]. The 'long' bonds in the pentagonal rings are weak and under considerable strain and we may therefore expect that nitrogen atoms would bond across them to form configurations similar to that of Fig. 4.2(b) and 4.2(c). These reconstructed defects can then react with the ambient atmosphere upon exposure to air[36]. Reconstruction of a monovacancy defect results in a five membered ring eliminating a pair of dangling bonds leaving a single under co-ordinated

carbon atom, while a divacancy can reconstruct to satisfy all dangling bonds forming two pentagons and an octagonal ring. The 'long' bonds in the pentagonal rings are weak and under considerable strain and we may therefore expect that nitrogen atoms would bond across them to form configurations similar to that of Fig. 4.3(b) and 4.3(c).

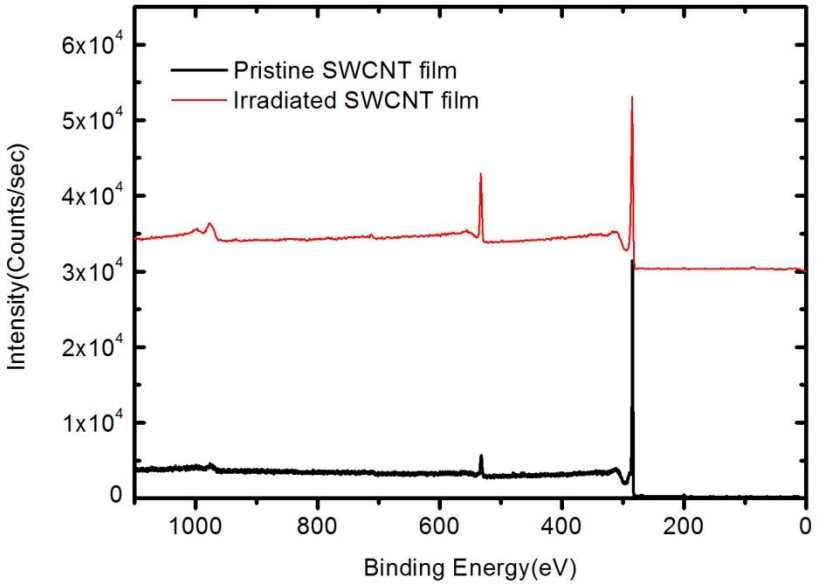

Fig. 4.7: XPS survey spectra from a pristine as-prepared SWCNT film (bottom, black line) and a SWCNT film irradiated by 4±1 μC/cm^2 Ar^+ ions at 2.5 keV and subsequently exposed to air (top, red line). The spectrum of the irradiated film has been shifted upward for clarity. The increase in intensity of the O1*s* signal with respect to the C1*s* signal is readily apparent, indicating oxygen functionalisation of irradiation induced defects.

Fig. 4.7 shows a broad survey spectrum from a SWCNT sample subjected to an Ar^+ ion dose of 4±1 μC/cm^2 and subsequently exposed to ambient atmosphere compared with that from a pristine SWCNT sample with no subsequent treatment. As expected from the work of Houchin[36], there is a substantial increase in the O1*s* signal associated with the binding of atmospheric oxygen to the reactive defect sites created through the irradiation process. However, a close inspection of the N1*s* region, Fig 4.8, unexpectedly shows the presence not only of a broad (FWHM 4.2 eV) peak at a binding energy of 405.2±0.1 eV which can be associated with physisorbed molecular nitrogen but a narrower (FWHM of 1.76 eV – similar to the fit components used above) peak at a binding energy of 399.9±0.1 eV. On the basis of

the discussion above, we can assign this peak to nitrogen in a pyrrolic configuration. The simplest pyrrolic configuration involves the removal of two carbon atoms coupled with the addition of one nitrogen atom (Fig 4.3(e)), which suggests that molecular nitrogen from the ambient atmosphere has reacted with divacancy (or larger vacancy cluster) sites, dissociated and the nitrogen atomic radicals combined with the vacancies to form a pyrrolic structure.

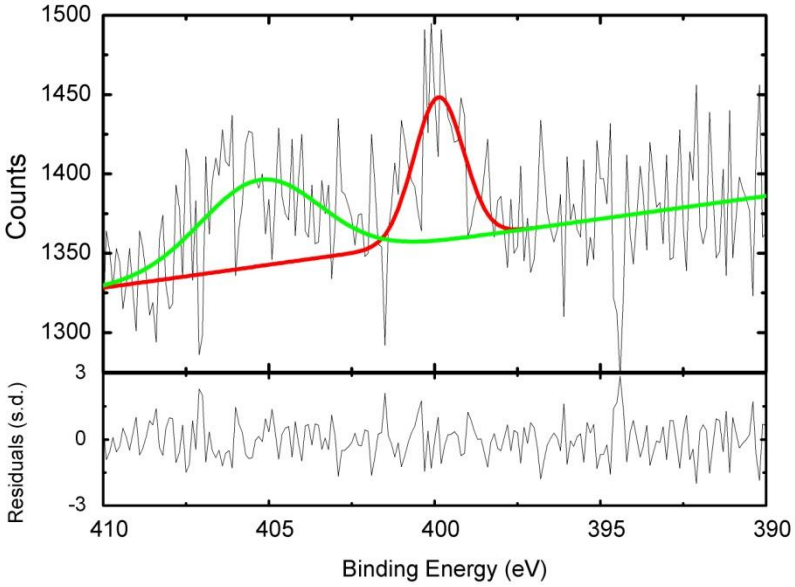

Fig. 4.8: N1*s* core level spectrum of Ar-irradiated SWCNT film subjected to an ion-dose of 4±1 μC/cm^2. The top panel shows the data (black line) and associated fit (coloured lines), whilst the bottom panel shows the residuals associated with the fit.

In a theoretical study of nitrogen-doped nanotubes containing vacancy structures, Fujimoto and Saito[87] came to the conclusion that pyridinic nitrogen next to a monovacancy (often termed an N1V defect), which would be formed by nitrogen addition across one of the long bonds of the 5-8-5 divacancy, was the most energetically favourable structure. For defect structures including more nitrogen substituents three pyridinic nitrogen atoms surrounding a vacancy was favoured, although if only two nitrogen atoms were present one adopted each of the pyridinic and pyrrolic structures. However, it should be noted that the size of the supercell chosen was extremely small (with the result that the defect repeated every two unit cells) and such a small structure is likely to introduce spurious defect-defect interactions. It has been shown by Hunt and Clark[88] that erroneous results can be obtained from theoretical investigation of carbon nanotubes if incorrect supercell size and boundary

conditions are selected. In a related nitrogen-graphene system the same authors[89], found that the lowest formation energy was associated with substitutional nitrogen in pristine graphene. In the presence of defects, the most energetically favourable structure (in terms of energy cost per nitrogen atom) was a structure involving three pyridinic nitrogen atoms surrounding a monovacancy defect, with no reconstruction (often termed an N_3V defect). However, this work was criticised by Hou and co-workers in a subsequent study[60], again on the grounds of insufficient supercell size. Although several of the results found by Hou *et al.* were similar to those of Fujimoto and Saito (such as the preferential occupation of a pyridinic site in the N_1V – one nitrogen next to one vacancy – structure) they found that the optimum position of nitrogen dopants near a reconstructed divacancy was in a five-membered ring (pyrrolic configuration). They also came to the conclusion that in the presence of defects the formation energy associated with nitrogen incorporation into the graphene lattice could become exothermic (that is, thermodynamically favourable, rather than metastable) with the result that the presence of defects would enhance nitrogen doping.

The observation of pyrrolic nitrogen in Ar^+-irradiated SWCNTs exposed to ambient atmosphere suggests an endothermic addition of nitrogen, compatible with the theoretical results of Hou *et al.*[60], as is the pyrrolic nature of the nitrogen. However, the exact, thermodynamically stable, structures present by Hou *et al.* for the pyrrolic nitrogen may not be accessible for room temperature incorporation of nitrogen due to the extensive rearrangement of bonds which would be expected. We should note, though, the importance of curvature in determining the exact details of bonding in doped CNTs – for example, in a theoretical study of nitrogen adsorption on monovacancy defects in curved graphene sheets Srivastava *et al.*[90] showed that nitrogen adsorbed on low curvature sheets, on which the monovacancy defect cannot reconstruct due to the strain energy barrier, bound substitutionally while if there was sufficient curvature for vacancy reconstruction the nitrogen was co-ordinated to two carbon atoms, although the precise bonding details were unclear. Hence, the further theoretical investigation is required to unambiguously determine the likely bonding configuration in the irradiated N_2-exposed SWCNTs.

The N1*s* spectra from SWCNT samples irradiated with Ar^+ ions and exposed to N_2 at elevated temperatures are shown, with the corresponding fits and residuals, in Fig. 4.9. There is clearly a strong evolution of the lineshape with temperature, indicating that the various nitrogen configurations have differing thermal stabilities. The total nitrogen content and

contribution of the various chemically bound configurations is presented in Fig. 4.10. It is clear that annealing at the relatively low temperature of 500°C leads to a significant increase in nitrogen from that found by exposure at room temperature. Indeed, samples produced under these conditions have the largest nitrogen content found in the work reported in this Chapter. It is also notable that nitrogen in the pyrrolic configuration is the dominant species and that, from the spectra presented in Fig. 4.9, that there is a considerable concentration of molecular nitrogen trapped within the nanotube film. With increasing annealing temperature the molecular nitrogen disappears rapidly and the concentration of the chemically bound nitrogen species decreases significantly. However, while the concentration of pyridinic and graphitic nitrogen remain in approximately the same ratio (of almost 1:1) the relative abundance of the pyrrolic nitrogen decreases strongly. From this behaviour we can draw the conclusion that the pyrrolic configuration is the least thermodynamically stable of the three pure chemically bound nitrogen species reported here, in general agreement with the observations reported by Xu and co-workers[42,43]. The relative instability of the pyrrolic species found in the annealing experiments may go some way to explaining the decreasing relative concentration of pyrrolic to graphitic nitrogen in the N^+ ion irradiated samples with increasing ion dose, reported above – as irradiation continues the less stable species is more likely to be either preferentially sputtered or undergo an ion-stimulated structural re-arrangement to a lower energy configuration.

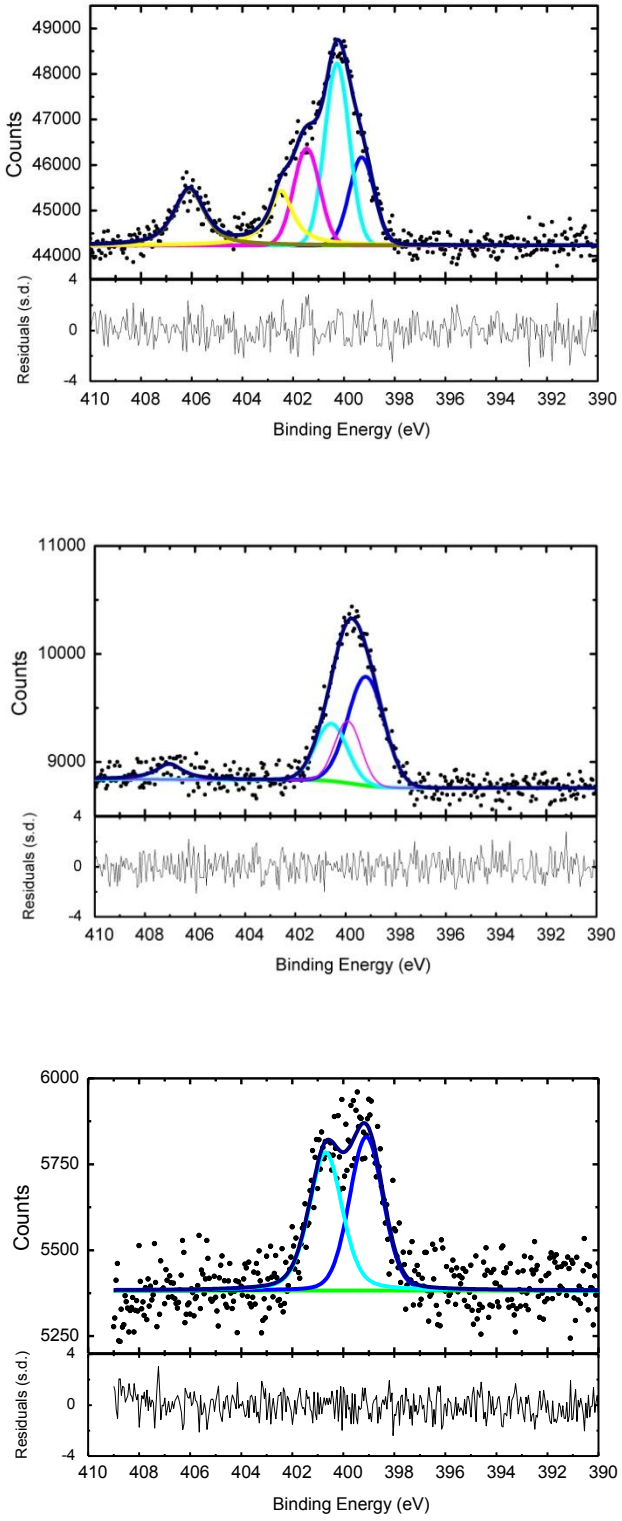

Fig. 4.9: N1*s* spectra and associated fits from SWCNT films irradiated with Ar^+ ions followed by exposure of nitrogen atmosphere at 500 °C (a), 600 °C (b) and 700 °C (c).

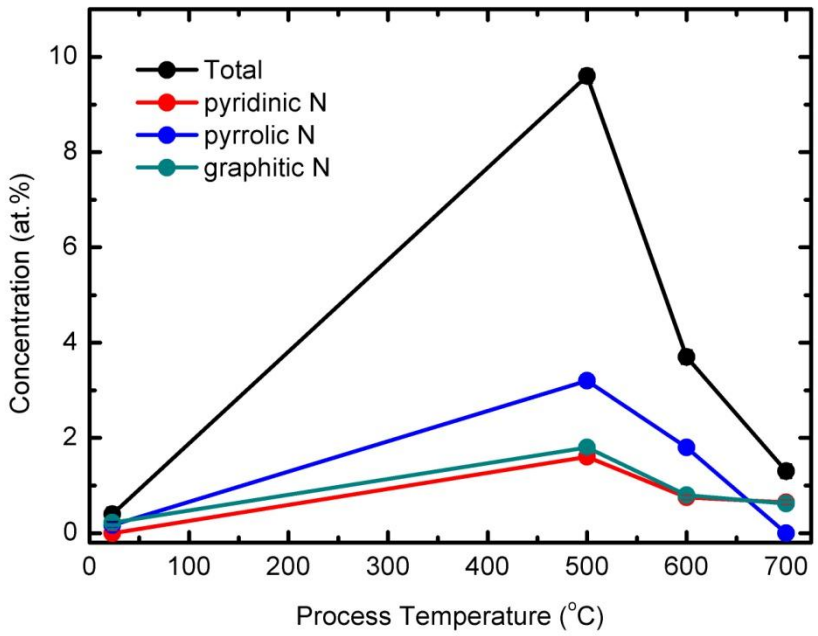

Fig. 4.10: Variation of (bound) nitrogen concentration with process temperature for SWCNT films irradiated with Ar^+ ions and exposed to N_2 gas. The lines are a guide to the eye.

It is clear from the N1*s* spectra that the already established N^+ ion irradiation approach is the most successful in producing samples in which graphitic nitrogen is the dominant nitrogen form in the SWCNT lattice. However, the new approach of inert (Ar^+) ion irradiation followed by annealing has the advantage of producing a much higher total nitrogen content as a function of ion dose (and hence damage, as discussed below) and, through choice of annealing temperature, gives significant scope for controlling the relative concentration of pyrrolic nitrogen which is important in determining the chemical activity (or otherwise) of this nitrogen species.

4.3.1.2 C1s spectra from nitrogen doped SWCNTs

C1*s* spectra are able to provide valuable insight into the chemical state, order and electronic structure of the nitrogen doped SWCNT films discussed in the previous section and, as such a series of spectra as a function of N^+ ion irradiation are presented in Fig. 4.11. A similar C1*s* series, is shown as a function of temperature at which the films were annealed in N_2 after Ar^+ irradiation in Fig. 4.12. The spectra were fit using the same approach described for the N1*s* spectra detailed above, in which the smallest number of physically realistic peaks (Gaussian-Lorentzian sums apart from a single Doniac-Šunjić lineshape used to model the graphitic carbon, as in previous work[57,91]) were used in combination with a Shirley background. A typical fit of the C1*s* spectrum obtained from a pristine SWCNT film is shown in Fig. 4.13 and that from a relatively heavily nitrogen doped film in Fig. 4.14. The fit parameters for all the C1*s* spectra analysed are reported in table 4.4, in which errors in peak position are typically ±0.05 eV and those in FWHM ±0.1 eV.

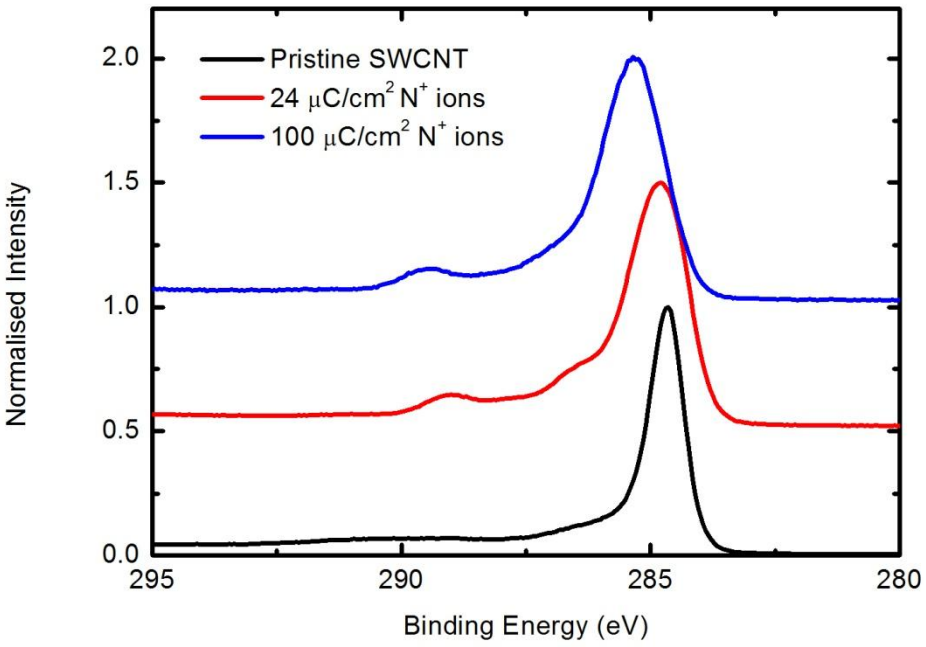

Fig. 4.11: C1*s* spectra from pristine and N^+ ion irradiated SWCNT films.

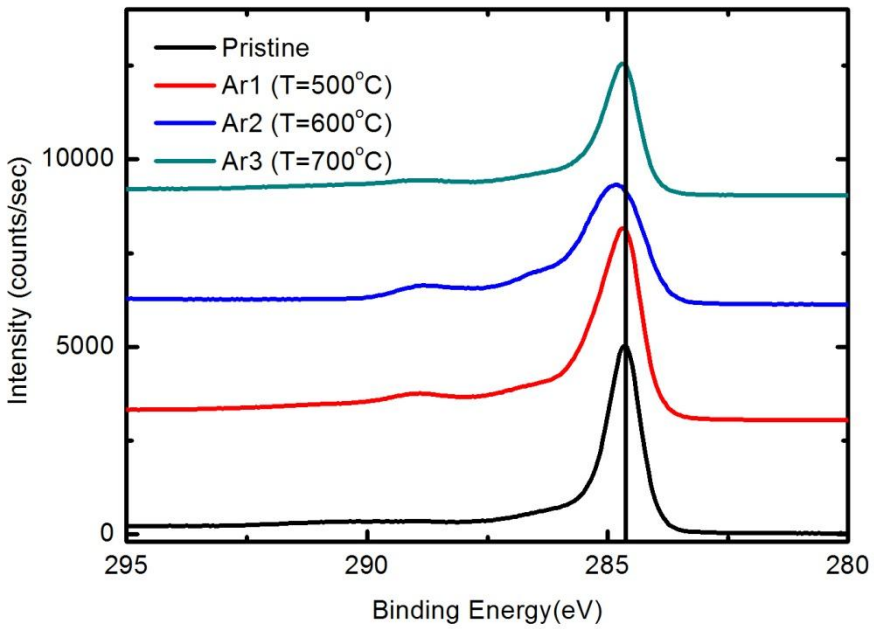

Fig. 4.12: C1*s* spectra from pristine and Ar^+ ion irradiated SWCNT films annealed under an N_2 gas flow at various temperatures.

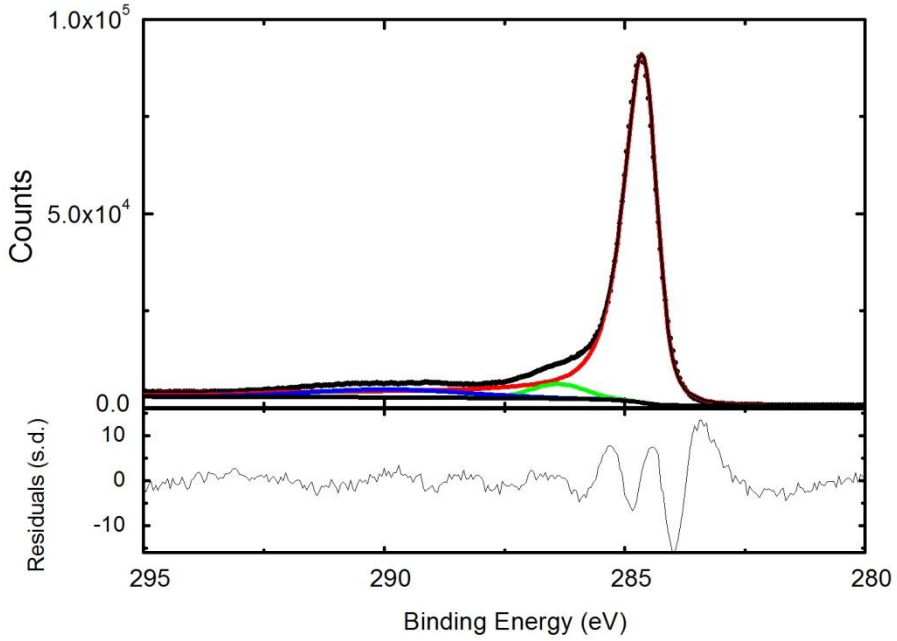

Fig 4.13: Fit to C1*s* spectrum of a pristine (as-introduced) SWCNT film. The bottom panel displays the fit residuals in units of standard deviation of the data.

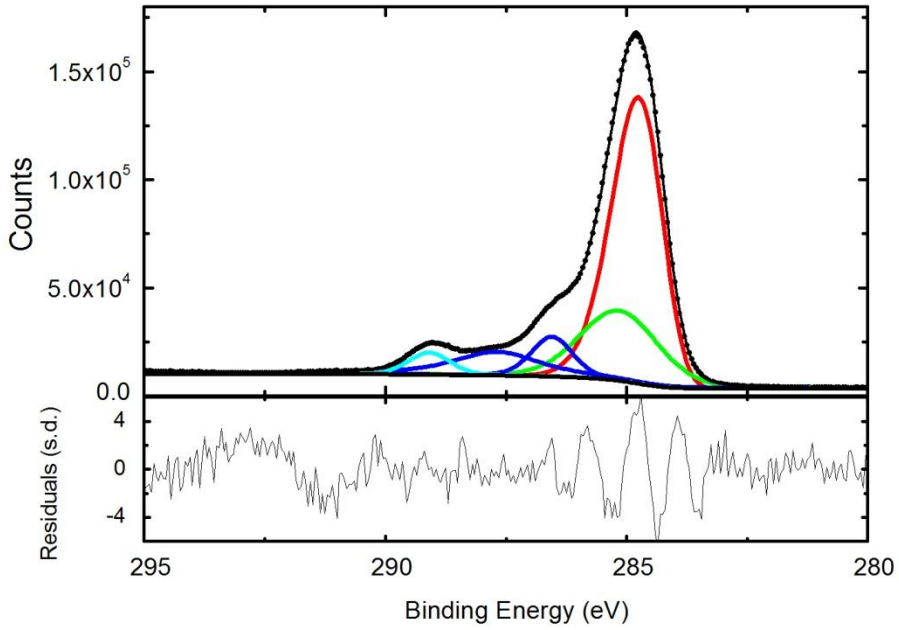

Fig. 4.14: Fit to C1*s* spectrum obtained from a SWCNT irradiated with 2.5 keV N^+ ions to a dose 24 μC/cm^2. The bottom panel displays the fit residuals in units of standard deviation of the data.

It is clear from the summary presented in Table 4.5 that the position of the main C1*s* line, associated with sp^2 bound carbon is not constant from sample to sample. Maldonado *et al.* found that upon nitrogen doping of CVD grown MWCNTs that there was an upward shift in the C1*s* binding energy which was independent of nitrogen content, which they attributed to disorder[75]. However, there is not such correlation in the data here. However, upon doping SWCNT samples one would expect that the low density of states close to the Fermi level would lead to a significant upward shift in C1*s* binding energy for *n*-type doping (and a corresponding downward shift for *p*-type doping). Such behaviour was observed in alkali metal doped SWCNT films by Larciprete *et al.* where the introduction of the alkali metal and subsequent transfer of (negative) charge to the SWCNTs produced an upward shift in C1*s* binding energy[92]. In order to explore the relationship between nitrogen doping and C1*s* binding energy shift the position of the sp^2-related C1*s* component is nitrogen plotted against total nitrogen content for the samples studied in this work in Fig. 4.15. When compared with total nitrogen concentration the C1*s* line position shows significant scatter. Moreover, the

samples labelled N1 and Ar2 in Table 4.5, produced by different approaches have binding energies for the C1*s* sp^2 component which agree closely, yet the total nitrogen content of these samples is strongly divergent. This analysis suggests that there is no well-defined relationship between the total amount of nitrogen and the C1*s* binding energy, which one might expect from a naïve expectation of the effects of nitrogen doping.

Peak	**Position and width (eV)**	**Pristine**	**N1 (24μC/cm^2 N_2)**	**N2 (100μC/cm^2 N_2)**	**Ar0 (4μC/cm^2 Ar + air)**	**Ar1 (12μC/cm^2 + N_2 500°C)**	**Ar2 (12μC/cm^2 + N_2 600°C)**	**Ar3 (12μC/cm^2 + N_2 700°C)**
C1 (sp^2)	Position	284.63	284.76	285.12	284.60	284.72	284.76	284.66
	FWHM	0.8	1.23	1.41	1.41	1.0	1.30	0.8
	α	0.13	0.08	0.14	0.13	0.10	0.08	0.05
C2 (sp^3/ C-N graphitic, pyrindinic)	Rel. Position	-	0.40	0.48	-	0.87	0.53	0.48
	FWHM	-	1.9	0.9	-	0.8	1.2	1.6
C3 (C-O-C, C-OH)	Rel. Position	1.75	1.78	1.59	-	1.71	1.69	1.7
	FWHM	1.4	1.0	1.0	-	1.0	1.2	1.7
C4 (epoxy, C-N)	Rel. Position	-	2.84	2.37	2.39	2.57	3.1	4.0
	FWHM	-	2.1	1.0	1.5	1.2	2.1	2.4
C5 (plasmon)	Position	5.4	4.3	4.4	3.6	4.2	4.2	6.1
	FWHM	3.8	1.0	2.4	3.1	1.7	1.1	4.0
N content at.%			2	5.6	0.4	9.6	3.7	1.3
Graphitic N at. %			0.8	3.9	0	1.8	0.8	0.6

Table 4.5: Summary of the parameters used in fitting the C1*s* spectra obtained from pristine and nitrogen-doped SWCNT films.

As discussed in Section 4.1, Robertson and Davis[53] have argued, via a simple chemical bonding model, that only nitrogen incorporated into a carbon nanotube in a graphitic geometry should lead to a donor state. Recognising the variation in relative concentration of graphitic nitrogen reported in Section 4.3.1.1, the position of the main C1*s* core line is plotted against the concentration of graphitic (rather than total) nitrogen in Fig. 4.16. The scatter which was evident when plotting C1*s* sp^2 binding energy against total

nitrogen content in Fig. 4.15 is much reduced and shows (as far as the limited range of data allows) a linear relationship. Most importantly, the samples with the same C1*s* sp^2 binding energy have the same concentration of graphitic nitrogen to within error and therefore closely coincide in the plot. Therefore, it is demonstrated for the first time that it is possible to relate the position of the main C1*s* core level component to the content of graphitic nitrogen within a carbon nanotube sample. Moreover, since the samples produced in this work generally contain nitrogen in a variety of bonding configurations, it is clear that the *n*-type doping originating from the nitrogen bound in a graphitic state is dominant.

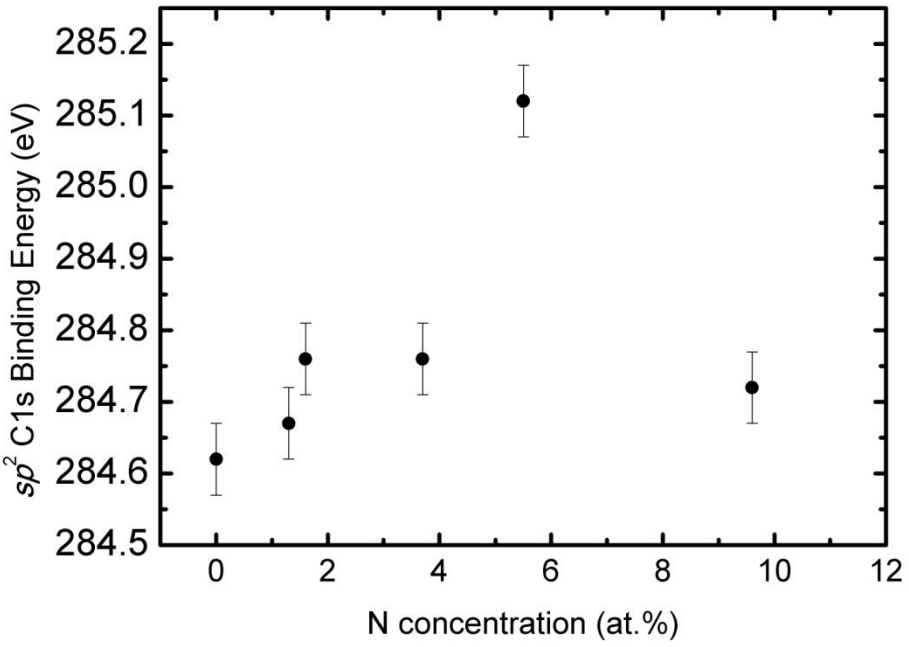

Fig. 4.15: Binding energy of the C1*s* component associated with sp^2 bonding and the total N concentration. It can be seen that there is no well-defined relationship between these two properties.

In order to assign the component labelled C2 in table 4.5, we recognise that in disordered or defective graphitic systems a component associated with sp^3 bound carbon usually appears between 0.5 to 1.3 eV higher binding energy that carbon in an sp^2 configuration[62,93,94]. Whilst it may be tempting to associate the C2 component with sp^3 bound carbon alone, there can be a unresolved contribution to this peak originating from carbon bound to nitrogen within the graphitic nanotube lattice. For example, using CVD Luo *et al.*[82]

have managed to produce nitrogen-doped graphene samples with only pyridinic nitrogen species, as evidenced by a single N1*s* line at ~399.3 eV, the accompanying C1*s* spectra could be decomposed into two lines – the main, graphitic line at 284.35 eV associated with graphitic carbon and a peak at 285.5 eV which they attributed to carbon bound to pyridinic nitrogen. Similarly, Lim *et al.*[95] find a C1*s* component which they attribute to carbon bound to graphitic nitrogen at a binding energy 1.1 eV above the graphitic component (the poor resolution of the peaks in that work will affect the accuracy of this difference). Although the pyridinic C-N peak is at a higher binding energy relative to the sp^2 carbon peak than the C2 component, it is likely that it would not be readily resolved from and sp^3 contribution to the fits presented here – the difference in energy between the sp^3 line reported in the literature and the C-N pyridinic C1*s* component is in the range of 0.35-0.65 eV, which is close to the resolution of the XPS measurements presented in this thesis.

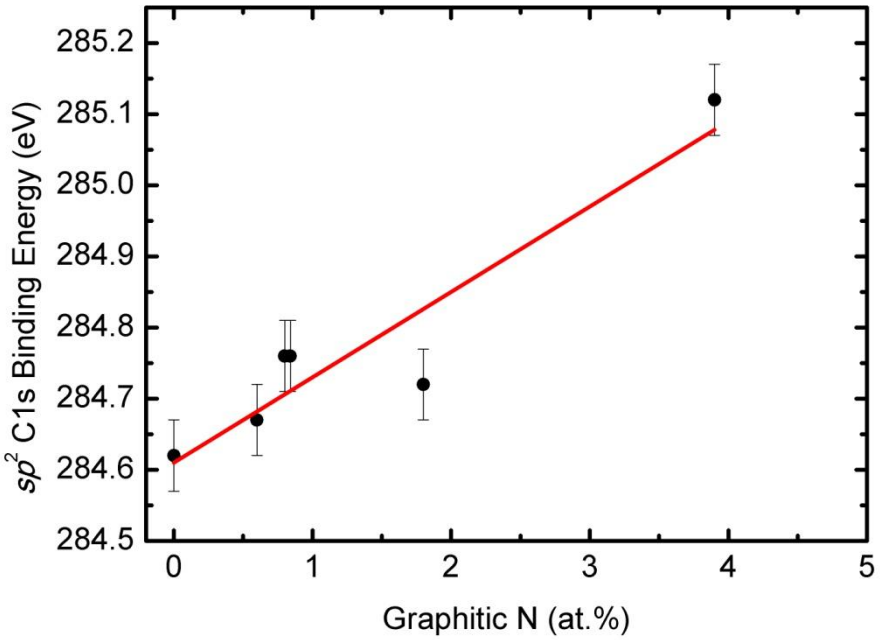

Fig. 4.16: Variation of the sp^2 C1*s* component at the concentration of nitrogen in 'graphitic' sites.

On the basis of previous work (see ref. [36] and references therein) components C3, C4 and C5 may be attributed to the presence of ether (O-C-O) and/or alcohol (C-OH) groups, epoxy groups and the π plasmon loss, respectively. However, it should be noted that in amorphous CN_x films a C1*s* component associated with C-N bonding is found at ~2.4 eV

above the main sp^2 carbon line in addition to the component at ~1.3 eV[96]. As a result, the component C4 is also likely to contain contributions from C-N (possibly pyrrolic) bonds. It is clear from these considerations that the N1*s* line is the most valuable in understanding the bonding configuration within the doped SWCNT films.

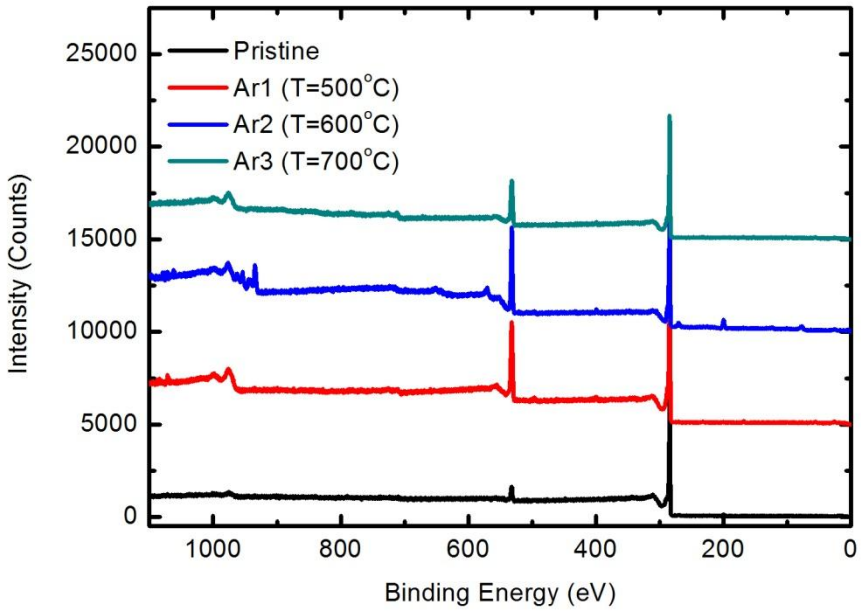

Fig. 4.17: Survey spectra from SWCNT films irradiated with Ar^+ ions and annealed under N_2 flow at various temperatures, compared with a pristine SWCNT film.

Houchin[36] has previously shown that the binding energy associated with the π plasmon loss changes significantly with the presence of defects within a SWCNT film and thus, the differences in relative position with respect to the main sp^2 line reported in Table 4.5 are likely to reflect the differences in disorder and doping between the samples. The presence of oxygen–related C1*s* components arises from the fact that the samples underwent XPS analysis *ex-situ* and, as a result, were transported through air. Consequently, all samples show an unavoidable presence of oxygen in XPS data (a peak at about 532 eV binding energy, as seen in the survey spectra presented in Fig. 4.17). The observation of a significant O1*s* signal even in a pristine sample is likely to result from the physisorption and chemisorption of oxygen-containing species from the ambient atmosphere. Indeed, Houchin[36] demonstrated that SWCNT samples annealed in UHV such that there was a negligible oxygen signal in the

XP spectra displayed a significant O1*s* line after a brief (70 minute) exposure to air and that the C1*s* spectra showed a small increase in intensity between ~286-289 eV.

4.3.2 Raman spectroscopy of N-doped SWCNTs

4.3.2.1 Intensity Ratio of D, G and G' bands

Raman spectroscopy has emerged as a key technique for the investigation of carbon nanomaterials (see e.g. Ref. [97] for a review) and is often used as an almost routine tool to characterize nanotube materials. As such it has been logical to apply it to the study of nitrogen-doped CNTs and graphene. The nature of the graphene Raman spectrum and the origin of the modes in each of the energy regions is described in Chapter 2, Section 2.3.2. An overview of spectra from undoped, and N ion irradiated samples exposed to ion doses of 20±2 and 100±5 μC/cm^2 (labelled N1 and N2, respectively) is shown in Fig. 4.18, and that for Ar^+ irradiated samples annealed in N_2 in Fig. 4.19. It can be seen that in both cases, upon ion irradiation mediated nitrogen doping, there is a decrease in the increase in the relative intensity of the defect-related double-resonant *D* (~1330 cm^{-1}) band and a decrease in intensity of the *G'* (~2670 cm^{-1}) band (which is also double resonant, but visible in the absence of defects/disorder) with respect to the 'graphitic' *G* (~1580 cm^{-1}) band. These changes are characteristic of an increasing degree of disorder within the sample and a similar evolution of the Raman spectrum of carbon nanotubes has been observed in the γ irradiation of SWCNTs[98] and as a result of the increasing boron doping of MWCNTs[99] indicating that such changes are independent of the precise nature of the 'disorder' or symmetry breaking introduced into the nanotube lattice.

The result of fitting the *G* and *D* band regions of the Raman spectra of pristine N doped SWCNT samples is presented in Table 4.6, with a example fits and the associated residuals presented in Fig. 4.20. The spectral region containing the *D* and *G* bands was fitted with a series of Lorentzian functions with the number chosen to reflect a compromise between the theoretically expected bands and the spectral broadening which is associated with both instrumentation and dispersion in the diameter and chirality of the SWCNTs in the samples. The SWCNT *D* band from an individual is, for example, expected to consist of two closely spaced components with the exact splitting and position being a function of the Chiral

vector (see Chapter 1, Section 1.1) of the nanotube and the excitation energy in the Raman experiment[100]. Since it is clear from the RBM region of the Raman spectra (see below) that we are sampling a number of tube diameters/chiralities (all those in resonance with the incident or outgoing photon energy) we would expect the *D* band to be the superposition of a large number of closely spaced Lorentzian peaks. At present there is not enough data in the literature to determine the precise location of those bands within the overall peak envelope and thus it is most appropriate to fit the *D* band with a single Lorentzian function.

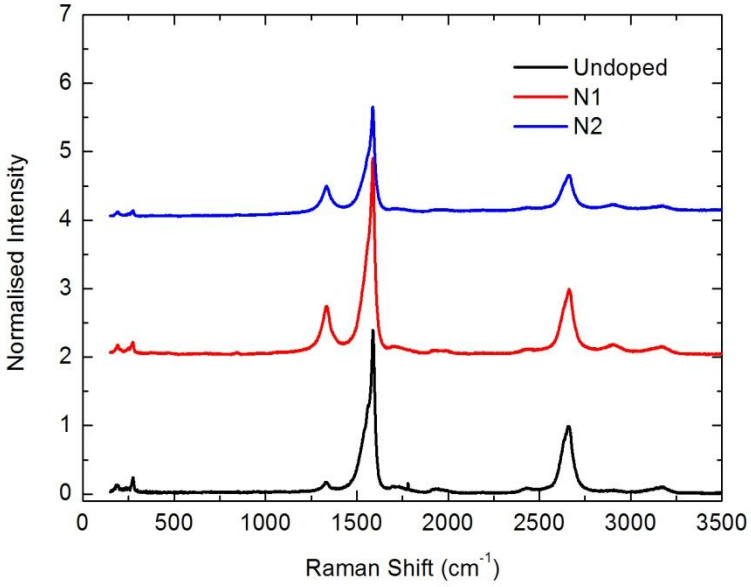

Fig. 4.18 Raman spectra of undoped SWCNTs, N doped SWNTs irradiated with N^+ ions to doses of 20±2 µC (N1) and with 100±5 µC (N2) respectively.

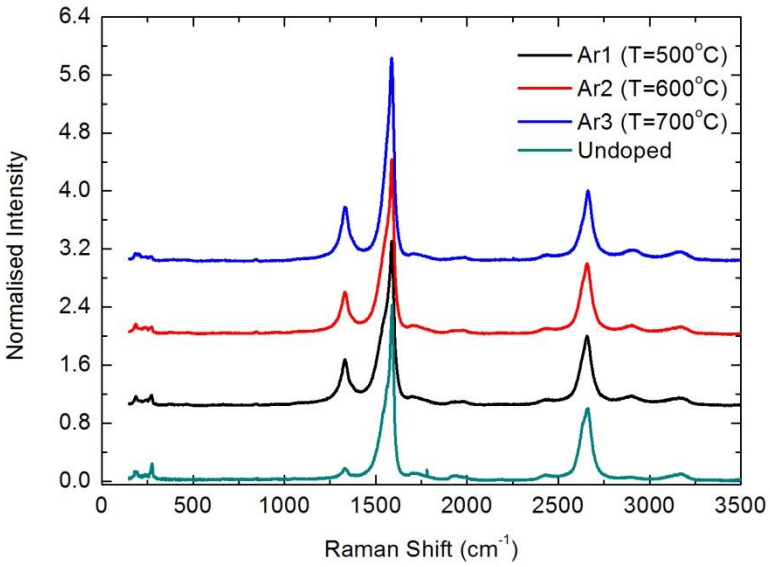

Fig. 4.19 Raman spectra of undoped and N-doped SWCNTs, the latter produced by Ar^+ ion irradiation and subsequent annealing in N_2 gas (at the temperature specified).

Sample	*D* Band Position (cm^{-1})	*G* Band position (cm^{-1})		FWHM (cm^{-1})			I_D/I_G
Pristine SWCNTs	1330±1	(*G*-) 1561±1	(*G*+) 1589.3±0.5	(*D*) 75±2	(*G*-) 24±4	(*G*+) 13±1	0.06±0.01
N1 (20μC)	1332.6±0.2	1560±1	1588.9±0.2	60±1	24±4	16±1	0.31±0.03
N2 (100μC)	1333.7±0.3	1560±1	1589.3±0.3	64±1	26±8	19±1	0.40±0.04
Ar1 (500˚C)	1332±1	1559±2	1588.4±0.4	62±20	26±10	17±2	0.22±0.02
Ar2 (600˚C)	1330±1	1555±2	1587.0±0.6	100±20	30±6	16±2	0.17±0.02
Ar3 (700˚C)	1331±3	1561±2	1588.5±0.6	72±20	47±8	21±3	0.41±0.01

Table 4.6: Summary of key parameters obtained from fits to the *D* and *G* bands of the N-doped SWCNT samples.

The single Raman-active *G* band, found at 1582cm^{-1} in pristine graphite is predicted to split into six distinctive components due to the symmetry breaking and quantum confinement effects which occur when a single graphene sheet is (conceptually) rolled into the form of a nanotube[101]. It is found that in practice the *G* band spectra of individual semiconducting nanotubes can be fit with four Lorentzian components due to the small energy difference between two pairs of modes, preventing them from being resolved, similarly the broadening associated with electron-phonon coupling results in two peaks being sufficient to fit the *G* band region in a metallic nanotube[102]. The *G*$^-$band components are usually split into two groups, those at higher energy labelled G^+ and those at lower energy G^-. The difference in energy of these modes arises from the partial rehybridisation of the sp^2 carbon bonds associated with the curvative of the nanotube – the rehybridisation leads to a softening of modes which primarily lowers the frequency of vibrational modes with atomic displacements perpendicular to the nanotube axis[103]. Both *G*+ and *G*- modes show a stiffening with increasing diameter, although this is naturally much more pronounced for the *G*- branch. It should also be noted that the relative intensity of the two branches also varies significantly as a function of chirality[103]. Clearly, the *G* band region of Raman spectra obtained from an ensemble, rather than individual, SWCNTs is potentially complex and will involve a number of closely-spaced, unresolved peaks.

In order to determine the appropriate number of individual Lorentzian components to fit the *G* band an empirical approach was adopted, which involved finding the minimum number of peaks which could fit the dataset which minimised systematic excursions in the residuals. As a result of this process it was found that the optimum number of distinct peaks required to fit this region was five. It is notable that the lowest energy peak (at 1539±3 cm^{-1}) is broader than the others (40 cm^{-1} in the pristine sample compared with 13-24 cm^{-1} for the other peaks) and it is therefore possible that this peak is associated with metallic SWCNTs since the low energy component is typically much broader due to electron-phonon coupling[102]. As a result of electron-phonon coupling this feature is often fit with an asymmetric Breit-Wigner-Fano (BWF) lineshape, however, in the absence of definitive attribution of the origin of this component and bearing in mind the fact that it is likely to be composed of a superposition of closely spaced lines it was decided to retain the same overall lineshape as the other peaks. During the fitting process the number of peaks was the only parameter which was fixed with all other quantities (such as peak position, width and intensity) allowed to vary freely.

The dependence of the G^- mode energy on nanotube diameter[103,104] means that splitting between the largest peaks associated with the G^+ and G^- groups in Table 4.6 can be related to the mean diameter of the nanotubes in resonance with the laser light[101], using the relation[104]

$$d_t = \sqrt{\frac{-C}{\omega_G^- - \omega_G^+}} \qquad (4.1)$$

where C is a constant equal to 45.7 $nm^2\,cm^{-1}$ for metallic nanotubes and 79.5 $nm^2\,cm^{-1}$ for semiconducting SWCNTs and $\omega_G^{+/-}$ are the Raman shifts of the G^+ and G^- bands. Applying this formula we find an average diameter of 1.28 nm for metallic nanotubes and 1.69 nm for semiconducting nanotubes. These values are in very good agreement with the mean diameters of metallic and semiconducting nanotubes which should, from examination of a Kataura plot[104], be in resonance with the laser light (532 nm, 2.33 eV). This level of agreement provides strong justification for the fitting approach which has been adopted here.

The ratio between the intensity of the defect-induced *D* band and the graphitic *G* band has often been used as a means of qualitatively measuring the perfection (or at least the degree of disorder or symmetry-breaking doping) within a carbon nanotube sample[105,106,107]. For example, Zhi *et al.*[106] related the relative intensity of the *D* to the *G* band to the disorder dependent upon the concentration of N and B in boron carbonitride nanotubes. The ratio of the areas of the *D* and *G* bands, I_D/I_G found from analysis of the Raman data in Figs. 4.18 and 4.19 are presented as a function of the nitrogen content (determined by XPS) in Fig 4.21. It is clear that the relative *D* band intensity does not vary monotonically with nitrogen content, as might be expected, indeed it would be reasonable to conclude that there is no correlation between N content and I_D/I_G. A similar lack of correlation (not shown) is found between the I_D/I_G ratio and the content of any of the individual nitrogen species (pyrrolic, graphitic or pyridinic).

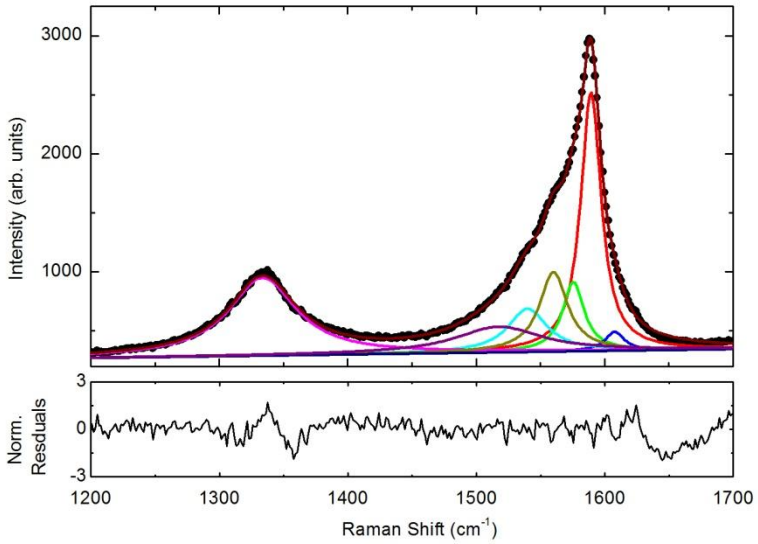

Fig. 4.20: A typical fit to the *D* and *G* band region of an SWCNT sample, with residuals (in units of standard deviation) plotted in the lower panel. The spectrum shown was obtained from an SWCNT sample irradiated with N^+ ions to a dose of 100±5 μC.

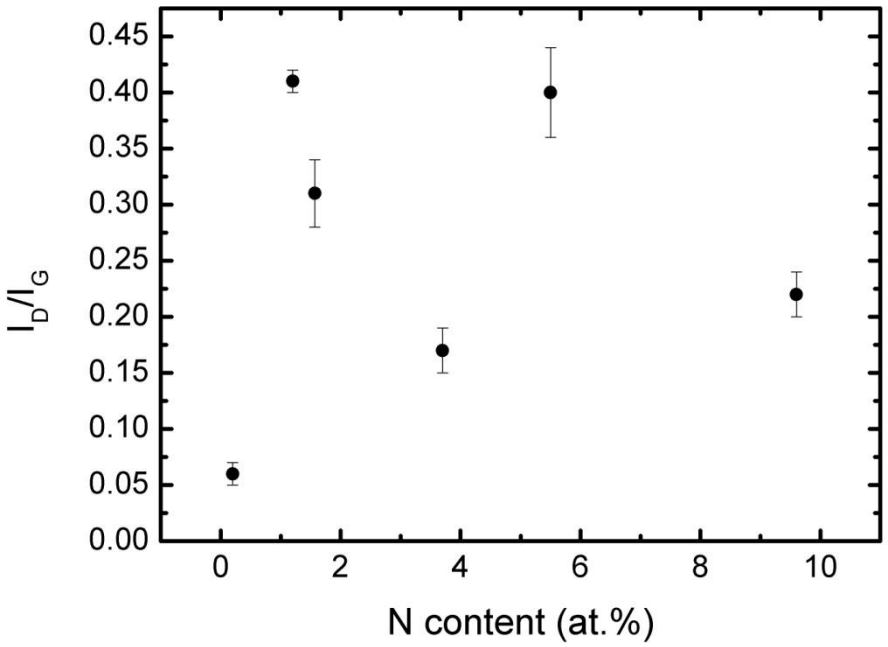

Fig. 4.21: A plot of the ratio of *D* and *G* band intensities as a function of nitrogen content determined by XPS. Note the lack of any well-defined correlation.

There have been a number of studies which have reported the I_D/I_G ratio in nitrogen doped carbon nanotubes. Bulusheva *et al.*[74] found a monotonic increase in relative *D* band intensity as a function of the graphitic and pyridinic N content in CVD grown MWCNTs, but that the variation was non-linear with a smaller rate of increase with increasing N concentration. Similarly Sharifi and co-workers[108] suggest, from their results on N-doped MWCNTs grown by CVD with different precursors, that there is a linear increase in the I_D/I_G ratio with total N concentration to a value of 5%, whereupon the relative *D* band intensity saturates. They argue that the ratio of pyridinic to pyrrolic nitrogen (determined from XPS) begins to saturate at this point and that, therefore the *D* band intensity may be more sensitive to one substituent type than another. However, the number of data points is relatively small and their conclusions are at odds with the data presented here, therefore any conclusions which Sharifi *et al.* draw must be treated as tentative.

In their study of N-doped graphene Podila *et al.*[81] correlated Raman spectra with XPS data and found that the intensity of the defect-related *D* band did not scale with the density of defects, but rather with their *type*, with samples possessing significant concentrations of non-graphitic nitrogen showing enhanced *D* band intensity. A lack of correlation between N concentration and I_D/I_G ratio was observed in a similar combined XPS and Raman study by Zhao *et al.*[109] in MWCNTs irradiated with 200 eV N^+ ions, providing support to the concept that the relationship between N ion concentration and relative *D* band intensity is more complex than simply one of overall concentration.

Recognizing that activation of the *D* band can occur due to the presence of *any* type of disorder, we plotted I_D/I_G ratio against the ratio of non-sp^2 to sp^2 carbon determined from the C1*s* line found measured by XPS, (Fig 4.22). The main sp^2 carbon line can be associated with carbon in the unperturbed lattice whilst non-sp^2 bound carbon is naturally associated with disorder from all forms (including defects, adsorbates, dopants). From Fig. 4.22 it is clear that there is a general trend of increasing I_D/I_G ratio with non-sp^2:sp^2 ratio, which supports the concept that the relative intensity of the *D* band is a function of order originating from all sources, not simply from the presence of dopants. Hence, from the I_D/I_G ratios presented in Table 4.6 we can conclude that for direct ion irradiation the overall defect density increases with ion dose and is larger than that in samples which are irradiated with Ar^+ ions and annealed in N_2 gas. Moreover, for the Ar^+ irradiated SWCNTs annealed in N_2 gas the level of disorder when increasing annealing temperatures from 500˚C to 600˚C decreases slightly as

defects are annealed out, but that annealing at 700˚C induces additional disorder (reflected in both I_D/I_G and sp^3:sp^2 ratios) presumably due to thermal decomposition. Hence, of the two methods Ar^+ irradiation followed by annealing at temperatures up to 600˚C produces the samples with the highest concentration of chemisorbed N and the lowest defect densities.

It should be noted that it has been recognized that the intensity of the *G* band is itself not constant when disorder is introduced into graphitic materials. Originally it was argued by Maultzsch and co-workers[99,110] that the *G* band also originates from a double-resonance process associated with defects, but that it can be activated with significant intensity at much lower defect densities. Later work by Kuzmany's group[98] showed that there was no dispersion of the *G* band with photon energy in either pristine or defective SWCNTs and that a double-resonance process is not an appropriate explanation for the behaviour of *G* band intensity. As a result they presented a qualitative argument that the presence of defects relaxes the q~0 selection rule (i.e., that phonons must be close to the Brillouin Zone centre due to the small momentum associated with photons) which both broadens the *G* band and (moderately) increases its intensity. Jorio *et al.*[97] take the middle ground and are of the opinion that the *G* band originates from a single-resonance process in defect-free SWCNTs but that in the presence of defects it may acquire double-resonance character. Although the origin of the response of *G* band intensity to defects still requires a better understanding, it is clear that the ratio I_D/I_G may, under some circumstances, be a poor measure of disorder and that comparison should instead be made with the non-defect mediated double-resonant *G'* mode.

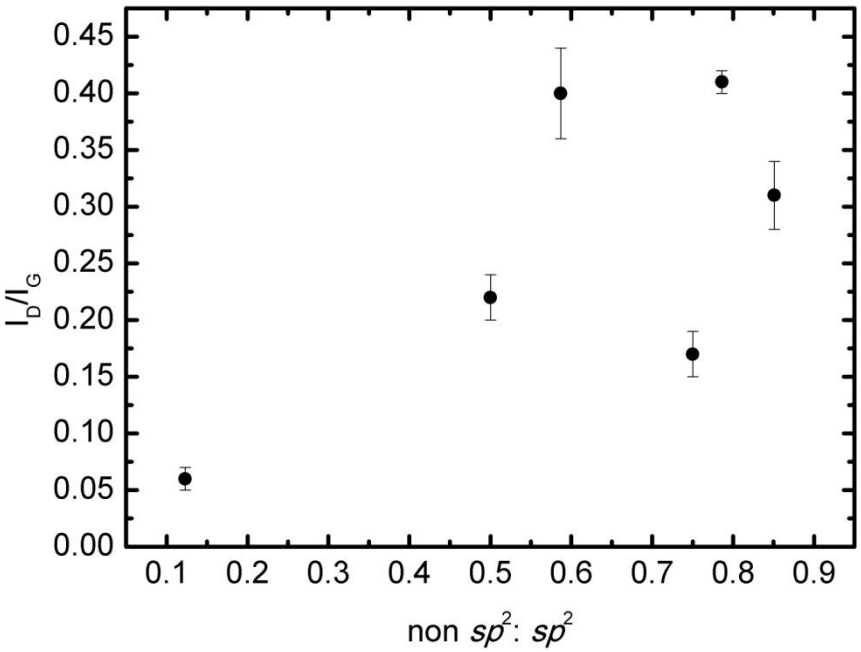

Fig. 4.22: Ratio of the *D* to *G* band intensities as a function of non-sp^3:sp^2 ratio measured by XPS.

To explore this issue fits were made to the *G*' band of the SWCNT samples as illustrated in Fig. 4.23. It can be seen that the *G'* peak itself is best fit with two Lorentzian components, the nature of which is discussed below, with additional components required to model overtone peaks which since they result from double (or higher order) resonance processes become more active with increasing disorder. A plot of the ratio of the *D* band intensity to that of the *G'* band, as shown in Fig. 4.24 presents a variation with a similar scatter to that seen for I_D/I_G. A plot of $I_D/I_{G'}$ against N content alone (not shown) once more presents no correlation. From the data in Figs. 4.22 and 4.24 it is clear that both I_D/I_G and $I_D/I_{G'}$ are a function of the total disorder in the system rather than simply reflecting the presence and concentration of nitrogen.

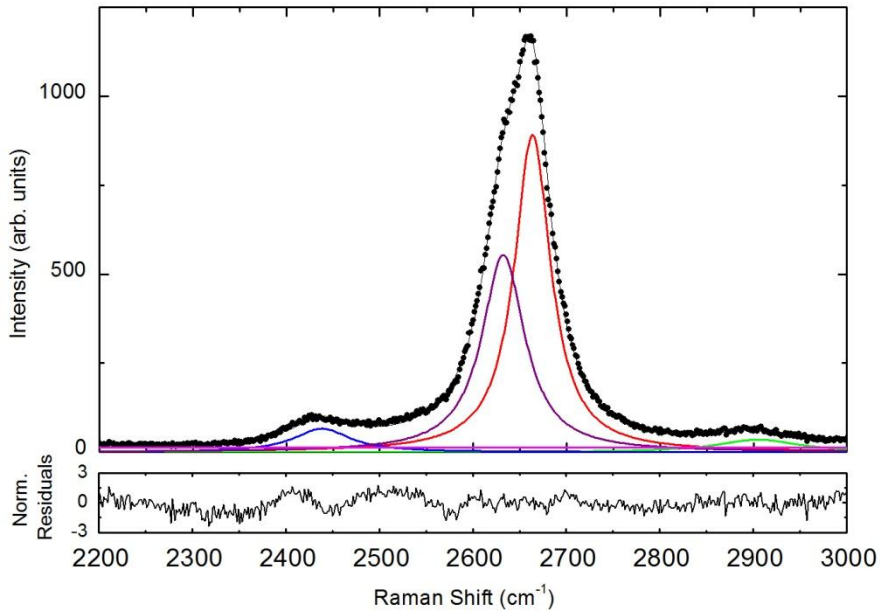

Fig. 4.23: Typical fit to the *G*' region of a SWCNT sample.

The observation of a strong increase in *D* band intensity upon irradiation raises questions regarding the sampling depth associated with the Raman spectra. On the basis of Monte-Carlo simulations[36] we would expect that the Ar^+ and N^+ ions have a range of around 10-15 nm at the energies used in this work. For the Al *K*α excitation the information depth associated with the C1*s* line (the depth from which 95% of the detected signal is generated) is about 10 nm and is slightly lower for the more strongly bound N1*s* electrons, which means that the XPS data reported in Section 4.3.1 originate from a region which coincides well with the ion-modified depth of the SWCNT film and accurately reflect the changes brought about by ion-mediated doping. However, the extinction coefficient of graphite is 1.3 (Ref. [111]) and as a result we would expect that light from a 532 nm laser would penetrate about 50 nm into the bulk material[112] and that the Raman signal would therefore originate primarily from the uppermost 25 nm of the sample (since the light must make a round trip through the sample). Therefore, we might expect that the Raman signal would originate from a combination of the modified layers and those below, with the greater part of the signal arising from the uppermost (modified) region. The sampling depth of the Raman experiment is likely to be reduced by other factors, such as the resonant nature of the interaction of the laser light with the nanotubes and potential interference effects. For example Wang *et al.* have demonstrated

that due to interference effects the Raman signal from a bilayer on graphene is more intense than the bulk material[113], and that a maximum of intensity occurs at a thickness of 9 layers at which the Raman intensity is approximately six times larger than a semi-infinite film. Such interference effects could be expected in the SWCNT samples here. Indeed, if the ratios of *D* to *G* intensities found in our study were associated with a Raman information depth greater than twice the ion range the *D* band intensities would need to be at least as large as the *G* band intensity in the upper layers of the film, something only found in amorphous carbon. As shown in the C1*s* XPS data in Section 4.3.1.2 and discussed in detail in Section 4.3.1.1, the ion doses chosen in the experiments reported here are well below the amorphisation threshold and therefore the relative intensity of the *D* band strongly suggests that the information depth in the Raman experiment is strongly suppressed as observed in graphene and that this observation is worthy of further, theoretical, study.

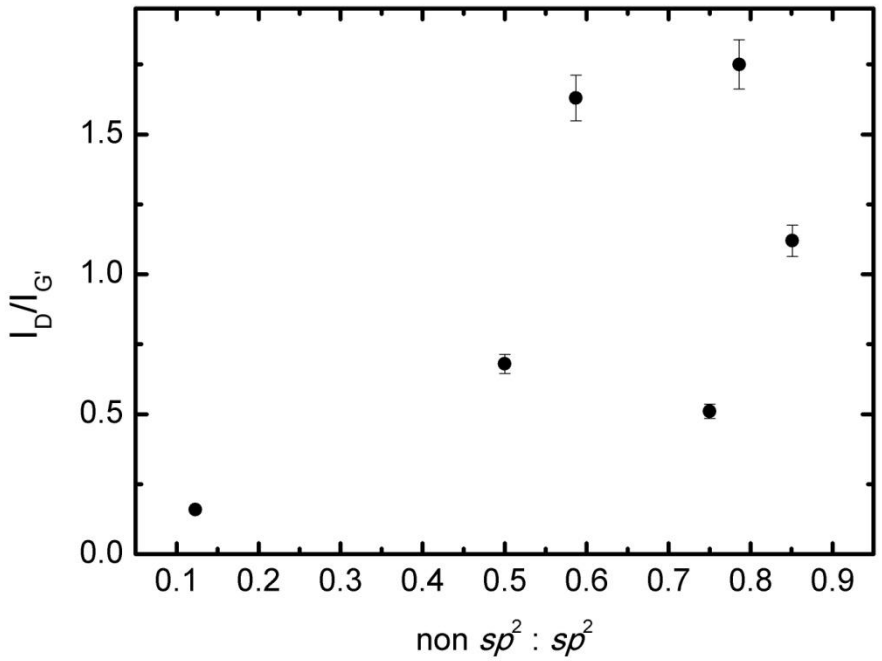

Fig. 4.24: Ratio of *D* band to *G'* band intensity as a function of non-sp^2 to sp^2 carbon ratio in nitrogen doped SWCNTs.

4.3.2.2 G band frequency

The frequency of vibrational modes in graphitic nanomaterials has often been used to probe charge transfer and doping. In the fullerenes transfer of negative charge resulting from alkali intercalation[114], electrochemical doping[115] and adsorption on surfaces[116] all led to a softening of infra-red and Raman-active modes. Similarly, Raman spectra of alkali metal doped SWCNT samples have previously demonstrated a downward frequency shift and broadening of the *G*-band [10,117]. The observed phonon softening has been directly related to the transfer of electrons from the alkali metal (i.e., *n*-type doping) and the filling of the π^*-derived bands of the nanotubes [10,117], whilst the broadening can be associated with either increased electron-phonon coupling or the irreversible introduction of disorder in the system[117]. In their study of electrochemical doping of purified SWCNTs with K and Li, Claye and co-workers[117] found that the shift in *G*-band frequency was not monotonic – an initial downshift occurred at very low doping levels (K:C < 0.005) followed by an *upshift* in frequency for intermediate doping ($0.005 <$ K:C < 0.01) then a strong downshift for doping to saturation ($0.015 <$ K:C < 0.04). For Li doping the same authors found that the rate of shift in frequency was larger for low alkali concentrations than high. Although the latter could be simply explained in terms of there being a decreasing charge transfer from the Li with increasing concentration, the behaviour under K doping is not well understood. Bendiab *et al.*[118], on the other hand, found an upshift in *G* band position for low (Li:C < 0.17) concentrations of both Li and Rb but observed the previously reported softening for saturation doping.

In contrast to the results found for alkali metal doping, Das *et al.*[119] find a notably different behaviour due to electrochemical doping of purified SWCNT bundles. Doping was achieved by applying a polymer electrolyte as the gating material and the nanotube bundle field effect transistors so formed displayed ambipolar behaviour (i.e., symmetric behaviour for electron and hole conduction). The *G* bands of the SWCNT bundles were fitted with three Lorentzians, the attribution of which was determined from the expected nanotubes in resonance with the laser light. The three peaks corresponded to the G^- line of smaller diameter metallic nanotubes, a combination of the G^- line of larger diameter metallic nanotubes and of semiconducting nanotubes and the G^+ line of all nanotube types. Upon either electron or hole doping the lowest frequency line shifted upward even for small bias,

the intermediate line shifts less and the highest frequency line only shifted significantly upward under high bias. The hardening of the phonon modes was explained in terms of changes in the electron-phonon coupling within the SWCNTs upon doping: for example, in metallic nanotubes the presence of a phonon associated with the G^- band leads to an atomic distortion which opens up a band gap at the Fermi level of the undoped nanotubes. Upon doping, a greater energy is required to open this gap, increasing the energy (and hence frequency) of the phonon mode. In analogous Raman measurements on an electrochemically gated single layer of graphene Das and co-workers observed that an increase in carrier concentration – either electrons and holes – from the charge neutrality point led to a stiffening (upward shift) of the *G* band by up to ~30 cm^{-1} associated with reduced electron-phonon coupling[120]. The 'clean' nature of these systems, in which doping is achieved electrostatically with minimum perturbation of the lattice indicates that softening of the *G* band is not simply associated with the presence of increased carrier density.

From Table 4.6 it can be seen that there is no shift to within experimental error for the main G^+ line in all the samples in investigated in this work and that only one, the sample annealed in N_2 at 600°C after Ar^+ irradiation, shows a change in position of the main G^- line greater than error (the difference in position from the pristine value being twice the standard errors). This behaviour is in marked contrast to the clear evidence of *n*-type doping in the samples provided by the position of the C1*s* sp^2 component in Section 4.3.1.2 and the hardening/softening previously reported for alkali metal/electrochemical doping of SWCNT films. Hence, it would appear that the relationship between doping and *G* mode frequency is complicated by the presence of the local distortion associated with the presence of nitrogen.

In the literature a range of different behaviours has been observed upon the introduction of nitrogen into carbon nanotubes. Droppa *et al.*[30] fitted three components to the *G*-band in their comparison of the Raman *G* bands of N-doped and undoped SWCNTs produced by the arc-discharge process. They found that upon nitrogen doping two of the components (located at 1556 and 1595 cm^{-1} in the pristine material) hardened, although by differing amounts whilst the most intense line remained at the same energy (1582cm^{-1}). These changes in the *G*-band were accompanied by a large increase in the I_D/I_G ratio indicating that the incorporation of nitrogen was associated with a significant increase in disorder in the nanotubes. The upshift of some of the *G*-band features was naïvely associated with the larger strength of the C-N versus the C-C bond[30], although this does not explain why some

components remain unchanged. An initial hardening of the *G* band was observed by Bulusheva and co-workers[74] in Raman spectra from nitrogen doped MWCNTs fit with two components for each of the *G* and *D* bands. They found an initial increase in *G* band position from 1589 to 1596 cm^{-1} upon N doping to a concentration of 2.36 at.% and then a shift back to 1590 cm^{-1} at a doping level of 2.89 at.%. Bulusheva *et al.* argued that these changes were 'not related to structural defects' but instead to some unspecified 'modification in the electronic structure'[74]. In contrast to these results Lim *et al.*[95] observed a softening of the *G*-band 1589 cm^{-1} to 1580 cm^{-1} upon incorporation of nitrogen into MWCNTs. This shift was seen to be accompanied by a strong increase in the I_D/I_G ratio. Yang *et al.*[121] also observed a downward shift of the *G*-band upon N-doping accompanied by an upward shift of the *D*-band.

The strong variation in the frequency behaviour of the *G*-band as a function of nitrogen incorporation reported in the literature, the differences observed between alkali metal and electrostatic doping and the presence of doping without an associated *G*-band shift reported here, indicate that the relationship between vibration mode softening/hardening and doping level and type may be significantly more subtle in carbon nanotubes and graphene than in the fullerenes. Indeed, Zafar and co-workers[84] have argued that, in the case of graphene doped exclusively with pyrrolic nitrogen, compressive strain in the lattice leads to shift in *G* band position with more than compensates that due to doping. Hence, based on the results presented here, the conclusion can be drawn that the *G*-band frequency is not a good measure of the doping state of a SWCNT sample and that alternative approaches (such as the position of the graphitic C1*s* core-level component, discussed in Section 4.3.1.2) are required to probe doping-induced changes in electronic structure.

4.3.2.3 G' band

A typical fit to the *G'* band in the Raman spectra from the SWCNTs studied in this thesis has already been presented in Fig. 4.23 and details of the fits are presented in table 4.7. In order to fit the *G*' band it is clear that two Lorentzian components are required. As pointed out by Maciel *et al.*[122] defects, including substitutional dopants, break the symmetry of the graphitic lattice of carbon nanotubes enabling new peaks to observed which are absent in the Raman spectra of the pristine materials. In addition charged defects can change the velocity of valence electrons which, due to the strong interaction between charge carriers and phonons

in sp^2 hybridised carbon materials, can have a significant influence on lattice vibrations associated with double-resonance processes. For example, Maciel *et al*. show that upon doping a new additional *G*' peak is observed at energies above or below the *G*' peak of the pristine material for *p* and *n* type doped SWCNTs respectively[122]. This new *G*' peak, labeled G'_D, is also found in pristine, unannealed SWCNTs, reflecting an intrinsic defect concentration with *n* type character (consistent with the *n*-type self-doping deduced from XPS by Chakraborty *et al.*[57] but increases in intensity with N or P doping without changing position (the lack of positional change reflecting the local, non-interacting nature of the dopants). With B doping a G'_D peak is observed at higher energy, consistent with *p*-type doping.

The interpretation of the role of bonding in *G'* band position advanced by Maciel and co-workers[122] is supported by Raman studies on electrochemically doped graphene undertaken by Das *et al.*[120] in which the evolution of Raman active modes was monitored as a function of the carrier density (varied in a controlled fashion through an applied gate voltage). It was found that the graphene *G'* peak stiffened upon hole doping and softened upon electron doping but that the effect was both asymmetric between electrons and holes and non-linear. In particular, it was found that the *G'* peak shifted from relatively low hole densities but that an electron density of around 3.2 x 10^{13} cm^{-2} was required before an appreciable (and rapid) softening in *G'* band position occurred.

A plot of the ratio of G'_D to G'_P peaks against N concentration, and separately against non-sp^2 to sp^2 carbon ratio (neither shown), is very similar to the plots for I_D/I_G and $I_D/I_{G'}$ in Figs. 4.21, 4.22 and 4.24 confirming that the G'_D peaks originates from the presence of defects of all types rather than just the presence of nitrogen dopants within the SWCNTs. From Table 4.7 it can be seen that there is a stiffening of the G'_P band upon nitrogen doping and that the G'_D band always lies below the G'_P line. Taken together these observations indicate the presence of *n*-type dopants within the SWCNTs as one would expect from the XPS results presented in Section 4.3.1.2. However, there is no clear correlation between the position of the peaks and either the total concentration of nitrogen or that in graphitic form. As with the position of the *G* peaks, it can only be concluded that the relationship between peak position and doping level is non-trivial and understanding requires further experimental and theoretical study.

Sample	*G'* Band Position (cm^{-1})		FWHM(cm^{-1})		$I_{G'(D)}/I_{G'(P)}$ Ratio
	(G_P')	(G_D')	(G_P')	(G_D')	
Pristine SWCNTs	2663±1	2632±1	47±1	56±1	0.73±0.05
N1	2667±1	2636±1	48±1	68±1	0.86±0.05
N2	2667±1	2640±2	49±2	77±2	1.2±0.1
Ar1	2661±1	2636±3	54±1	80±1	0.77±0.08
Ar2	2661±1	2633±2	54±1	70±2	0.59±0.05
Ar3	2665±1	2645±3	47±1	92±2	1.0±0.1

Table 4.7: Summary of the parameters used in the fitting of the *G'* of pristine and nitrogen-doped SWCNT films.

4.3.2.4 Radial breathing modes

The radial breathing modes (RBMs) are able to provide rich information on the electronic and geometric structure of SWCNT samples. The RBMs arise from the radial expansion and contraction of a nanotube and, as such, the frequency has been found to depend inversely upon the diameter of the nanotubes as[123]:

$$\omega_{RBM} = \frac{C_1}{d} + C_2 \qquad (4.2)$$

where C_1 and C_2 are constants and d is the nanotube diameter.

The RBM is excited by a single resonance process and therefore nanotubes in which electronic transitions between band edges (at which the density of states is high due to the van Hove singularities in the density of states of one dimensional solids) match the laser excitation energy in the Raman process dominate the spectrum. A Kataura plot – a plot of optical transition energies as a function of nanotube diameter – can, provided that few

nanotubes are in resonance with the incident photons – be used to determine the chiral indicies, (*n*,*m*) of the nanotubes contributing strongly to the Raman spectrum[124].

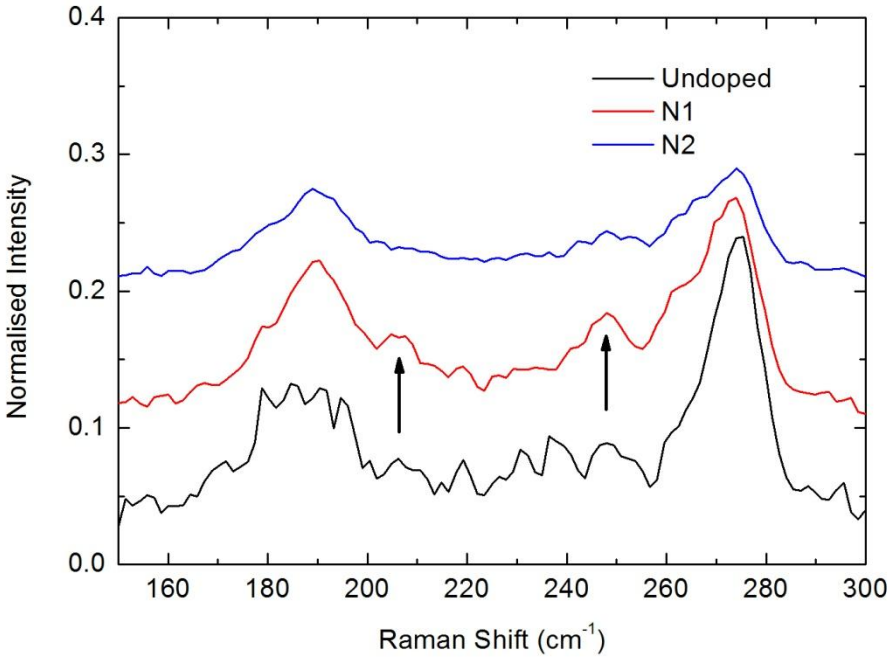

Fig. 4.25: Effects of N doping on and RBM bands of 20 µC N-doped SWCNTs (N1), and 100 µC N-doped SWCNTs (N2) excited with 532 nm light.

Figs. 4.25 and 4.26 show the RBM region of the Raman spectra of pristine and N^+ ion irradiated SWCNT films excited with lasers of wavelength 532 and 633 nm, respectively. The clear differences between the spectra presented in the lower (black) curves, measured on pristine SWCNT samples, indicate that the incident photons probe different portions of the diameter distribution within the film. In Fig. 4.27 a section of a Katuara plot centred on an optical transition energy of 2.33 eV (that of a 532 nm laser) from Murakami *et al.*[124] is plotted. From this plot we can assign the peaks observed in Fig. 4.25: the broad feature at about 185 cm^{-1} arises from an unresolved set of RBMs associated with semiconducting nanotubes whilst the peak at ~275 cm^{-1} can be seen to originate from metallic (9,3) SWCNTs. Using the values of C_1 =214.4 cm^{-1} nm and C_2 = 18.7 cm^{-1} from Telg *et al.*[125] the diameter of the metallic nanotube is found to be 0.77 nm (against an expected value, from the chiral indices, of 0.8 nm) and that of the semiconducting nanotubes 1.19 nm. These values are different to those found by considering the separation between G^- and G^+ bands in Section

4.3.2, but do not contradict those results – the larger diameters found from the *G* bands lead to RBM frequencies which are below the minimum which can be determined in the spectrometer used in these investigations.

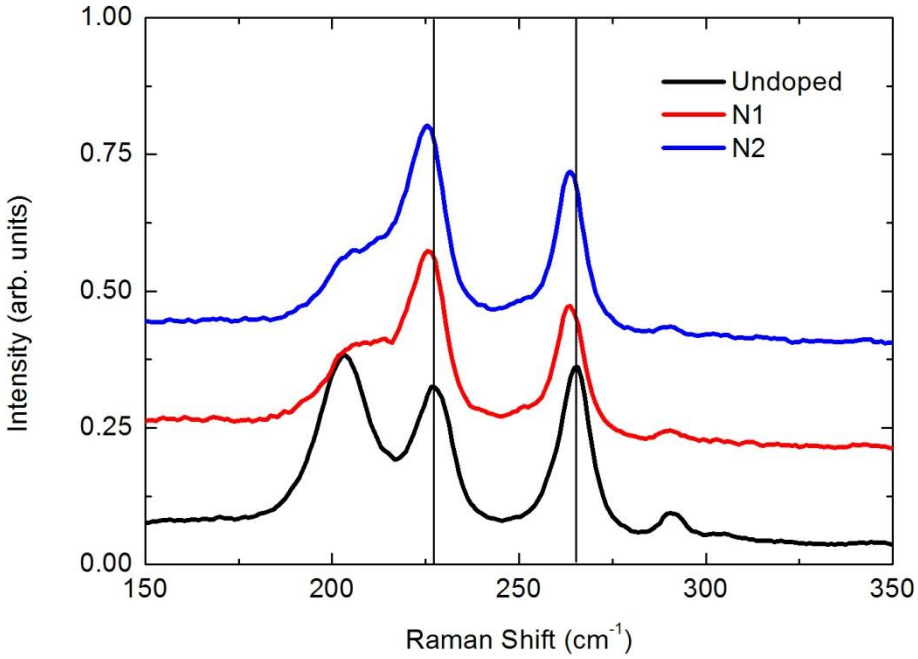

Fig. 4.26: Effects of N doping on and RBM bands of 20 µC N-doped SWCNTs (N1), and 100 µC N-doped SWCNTs (N2) excited with 633 nm light.

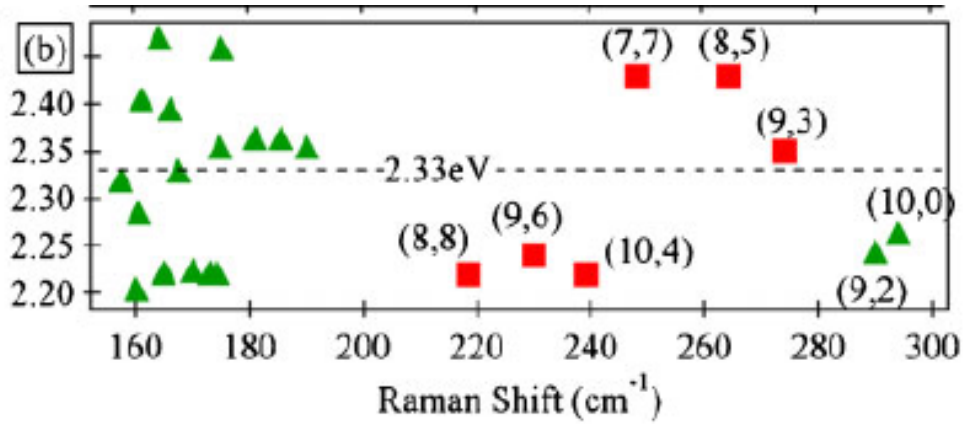

4.27: Section of a Kataura plot close to the excitation energy of a 532 nm laser (2.33 eV). (From Ref. [124])

Upon N^+ ion irradiation it can be seen from Fig. 4.25 that there is a slight downshift of the RBM associated with the (9,3) SWCNTs, which gains a low energy shoulder, and that

two new peaks appear, marked by arrows. Using the Kataura plot of Fig, 4.27, the shoulder and higher energy peak which appear upon irradiation can be attributed to (8,5) and (7,7) metallic nanotubes, respectively. The appearance of the RBM signature of the (7,7) and (8,5) SWCNTs in the N^+ ion irradiated films may be associated either with a broadening of the van Hove singularities and consequently electronic transitions (in particular the $E_{11(M)}$ transition between the first van Hove singularities above and below the Fermi energy of the metallic nanotubes) which brings the nanotubes into resonance or a shift in the $E_{11(M)}$ transition energy. Gerber *et al.*[123] suggest, from density functional theory (DFT) calculations, that the E_{11} transition energy should shift upward by 0.05 eV upon nitrogen doping of a (8,0) nanotube. Although this magnitude of the energy shift is small, it may be sufficient to bring new nanotubes into resonance with the incident laser light. Gerber and co-workers[123] also examined the shift in RBM mode positions to be expected upon nitrogen doping using both a simple spring-constant model and more sophisticated DFT calculations. They found that for all nitrogen configurations, and for vacancies, that a downshift in frequency is expected as observed in the data for both 532 and 633 nm excitation presented here. The new lower energy RBM (at around 205 cm^{-1}) in Fig. 4.25 is as yet not understood, since it does not correspond to what would be expected from the Kataura plot of Fig. 4.27 and requires further theoretical work for its interpretation.

The evolution of the RBM spectra in Ar^+ irradiated samples annealed in N_2 atmosphere is presented in Fig. 4.28 and shows considerable differences from the sequence presented in Fig. 4.25. The downshift of the RBM peak associated with the (9,3) nanotubes is still present as are the (currently unexplained) new peak at ~205 cm^{-1} and the shoulder associated with the RBM of the (8.5) metallic SWCNTs. However, upon nitrogen doping there is a more pronounced loss in overall RBM intensity, coupled with a broad increase in relative intensity between about 220 and 250 cm^{-1}. The features in this energy region are most likely associated with the unresolved RBMs of (8,8), (9,6) and (10,4) nanotubes which have come into resonance in addition to the (7,7) and (8,5) SWCNTs. To bring all these SWCNTs into resonance with the 2.33 eV incident photons requires a broadening of the $E_{11(M)}$ transition from the < 0.1 eV expected in pristine nanotubes to at least 0.25 eV, indicating that the Ar^+ irradiated, nitrogen annealed nanotubes although possessing less overall disorder (at least according to the I_D/I_G ratios reported in Section 4.3.2.1) nevertheless have a more significant broadening of the van Hove singularities upon nitrogen doping.

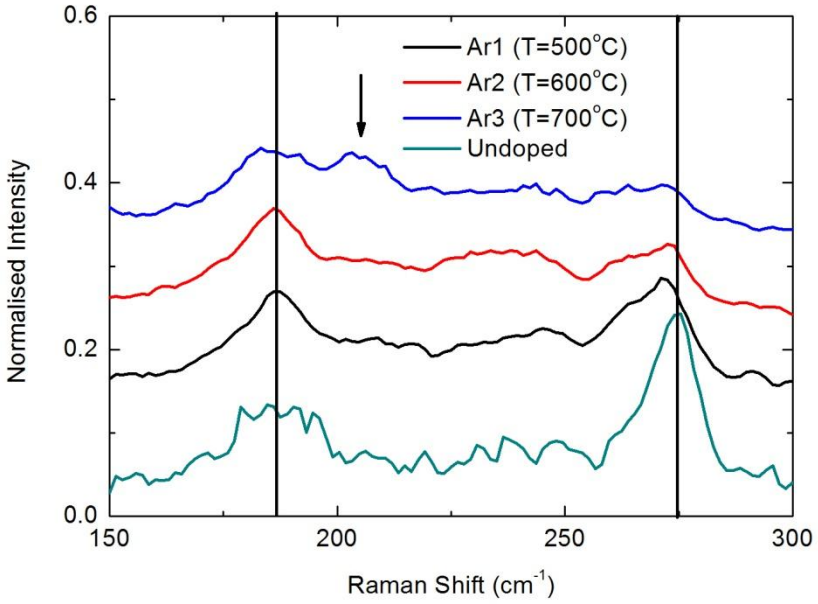

Fig. 4.28 RBM band spectra of Ar^+ irradiated SWCNTs exposed to nitrogen atmosphere at elevated temperature, measured with a 532 nm laser.

4.4 Summary

In this chapter the results of ion-bombardment mediated nitrogen doping of SWCNT films has been explored. Two approaches were employed – direct doping through bombardment with N^+ ions and a novel technique involving the annealing of Ar^+ irradiated films in N_2 gas at elevated temperatures, which exploited the hitherto undiscovered reactivity of SWCNT defects to N_2 gas even at room temperature. It was found that both techniques were successful in incorporating nitrogen into the SWCNT lattice with the exact species and their relative abundance dependent on doping conditions. Hence, it is possible to fabricate doped SWCNTs by this approach, with a dominant nitrogen species appropriate to a particular application.

Detailed investigation of the core-level spectra of the nitrogen doped SWCNTs showed that there is a linear relationship between the concentration of graphitic nitrogen substituted into the SWCNT lattice and the position of the C1*s* line associated with sp^2

carbon, which has not been previously observed. These results indicate rigid band filling within the concentration range investigated and that the graphitic nitrogen is an *n*-type dopant, as expected. It is also clear that the presence of other nitrogen containing species has little effect on the doping of the SWCNT films.

From Raman spectroscopy of the nitrogen doped SWCNT films it is apparent that the I_D/I_G or $I_D/I_{G'}$ ratios reflect the total disorder within the SWCNTs and should not be used to determine the concentration of dopants, as is occasionally reported in the literature. It is found that there is no change in *G* band position upon doping whereas both hardening and softening of this mode has been observed in the literature upon nitrogen doping. Given that XPS data show clear evidence of *n*-type doping the conclusion can be drawn that the *G* band frequency is a very poor measure of doping level and that the position of this peak is determined by a more complex set of factors which still need to be understood. The behaviour of the *G'* band is found to primarily be the result of disorder and also shows no systematic change in position with doping. Whilst other Raman features do not show any significant differences between nanotube films doped by the two techniques, the evolution of RBMs upon doping suggest that Ar^+ bombardment followed by annealing in N_2 broadens the electronic structure more substantially than N^+ ion irradiation. However, further theoretical work is required in order to understand the origin of these differences.

4.5 References

[1] M.M.J. Treacy, T.W. Ebbesen, and J.M. Gibson, Nature **381**, 678 (1996).
[2] E.W. Wong, P.E. Sheehan, and C.M. Lieber, Science (80-.). **277**, 1971 (1997).
[3] M.R. Falvo, G.J. Clary, R.M. Taylor II, V. Chi, F.P. Brooks Jr, S. Washburn, and R. Superfine, Nature **389**, 582 (1997).
[4] S. Berber, Y. Kwon, and D. Tománek, Phys, Rev. Lett. **84**, 4613 (2000).
[5] P. Kim, L. Shi, a. Majumdar, and P. McEuen, Phys. Rev. Lett. **87**, 215502 (2001).
[6] Y. Maniwa, R. Fujiwara, H. Kira, H. Tou, H. Kataura, S. Suzuki, Y. Achiba, E. Nishibori, M. Takata, M. Sakata, A. Fujiwara, and H. Suematsu, Phys. Rev. B **64**, 241402 (2001).
[7] H. Shimoda, B. Gao, X. Tang, a. Kleinhammes, L. Fleming, Y. Wu, and O. Zhou, Phys. Rev. Lett. **88**, 015502 (2001).
[8] R.C. Haddon, R.M. Fleming, M.D. W, C.H. Chen, A.P. Ramirez, and S.H. Glarum, Science (80-.). **263**, 1744 (1994).
[9] R.S. Lee, H.J. Kim, J.E. Fischer, and A. Thess, Nature **388**, 255 (1997).
[10] A.M. Rao, P.C. Eklund, S. Bandow, A. Thess, and R.E. Smalley, Nature **388**, 257 (1997).
[11] L. Grigorian, K.A. Williams, S. Fang, G.U. Sumanasekera, A.L. Loper, E.C. Dickey, S.J. Pennycook, and P.C. Eklund, Phys. Rev. Lett. **80**, 5560 (1998).

[12] S. Suzuki, C. Bower, T. Kiyokura, and K.G. Nath, J. Electron Spectros. Relat. Phenomena **114-116**, 225 (2001).
[13] S. Suzuki, C. Bower, Y. Watanabe, and O. Zhou, Appl. Phys. Lett. **76**, 4007 (2000).
[14] A. Wadhawan, R.E. Stallcup, and J.M. Perez, Appl. Phys. Lett. **78**, 108 (2001).
[15] F. Villalpando-Páez, a. H. Romero, E. Muñoz-Sandoval, L.M. Martínez, H. Terrones, and M. Terrones, Chem. Phys. Lett. **386**, 137 (2004).
[16] P. Ayala, A. Rubio, and T. Pichler, Rev. Mod. Phys. **82**, 1843 (2010).
[17] A.K. Chakraborty, Synthesis Characterisation and Modification of Carbon Nanotube and Related Carbon Nanostructures, University of Durham, 2005.
[18] K. Jiang, L.S. Schadler, R.W. Siegel, X. Zhang, H. Zhang, and M. Terrones, J. Mater. Chem. **14**, 37 (2004).
[19] S. Peng and K. Cho, Nano Lett. **3**, 513 (2003).
[20] M. Zhao, Y. Cao, X. Liu, J. Deng, D. Li, and H. Gu, Nanoscale Res. Lett. **9**, 142 (2014).
[21] D. Yu, Q. Zhang, and L. Dai, J. Am. Chem. Soc. **132**, 15127 (2010).
[22] D.H. Lee, W.J. Lee, W.J. Lee, S.O. Kim, and Y. Kim, Phys, Rev. Lett. **106**, 175502 (2011).
[23] Z. Mo, S. Liao, Y. Zheng, and Z. Fu, Carbon N. Y. **50**, 2620 (2012).
[24] G. Zhang, W. Duan, and B. Gu, Appl. Phys. Lett. **80**, 2589 (2002).
[25] H.-S. Ahn, K.-R. Lee, D.-Y. Kim, and S. Han, Appl. Phys. Lett. **88**, 093122 (2006).
[26] S.K. Srivastava, V.D. Vankar, D.V. Sridhar Rao, and V. Kumar, Thin Solid Films **515**, 1851 (2006).
[27] L. Qiao, W.T. Zheng, H. Xu, L. Zhang, and Q. Jiang, J. Chem. Phys. **126**, 164702 (2007).
[28] L.-J. Li, M. Glerup, a. N. Khlobystov, J.G. Wiltshire, J.-L. Sauvajol, R. a. Taylor, and R.J. Nicholas, Carbon N. Y. **44**, 2752 (2006).
[29] J.Y. Yi and J. Bernholc, Phys. Rev. B **47**, 1708 (1993).
[30] R.D. Jr, P. Hammer, A.C.M. Carvalho, M.C. Santos, and F. Alvarez, **302**, 874 (2002).
[31] M. Glerup, J. Steinmetz, D. Samaille, O. Stephan, S. Enouz, A. Loiseau, S. Roth, and P. Bernier, Chem. Phys. Lett. **387**, 193 (2004).
[32] M. Terrones, H. Terrones, N. Grobert, W.K. Hsu, Y.Q. Zhu, J.P. Hare, H.W. Kroto, D.R.M. Walton, P. Kohler-Redlich, M. Ruhle, J.P. Zhang, and A.K. Cheetham, Appl. Phys. Lett. **75**, 3932 (1999).
[33] M. Yudasaka, R. Kikuchi, Y. Ohki, and S. Yoshimura, Carbon N. Y. **35**, 195 (1997).
[34] C. Tang, Y. Bando, D. Golberg, and F. Xu, Carbon N. Y. **42**, 2625 (2004).
[35] C. Ewels, M. Glerup, and V. Krstić, in *Chem. Carbon Nanotub.* (American Scientific Publishers, 2007).
[36] R.M. Houchin, Ph.D. Thesis, Durham University, 2011.
[37] D. Golberg, Carbon N. Y. **38**, 2017 (2000).
[38] K. Suenaga, M.. Johansson, N. Hellgren, E. Broitman, L.. Wallenberg, C. Colliex, J.-E. Sundgren, and L. Hultman, Chem. Phys. Lett. **300**, 695 (1999).
[39] J. Kotakoski, J. Pomoell, a Krasheninnikov, and K. Nordlund, Nucl. Instruments Methods Phys. Res. Sect. B Beam Interact. with Mater. Atoms **228**, 31 (2005).
[40] J. Kotakoski, A. Krasheninnikov, Y. Ma, A.S. Foster, K. Nordlund, and R.. Nieminen, Phys. Rev. B **71**, 205408 (2005).
[41] K. Yamamoto, T. Kamimura, and K. Matsumoto, Jpn. J. Appl. Phys. **44**, 1611 (2005).
[42] F. Xu, M. Minniti, C. Giallombardo, a Cupolillo, P. Barone, a Oliva, and L. Papagno, Surf. Sci. **601**, 2819 (2007).
[43] F. Xu, M. Minniti, P. Barone, A. Sindona, A. Bonanno, and A. Oliva, Carbon N. Y. **46**, 1489 (2008).
[44] R. Sen, B.C. Satishkumar, A. Govindaraj, K.R. Harikumar, G. Raina, J.-P. Zhang, A.K. Cheetham, and C.N.R. Rao, Chem. Phys. Lett. **287**, 671 (1998).

[45] M. Glerup, M. Castignolles, M. Holzinger, G. Hug, A. Loiseau, and P. Bernier, Chem. Commun. 2542 (2003).
[46] M.R.C. Hunt, (2014).
[47] M. Castignolles, Ph.D Thesis, Universite Montpellier II, 2004.
[48] H.C. Choi, S.Y. Bae, J. Park, K. Seo, C. Kim, B. Kim, H.J. Song, and H.J. Shin, Appl. Phys. Lett. **85**, 5742 (2004).
[49] H.C. Choi, J. Park, and B. Kim, J. Phys. Chem. Phys. Chem. B **109**, 4333 (2005).
[50] V. Krstic, G.L.J.A. Rikken, P. Bernier, S. Roth, and M. Glerup, Europhys. Lett. **77**, 37001 (2007).
[51] M. Zhao, Y. Xia, J.P. Lewis, and R. Zhang, J. Appl. Phys. **94**, 2398 (2003).
[52] H. Kang and S. Jeong, Phys. Rev. B **70**, 1 (2004).
[53] J. Robertson and C.A. Davis, Diam. Relat. Mater. **4**, 441 (1995).
[54] A. Nevidomskyy, G. Csányi, and M. Payne, Phys. Rev. Lett. **91**, 1 (2003).
[55] P. Lammert, V. Crespi, and A. Rubio, Phys. Rev. Lett. **87**, 1 (2001).
[56] Z. Luo, S. Lim, Z. Tian, J. Shang, L. Lai, B. MacDonald, C. Fu, Z. Shen, T. Yu, and J. Lin, J. Mater. Chem. **21**, 8038 (2011).
[57] A. Chakraborty, R. Woolley, Y. Butenko, V. Dhanak, L. Siller, and M. Hunt, Carbon N. Y. **45**, 2744 (2007).
[58] A. Krasheninnikov and K. Nordlund, Nucl. Instruments Methods Phys. Res. Sect. B Beam Interact. with Mater. Atoms **216**, 355 (2004).
[59] A. V Krasheninnikov and F. Banhart, Nat. Mater. **6**, 723 (2007).
[60] Z. Hou, X. Wang, T. Ikeda, K. Terakura, M. Oshima, M. Kakimoto, and S. Miyata, Phys. Rev. B **85**, 1 (2012).
[61] A. Tolvanen, J. Kotakoski, A. V. Krasheninnikov, and K. Nordlund, Appl. Phys. Lett. **91**, 173109 (2007).
[62] Y.V. Butenko, S. Krishnamurthy, A.K. Chakraborty, V. Kuznetsov, V.R. Dhanak, M.R.C. Hunt, and L. Šiller, Phys. Rev. B **71**, 075420 (2005).
[63] D.A. Shirley, Phys. Rev. B **5**, 4709 (1972).
[64] S. Souto, M. Pickholz, M. dos Santos, and F. Alvarez, Phys. Rev. B **57**, 2536 (1998).
[65] Å. Johansson and S. Stafström, J. Chem. Phys. **111**, 3203 (1999).
[66] D. Marton, K. Boyd, A. Al-Bayati, and S. Todorov, Phys. Rev. Lett. **73**, 118 (1994).
[67] J.M. Ripalda, I. Montero, and L. Galan, Diam. Relat. Mater. **7**, 402 (1998).
[68] J. Ripalda, E. Román, N. D'\iaz, L. Galán, I. Montero, G. Comelli, A. Baraldi, S. Lizzit, A. Goldoni, and G. Paolucci, Phys. Rev. B **60**, 3705 (1999).
[69] I. Shimoyama, G. Wu, T. Sekiguchi, and Y. Baba, Phys. Rev. B **62**, 6053 (2000).
[70] J. Casanovas, J.M. Ricart, J. Rubio, F. Illas, and J.M. Jiménez-Mateos, J. Am. Chem. Soc. **118**, 8071 (1996).
[71] M.. Brzhezinskaya, E.M. Baitinger, and V. V Shnitov, Phys. B Condens. Matter **348**, 95 (2004).
[72] A.G. Kudashov, A. V. Okotrub, L.G. Bulusheva, I.P. Asanov, Y. V. Shubin, N.F. Yudanov, L.I. Yudanova, V.S. Danilovich, and O.G. Abrosimov, J. Phys. Chem. B **108**, 9048 (2004).
[73] L.G. Bulusheva, A. V. Okotrub, A.G. Kudashov, I.P. Asanov, and O.G. Abrosimov, Eur. Phys. J. D **34**, 271 (2005).
[74] L.G. Bulusheva, A. V. Okotrub, I.A. Kinloch, I.P. Asanov, A.G. Kurenya, A.G. Kudashov, X. Chen, and H. Song, Phys. Status Solidi **245**, 1971 (2008).
[75] S. Maldonado, S. Morin, and K.J. Stevenson, Carbon N. Y. **44**, 1429 (2006).
[76] G. Tian, M. Zhao, Q. Zhang, J. Huang, and F. Wei, Carbon N. Y. **50**, 5323 (2012).
[77] Z. Chen, D. Higgins, and Z. Chen, Carbon N. Y. **48**, 3057 (2010).

[78] D. Usachov, A. Fedorov, O. Vilkov, B. Senkovskiy, V.K. Adamchuk, L.V. Yashina, A.A. Volykhov, M. Farjam, N.I. Verbitskiy, A. Gruneis, C. Laubschat, and D.V. Vyalikh, Nano Lett. **14**, 4982 (2014).
[79] M. Scardamaglia, B. Aleman, M. Amati, C. Ewels, P. Pochet, N. Reckinger, J.-F. Colomer, T. Skaltsas, N. Tagmatarchis, R. Snyders, L. Gregoratti, and C. Bittencourt, Carbon N. Y. **73**, 371 (2014).
[80] K.-J. Kim, H. Lee, J. Choi, H. Lee, M.C. Jung, H.J. Shin, T.-H. Kang, B. Kim, and S. Kim, J. Phys. Condens. Matter **22**, 045005 (2010).
[81] R. Podila, J. Chacón-Torres, J.T. Spear, T. Pichler, P. Ayala, and a. M. Rao, Appl. Phys. Lett. **101**, 123108 (2012).
[82] Z. Luo, S. Lim, Z. Tian, J. Shang, L. Lai, B. MacDonald, C. Fu, Z. Shen, T. Yu, and J. Lin, J. Mater. Chem. **21**, 8038 (2011).
[83] L. Qu, Y. Liu, J.-B. Baek, and L. Dai, ACS Nano **4**, 1321 (2010).
[84] Z. Zafar, Z.H. Ni, X. Wu, Z.X. Shi, H.Y. Nan, J. Bai, and L.T. Sun, Carbon N. Y. **61**, 57 (2013).
[85] A. V. Krasheninnikov and K. Nordlund, J. Appl. Phys. **107**, 071301 (2010).
[86] A. V. Krasheninnikov and K. Nordlund, J. Vac. Sci. Technol. B Microelectron. Nanom. Struct. **20**, 728 (2002).
[87] Y. Fujimoto and S. Saito, Phys. E Low-Dimensional Syst. Nanostructures **43**, 677 (2011).
[88] M.R.C. Hunt and S.J. Clark, Phys. Rev. Lett. **109**, 265502 (2012).
[89] Y. Fujimoto and S. Saito, Phys. Rev. B **84**, 1 (2011).
[90] D. Srivastava, M. Menon, C. Daraio, S. Jin, B. Sadanadan, and A.M. Rao, Phys. Rev. B **69**, 153414 (2004).
[91] M.R.C. Hunt, Phys. Rev. B **78**, 153408 (2008).
[92] R. Larciprete, a. Goldoni, S. Lizzit, and L. Petaccia, Appl. Surf. Sci. **248**, 8 (2005).
[93] J. Diaz, G. Paolicelli, S. Ferrer, and F. Comin, Phys. Rev. B **54**, 8064 (1996).
[94] P. Reinke, M.. Garnier, and P. Oelhafen, J. Electron Spectros. Relat. Phenomena **136**, 239 (2004).
[95] S. Lim, H. Elim, X. Gao, a. Wee, W. Ji, J. Lee, and J. Lin, Phys. Rev. B **73**, 1 (2006).
[96] M. Aono, S. Aizawa, N. Kitazawa, and Y. Watanabe, Thin Solid Films **516**, 648 (2008).
[97] A. Jorio, R. Saito, G. Dresselhaus, and M.S. Dresselhaus, Philos. Trans. A. Math. Phys. Eng. Sci. **362**, 2311 (2004).
[98] M. Hulman, V. Skákalová, S. Roth, and H. Kuzmany, J. Appl. Phys. **98**, 024311 (2005).
[99] J. Maultzsch, S. Reich, C. Thomsen, S. Webster, R. Czerw, D.L. Carroll, S.M.C. Vieira, P.R. Birkett, and C. a. Rego, Appl. Phys. Lett. **81**, 2647 (2002).
[100] J. Maultzsch, S. Reich, and C. Thomsen, Phys. Rev. B **64**, 1 (2001).
[101] M.S. Dresselhaus, G. Dresselhaus, R. Saito, and a. Jorio, Phys. Rep. **409**, 47 (2005).
[102] S. Brown, A. Jorio, P. Corio, M. Dresselhaus, G. Dresselhaus, R. Saito, and K. Kneipp, Phys. Rev. B **63**, 155414 (2001).
[103] H. Telg, J.G. Duque, M. Staiger, X. Tu, F. Hennrich, M.M. Kappes, M. Zheng, J. Maultzsch, C. Thomsen, and S.K. Doorn, ACS Nano **6**, 904 (2011).
[104] A. Jorio, A.G.S. Filho, G. Dresselhaus, M.S. Dresselhaus, A.K. Swan, M.S. Unlu, B.B. Goldberg, M.A. Pimenta, J.H. Hafner, C.M. Lieber, and R. Saito, Phys. Rev. B **65**, 155412 (2002).
[105] L. Zhang, H. Li, K. Yue, S. Zhang, X. Wu, and J. Zi, Phys. Rev. B **65**, 10 (2002).
[106] C.Y. Zhi, X.D. Bai, and E.G. Wang, Appl. Phys. Lett. **80**, 3590 (2002).
[107] M.S. Dresselhaus, a Jorio, a G. Souza Filho, and R. Saito, Philos. Trans. A. Math. Phys. Eng. Sci. **368**, 5355 (2010).
[108] T. Sharifi, F. Nitze, H.R. Barzegar, C. Tai, M. Mazurkiewicz, A. Malolepszy, L. Stobinski, and T. Wågberg, Carbon N. Y. 1 (2012).

[109] M. Zhao, Y. Cao, X. Liu, J. Deng, D. Li, and H. Gu, Nanoscale Res. Lett. **9**, 142 (2014).
[110] C. Thomsen, S. Reich, and J. Maultzsch, Philos. Trans. A. Math. Phys. Eng. Sci. **362**, 2337 (2004).
[111] P. Blake, E.W. Hill, a. H. Castro Neto, K.S. Novoselov, D. Jiang, R. Yang, T.J. Booth, and a. K. Geim, Appl. Phys. Lett. **91**, 2007 (2007).
[112] Z. Ni, Y. Wang, T. Yu, and Z. Shen, Nano Res. **1**, 273 (2010).
[113] Y.Y. Wang, Z.H. Ni, Z.X. Shen, H.M. Wang, and Y.H. Wu, Appl. Phys. Lett. **92**, 043121 (2008).
[114] T. Pichler, M. Matus, and H. Kuzmany, Solid State Commun. **86**, 221 (1993).
[115] Y. Zhang, G. Edens, and M. Weaver, J. Am. Chem. Soc. **724**, 9395 (1991).
[116] M.R.C. Hunt, S. Modesti, P. Rudolf, and R.E. Palmer, Phys. Rev. B **51**, 10039 (1995).
[117] A. Claye, S. Rahman, J.E. Fischer, A. Sirenko, G.U. Sumanasekera, and P.C. Eklund, Chem. Phys. Lett. **333**, 16 (2001).
[118] N. Bendiab, E. Anglaret, J.-L. Bantignies, a. Zahab, J. Sauvajol, P. Petit, C. Mathis, and S. Lefrant, Phys. Rev. B **64**, 245424 (2001).
[119] A. Das, A. Sood, A. Govindaraj, and A. Saitta, Phys. Rev. Lett. **136803**, 1 (2007).
[120] a Das, S. Pisana, B. Chakraborty, S. Piscanec, S.K. Saha, U. V Waghmare, K.S. Novoselov, H.R. Krishnamurthy, a K. Geim, a C. Ferrari, and a K. Sood, Nat. Nanotechnol. **3**, 210 (2008).
[121] Q.-H. Yang, P.-X. Hou, M. Unno, S. Yamauchi, R. Saito, and T. Kyotani, Nano Lett. **5**, 2465 (2005).
[122] I.O. Maciel, N. Anderson, M. a Pimenta, A. Hartschuh, H. Qian, M. Terrones, H. Terrones, J. Campos-Delgado, A.M. Rao, L. Novotny, and A. Jorio, Nat. Mater. **7**, 878 (2008).
[123] I.C. Gerber, P. Puech, A. Gannouni, and W. Bacsa, Phys. Rev. B - Condens. Matter Mater. Phys. **79**, 1 (2009).
[124] T. Murakami, Y. Yamamoto, M. Matsuda, K. Kisoda, and C. Itoh, Jpn. J. Appl. Phys. **53**, 02BD11 (2014).
[125] H. Telg, J. Maultzsch, S. Reich, F. Hennrich, and C. Thomsen, Phys. Rev. Lett. **93**, 177401 (2004).

Chapter 5

Graphene growth on copper from a solid hydrocarbon precursor

In this chapter the results of ambient pressure chemical vapour deposition (APCVD) growth of graphene on copper from a solid hydrocarbon precursor, nonadecane, are reported. Although graphene is found to be successfully produced by this route, island size and coverage saturate with growth time leading to an incomplete coverage of the substrate which cannot be overcome by increasing the mass of precursor during growth. The kinetics of the growth process are found to be well described by a literature model involving the continuous supply of 'active' species to the graphene islands during growth. XPS and AES measurements demonstrate that the degree of graphitisation in the films increases with the growth temperature. The presence of trace oxygen during the growth process explains the observed insensitivity of island size and coverage to growth temperature.

5.1 Introduction

As discussed in Section 1.4 of Chapter 1, graphene can be obtained by several approaches, including mechanical exfoliation[1], thermal decomposition of silicon carbide[2], wet chemical methods[3,4], exfoliation[5], plasma deposition[6], deposition of atomic carbon[7] and chemical vapour deposition (CVD)[8]. Of these techniques CVD is perhaps the most promising for the development of large-scale production processing[9] due to its relatively low cost, scalability and simplicity. Graphene nucleation and growth depends on many different factors that can be optimized during gas-phase CVD growth such as substrate morphology[10], temperature[11,12], growth time[11,12,13], pressure and gas flow, all of which need to be controlled in order to pave the way toward the fabrication of electronic devices and films appropriate for other applications. In order to address some of the complexity of conventional low pressure chemical vapour deposition approaches a number of groups have successfully demonstrated graphene growth from gas-phase precursors under atmospheric pressure conditions[13,14,15], known as atmospheric pressure CVD (APCVD). A further simplification, based upon the principles of CVD but which dispenses with the cost and complexity of gas handling is solid phase growth[16,17,18,19,20,21,22]. Such an approach has the potential to open a route towards growing graphene by a simple, inexpensive and scalable production method which dispenses with the requirement for explosive gaseous sources, and is the focus of this Chapter. In particular, a soft solid phase precursor material, nonadecane, is used coupled with an atmospheric pressure growth step, since it is straightforward to spread this hydrocarbon over a suitable catalytic substrate and atmospheric pressure heating is cheap, simple and rapid. By using a solid hydrocarbon precursor, it is demonstrated that graphene formation is possible in the absence of a hydrogen gas flow which is a requirement for solid phase CVD on copper from other sources[21] due to the inability of copper to graphitise solid carbon. Moreover, in addition to simplicity, solid phase growth opens up the possibility of introducing dopants in a straightforward and controlled manner[16], as is discussed in more detail in Chapter 6.

A wide range of solid precursors have been employed in graphene growth. Large single or bilayer graphene films were first obtained from different solid carbon sources by Sun *et al* in 2010[16]. Polymer films, such as poly methyl methacryate (PMMA) were deposited on catalytic metal substrate and heated under low pressure. Sun and co-workers found that graphene can be successfully produced with controllable thickness by heating the substrate and solid source at temperatures between 800 and 1000°C and that is was possible to dope

graphene with nitrogen through growth. Raman spectroscopy was used to reveal the presence of single graphene layers. The growth of graphene on nickel films using a molecular source and its subsequent transfer to a SiO_2 substrate, has been also demonstrated[19]. In that study, C_{60} molecules were used as the carbon source for graphene growth in vacuum. The great advantage of this method is the control of total dosage of sublimed molecular layers. Graphene films have even been produced from waste products such as food, insects, solid animal wastes[17] and waste plastics[23] highlighting the flexibility of the solid-phase growth approach.

Ji *et al*. explored the growth of graphene on copper from solid hydrogen-free amorphous carbon films sputtered onto the substrate and subsequently annealed at high temperature[21]. They found that no graphene growth occurred under an inert gas flow at 1035°C, and that the amorphous carbon film desorbed. However, in the presence of a small (2 sccm) flow of hydrogen gas high quality graphene films were observed. These results were attributed to the aforementioned inability of copper to graphitise solid carbon[24] (unlike, say Ni[19,22]), with Ji and co-workers arguing that the gaseous H_2 reacted with the amorphous carbon at high temperature to generate hydrocarbons which provide the as yet poorly understood 'active' carbon containing species from which the graphene grows.

5.2 Experiment

As discussed in Chapter 3, Section 3.4, pure copper foils (99.9%) of 200 μm thickness were used as the catalytically active substrate for graphene growth from a 'soft' solid phase precursor, nonadecane. The copper was cut into samples with lateral dimensions of 5 x 7 mm^2 and then prepared by a two-step cleaning and surface preparation procedure (described in detail in Chapter 3) which involved an acetic acid etch followed by a high temperature anneal.

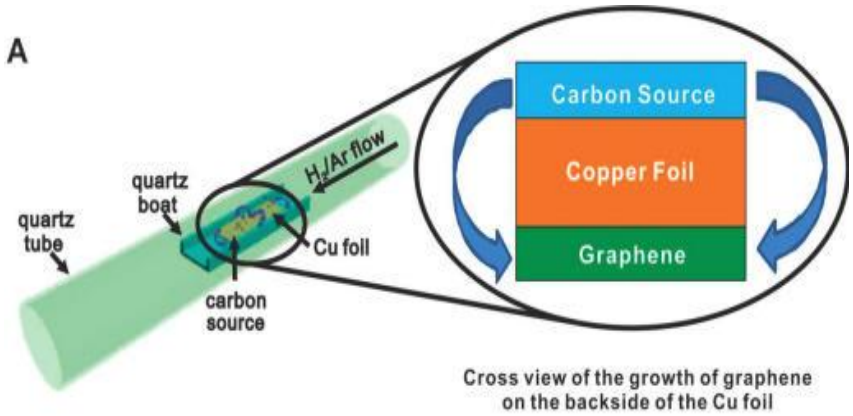

Fig. 5.1: Schematic diagram of the solid-phase graphene growth approach adopted in this work (from Ref. [17]).

After substrate preparation a carefully controlled quantity of nonadecane (typically 5.0±0.1 mg, unless otherwise stated) was added to one face of the sample, with the other left clean (or unloaded), following the approach of Ruan *et al.* , Fig 5.1[17]. The rationale behind this approach was that the diffusion of precursors (consisting of the starting material or [partially] dehydrogenated species arising from its catalytic decomposition) would diffuse to the 'clean' side, so forming graphene with cracking products and other contamination left on the other face. The low solubility of carbon in copper ensured that diffusion would occur over the surface. However, as reported in the next section, it was found that amorphous carbon related to precursor cracking was also present on the 'clean' unloaded surface, indicating considerable precursor decomposition occurred after diffusion from the loaded to the unloaded surface.

Growth was carried out in the quartz tube of a furnace at atmospheric pressure under a flow of pure Ar gas (340 sccm), introduced to prevent oxidation. Ar was chosen over nitrogen as the inert gas species due to the reaction between nitrogen and defects in SWCNTs reported in Chapter 4. The copper foil substrate and precursor were supported by a ceramic boat placed in the centre of the furnace. The boat and quartz tube were cleaned successively by acetone, isopropanol and de-ionised water between each growth run to prevent cross-contamination.

In order to examine the kinetics of graphene growth (reported in Section 5.3) a series of samples were produced at a growth temperature of 1000°C and a fixed nonadecane mass (5.0±0.1 mg) with growth time varying from 5 to 600 minutes. After noting that the saturation coverage of the graphene was considerably less than 100% the precursor mass was then varied between 5.0±0.1 and 30.0±0.1 mg again at a growth temperature of 1000°C, for a fixed growth time of 120 min. Finally, in order to explore the role of temperature in determining coverage, island size and graphene quality samples were grown at temperatures between 880 and 1000˚C with a growth time of 120 min and 5.0±0.1 mg of precursor. No growth was observed at temperatures below 900˚C.

After growth the samples were transferred through air to the analytical tools described in Chapter 3. Optical microscopy was used to determine if graphene growth had occurred and SEM was used to determine the overall morphology of the samples, the graphene coverage and island size, whilst XPS was employed to measure the degree of sample graphitisation and the presence of contamination. Although Raman spectroscopy was attempted on the samples reported in this Chapter, the combination of incomplete coverage and high fluorescence background from the copper substrate meant that it was not possible to obtain useful data.

5.3 Results

5.3.1 Graphene growth by a solid carbon source

As described in section 5.2, graphene was grown on copper foils at temperatures of up to 1000°C for by the CVD of a solid carbon feedstock (nonadecane) under an Ar gas flow. Due to the high transparency and excellent thermal stability of graphene, the interference colour against the naked regions of copper foils can be altered after the thermal oxidation process, making graphene material directly observable by the naked eye and under polarised optical microscopy (POM) as illustrated in Fig 5.2. It is clear in the large scale images that the colour of the copper foil after graphene growth is significantly different from that of the pristine copper and that the evolution upon oxidation also changes. It has been reported that graphene works as an effective protective barrier against oxidation of metal surfaces[25], which is confirmed by POM at 50x magnification (lower images, Fig. 5.2). Graphene can be identified by its interference colour contrast, indicating that the copper is covered by

graphene islands and confirming that graphene growth from the solid phase precursor has been achieved.

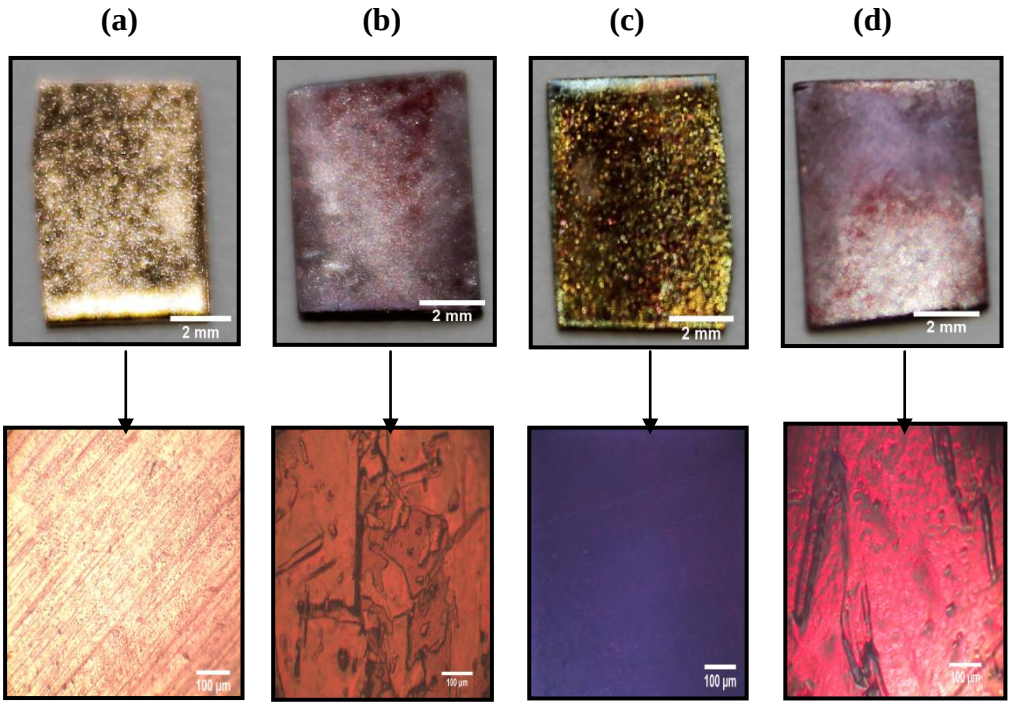

Fig. 5.2: Photographs of copper foils (a) pure copper, (b) graphene grown at 1000°C for 600min before oxidation, (c) pure copper after oxidation, (d) graphene grown after oxidation. Lower images show the optical microscope images corresponding to photographs.

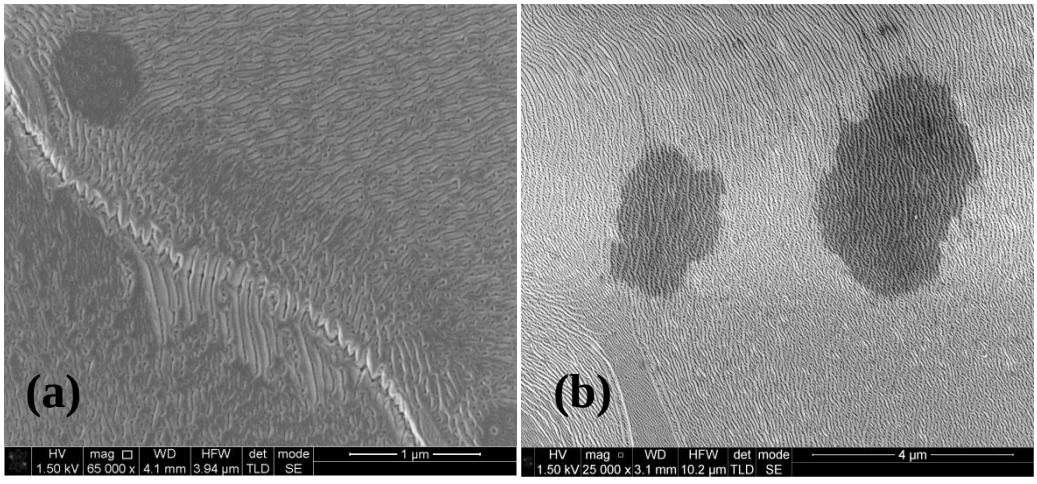

Fig. 5.3: SEM images of graphene islands grown from 5.0±0.1mg nonadecane on copper at 1000ºC for 120 minutes.

Fig. 5.3 presents SEM images of graphene islands grown on copper foil at 1000ºC for 120 minutes. These island morphologies are typical of those found on the samples reported in this chapter. The graphene island shown in Fig 5.3(a) displays faceting and the hexagonal island shape reflects the underlying symmetry of the graphitic lattice. However, the islands shown in Fig. 5.3(b), which are obtained on the same sample, have a more irregular shape and may result from the coalescence of smaller grains which have nucleated in close proximity or reflect local differences in growth conditions. Local differences in growth may arise from the non-uniform roughness and the polycrystallinity of the substrate which would impact upon the diffusion rate of precursors or may be related to the local precursor density available for growth, the origin of which is discussed below. Moreover, the copper foil sample is polycrystalline and the island morphology will reflect the crystal facet upon which growth takes place[26]. The images in Fig. 5.3(a) and 5.3(b) show a rough copper background, which is not seen at lower temperatures. It has been argued that such features are related to copper steps and vanish upon oxidation[25,27] and that their presence therefore corresponds to a complete graphene overlayer, with the 'island' features being due to second layer growth. However, the X-ray photoemission studies (Section 5.3.3) show copper oxide formation on all samples (not shown) ruling out the possibility of a continuous film, which would otherwise protect the whole surface from oxidation[25].

The results of both optical microscopy and SEM demonstrate that graphene growth clearly occurs even in the absence of a hydrocarbon gas flow, which is found to be a requirement for growth from other solid carbon sources on copper[21].

5.3.2 Kinetics of graphene growth

SEM images such as those presented in Fig. 5.3 readily enable the average graphene island size and coverage to be determined through the analysis of multiple images, and the variation of average island size with growth time is presented in Fig. 5.4. It is clear that the evolution of graphene island size is non-linear and appears to saturate at a sufficiently prolonged growth period, which is coupled with a saturation in overall film coverage, Fig. 5.5. A linear relation is found between coverage and island size (Fig. 5.6) suggesting that after initial nucleation graphene growth proceeds via the capture of precursor species by existing grains rather than the nucleation of new islands.

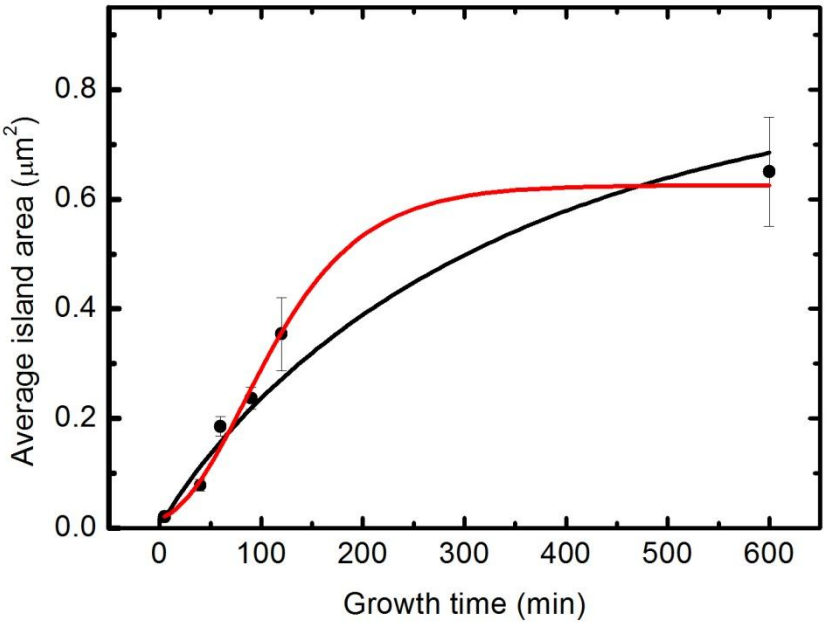

Fig. 5.4: Variation of average graphene island area with growth time (data points) fitted with the modified JMAK equation proposed by Kim *et al.*[11] (black line) and the Gompertz equation derived by Celebi *et al.*[12] (red line).

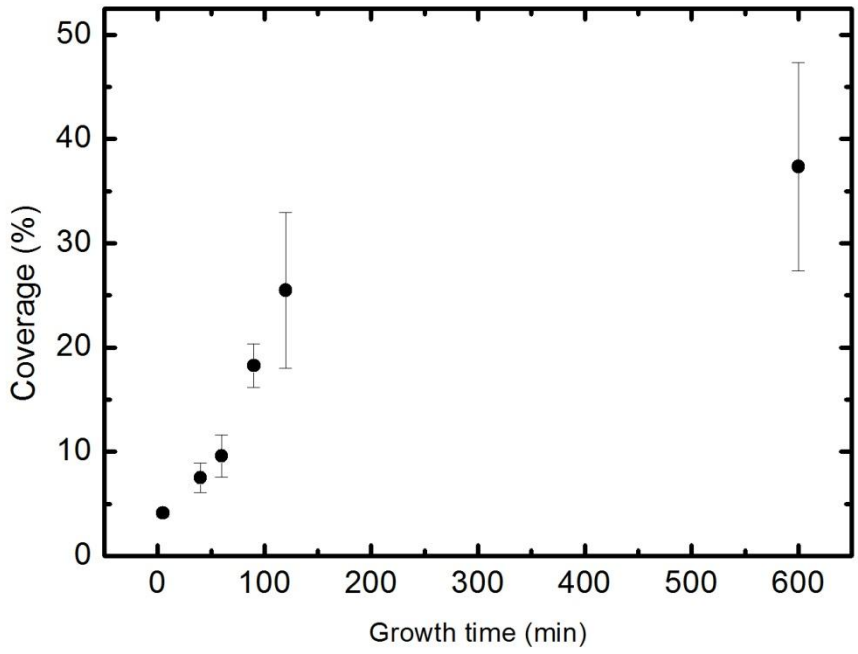

Fig. 5.5: Variation of graphene coverage with time for solid phase growth with nonadecane at 1000ºC.

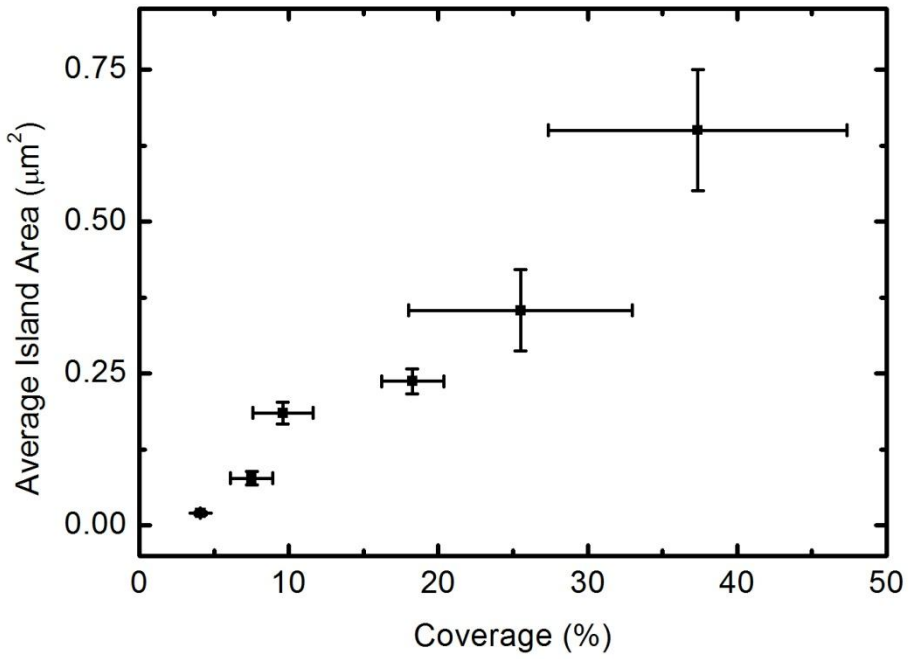

Fig. 5.6: Variation of graphene island area with coverage for solid phase growth with nonadecane at 1000ºC.

The variation of graphene island size and coverage with growth time provides valuable insight into the kinetics of graphene growth, but such studies have been limited – most studies of CVD graphene growth have focused more on the empirical determination of the 'optimal' growth conditions (see Ref. [8] and references therein) – and even fewer have specifically addressed graphene growth on copper, where the low solubility of carbon in the catalyst/substrate has a significant impact on the growth mechanism, as described in Section 5.1.

One of the few studies of graphene growth kinetics on copper has been reported by Kim *et al.* [11] who examined CVD growth using methane as a precursor. The approach adopted by Kim and co-workers is based upon a model previously developed for nucleation of metal films on ceramic substrates and is illustrated in Fig. 5.7. Dissociative chemisorption of methane on the copper surface leads to a concentration of 'active carbon species' (assumed to be carbon monomers) involved in graphene growth which increases to a critical

supersaturation level at which the nucleation of stable graphene islands occurs. As these islands grow they deplete the active carbon species until the concentration falls to a level at which no further nucleation can occur and growth continues to form either a complete or partial film. Kim *et al.* describe this process as a 'two-dimensional crystallisation' of graphene which can be described by the Johnson-Mehl-Avrami-Kolmogorov (JMAK) model and fit their data with a modified JMAK equation:

$$A_G = A_{sat}(1 - \exp(k(t - t_0)^n)) \qquad (5.1)$$

where A_G is the graphene area coverage, A_{sat} is the saturation coverage, t_0 is the time required for nuclei to form before observable growth occurs and n is known as the Avrami constant, which reflects the dimensionality of the system. Their fit to the data is shown in the right hand panel of Fig. 5.7.

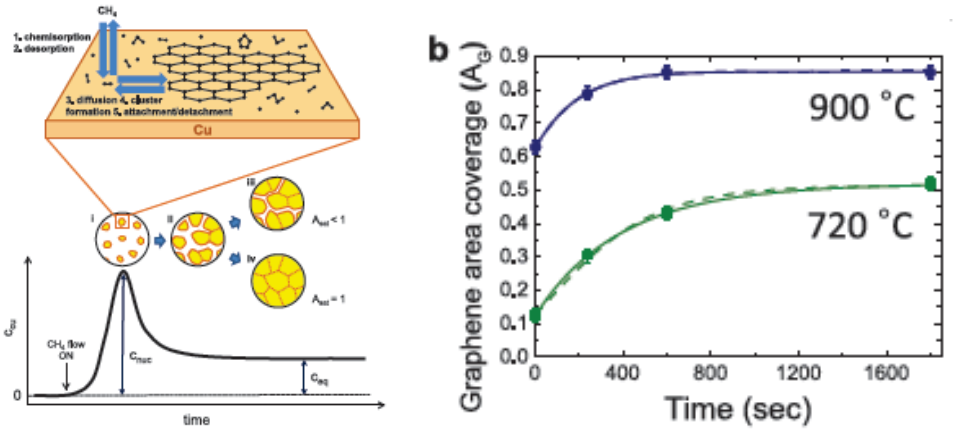

Fig. 5.7: (left panel) Schematic view of graphene growth based on nucleation from a supersaturated layer. Bottom: the density of the carbon adatoms versus time. Here an initial supersaturated state is depleted by the growing graphene crystal. (right panel) JMAK fits to the variation of graphene coverage with time (Ref. [11]).

Celebi and co-workers[12] have pointed out that an inherent assumption of the model used by Kim *et al.*[11] is that no additional carbon input occurs after the initial supersaturation stage. Such an assumption is inappropriate for gas-phase CVD (however, it may be applicable for the solid phase growth approach reported here, since there is no addition of precursor material during the growth process). Celebi *et al.*[12] also argue that the JMAK model is rooted in growth mechanisms appropriate for high carbon solubility surfaces such as Ni, rather than copper. Moreover, in their own experiments they found that growth only occurred

under the supply of a precursor gas which contradicts the idea that no additional precursor is required after growth initiation.

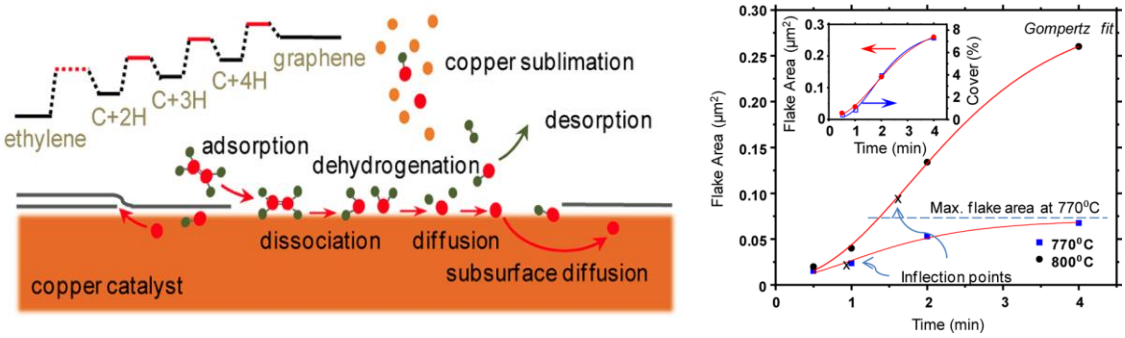

Fig. 5.8: (left panel) Schematic of the possible growth mechanism in a CVD technique using ethylene, showing the different stages involved in the formation of both monolayer and bi-layer graphene at the copper surface. (right panel) modified Gompertz fit to measured graphene island sizes. (Ref. [12])

As an alternative to the JMAK model, Celebi *et al.* derive a model (Fig. 5.8) which involves the adsorption, dehydrogenation and dissociation of a precursor gas (in their case ethene) in which dehydrogenation was the rate limiting step, and in which the limiting rate is time-dependent. By assuming that a time-dependent rate determines the active species they find that the time-dependence of the area of a graphene island should be described by a modified Gompertz function[12]:

$$A(t) = A_{max}\exp\left[-\exp\left(-\frac{\mu e}{\mathrm{A_{max}}}(t-\lambda)+1\right)\right] \quad (5.2)$$

where $A(t)$ is the graphene flake area, A_{max} is the area at saturation growth, μ is the maximum growth rate, e is Euler's number, λ the time lag associated with growth, and t the growth time. Their fit to the data is shown in the right hand panel of Fig. 5.8.

Given the linear relationship between graphene island area and coverage in the studies reported here (also found by Celebi *et al.*[12]) it is possible to compare the two model equations for the time-dependence of graphene growth, (5.1) and (5.2), with the data obtained in this work. In Fig. 5.4, both the modified JMAK equation (black line) and the Gompertz equation (red line) are fitted to the data. Although both equations seem to provide a 'reasonable' fit by

eye, a χ^2 analysis of the data indicates that there is a probability that the JMAK model describes the data of $p = 0.0004$ ($\chi^2 = 15.86$, degrees of freedom = 2) whilst the Gompertz model fit suggests $p = 0.12$ ($\chi^2 = 5.79$, degrees of freedom = 3) and hence is far more probable as a correct description of the data. It should be noted that there is a relatively small number of degrees of freedom (number of data points – number of fit parameters) in the fit and the probability of the Gompertz fit being correct may increase. Astonishingly, in the published work of Kim *et al.* the JMAK equation is fit to a mere four points[11] (right panel of Fig. 5.7) leaving no degrees of freedom, whilst Celebi *et al.* fit a model with three adjustable parameters to four points[12]. Therefore, whilst some conclusion may be drawn about the applicability of the two models to the data presented here, it is not clear if they have actually been tested for gas-phase CVD.

It may initially appear counterintuitive that a model which involves the continuous supply of a carbon containing precursor (Gompertz model) provides a better fit to the data measured for the soft solid phase growth of graphene than one in which there is no further supply after nucleation (JMAK model). It could be expected that the volatile nonadecane (boiling point 330ºC) would rapidly evaporate from the copper surface well below the temperature at which growth could occur leaving a small concentration of partially dehydrogenated precursor resulting from the catalytic action of the substrate, with no further addition of material. However, SEM images often show surface species which, owing to their strong contrast, are suggestive of multilayers of material, presumably partially hydrogenated amorphous carbon resulting from nonadecane decomposition (some remaining hydrogenation being necessary for graphene growth[21]). This is especially apparent for short growth times, and Fig. 5.9, shows relatively large droplet shaped solids found in addition to graphene islands for a 5 minute growth time. Although patches with significantly greater contrast than the graphene islands are seen at longer growth times, such well-defined large solid are not seen, indicating their loss with increasing growth time. As a result of these observations it is possible to suggest that during the initial stage of sample heating the nonadecane (complete or partially decomposed) diffuses to the unloaded surface where it decomposes as temperature increases, leaving behind amorphous (and possibly partially hydrogenated) solid 'droplets'. As growth temperature is reached, these droplets decay by losing carbon-containing species which can diffuse across the surface enabling graphene growth to occur. The constant supply of carbon species from the 'droplets' would then mimic the supply of

gaseous species in a CVD experiment, therefore explaining why a model involving the continuous supply of carbon species should be the most appropriate fit to the data. A slightly similar mechanism of graphene growth has been suggested by Zhang and co-workers[13], in which carbon supersaturated copper nanoparticles provide carbon species in addition to dissociatively chemisorbed methane during APCVD.

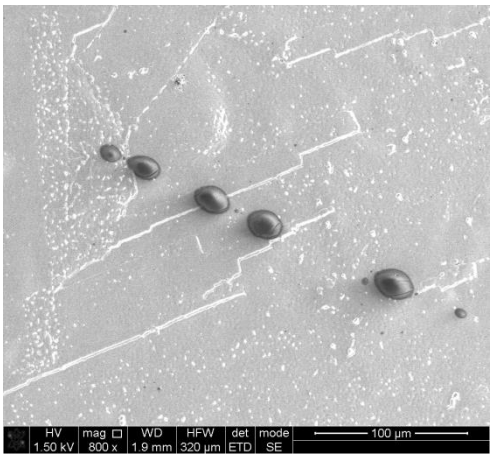

Fig. 5.9: SEM image of the surface of a sample after 5 minutes growth time at 1000ºC.

As can be seen in Fig. 5.5, graphene growth using 5.0±0.1 mg of nonadecane precursor saturates at a coverage of about 40±10%, which is well below the ideal of a complete graphene layer over the entire surface. In order to explore if the limitation in coverage was associated with an insufficient initial quantity of precursor material a series of samples were produced in which the precursor mass was varied from 5.0±0.1 to 30.0±0.1 mg. Fig. 5.10 and 5.11 present the variation of average island size and surface coverage with initial nonadecane mass. Fig. 5.10 shows that as the mass of initial precursor material increases the average island area decreases whilst the coverage (Fig. 5.11) increases, albeit less rapidly. Decreasing island size with increasing coverage is indicative of an increasing density of nucleation sites (as observed in the SEM image shown Fig. 5.12) which suggests that an initially higher density of precursor material may lead to the more rapid formation of critical nuclei before the loss of carbon containing material ultimately limits coverage. One possibility is that there is a greater initial density of precursors at the surface which increases the rate of critical nucleus formation if the stable nucleus comprises of more than a single 'active' species. However, in the absence of knowledge of the precise nature of the species

involved in graphene growth and a detailed modelling of the influence of the initial species concentration upon nucleation it is not currently possible to draw any definitive conclusion.

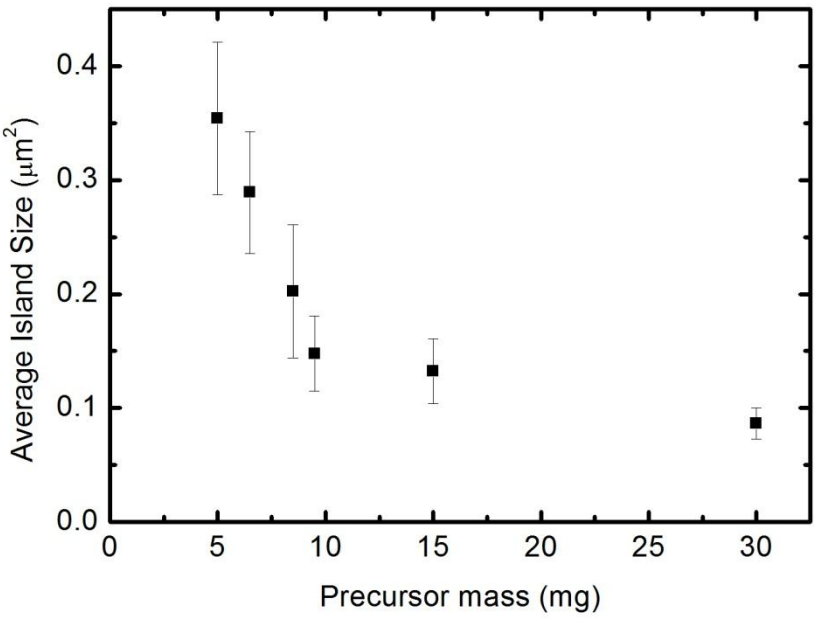

Fig. 5.10: Variation of average graphene island area with initial mass of precursor.

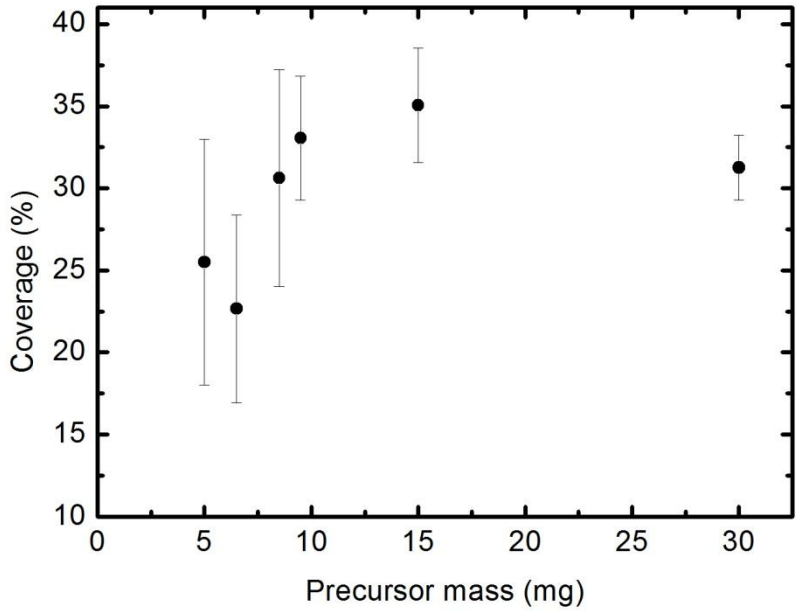

Fig. 5.11: Variation of graphene coverage with initial mass of precursor.

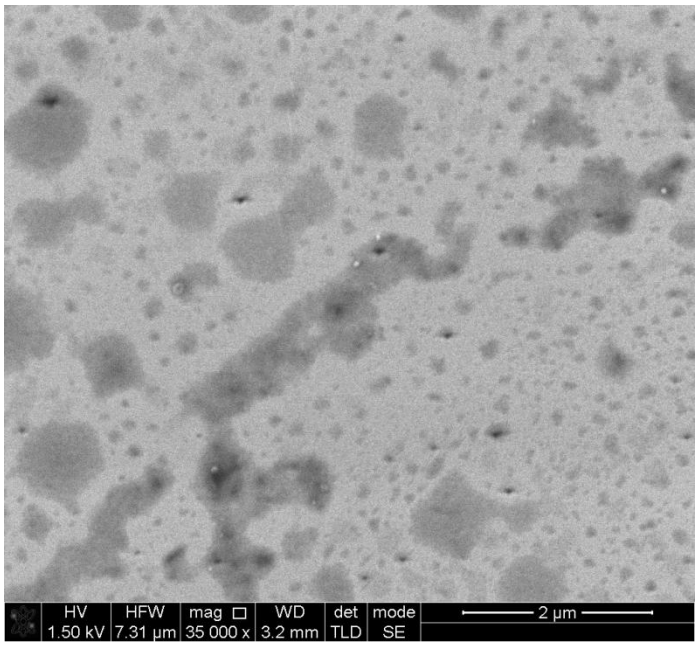

Fig. 5.12: SEM image of a sample grown with a precursor mass of 30.0±0.1 mg. Note the high density of islands, some of which have begun to merge.

5.3.3 Temperature dependence of graphene growth.

The temperature at which the growth process occurs plays an important role in graphene synthesis. Whilst the lowest possible substrate temperature would be beneficial from a manufacturing viewpoint, due to the costs associated with high thermal budget processes, elevated temperature usually produces graphene films with the most desirable properties. For example, according to several reports in the literature[11,12] increasing temperature in gas phase CVD growth of graphene should lead to a lower nucleation density (and therefore domain size increases for layer nucleation density), a lower concentration of contaminants and a greater degree of graphitisation/graphene quality. In order to understand the influence of temperature on graphene by the soft solid-phase approach reported here, a series of samples were produced at temperatures ranging from 940 to 1000ºC, the lower limit determined by the temperature at which significant graphene growth is observed and the upper limit by the constraints imposed by the growth apparatus. In all cases the graphene growth process involved holding the sample at the growth temperature for 120 minutes and used 5.0±0.1 mg of precursor.

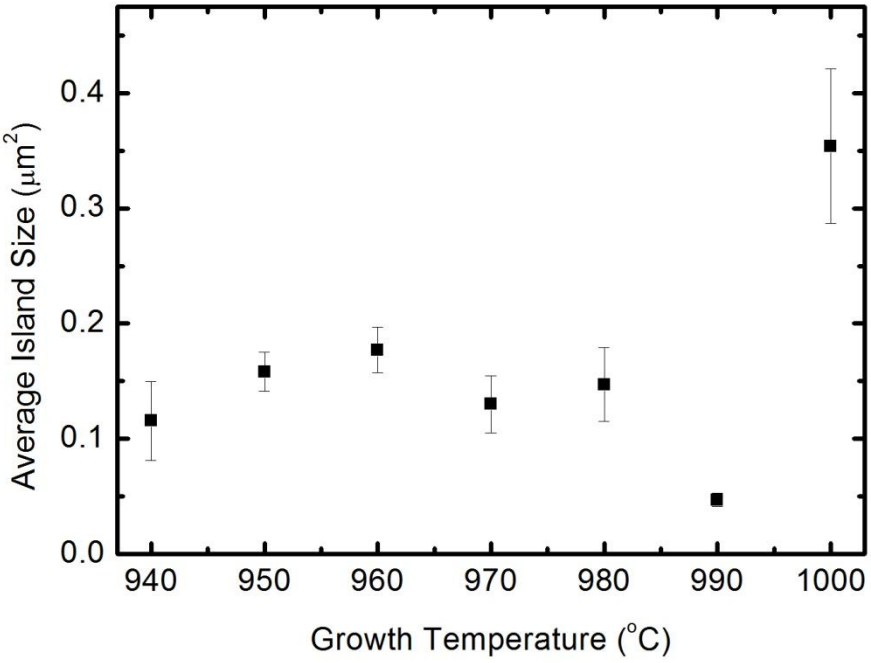

Fig. 5.13: Variation of average graphene island size with growth temperature in the solid phase growth of graphene from nonadecane on copper.

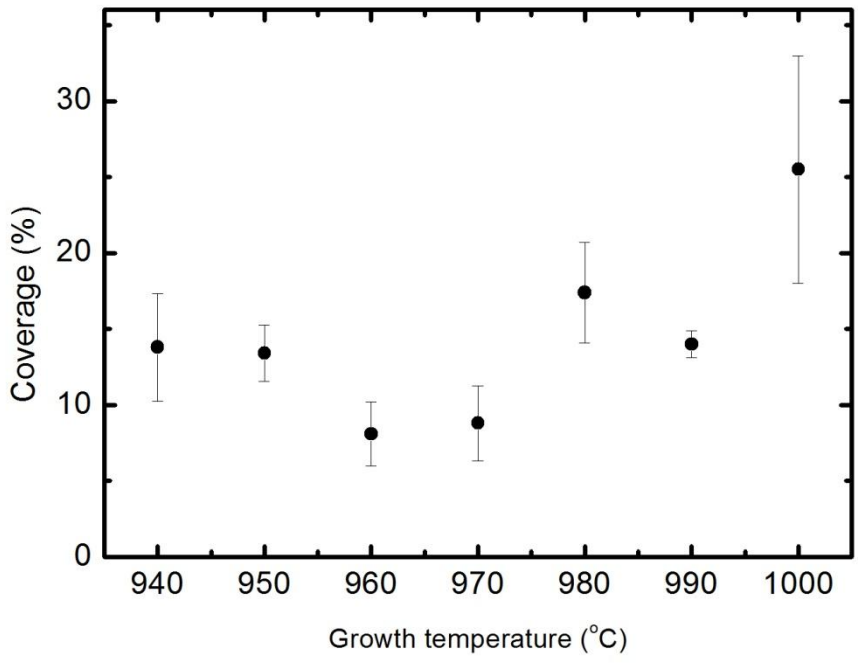

Fig. 5.14: Variation of graphene coverage with growth temperature in the solid phase growth of graphene from nonadecane on copper.

Figs. 5.13 and 5.14 show the variation of average graphene island size and the total graphene coverage as a function of growth temperature, respectively. It is apparent that, contrary to expectations[11,12], there is no clear trend in either quantity with increasing growth temperature and that neither the island size nor coverage show any significant change over the temperature window studied. Possible reasons for these observations are discussed below.

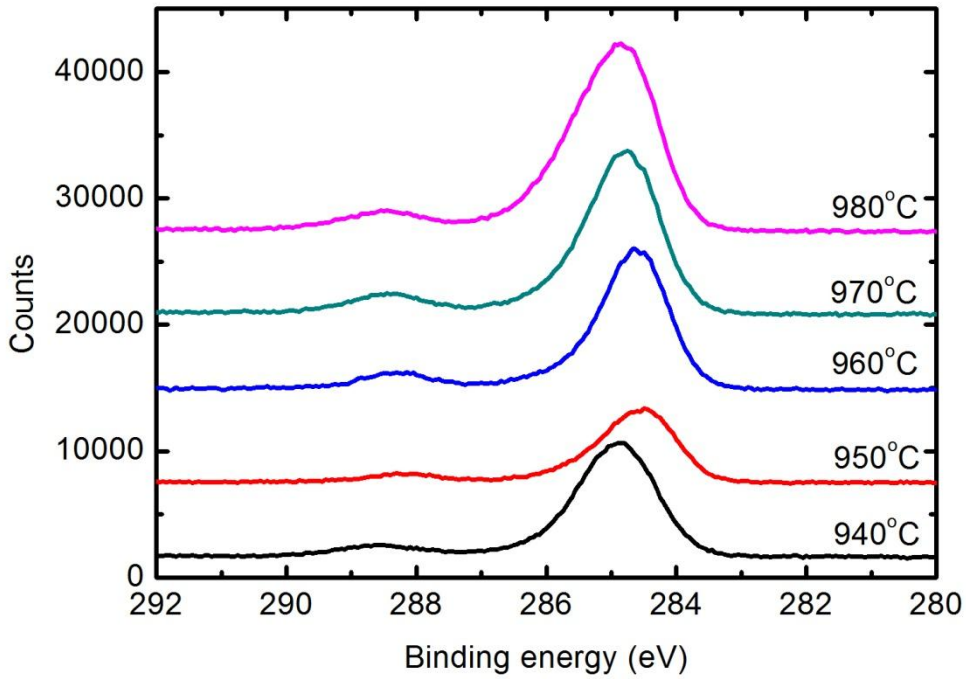

Fig. 5.15: C1*s* photoelectron spectra from graphene films on copper grown at the temperatures indicated. The spectra have been shifted vertically for clarity.

C1*s* X-ray photoelectron spectra from graphene samples grown in the temperature range of 940 – 980ºC are presented in Fig. 5.15. The spectra consist of a broad asymmetric line located at a binding energies between 284.5 and 285 eV with a second peak visible at about 288.5±0.05 eV. Spectra were fitted according to the procedure outlined in Chapter 4, Section 4.3.1.1, by which the number of components was determined through monitoring the evolution of the χ^2 statistic and the shape of the residual spectrum. It was found that three peaks were sufficient to fit the spectra – a Doniac-Šunjić lineshape with an asymmetry

parameter between 0.05 and 0.08 (characteristic of sp^2 bound graphitic carbon carbon[28,29]), a Gaussian/Lorentzian line between 0.5 and 1 eV above the sp^2 line which can be attributed to sp^3 carbon[29,30] and a line 3.8 eV above the main line, which can be associated with carboxylic carbon (O=C-O). An example fit is shown in Fig. 5.16, and the fit parameters for all the spectra presented in Table 5.1.

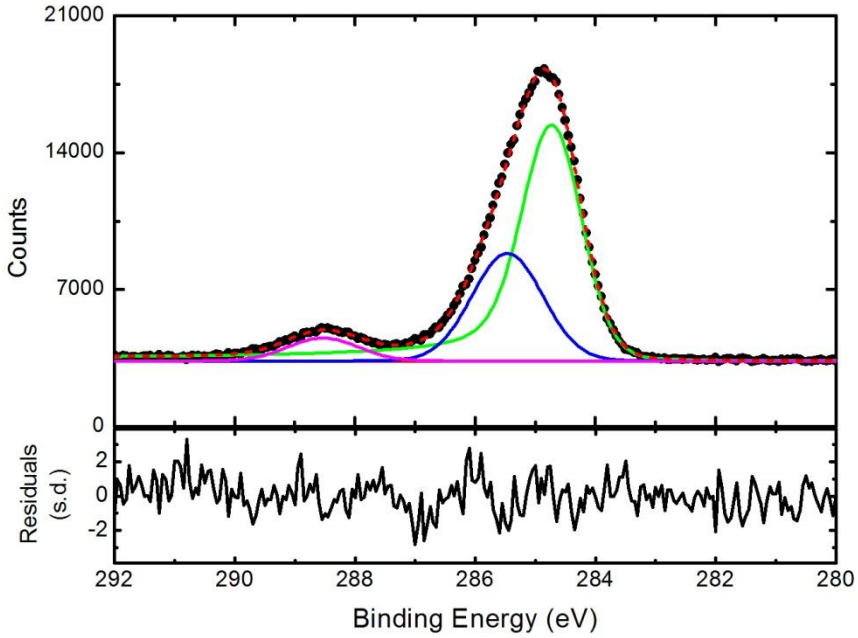

Fig. 5.16: Fit to C1*s* photoelectron spectrum from graphene grown on copper at 980°C (top panel), with associated fit residuals (bottom panel). Dots represent the data points, the dotted line the fit and solid lines the fit components.

It can be seen from Table 5.1 that the main sp^2-related C1*s* component first shifts from a binding energy ~0.3±0.1 eV above that typically expected for graphite (284.4±0.1 eV) at 940°C to the accepted graphite value before shifting upwards again. Survey spectra (not shown) only show peaks originating from Cu, O and carbon and there is no correlation between the sp^2 C1s binding energy, oxygen content, or graphene coverage. Kidambi *et al.*[29] found in an *in-situ* XPS study of CVD growth of graphene on copper from a benzene precursor that, in the absence of oxygen contamination, the main C1*s* line (a Doniac-Šunjić lineshape with an asymmetry parameter of 0.09, consistent with graphitic carbon) was found

at a binding energy of 284.75 eV. However, upon exposure of the monolayer graphene film (thickness checked *ex*-situ by Raman spectroscopy) to air for 45 minutes the main C1*s* component was found to have shifted downward in energy to 284.4 eV, closer to that observed by other groups for *ex-situ* grown graphene films[6,31]. This shift was found to be reversible on annealing in vacuum and was attributed to a 'coupling' (possibly *n*-type doping) of the graphene when in contact with a clean metal surface and decoupling after exposure to ambient air due to intercalation of oxygen beneath the graphene and oxidation of the copper surface[29]. Kidambi and co-workers also reported that there was significant sensitivity of the C1*s* line position to oxygen contamination and that a small amount of air present in their reaction led to both 'coupled' and 'decoupled' C1*s* features in their data[29]. Given that no special precautions were implemented to reduce potential oxygen contamination in the ambient pressure growth experiments reported in this thesis, it is probable that there is an uncontrolled contribution of 'coupled' and 'decoupled' graphene in the data reported in Fig. 5.15 – the small binding energy difference between the C1*s* line from the two graphene states is below the resolution of the spectrometer used in these experiments (~0.48 eV) and would therefore be manifested in a change in the position of the peak resulting from superposition of the two signals. The partial coverage of graphene found in the experiments performed for this thesis prevents the use of the copper core or Auger lines as a means to determine whether or not oxygen intercalation has occurred[29], since the uncovered regions of the copper surface would be directly exposed to the air.

It is important to remark, as pointed out by Kidambi *et al.*[29], that bulk oxidation is a rather different process to the intercalation of oxygen beneath graphene observed by XPS. The former is expected to occur over a timescale of days to weeks and as a result optical measurements such as those reported by Chen *et al.*[25] and in Section 5.3.1 would expect to display oxidation resistance, whilst oxygen intercalation is found to occur over a timescale of minutes.

Growth temperature (°C)		**940**	**950**	**960**	**970**	**980**
***sp*² carbon**	Position (eV)	284.73	284.42	284.57	284.70	284.66
	FWHM (eV)	1.2	1.0	1.0	1.1	1.1
	Asymmetry	0.07	0.05	0.06	0.07	0.07
***sp*³ carbon**	Position (eV)	285.22	285.21	285.55	285.53	285.98
	FWHM (eV)	1.1	1.2	1.1	1.1	1.6
O=C-O	Position (eV)	288.61	288.20	288.32	288.46	288.51
	FWHM (eV)	1.2	1.0	1.0	1.1	1.1

Table 5.1: Fit parameters for the analysis of the C1*s* spectra of Fig. 5.15. Fit errors in peak positions and FWHM are estimated as ±0.05 eV and ±0.1 eV, respectively. The error in asymmetry parameter is ±0.01.

Siokou *et al.*[7] used XPS to analyse graphene films grown on copper by conventional gas-phase CVD with a methane feedstock. The graphene was determined to be predominantly single layer from Raman spectroscopy. In the as-introduced films Siokou and co-workers measured a C1*s* peak which could be fitted by four components with binding energies of 284.5, 285.6, 286.7 and 288.3 eV, which were attributed to sp^2 carbon, sp^3 carbon, C-OH and O-C=O groups respectively. Upon annealing the graphene films in UHV, the C-OH related component was found to reduce rapidly in intensity and had completely vanished at a temperature of 450ºC, whilst the higher lying O-C=O component only vanished at 550ºC, accompanied by a reduction in the intensity associated with sp^3 hybridised carbon. However, electron energy loss spectroscopy experiments indicated that the characteristic plasmon losses associated with graphitic carbon vanish at this temperature, pointing to decomposition. The thermal stability of the carboxylic C1*s* component, which only vanishes close to the point of decomposition suggests that this species, observed in the graphene films reported here, is chemisorbed to the graphene lattice, an assertion supported by the results of Qi and co-workers[27] who only observe such a peak in incomplete graphene films on copper and attribute it to oxidation of the perimeter of graphene islands in contact with CuO. Similarly, oxidation

limited to graphene island edges due to mild oxidising conditions is inferred from Raman spectroscopy data from CVD grown graphene on copper by Han *et al.*[10].

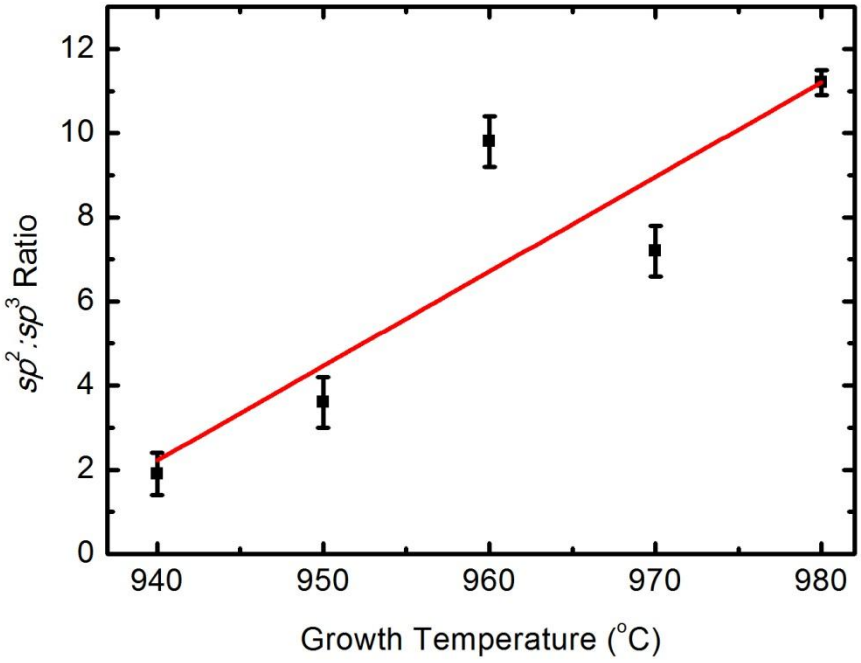

Fig. 5.17: Variation of sp^2 to sp^3 carbon ratio in graphene grown on copper from a nonadecane precursor, as a function of growth temperature. The red line is a linear fit to the data.

To gain further insight into the evolution of the graphene films as a function of growth temperature the ratio between the sp^2 and sp^3 carbon components in the C1*s* core level spectra are plotted as a function of graphene growth temperature, Fig. 5.17. The graph shows a linear trend (red line) demonstrating that, as might be expected from annealing in other mixed sp^2:sp^3 systems[30,32], that there is an increased graphitisation (and hence graphene quality) with annealing temperature despite the relative intensity of the carboxylic carbon component remaining constant, to within error, at a fraction 0.10±0.5 of the total C1*s* area. A similar exercise can be performed using the *W* parameter from the C *KLL* Auger spectra. The variation of *W* with annealing temperature is plotted in Fig. 5.18, with a typical Auger spectrum from a graphene film presented in the inset (the particular example shown is associated with growth at 980°C). The value of *W* rises from about 23 eV, similar to that found in SWCNTs[33,34,35], to around 25.5 eV with increasing growth temperature, confirming

the conclusions drawn from analysis of the C1*s* core level spectra, that graphitisation increases with increasing growth temperature.

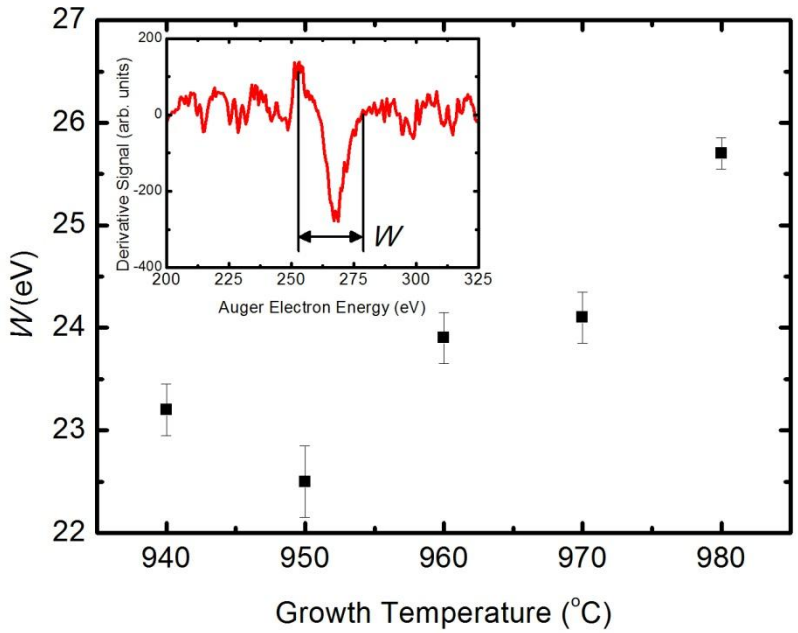

Fig. 5.18: Variation of the parameter *W* as a function of growth temperature. The inset shows a typical derivative Auger spectrum, with the width *W* marked. See text for details.

Returning to the lack of variation in graphene island size and coverage reported in Figs. 5.13 and 5.14, the presence of trace amounts of oxygen in the processes gases during the solid phase CVD growth reported in this thesis offers an attractive explanation. Robinson an co-workers[36] investigated the growth of graphene on single crystal Cu(100) (the most common face expected in cold-rolled foils at typical CVD growth temperatures[37]) both with and without a predosed oxygen layer. They found that predosing the copper surface with oxygen suppressed graphene island nucleation, with an island density about 30 times smaller than that of a clean surface coupled with a lower overall coverage. The reduced nucleation rate was attributed to oxygen blocking terrace sites, while an overall decrease in coverage resulted from reaction of carbon atoms with surface oxygen and subsequent desorption. Given that Robinson *et al.* observe these effects for even half a monolayer oxygen coverage[36], it is likely that the copper surfaces used in the solid phase growth of this work have sufficient contamination to suppress nucleation at terrace sites, limiting initial growth to

defects such as steps, grain boundaries and terraces. Indeed, linear arrays of graphene islands such as that presented in Fig. 5.19 are often observed, which is indicative of such defect-site nucleation[10]. If nucleation only occurs at a limited range of defects then the increased diffusion rate of the 'active' carbon precursors with increasing temperature will have only a small influence upon island nucleation rate, as observed.

On the basis of the data presented here, the conclusion can be drawn that for graphene growth on copper from a soft solid precursor the role of temperature is primarily to control the degree of graphitisation of the films with coverage, island size and oxygen-related impurities found to be constant within the temperature window investigated. The C1*s* line position reflects a variation in graphene-copper interaction which is likely to result from uncontrolled trace oxygen contamination in the growth process, indicating the importance of controlling this parameter in future work.

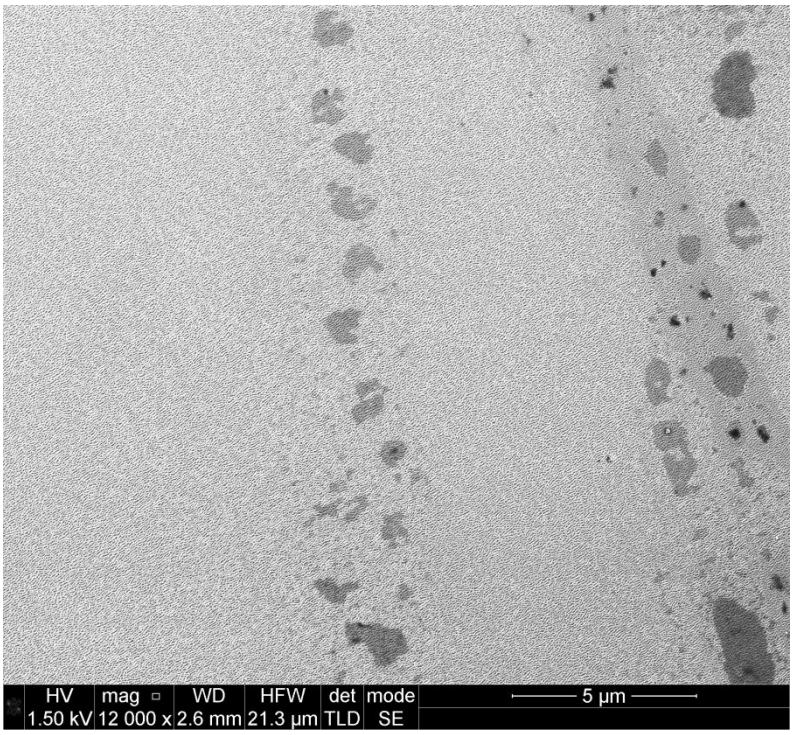

Fig. 5.19 SEM image of graphene island distribution showing a linear array indicative of defect-mediated nucleation.

5.4 Summary

In this chapter the solid phase growth of graphene from a novel soft solid phase precursor (nonadecane) at atmospheric pressure was reported. Growth was successfully achieved at atmospheric pressure without a hydrogen flow. However, the films were found to be incomplete with a maximum surface coverage of approximately 40% achieved. The kinetics of graphene growth were explored and it was found that the variation of island size (or equivalently coverage since they were determined to be linearly related) with time was best described by a kinetic model, previously derived in the literature, which presupposed a continuous supply of precursor. This observation was rationalised in terms of the formation of small amorphous carbon islands on the growth surface during initial heating, which then acted as 'secondary' carbon sources. Variation of the growth temperature was found not to lead to significant changes in island size and coverage, suggesting no changes in graphene nucleation density occurred, contrary to expectations. However, XPS indicated that uncontrolled oxygen contamination may have been present during growth, which would act to suppress nucleation at all except defect sites, in accord with the distribution of graphene islands often observed by SEM in this work. XPS measurements also indicated that the ratio between graphitic and sp^3 hybridised carbon increased with annealing temperature, confirming that increased growth temperature led to increased graphene island quality.

5.5 References

[1] K.S. Novoselov, A. K. Geim, S. V Morozov, D. Jiang, Y. Zhang, S. V Dubonos, I. V Grigorieva, and A.A. Firsov, Science **306**, 666 (2004).
[2] C. Berger, Z. Song, T. Li, X. Li, A.Y. Ogbazghi, R. Feng, Z. Dai, A.N. Marchenkov, E.H. Conrad, P.N. First, and W.A. de Heer, J. Chem. Phys. B **108**, 19912 (2004).
[3] S. Gilje, S. Han, M. Wang, K.L. Wang, and R.B. Kaner, Nano Lett. **7**, 3394 (2007).
[4] S. Eigler, M. Enzelberger-Heim, S. Grimm, P. Hofmann, W. Kroener, A. Geworski, C. Dotzer, M. Rockert, J. Xiao, C. Papp, O. Lytken, H.-P. Steinrueck, P. Müller, and A. Hirsch, Adv. Mater. **25**, 3583 (2013).
[5] Y. Hernandez, V. Nicolosi, M. Lotya, F.M. Blighe, Z. Sun, S. De, I.T. McGovern, B. Holland, M. Byrne, Y.K. Gun'Ko, J.J. Boland, P. Niraj, G. Duesberg, S. Krishnamurthy, R. Goodhue, J. Hutchison, V. Scardaci, A.C. Ferrari, and J.N. Coleman, Nat. Nanotechnol. **3**, 563 (2008).
[6] A. Kumar, A.A. Voevodin, D. Zemlyanov, D.N. Zakharov, and T.S. Fisher, Carbon N. Y. **50**, 1546 (2012).

[7] A. Siokou, F. Ravani, S. Karakalos, O. Frank, M. Kalbac, and C. Galiotis, Appl. Surf. Sci. **257**, 9785 (2011).
[8] C. Mattevi, H. Kim, and M. Chhowalla, J. Mater. Chem. **21**, 3324 (2011).
[9] S. Bae, H. Kim, Y. Lee, X. Xu, J.-S. Park, Y. Zheng, J. Balakrishnan, T. Lei, H.R. Kim, Y. Il Song, Y.-J. Kim, K.S. Kim, B. Ozyilmaz, J.-H. Ahn, B.H. Hong, and S. Iijima, Nat. Nanotechnol. **5**, 574 (2010).
[10] G.H. Han, F. Güneş, J.J. Bae, E.S. Kim, S.J. Chae, H.-J. Shin, J.-Y. Choi, D. Pribat, Y.H. Lee, and F. Güneş, Nano Lett. **11**, 4144 (2011).
[11] H. Kim, C. Mattevi, M.R. Calvo, J.C. Oberg, L. Artiglia, S. Agnoli, C.F. Hirjibehedin, M. Chhowalla, and E. Saiz, ACS Nano **6**, 3614 (2012).
[12] K. Celebi, M.T. Cole, J.W. Choi, F. Wyczisk, P. Legagneux, N. Rupesinghe, J. Robertson, K.B.K. Teo, and H.G. Park, Nano Lett. **13**, 967 (2013).
[13] J. Zhang, P. Hu, X. Wang, and Z. Wang, Chem. Phys. Lett. **536**, 123 (2012).
[14] A.W. Robertson and J.H. Warner, Nano Lett. **11**, 1182 (2011).
[15] Q. Yu, L. a Jauregui, W. Wu, R. Colby, J. Tian, Z. Su, H. Cao, Z. Liu, D. Pandey, D. Wei, T.F. Chung, P. Peng, N.P. Guisinger, E. a Stach, J. Bao, S.-S. Pei, and Y.P. Chen, Nat. Mater. **10**, 443 (2011).
[16] Z. Sun, Z. Yan, J. Yao, E. Beitler, Y. Zhu, and J.M. Tour, Nature **468**, 549 (2010).
[17] G. Ruan, Z. Sun, Z. Peng, and J.M. Tour, ACS Nano **5**, 7601 (2011).
[18] J. Hofrichter, B.N. Szafranek, M. Otto, T.J. Echtermeyer, M. Baus, A. Majerus, V. Geringer, M. Ramsteiner, and H. Kurz, Nano Lett. **10**, 36 (2010).
[19] L. Perdigão, S. Sabki, J.M. Garfitt, P. Capiod, and P.H. Beton, J. Phys. Chem. C **115**, 7472 (2011).
[20] B. Kiraly, E. V Iski, A.J. Mannix, B.L. Fisher, M.C. Hersam, and N.P. Guisinger, Nat. Commun. **4**, 2804 (2013).
[21] H. Ji, Y. Hao, Y. Ren, M. Charlton, W. Lee, Q. Wu, H. Li, Y. Zhu, Y. Wu, R. Piner, and R.S. Ruoff, ACS Nano **9**, 7656 (2011).
[22] R. Weatherup, C. Baehtz, B. Dlubak, B.C. Bayer, P.R. Kidambi, R. Blume, R. Schlogl, and S. Hofmann, Nano Lett. **13**, 4624 (2013).
[23] S. Sharma, G. Kalita, R. Hirano, S.M. Shinde, R. Papon, H. Ohtani, and M. Tanemura, Carbon N. Y. **72**, 66 (2014).
[24] R. Sinclair, T. Itoh, and R. Chin, Microsc. Microanal. **8**, 288 (2002).
[25] S. Chen, L. Brown, M. Levendorf, W. Cai, S.-Y. Ju, J. Edgeworth, X. Li, C.W. Magnuson, A. Velamakanni, R.D. Piner, J. Kang, J. Park, and R.S. Ruoff, ACS Nano **5**, 1321 (2011).
[26] R.M. Jacobberger and M.S. Arnold, Chem. Mater. **25**, 871 (2013).
[27] K.W. Hipps, Y. Qi, U. Mazur, and J.R. Eskelsen, Langmuir **28**, 3489 (2012).
[28] M.R.C. Hunt, Phys. Rev. B **78**, 153408 (2008).
[29] P.R. Kidambi, B.C. Bayer, R. Blume, Z.-J. Wang, C. Baehtz, R.S. Weatherup, M.-G. Willinger, R. Schloegl, and S. Hofmann, Nano Lett. **13**, 4769 (2013).
[30] J. Diaz, G. Paolicelli, S. Ferrer, and F. Comin, Phys. Rev. B **54**, 8064 (1996).
[31] A. Pirkle, J. Chan, A. Venugopal, D. Hinojos, C.W. Magnuson, S. McDonnell, L. Colombo, E.M. Vogel, R.S. Ruoff, and R.M. Wallace, Appl. Phys. Lett. **99**, 2012 (2011).
[32] Y.V. Butenko, S. Krishnamurthy, A.K. Chakraborty, V. Kuznetsov, V.R. Dhanak, M.R.C. Hunt, and L. Šiller, Phys. Rev. B **71**, 075420 (2005).
[33] J. Lascovich, R. Giorgi, and S. Scaglione, Appl. Surf. Sci. **47**, 17 (1991).
[34] Y. Mizokawa, T. Miyasato, S. Nakamura, K.M. Geib, and C.W. Wilmsen, Surf. Sci. **182**, 431 (1987).
[35] R.M. Houchin, Ph.D. Thesis, Durham University, 2011.
[36] Z.R. Robinson, E.W. Ong, T.R. Mowll, P. Tyagi, D.K. Gaskill, H. Geisler, and C.A. Ventrice, J. Phys. Chem. C **117**, 23919 (2013).

[37] Z.R. Robinson, P. Tyagi, T.M. Murray, C.A. Ventrice, S. Chen, A. Munson, C.W. Magnuson, and R.S. Ruoff, J. Vac. Sci. Technol. A Vacuum, Surfaces, Film. **30**, 011401 (2012).

Chapter 6

Solid Phase Growth of Doped Graphene

This chapter presents evidence for the growth of silicon-doped graphene by solid-phase CVD from a polydimethylsiloxane (PDMS)/SiO_2 precursor, obtained by SEM, XPS and Raman spectroscopy.

6.1 Introduction

The absence of a band gap in pristine graphene, touched upon in Section 1.5, is a serious impediment to its adoption as a material for digital electronics – the on:off ratio typically achieved in an unmodified graphene field effect transistor (FET) is < 30 (Ref. [1]), which is orders of magnitude smaller than that found for silicon FET devices (even an early 30 nm channel MOSFET had an on-off ratio of 10^5 – Ref. [2]). As a result, intense experimental and theoretical effort has been brought to bear in order to engineer a band gap in graphene. It has, for example, been recognised that a perpendicular electric field can create a band gap in bilayer graphene without structural or chemical modification[3,4]. However, in order to obtain a band gap of up to ~130 meV and an on:off ratio of 100, back gate voltages of 120 V have to be applied to typical FET structures[5] rendering them impractical for widespread adoption. Strain is also predicted to open a band gap, with tight-binding calculations suggesting a threshold of 20% deformation along preferred directions for gap opening to occur[6], although *ab-initio* calculations[7] suggest that a 1% uniaxial strain should open a gap of 300 meV. Lateral confinement through the creation of quasi one-dimensional graphene nanoribbons (GNRs) has also been shown to induce a band gap through quantum confinement, with band gaps of around 200 meV achieved for lithographically patterned GNRs 15 nm wide[8]. Whilst on:off ratios as high as 10^6 have been achieved in GNR FETs, mobility is much lower than in 'unconfined' graphene[9], likely a result of the defect and edge scattering inherently arising from GNR fabrication.

An alternate approach to the physical modification of graphene or its environment is to achieve a band gap thorough substitutional doping. Direct doping of the hexagonal graphene lattice has typically focussed on the incorporation of nitrogen[10,11,12,13,14,15,16,17] and boron[16,18,19] dopants which would be expected to behave as donors (*n*-type) or acceptors (*p*-type). Wei *et al.* found nitrogen doped graphene grown by chemical vapour deposition from methane and ammonia precursors to behave as an *n*-type semiconductor, although the band gap was not determined[10], while Guo and co-workers did not observe a band gap opening, but did find clear *n*-type behaviour with a carrier mobility superior to that found in GNRs[12].

.

The substitutional incorporation of silicon into the graphene lattice has been predicted, on the basis of density functional theory (DFT) calculations, to open a band gap which is dependent upon silicon concentration, initially increasing (to ~2 eV) until a 1:1 stoichiometry is realised and then decreasing as the material approaches the composition of silicene[20]. Very recently, Ding and Wang[21] reported a computational study of the specific case of a 1:3 Si:C ratio, using an automated searching approach to determine potential low energy (stable) structures. Three dynamically stable structures were found which were energetically degenerate to within error and all of which consisted of planar structures in which there was a hexagonal arrangement of atoms, analogous to graphene. On the basis of DFT calculations one of the structures (meta-SiC_3) was predicted to possess a band gap whilst the other two iso-energetic para-SiC_3 structures remained semimetals, the semiconducting structure arising from a breaking of the symmetry between the two sublattices of the graphene structure. Significantly lower Si dopant concentrations were considered by Denis[22] who examined concentrations between 0.78 and 3.1 at.% and found that, at most, a band gap of < 0.1 eV was induced by doping. Moreover, the magnitude of the band gap did not vary monotonically with Si concentration. In these low concentration systems the silicon atom was found to protrude from the graphene plane resulting from the covalent radius of silicon being greater than that of carbon.

For fully stoichiometric SiC, Huda *et al.*[23] and Bekaroglu *et al.*[24] found in density functional theory (DFT) studies that a planar sp^2 bonded configuration formed a metastable structure despite the large covalent radius of Si making π bonding unfavourable (and leading to the requirement of a supporting substrate for silicene growth[25]) . Moreover, Huda and co-workers[23] found that segregation of silicon and carbon within the layers was unfavourable. However, they also determined that unless layers are stacked with like atoms above each other the planar SiC buckles introducing sp^3 character into the system, described as a 'collapse' into tetrahedral bonding.

Escaño and co-workers[26] theoretically examined the adsorption of silicon atoms and small clusters Si_n (with n = 2,3) and found that while atomic adsorption left graphene in a metallic state the adsorption of a small cluster could open a band gap. This gap was found to decrease upon increasing size from n = 2 to n = 3, which might indicate that it would close

with a sufficiently large Si cluster size. Given that Si is not known to wet graphitic surfaces it would be expected that larger clusters should form.

Silicon doping of graphene has so far only been seen experimentally at the atomic scale inside a transmission electron microscope (TEM) in very recent studies[27,28,29,30] due to 'accidental' incorporation of silicon during graphene growth and/or handling[27]. Yang *et al.*[30] observed two substitutional atoms at a topological defect site followed by insertion of a third silicon atom to form a trimer which rotated with time, while the groups of both Pennycook[27] and Bangert[28] have also observed silicon in both a threefold co-ordinated substitutional (graphitic-like) configuration and in a fourfold configuration occupying a divacancy site. Bangert and co-workers found that the three-fold co-ordinated silicon was most usually found in otherwise pristine regions of the graphene lattice whereas the four-fold co-ordinated silicon was discovered in regions with a high density of defects, such as five and seven membered rings[28]. The two different geometries were found to having differing near-edge electron energy loss spectra (EELS) with the trivalent co-ordination showing an onset at 99 eV and a first maximum at 102.5 eV, while the four-fold co-ordinated silicon shows a peak doublet at 105 and 108 eV. By comparing experimental EELS with that derived from *ab-initio* calculations it was concluded that the Si atom in the trivalent co-ordination buckles out of plane by about 0.1 nm. Similar results were found by Pennycook and co-workers in their slightly earlier study, the key difference being that the EEL spectra found in this case for threefold co-ordinated silicon had a strong peak at about 105 eV with a weak onset at about 101 eV[27]. Both groups come to the conclusion that the out-of plane distortion of the three-fold co-ordinated silicon induces sp^3 character in the silicon dopant, whilst the situation for the four-fold co-ordinated case is more complex and possible reflects an sp^2d configuration in which the silicon *d* orbitals also play a role in bonding[27].

Given the theoretical metastability of two-dimensional silicon-doped graphene and the observation of such doping at an atomic scale within the TEM it is logical to use the solid phase approach outlined in Chapter 5 of this thesis to attempt to produce silicon-doped graphene films and the results of such studies are reported here.

6.2 Experiment

Samples of copper foil 5.0 x 7.0 x 0.1 mm^3 were cleaned sequentially in an ultrasonic bath for 10 minutes in acetone, ~5% concentrated sulphuric acid, isopropyl alcohol (IPA) and then rinsed in distilled water and dried under argon flow. Graphene growth was achieved in the same manner as reported in Chapter 5, Section 5.2: The copper foil was placed into a clean ceramic boat and approx. 5 mg of the polydimethylsiloxane/SiO_2 precursor material placed on top. The substrate and precursor were heated to 1000°C in a Carbolite tube furnace under a stream of argon, before the furnace was switched off and the sample left to cool.

The solid precursor used was Dow Corning Vacuum Grease, containing ~90% polydimethylsiloxane (PDMS) and ~10% silicon dioxide. In order to find the optimum growth conditions, growth time was varied between 5 minutes and 16 hours. Between growth cycles the quartz tube used inside the furnace was rinsed with acetone, IPA and distilled water to reduce cross contamination. As grown samples were investigated by SEM and selected samples measured by Raman spectroscopy and XPS.

6.3 Results and discussion

6.3.1 SEM measurements

Fig. 6.1 presents SEM images from graphene films grown at 1000°C from the PDMS/SiO_2 precursor for growth times of 120 minutes (Fig. 6.1(a)) and 600 minutes (Fig. 6.1(b)). The formation of a partial surface coverage of small islands with lateral dimensions of the order of a micrometre is observed, similar to those observed for growth from a nonadecane precursor, as reported in Chapter 5, Sections 5.3.1 and 5.3.2. The islands appear flat and two-dimensional and are sufficiently transparent to electrons for the morphology of the underlying copper surfaces to be seen beneath. The islands are found to have an irregular geometry with no significant faceting observed, are continuous over surface features and nucleation is inhomogeneous. Given that, apart from the precursor employed, the growth procedure is the same as that reported in Chapter 5 it is unsurprising that the morphology and distribution of the islands should be similar and it is likely that the inhomogeneous distribution of material arises from the same source: that is the presence of trace oxygen

contamination leading to the blocking of reactive sites[31], so provoking preferential nucleation at defects. It is noticeable that there is no evidence of significant contrast variation across the islands, indicating that they are, at least on the lengthscale of the resolution of the SEM (~5 nm) of uniform composition.

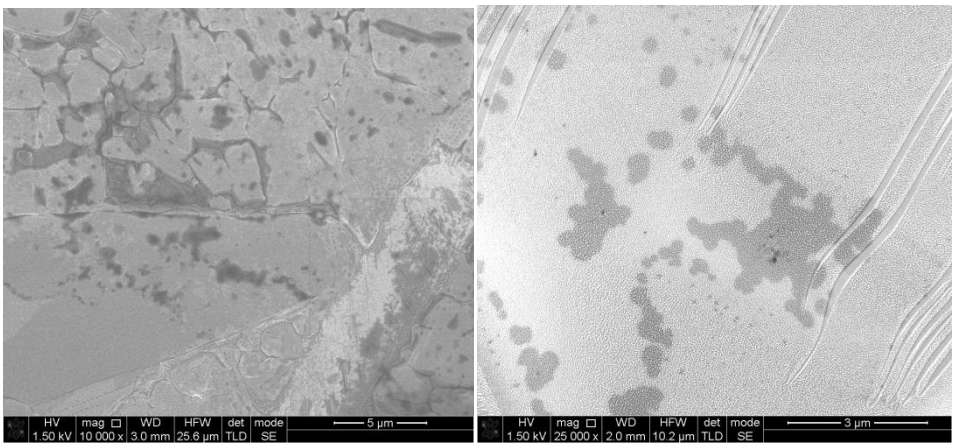

Fig. 6.1: SEM images of graphene grown from a PDMS/SiO_2 precursor under argon gas at 1000ºC: (a) 120 minutes, (b) 600 minutes.

Whilst the islands appear to be of approximately monolayer thickness, SEM imaging provides no compositional information, therefore core-level and Raman spectroscopies are required to furnish this information, as reported in the following sections.

6.3.2 Raman Spectroscopy

As mentioned in Chapter 5, Raman spectroscopy of graphene and doped graphene films on copper is often hampered by a strong fluorescence background from the metal. As a result it is usual, in many studies reported in the literature, to transfer the graphene from the growth substrate to one which has no such background before Raman analysis. An example of the differences in Raman spectra between monolayer graphene films on the copper growth substrate and after transfer to an oxidised silicon substrate is presented in Fig. 6.2 (Ref. [33]). Moreover, a submonolayer coverage of the graphene material, as has been found for all the growth studies reported in this thesis, will exacerbate this problem by reducing the graphene Raman signal still further. As a result of this issue it was only possible to obtain a spectrum

from one of the samples fabricated in this study (600 min) in which Raman peaks could be distinguished from the copper background fluorescence (Fig. 6.3, inset).

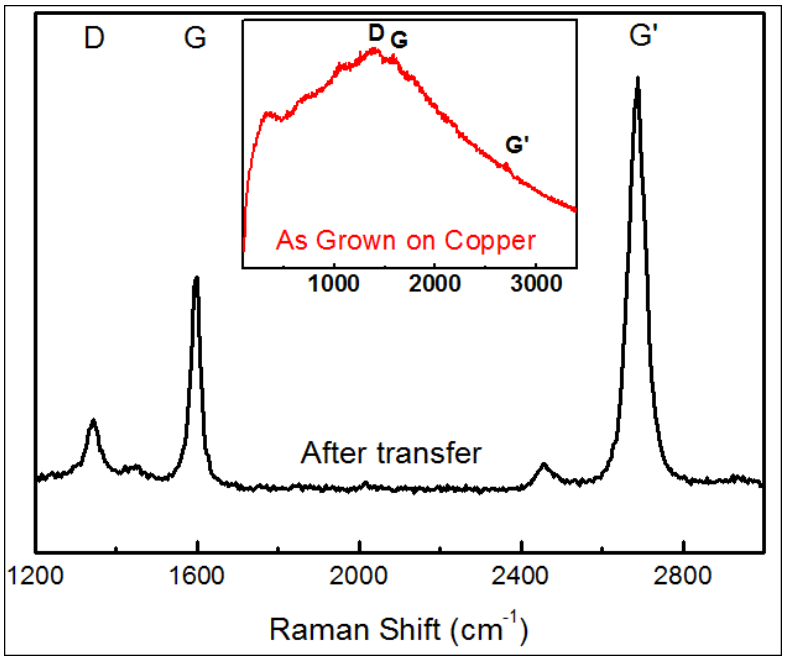

Fig. 6.2: Raman spectra of a CVD grown monolayer as grown on copper (inset) and after transfer to an oxidised silicon substrate. From Celebi[33]

Two sharp Raman lines, located at 1478 and 1216 cm^{-1} with FWHM of ~25 and ~15 cm^{-1} are visible in the spectrum of Fig. 6.3. The main graphene lines in this frequency range are the *G*-band, located at ~1580 cm^{-1} (Ref. [34]) and the defect-related double resonance *D* band[34] which, for an excitation wavelength of 532 nm (2.33 eV), as used for the data in Fig. 6.3, is located at around 1340 cm^{-1} (Ref. [35]) and are clearly very different from those observed here, ruling out the formation of pure graphene as a source of these features. Moreover, the spectra are also rather different from those observed in crystalline SiC, which displays a strong set of overlapping Raman active modes in the range ~1450-1950 cm^{-1} with a major peak at ~1520 cm^{-1} (Fig. 6.4(a))[36,37,38,39], the PDMS/SiO_2 precursor (Fig. 6.4(b)) with strong lines at 1185 and 1333cm^{-1}, the bare Cu substrate (not shown) or SiO_2 (silica)[40]. In consequence, the Raman spectrum of the PDMS/SiO_2 film resembles neither graphene nor bulk, stoichiometric SiC which might be considered the most likely products resulting from catalytic pyrolysis of the precursor material.

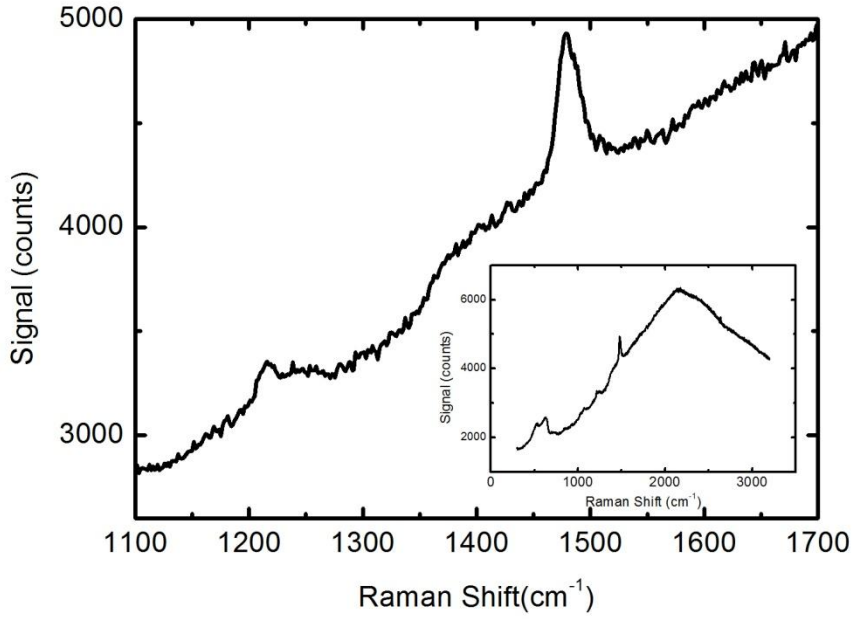

Fig. 6.3: Raman spectrum from a graphene sample grown with a PDMS/SiO_2 precursor, obtained with an excitation wavelength of 532 nm. The inset shows the full spectrum with strong copper fluorescence and low frequency CuO Raman modes visible.

There have been a number of Raman studies of amorphous hydrogenated[41,42,43] and non-hydrogenated[44] silicon carbide alloys of varying composition over the years in which a broad lines (FWHM >100 cm^{-1}) is observed for Raman shifts of between 1400 and 1600 cm^{-1}. Shi and co-workers[44] have undertaken a systematic study of the evolution of the Raman spectrum of non-hydrogenated amorphous silicon/carbon alloys as a function of stoichiometry and found that the position of Raman mode in the 1400 – 1600 cm^{-1} range shifted linearly with composition (Fig. 6.5). These results were interpreted in terms of the formation of a silicon-doped sp^2 carbon component within the *a*-Si:C matrix with the Raman mode in question corresponding to the *G* band of undoped sp^3 carbon and softening with increasing silicon content due to the larger mass of silicon compared with carbon. It is tempting to analyse the results presented in Fig. 6.3 within the framework developed by Shi *et al.*, in which case the Raman spectrum shown would correspond to an sp^2 bound carbon material incorporating approximately 25 ± 4 at.% silicon. The narrow width of the Raman

lines in Fig. 6.3, compared with that found by Shi *et al.* in their amorphous material suggests that the solid phase growth reported here leads to the formation of a film with a high degree of structural order.

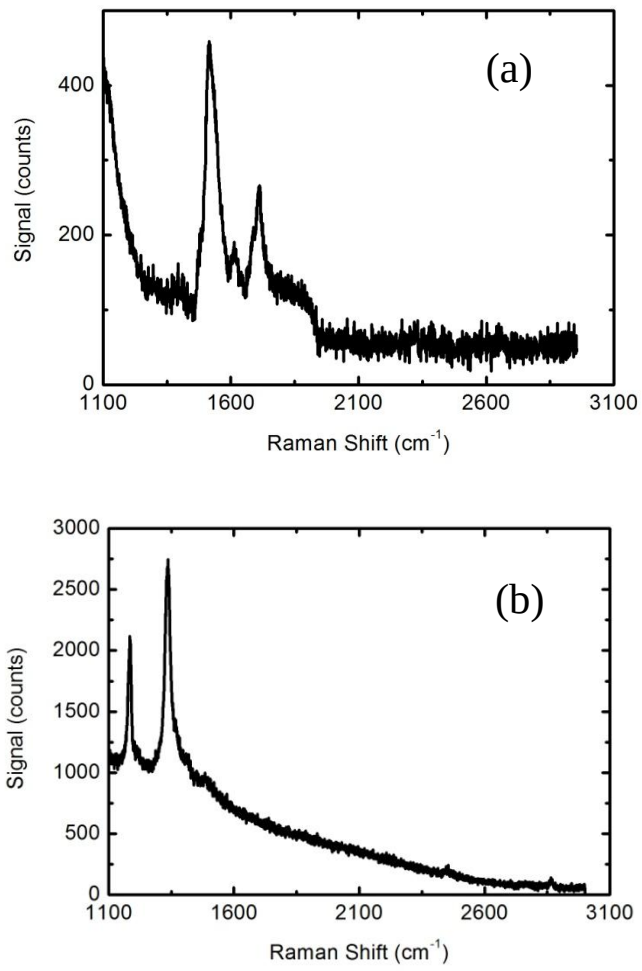

Fig. 6.4: Raman spectrum from (a) 6*H*-SiC and (b) the PDMS/SiO_2 precursor, obtained at an excitation wavelength of 532 nm (Ref. [39]).

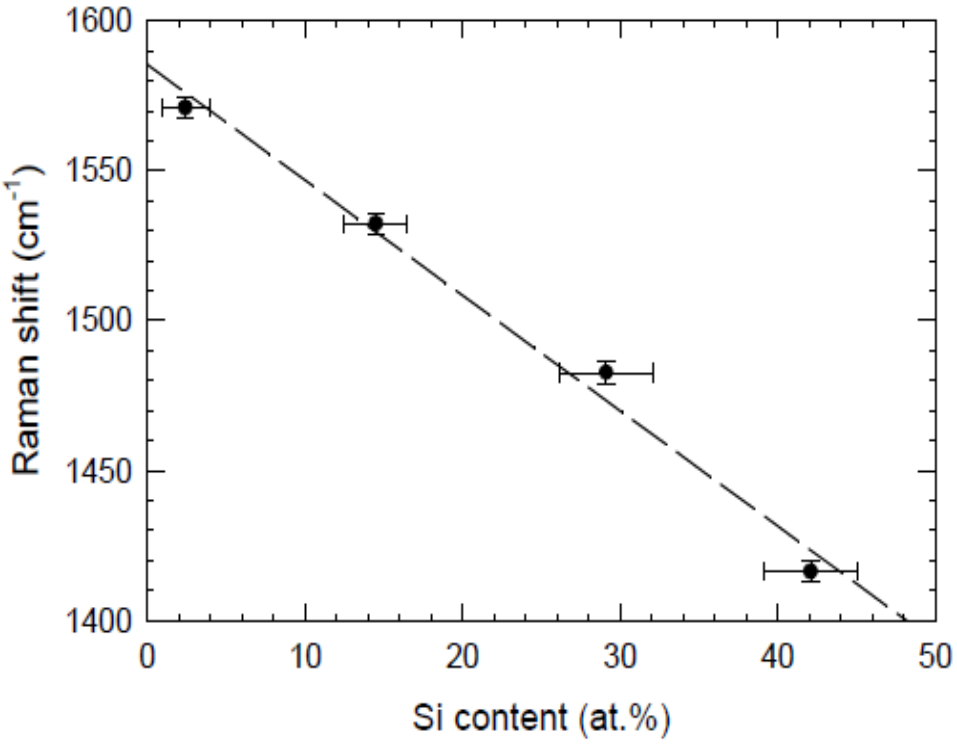

Fig. 6.5: Relationship between Raman *G* peak position and silicon doping in *a*-Si:C found by Shi and co-workers[44]

6.3.3 XPS measurements

In order to differentiate between the unreacted precursor and any graphene-related material that may have been produced during the growth process, it is important to have a clear understanding of the photoemission spectrum of that precursor. Core-level spectra from the polydimethylsiloxane/SiO_2 precursor used for this study are shown in Fig. 6.6. A broad, unresolved Si2*p* doublet is observed at a binding energy of 102 eV (Fig. 6.6(a)) and a C1*s* line consisting of a main peak at 284.4 eV with a smaller component at 288.3 eV (Fig. 6.6(b) is also presented). The position and width of the Si2*p* line is consistent with that reported for undoped PDMS films[45], as is the main C1*s* line. The secondary C1*s* line, which can be associated with carboxylic carbon[46], appears rather strong to arise from adventitious contamination from the ambient atmosphere and may be related to additives/contamination of the precursor material.

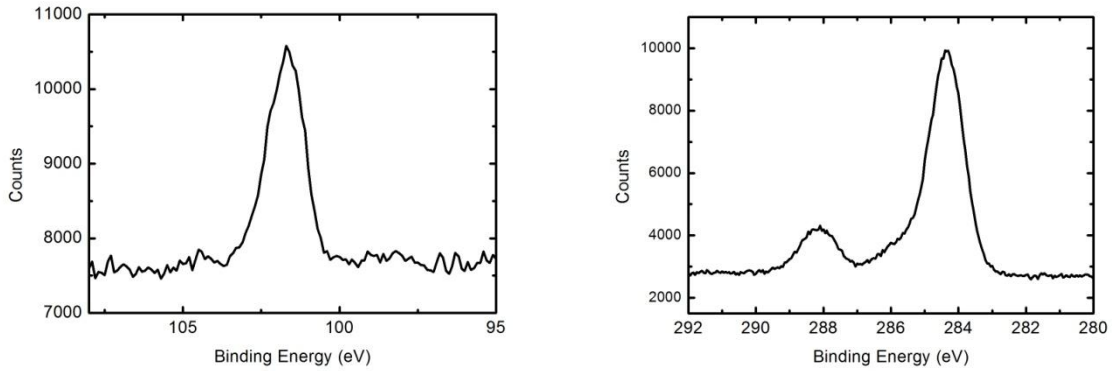

Fig. 6.6: X-ray photoelectron spectra of (a) the Si2*p* and (b) C1*s* core levels of the PDMS/SiO_2 precursor used in the graphene growth reported in this Chapter.

The Si2*p* and C1*s* core level spectra of a doped film grown at 1000°C for 600 minutes are shown in Figs. 6.7(a) and 6.7(b), respectively and are clearly very different from that of the precursor material and of bulk SiC[47,48] in which the C1*s* line is found at a binding energy of 283.4 to 283.7 eV with the Si2*p* doublet located at 101.1 to 101.3 eV. Johansson *et al.*[47] studied the graphitisation of the 6*H* SiC(0001) surface, which is known to lead to the formation of one or more graphene layers separated by a silicon containing carbon-rich buffer layer corresponding to the $6\sqrt{3}$ x $6\sqrt{3}R30°$ ($6\sqrt{3}$) surface reconstruction[48]. The C1*s* spectrum from the $6\sqrt{3}$ surface consists of a number of components associated with the bulk and with the partially graphitised surface, the main C1*s* surface component being a relatively broad line located at a binding energy of 285.3 eV with a narrower, weaker component at 285.7 eV. The Si2*p* spectrum from the $6\sqrt{3}$ surface also shows both bulk and surface components with the two surface doublets located at 100.3 eV and 99.7 eV binding energy. Upon heating beyond the formation of the $6\sqrt{3}$ surface graphitisation was found to occur with a strong C1*s* line appearing at 284.7 eV and an interface-related component (associated with the $6\sqrt{3}$ buffer layer) present at 285.3 eV binding energy. In their study of few-layer graphene films on SiC(0001) formed by thermal graphitisation Ferrah *et al.*[48] also observed two 'interfacial' C1*s* components – a strong peak at 285.6±0.1 eV and a weaker peak at 284.8±0.1 eV – in addition to the graphene-related C1*s* line.

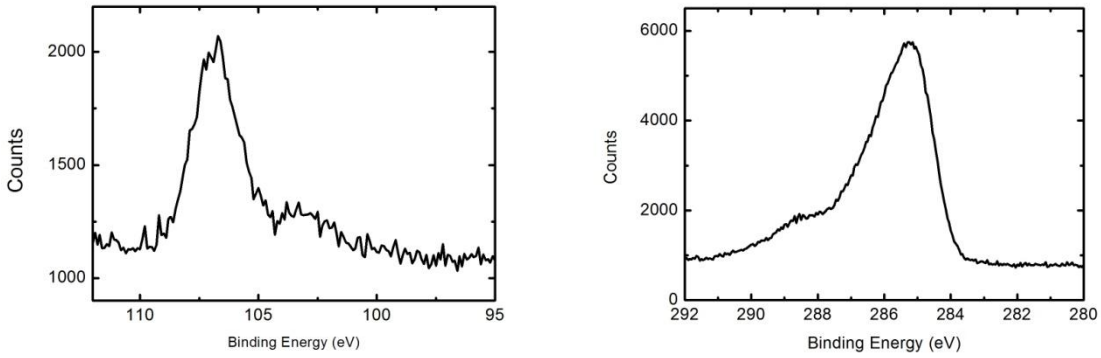

Fig. 6.7: X-ray photoelectron spectra of (a) the Si2*p* and (b) C1*s* core levels of the graphene film grown from a PDMS/SiO_2 precursor at 1000°C for 600 min.

The main peak in Fig. 6.7(b) is found at approximately 285.2 eV binding energy and corresponds well with the C1*s* binding energies found for the carbon-rich $6\sqrt{3}$ surface of SiC(0001)[47,48], which can be regarded as a silicon-doped graphene structure bound to the bulk SiC, whilst the shoulder at ~288.6 eV is likely to arise from carboxylic carbon, possibly from ambient contamination as discussed above or bound directly to graphene, as suggested in Chapter 5. It is therefore reasonable to conclude that the C1*s* photoelectron spectra from films grown from a PDMS/SiO_2 precursor are not incompatible with the suggestion that such growth results in silicon-doped graphene.

The Si2*p* spectrum shown in Fig. 6.7(a) is broad, with a strong feature at a binding energy of 106.8 eV and a weaker component located at 102.6 eV. The latter feature can be explained by the formation of mixed silicon-carbon oxides[48], but the former is at too high a binding energy to be associated with previously reported oxides or carbides. Gross charging of the sample surface and/or spectrometer mis-calibration can be ruled out since the core-lines from the copper substrate appear at the expected binding energies, while both strong Si2*p* and 2*s* lines appear shifted upward from their bulk binding energies by the same amount (Fig. 6.8). This leaves two possibilities to explain the Si2*p* binding energy observed in the films grown from PDMS/SiO_2: (a) the line actually corresponds to oxidised Si (possibly in the form of small particles, too small to be resolved by SEM) shifted upwards in binding energy due to charging related to poor electrical contact with the copper substrate, which Cu2*p* core level spectra (not shown) indicate is heavily oxidised. Such a binding energy shift would be similar to that seen for small Ag islands on C_{60} layers arising from poor

neutralisation[49]. (b) that the most intense line is associated with silicon doped into a graphene film. Further investigations, for example through the theoretical determination of core-level binding energies in silicon-doped graphene, are required before a definitive conclusion can be reached.

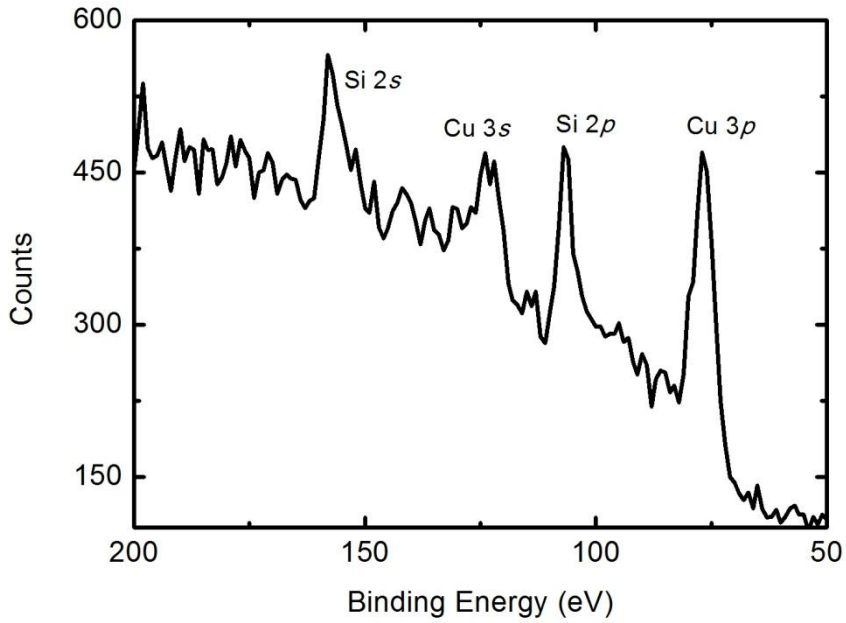

Fig. 6.8: X-ray photoelectron spectrum displaying both Si and Cu shallow core levels. The position of the copper peaks is as would be expected, whilst the Si peaks are shifted upward from their typical binding energies in silicon compounds.

6.4 Summary

The results of the solid phase growth of graphene films from a PDMS/SiO_2 precursor have been described in this Chapter. SEM measurements suggest the growth of thin planar islands compatible with previous observations of graphene (see Chapter 5). Raman spectroscopy indicates that these islands may possess a significant (approximately 25%) silicon content, a suggestion supported by C1*s*, and possibly Si2*p* core-level photoelectron spectra.

6.5 References

[1] K.S. Novoselov, A. K. Geim, S. V Morozov, D. Jiang, Y. Zhang, S. V Dubonos, I. V Grigorieva, and A.A. Firsov, Science **306**, 666 (2004).
[2] H. Kawaura, T. Sakamoto, T. Baba, Y. Ochiai, S. Matsui, and J. Sone, IEEE Electron Device Lett. **19**, 74 (1998).
[3] E. McCann, Phys. Rev. B **74**, 161403 (2006).
[4] E. Castro, K. Novoselov, S. Morozov, N. Peres, J. dos Santos, J. Nilsson, F. Guinea, a. Geim, and a. Neto, Phys. Rev. Lett. **99**, 216802 (2007).
[5] F. Xia, D.B. Farmer, Y.-M. Lin, and P. Avouris, Nano Lett. **10**, 715 (2010).
[6] V. Pereira, A. Castro Neto, and N. Peres, Phys. Rev. B **80**, 045401 (2009).
[7] Z.H. Ni, T. Yu, Y.H. Lu, Y.Y. Wang, Y.P. Feng, and Z.X. Shen, ACS Nano **2**, 2301 (2008).
[8] M. Han, B. Özyilmaz, Y. Zhang, and P. Kim, Phys. Rev. Lett. **98**, 206805 (2007).
[9] X. Wang, Y. Ouyang, X. Li, H. Wang, J. Guo, and H. Dai, Phys. Rev. Lett. **100**, 206803 (2008).
[10] D. Wei, Y. Liu, Y. Wang, H. Zhang, L. Huang, and G. Yu, Nano Lett. **9**, 1752 (2009).
[11] Z. Luo, S. Lim, Z. Tian, J. Shang, L. Lai, B. MacDonald, C. Fu, Z. Shen, T. Yu, and J. Lin, J. Mater. Chem. **21**, 8038 (2011).
[12] B. Guo, Q. Liu, E. Chen, H. Zhu, L. Fang, and J.R. Gong, Nano Lett. 4975 (2010).
[13] D. Geng, S. Yang, Y. Zhang, J. Yang, J. Liu, R. Li, T.-K. Sham, X. Sun, S. Ye, and S. Knights, Appl. Surf. Sci. **257**, 9193 (2011).
[14] R. Podila, J. Chacón-Torres, J.T. Spear, T. Pichler, P. Ayala, and a. M. Rao, Appl. Phys. Lett. **101**, 123108 (2012).
[15] Y. Wang, Y. Shao, D.W. Matson, J. Li, and Y. Lin, ACS Nano **4**, 1790 (2010).
[16] P. Nath, S. Chowdhury, D. Sanyal, and D. Jana, Carbon N. Y. **73**, 275 (2014).
[17] K. Brenner and R. Murali, Appl. Phys. Lett. **98**, 113115 (2011).
[18] X. Lü, J. Wu, T. Lin, D. Wan, F. Huang, X. Xie, and M. Jiang, J. Mater. Chem. **21**, 10685 (2011).
[19] S. Graphene, Y.A. Kim, K. Fujisawa, H. Muramatsu, T. Hayashi, M. Endo, C. Casiraghi, K.S. Novoselov, R. Saito, and M.S. Dresselhaus, ACS Nano **6**, 6293 (2012).
[20] M.S.S. Azadeh, a. Kokabi, M. Hosseini, and M. Fardmanesh, Micro Nano Lett. **6**, 582 (2011).
[21] Y. Ding and Y. Wang, J. Phys. Chem. C **118**, 4509 (2014).
[22] P.A. Denis, Chem. Phys. Lett. **492**, 251 (2010).
[23] M.N. Huda, Y. Yan, and M.M. Al-jassim, Chem. Phys. Lett. **479**, 255 (2009).
[24] E. Bekaroglu, M. Topsakal, S. Cahangirov, and S. Ciraci, Phys. Rev. B **81**, 1 (2010).
[25] A. Kara, H. Enriquez, A.P. Seitsonen, L.C. Lew Yan Voon, S. Vizzini, B. Aufray, and H. Oughaddou, Surf. Sci. Rep. **67**, 1 (2012).
[26] M.C. Sison Escaño, T. Quang Nguyen, and H. Kasai, Chem. Phys. Lett. **515**, 85 (2011).
[27] W. Zhou, M. Kapetanakis, M. Prange, S. Pantelides, S. Pennycook, and J.-C. Idrobo, Phys. Rev. Lett. **109**, 206803 (2012).
[28] Q.M. Ramasse, C.R. Seabourne, D.-M.M. Kepaptsoglou, R. Zan, U. Bangert, and A.J. Scott, Nano Lett. (2013).
[29] T. Susi, J. Kotakoski, D. Kepaptsoglou, C. Mangler, T.C. Lovejoy, O.L. Krivanek, R. Zan, U. Bangert, P. Ayala, J.C. Meyer, and Q. Ramasse, Phys. Rev. Lett. **113**, 115501 (2014).
[30] Z. Yang, L. Yin, J. Lee, W. Ren, H.-M. Cheng, H. Ye, S.T. Pantelides, S.J. Pennycook, and M.F. Chisholm, Angew. Chem. Int. Ed. Engl. **53**, 8908 (2014).
[31] Z.R. Robinson, E.W. Ong, T.R. Mowll, P. Tyagi, D.K. Gaskill, H. Geisler, and C.A. Ventrice, J. Phys. Chem. C **117**, 23919 (2013).
[32] A.C. Ferrari and D.M. Basko, Nat. Nanotechnol. **8**, 235 (2013).

[33] K. Celebi, Ph.D. Thesis, ETH Zurich, 2013.
[34] A.C. Ferrari, J.C. Meyer, V. Scardaci, C. Casiraghi, M. Lazzeri, F. Mauri, S. Piscanec, D. Jiang, K.S. Novoselov, S. Roth, and a. K. Geim, Phys. Rev. Lett. **97**, 1 (2006).
[35] I. Pocsik, M. Hundhausen, M. Koos, and L. Ley, J. Non. Cryst. Solids **227-230**, 1083 (1998).
[36] Z. Ni, W. Chen, X. Fan, J. Kuo, T. Yu, a. Wee, and Z. Shen, Phys. Rev. B **77**, 1 (2008).
[37] C. Faugeras, A. Nerrière, and M. Potemski, Appl. Phys. Lett. **92**, 011914 (2008).
[38] J. Röhrl, M. Hundhausen, K. V. Emtsev, T. Seyller, R. Graupner, and L. Ley, Appl. Phys. Lett. **92**, 201918 (2008).
[39] M.R.C. Hunt, *Private Communication* (2014).
[40] G.E. Walrafen, J. Chem. Phys. **74**, 5328 (1981).
[41] M. Veres, M. Koós, S. Tóth, M. Füle, I. Pócsik, a. Tóth, M. Mohai, and I. Bertóti, Diam. Relat. Mater. **14**, 1051 (2005).
[42] C. Ricciardi, a. Primiceli, G. Germani, a. Rusconi, and F. Giorgis, J. Non. Cryst. Solids **352**, 1380 (2006).
[43] B.P. Swain, Surf. Coatings Technol. **201**, 1589 (2006).
[44] J. Shi, X. Shi, Z. Sun, E. Liu, H. Yang, L. Cheah, and X. Jin, J. Phys. Condens. Matter **11**, 5111 (1999).
[45] D. Briggs and G. Beamson, *The XPS of Polymers Database* (Surface Spectra, 2000).
[46] C.D. Wagner, W.M. Riggs, L.E. Davis, J.F. Moulder, and G.E. Milenberg, *Handbook of X-Ray Photoelectron Spectroscopy* (Perkin-Elmer, 1978).
[47] L. Johansson, F. Owman, and P. Mårtensson, Phys. Rev. B. Condens. Matter **53**, 13793 (1996).
[48] D. Ferrah, J. Penuelas, C. Bottela, G. Grenet, and a. Ouerghi, Surf. Sci. **615**, 47 (2013).
[49] M.D.R. Taylor, P. Moriarty, B.N. Cotier, M.J. Butcher, P.H. Beton, and V.R. Dhanak, Appl. Phys. Lett. **77**, 1144 (2000).

Chapter 7

Summary, Conclusions and Future Work

In this chapter, the work presented in this thesis is summarised. Potential future work addressing as yet unresolved issues raised in previous chapters is suggested,

7.1 Summary

Although graphene and carbon nanotubes display a range of outstanding and potentially valuable physical/chemical properties, as outlined in Chapter 1, it is recognised that the introduction of dopants is required in order to modify their behaviour in a desirable fashion. In particular, nitrogen can be incorporated into the graphitic lattice of a SWCNT in a number of bonding configurations, with the resulting modification of physico-chemical behaviour dependent upon bonding type, as discussed in Chapter 4. For example, incorporation of nitrogen species can promote the oxygen reduction reaction (ORR), although the precise species involved is still controversial.

To investigate nitrogen doping in SWCNT films nitrogen atoms were introduced by two ion-mediated approaches: direct irradiation with nitrogen ions and a new technique involving the reaction of gaseous nitrogen with pre-existing defects in the SWCNT samples introduced by irradiation with inert gas ions. This latter technique exploits the observation, made for the first time in this work, that (predominantly vacancy) defects in SWCNTs are sufficiently reactive to abstract nitrogen atoms from the ambient atmosphere at room temperature to form chemically bound (pyrrolic) nitrogen. Annealing carbon nanotubes which had been damaged by irradiation with Ar+ ions of 2.5 keV energy to a dose of $12\pm1\mu C/cm^2$ in nitrogen substantially increased the chemisorbed nitrogen content, which was still dominated by pyrrolic species. However, annealing at higher temperatures eventually led to the loss of pyrrolic species whilst graphitic and pyridinic species remained. Direct ion bombardment provided a differing relative concentration of the nitrogen bonding configurations and provided the greatest proportion of substitutional nitrogen, although this was at the cost of increased sample damage.

The position of the main C1*s* component of the nitrogen doped nanotubes was found to be sensitive only to the graphitic nitrogen content, the first recognition of this phenomenon. The linear dependence of the main C1*s* component on graphitic nitrogen content demonstrated that nitrogen in this substitutional position produced *n*-type doping, in agreement with theoretical work and transport measurements in the literature. The

independence of C1*s* line position on total nitrogen content suggested that other nitrogen configurations either do not dope the SWCNTs or that the doping is weak.

In previous work Raman spectroscopy was used to infer nitrogen concentration based on the ratio between the intensity of the 'defect-related' *D* band and the pristine *G* band (related to vibrations in the plane of the SWCNT wall), the so-called I_D/I_G ratio. In this work no such relationship was seen, instead the I_D/I_G ratio was found to depend on the *total* concentration of defects which was dependent on preparation method and nitrogen content. Despite doping clearly being observed through the shift of the main C1*s* component in XPS, no shift was observed in the main *G*-band components, which might be expected upon doping, indicating that a relatively modest degree of doping had been achieved.

A novel soft solid phase CVD based growth approach using a nonadecane precursor was used to produce graphene on copper surfaces. Graphene islands were successfully produced and observed by SEM, although complete coverage could not be achieved. The two current models for graphene gowth on copper by CVD were used to analyse the kinetics of growth and it was found that a 'dispersive kinetic' model was the most appropriate. This model is appropriate for a continuous supply of 'active' carbon species for graphene growth, which is suggested to originate from islands of amorphous carbon formed on the opposite side of the substrate from the precursor, due to diffusion.

XPS and SEM were used to evaluate graphene growth from nonadecane as a function of the growth temperature. It was found that changing growth temperature had no significant systematic effect upon coverage or island size. However, XPS spectra demonstrated that as the annealing temperature increased the graphitisation (or quality) of the graphene films improved.

Although the solid phase technique was not successful in producing complete graphene coverage, the approach was used to explore the growth of silicon-doped graphene from a PDMS precursor. Silicon-doped graphene has great potential in that it is predicted to possess the band gas that graphene lacks, making it potentially useful in digital electronics. Raman spectra, SEM and XPS indicate that monolayer islands of Si doped graphene with a doping level of ~25% could be achieved, indicating that this is a promising route for doped graphene growth.

7.2 Further Work

The results reported in this thesis and summarised in the previous section suggest a number of routes by which our understanding of doping in SWCNTs and graphene and the soft solid phase growth of graphene could be improved in future work. Open questions arising from the nitrogen doping of SWCNTs include the apparent contradiction between the doping observed by the shift in C1*s* line position and the absence of hardening/softening of the Raman *G* lines. These results are suggestive of a limited doping concentration, but it would be productive to test this hypothesis. This could be achieved, for example, through theoretical calculation of the doping levels required to produce a rigid band shift equal to the C1*s* binding energy change which could be compared with the effects of such a level of doping previously reported for electrochemically doped SWCNTs and graphene. Given that it is possible to produce samples in which a particular chemisorbed nitrogen species is dominant, it would be highly productive to find conditions under which a single species could be exclusively produced. Parameters such as ion energy, dose, flux and sample temperature might be explored for 'direct' irradiation with inert ions whilst process temperature and gas composition (perhaps even the use of a nitrogen containing organic vapour such as pyridine) could be varied for the irradiation and annealing approach.

The preparation of copper surfaces may have a profound effect upon graphene growth as could the presence of oxygen containing contamination. In order to determine their roles in the growth of pristine and doped graphene from soft solid phase precursors it would be useful to consider a range of different substrate polishing/etching routes and compare their impact upon coverage and graphene quality. Similarly, the effect of oxygen on the process should be pursued by growth under vacuum – even if the ultimate aim is atmospheric pressure growth, any observation of a detrimental impact from oxygen contamination could be addressed through the use of ultra-pure gases and careful system purging.